THREE-DIMENSIONAL HOLOGRAPHIC OPTICAL ELEMENTS BASED ON NEW MICROSYSTEMS

Tyurin A.V., Zhukov S.A., Akhmerov A. Yu.

THREE-DIMENSIONAL HOLOGRAPHIC OPTICAL ELEMENTS BASED ON NEW MICROSYSTEMS

Monograph

2024

1

Recommended for publication by the
Academic Council
Odessa I. I. Mechnikov National University
Proc. № 10 dated 05.10.2022

Reviewers:

Gokhman A. R. – Doctor of Physical and Mathematical Sciences, Professor, Head of the Department of Physics, South Ukrainian State Pedagogical University named after K. D. Ushinsky;

Poletaev N. I. – Professor of the Department of Technical Cybernetics and of Information Technologies named after prof. R. V. Merkt of Odessa National Maritime University;

Nesterenko S. A. – Doctor of Technical Sciences, Professor, First Vice-Rector of the National University "Odessa Polytechnic".

The technology of creation of three-dimensional holographic optical elements with controlled characteristics on the basis of heterophase microsystem "CaF_2 core – $AgBr$ shell", alkaline halide crystals (AHC) and chalcogenide glassy semiconductors (CGS) is proposed. We also consider the applications of holographic optical elements based on three-dimensional transmitting diffraction structures for solving some practical problems. For students, graduate students, researchers.

TABLE OF CONTENT

INTRODUCTION

The origination and improvement of holographic methods, as well as technical equipment for their implementation [1–3] revived interest in light diffraction in three-dimensional periodic structures [4]. This is due to the fact that holographic methods allow to create a relatively simple and affordable technology for the manufacture of three-dimensional diffraction structures for both transmitted and reflected electromagnetic radiation of the visible range of the spectrum. Previously, light diffraction was used only in two-dimensional periodic diffraction structures, the manufacture of which was possible by other methods (chemical, photographic, mechanical, etc.) [5]. Diffraction in three-dimensional periodic structures for transmitted radiation has become widespread only for *X*-rays, for which a crystal lattice of various substances could be used as a three-dimensional periodic structure [6]. The use of diffraction of electromagnetic radiation of the visible spectrum on holographic three-dimensional structures (holograms) for practical purposes allows to create optical elements and optoelectronic devices of a fundamentally new class based on them, which have the widest range of applications [7–13].

For the first time the basic principles of obtaining three-dimensional diffraction structures for both transmitted and reflected electromagnetic radiation of the visible range of the spectrum by holographic optics (transmitting and reflecting holograms) were formulated by Denisyuk Yu.N. in 1962 [14]. The basis of this technology was a three-dimensional light-sensitive environment that provides registration (recording) of the interference pattern in its entirety. In order for the three-dimensional properties of diffraction (reading) on such a hologram to be most

pronounced, the thickness of the hologram should be ≈ 100 *μm* or more [15], and diffraction should be carried out not only by changing the absorption coefficient of light-sensitive layer, as in traditional silver containing photoemulsions (amplitude hologram), but also as a result of changes in the refractive index of the layer (phase hologram). In the case of pure phase hologram light losses at diffraction should be minimal and diffraction effectiveness may reach 100% [16].

In the development of light-sensitive carriers, there are two approaches to three-dimensional holograms, which provide diffraction when reading in transmitted light, as well as preservation at room temperature and diffraction in the absence of recording light. The first of them is a two-stage process [17–20]. In the first stage – exposure at room temperature – the recording medium plays a passive role, memorizing the distribution of intensities of beams passing through it, in the second stage, using various chemical and photographic treatments, also at room temperature, this distribution is amplified and fixed. The use of silver halide compounds [21] provides a two-step process, both of which are realized at room temperature, an important advantage, such as high (boundary) sensitivity to hologram recording. But dividing possibility of such holograms with high diffractive effectiveness did not exceed 1000 *lines*/*mm* [22].

The second way is to move to non-silver environments [23–26]. The most promising from this point of view are photochromic systems based on colored alkaline halide crystals (AHS) and chalcogenide glassy semiconductors (CGS) [27–32]. These materials do not require any intermediate work and change their optical characteristics directly under

the action of radiation, forming in the volume of the medium at elevated temperatures amplitude-phase hologram, which provides diffraction in light, as modulation of the absorption coefficient and refractive index. When cooled to room temperature, they are resistant to reading with high diffraction efficiency and angular selectivity [8, 31]. For such holograms, the stages of formation (at elevated temperatures) and fixation (by cooling to room temperature) are inextricably linked and occur simultaneously, and the process of recording-fixation can be considered as one-stage. The main disadvantage of such environments is the need for elevated temperatures and low sensitivity in rather narrow range ($400-650$ nm) of optical radiation, under the action of which a three-dimensional diffractive structure is formed.

In this paper, for the registration of three-dimensional transmitting holograms at room temperature, we proposed an emulsion containing a heterophase microsystem "core CaF_2 – shell $AgBr$", which provides recording of holograms with high resolution and diffraction efficiency; high (boundary) sensitivity and wide spectral range ($400-1000$ nm) optical radiation, under the action of which a three-dimensional hologram is formed. We also consider our proposed applications of holographic optical elements based on three-dimensional transmitting diffraction structures to solve some practical problems.

Photochemical transformations in monolithic CGSs of *As-S* composition corresponding to holographic recording are considered. When using photochromic systems based on colored alkali-halide crystals and chalcogenide glassy semiconductors for the registration of three-dimensional transmitting holograms at elevated temperatures, we

9

proposed spatial stabilization of the recording interference pattern, which achieves optimal characteristics of the recorded holograms. We also consider our proposed applications of optical elements based on three-dimensional transmitting diffraction structures to solve some practical problems.

CHAPTER 1. MANUFACTURE TECHNOLOGY, PROPERTIES AND SPECTRAL SENSITIZATION OF EMULSIONS CONTAINING MICROSYSTEMS "NON-SILVER NUCLEAR – SILVER HALIDE SHELL"

Extensive opportunities to solve the problem of creating photosensitive materials with new properties, to register three-dimensional transmitting holograms that more fully meet modern requirements, open when creating composite systems that combine the properties of both silver and non-silver halides. The basis of these systems are heterophase microsystems type "non-silver core – silver halide shell" and the production of such systems is one of the tasks of nanotechnology, the relevance of which is emphasized throughout the development of modern science and technology. The presence of two regions in heterophase microsystems – non-silver and silver halide, causes the appearance in the system a number of new properties and capabilities when used for holographic recording[33].

1.1 Obtaining emulsions containing microsystems "non-silver core – silver halide shell"

In the synthesis of the proposed emulsions it is necessary to ensure the fulfillment of two conditions:

1) the silver halide in the emulsion should settle in the form of thin, preferably solid, shells on extraneous particles – nuclei, and not a separate phase;

2) emulsions containing heterophase microsystems should not be

inferior in their basic photographic characteristics to conventional silver halide systems of the same size class.

As for the first condition, it can be fulfilled in the case of any incidental nuclei, the average size of which can be compared with the size nuclei of the solid phase of silver halides, which do not occur in a homogeneous medium of aqueous-gelatin solution, and in the presence of a suspension of foreign nuclei. Then you can choose the mode of precipitation of silver halide, which is likely to be the formation of shells than a separate phase.

The choice of this mode is made by selecting the feed rate of the reagents and technological parameters that affect the solubility of silver halides, and is determined by the following. As is known [34, 35], for the origination of a new phase it is necessary to overcome some energy barrier associated with the appearance of the interface. Therefore, to initiate a phase transition, it is not enough to reach equilibrium, but requires a certain "supersaturation" [35], which is generally determined by the difference between the values of chemical potentials for the first and second phases. With the formation of a new phase, the "supersaturation" decreases, and this reduction may lead to the fact that there will be an increase only in the formed phases, without the deposition of new ones.

The energy barrier of solid phase nucleation and the associated supersaturation are reduced in the case of the presence in the solution of foreign particles – crystallization nuclei [34]. Thus, in some modes of supply to the suspension containing foreign cores, silver ions and halogen, at supersaturations still insufficient for spontaneous precipitation *AgHal* by a separate solid phase in solution, it is possible to achieve the formation and

further growth of the solid phase of the silver halide on the surface of foreign nuclei (shell growth) [36].

To maintain high light sensitivity characteristics in composite microsystems, foreign nuclei must have a number of properties that significantly limit the number of inorganic compounds that are acceptable for use as nuclei. Consider some of these properties.

In the case of composite materials of the type described, it is necessary to ensure that the silver halide, epitaxially deposited in the form of thin shells on foreign cores, remains a pure substance of controlled composition. Otherwise, the resulting heterophase system may lose its light-sensitive properties. To do this, you must control the following processes.

Epitaxial growth of silver halide shells on foreign particles can be carried out only with a sufficiently slow supply to the suspension of silver and halogen ions. In this case, these ions during the whole process of shell building interact with cations (K^{m+}) and anions (A^{n-}), which are in solution as a result of dissociation of the solid phase of the "nuclear" suspension ($K_n A_m$). Figure 1.1 shows a general scheme of reactions, which occur at the stage of building a silver halide shell on a non-silver core.

As can be seen from Fig.1.1, the processes described by reactions 2 and 3 increase the dissociation of foreign nuclei (reaction 1). In addition, the products of reactions 2 and 3 may be part of the shells, precipitating with silver halide, which crystallizes after reaction 4. The degree of this undesirable and poorly controlled doping of silver halide shells is determined according to the law of active masses process.

13
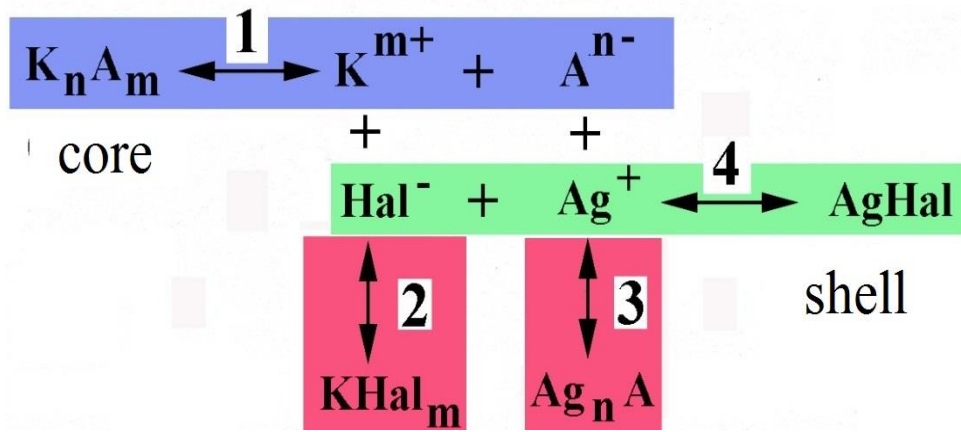
Fig.1.1. Scheme of chemical reactions when building a silver halide shell $AgHal$ on a non-silver core K_nA_m.

Inevitable side reactions 2 and 3 (Fig.1.1) will not be as effective if the product of the solubility (PS) of the compound of which the foreign nuclei are composed (K_nA_m) satisfies the ratio:

$$PS\ K_nA_m\ <\ PS\ Ag_nA \qquad (1.1)$$

$$PS\ K_nA_m\ <\ PS\ KHal_m \qquad (1.2)$$

Failure to comply with any of the above (1.1) and (1.2) attempts to build silver halide shells can result in either the dissolution of the nuclei or the formation of shells, very "contaminated" by foreign cations and anions. In this case, it is difficult to count on the preservation of a unique set of properties of the silver halide shell, which provides high light sensitivity characteristics of the microsystem "non-silver core – silver halide shell". Therefore, such microsystems, non-silver cores of which contain substances with solubility products that do not satisfy relations (1.1) and (1.2), will have light-sensitivity characteristics that are much inferior to silver-halide materials.

Thus, relations (1.1) and (1.2), which quantitatively describe the requirements for the composition of foreign nuclei [37], are a necessary condition and are fulfilled only for some inorganic compounds.

Only fluorides and, first of all, calcium fluoride (fluorite) satisfy the proposed criteria (1.1) and (1.2).

In addition, for the successful synthesis of emulsions with microsystems "non-silver core – silver halide shell" it is also necessary to take into account the peculiarities of the crystalline structures of the nucleus and shell, the size of ions in them, the state of the core surface. This further narrows the class of suitable inorganic compounds that can be used in the considered heterophase microsystems.

For example, fluorite is an ionic crystal in a unit cell whose calcium ions form a face-centered cubic lattice. To construct a fluoride sublattice, you need to mentally divide the elementary cube of the calcium sublattice into eight equal parts by planes passing through the middle of the opposite faces. A fluoride ion should be placed in the center of each of these eight cubes [37]. Thus, an elementary lattice of calcium fluoride is obtained, which includes eight fluoride ions and four calcium ions (Fig. 1.2, *a*).
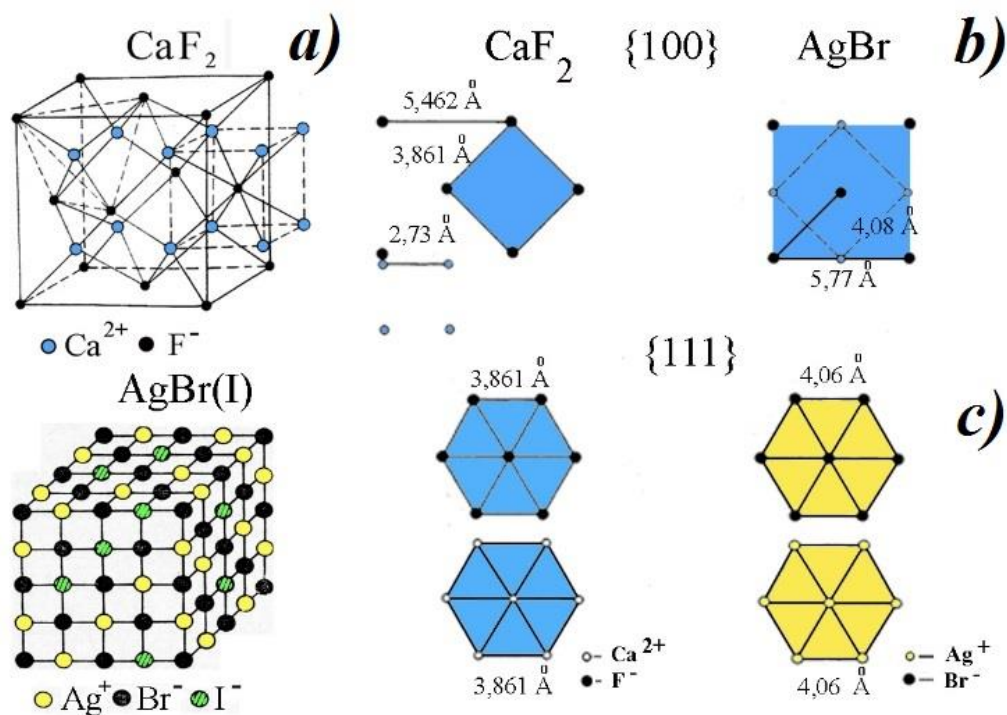
Fig.1.2. *a*) Elemental CaF_2 cell and statistical picture of solid solution *AgI* in *AgBr*;

b) Location of ions in fluorite and silver bromide on planes {100};

c) Location of ions in fluorite and silver bromide on the planes {111}.

Since the cocrystallization of fluorite and silver halide compounds requires the coincidence of lattice types and constants, as well as the sizes of ions and chemical bond types [37], the difference between the crystal lattices of fluorite and silver halides complicates cocrystallization. Therefore, for the crystallization of the shell of silver bromide on the particle of calcium fluoride, the nature of the location of ions on their surfaces may be important in facilitating this process (Fig. 1.2, *b, c*).

From Fig.1.2, (*b*) it follows that the surfaces {100} in fluorite and silver bromide are very different. In the case of surfaces {111} (Fig. 1.2, *c*) the location of ions is identical, and the inter-ion distances differ by ~6%. Therefore, to increase the silver halide shell, it should be borne in mind that

for fluorite microcrystals, in the facet of which planes are present {111}, crystallization conditions corresponding to the formation of the octahedral habitus of $AgHal$ microcrystals should be maintained.

Another important parameter that is important for the transition from a non-silver nucleus to a silver halide shell is the size of the ions. Table 1 shows the values of ionic radii of ions of interest to us [38]. The Table is based on the two most common systems (Goldschmidt and Pauling) [39].

Table 1. Radius of ions

System	Ag^+	Ca^{2+}	Br^-	I^-	F^-
Goldschmidt (*nm*)	0,113	0,106	0,196	0,220	0,133
Pauling (*nm*)	0,126	0,099	0,195	0,216	0,136

As can be seen from Table 1, the radii of the cations differ slightly. Both ions in calcium fluoride are much smaller than the corresponding ions in silver bromide. When comparing the values given in Table 1 with the inter-ions distances shown in Fig.1.2, *b, c*, we can assume that from the point of view of geometric considerations it is difficult for internodal silver ions to move along the fluorite lattice. Because calcium fluoride is a typical insulator, its own ions are not involved in charge transfer and will not penetrate the $AgHal$ shell.

To the described properties of the considered emulsions with microsystems "non-silver core – silver halide shell", which make them different from classical silver halide systems containing only $AgHal$ microcrystals, should be added the peculiarity of their developing. It is well known [40] that the chemical developing of $AgHal$ emulsion microcrystals in a methylhydroquinone developer leads to the appearance in the emulsion of threads or "whiskers" consisting of reduced silver and having a thickness of ~10

nm to ~30 *nm*. The length of the filaments can significantly exceed the linear dimensions of the *AgHal* microcrystals and thus degrade the resolution of the emulsion. These threads are in the process developings can be twisted into balls in place of the developed *AgHal* microcrystal, forming a quasi-solid silver particle, which creates the optical density of blackening of the developed emulsion (Fig. 1.3, *b*). For emulsions with microsystems "nonsilver core – silver halide shell" such formations are not observed (Fig. 1.3, *a*).
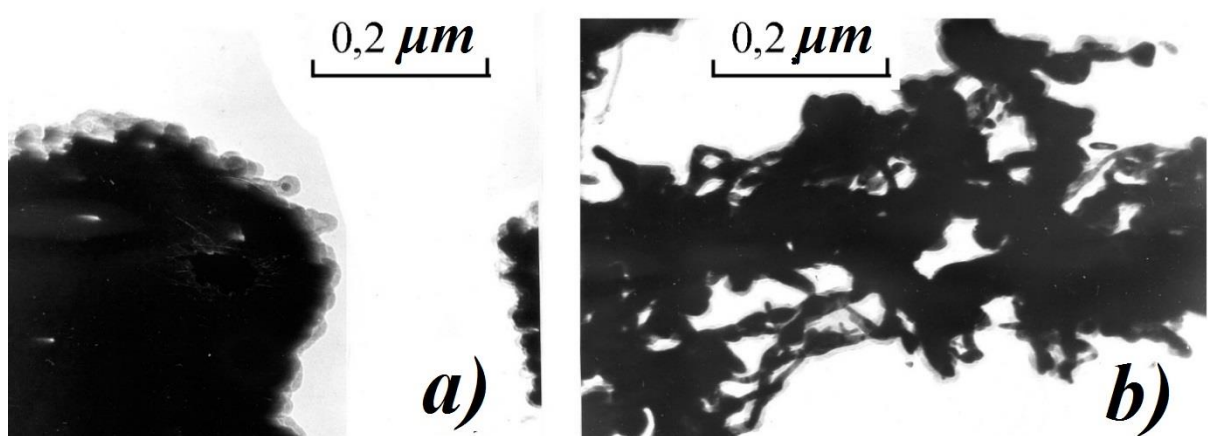
Fig.1.3. Photomicrographs of developed microcrystals:

a) "core CaF_2– shell $AgBr$" microsystem;

b) homophase $AgBr$ microcrystals.

Another very important problem is the development of emulsions with *AgHal* microcrystals, there is the formation of a halo on photographic plates (emulsion applied to a transparent substrate) in the area of high exposures. As is well known [41], the appearance of a halo is due to the reflection of light from the surfaces of emulsion microcrystals and from the boundary of the emulsion layer – the substrate. In this case, to reduce the reflection of light from the substrate, apply an anti-halo layer, which absorbs the light that has passed through the emulsion. It is much more

difficult to reduce the intensity of light scattered on the faces of microcrystals, and as a result can propagate along the emulsion layer, illuminating the microcrystals at considerable distances from the place where the scattering act occurred. Therefore, the size of the halo and, in accordance with the resolution of the emulsion with $AgHal$ microcrystals, will depend on the size, shape, surface condition of the emulsion microcrystals, correlation of gelatin and silver halide in the layer and other parameters.

Electron microscopic studies of the development of emulsions with microsystems "non-silver core – silver halide shell" in methylhydroquinone developer showed that the developed emulsion lacks "silver mustache" and on the surface of the nucleus formed particles of quasi-spherical silver nanometer size [42, 43], responsible for the optical density of the emulsion. For this reason, photographic layers based on microsystems "non-silver core – silver halide shell" with low silver content give quite good optical densities [44–46]. To confirm this conclusion, an experiment was conducted in which the emulsion with microsystems "core CaF_2 – shell $AgBr$" was compared with an emulsion containing homophase $AgBr$ microcrystals, which was obtained $AgBr$ under the same synthesis conditions as the shell CaF_2. Both emulsions were applied to substrates and contained the same amount of silver per unit surface area and were exposed to the same exposure. It turned out that the development of the emulsion with microsystems "core CaF_2– shell $AgBr$" achieved an optical density of 2,9, and with $AgBr$ microcrystals – only 0,5. Photomicrographs of these samples are presented in Fig.1.3, (*a* and *b*), respectively.

The absence of "whiskers" in the development of emulsions with microsystems "core CaF_2- shell $AgBr$" reduces the likelihood of infection, which leads to improved resolution of such emulsions. In the area of high exposures on photographic plates of composite materials there is almost no halo.

In addition, light scattering also depends on the structure of the heterophase microsystem. Calculations show [47] that if gelatin serves as the nucleus of a heterophase microsystem, such a particle will be much weaker in scattering light incident on it than a homophase microcrystal of similar size. The reason for this is that inside the heterophase microsystem is a medium with a refractive index less than the refractive index of the outer shell. Fluorite-based composite systems have similar properties and that is why they have a smaller halo compared to layers containing homophase microcrystals with the same sensitometric parameters. Therefore, in our further presentation we will focus on the heterophase microsystem "core CaF_2- shell $AgBr$".

1.2. Production of emulsion with microsystems "core $CaF_2 -$ shell $AgBr$ ".

1.2.1. Synthesis of nuclei CaF_2 in water-gelatin medium.

The first step in obtaining emulsions is that contain heterophase microsystems "core CaF_2- shell $AgBr$", is to obtain a suspension of CaF_2 nuclei in a water-gelatin medium. The synthesis of such nuclei was carried out using double exchange reactions on the installation, the schematic of which is shown in Fig.1.4, when mixed in aqueous and

aqueous-gelatin solutions of sodium fluoride (vessel 9) and calcium nitrate (vessel 10).

Ion activity F^- and Ca^{2+}, which carry out the main effect on the size of non-silver CaF_2 nuclei in the deposition process was measured using universal ionometers EV-74 and electrode systems consisting of ion-selective electrode (3) and silver chloride reference electrode (4) with a salt bridge of potassium nitrate (Fig. 1.4).

Since the volume of the reactor (1) (Fig.1.4) is 500 *ml*, and the synthesis time was from 40 to 60 minutes, it means that the feed rate of the solutions should be in the range from 1 *ml* to 2 *ml* per minute. If we take into account that the synthesis of CaF_2 nuclei requires maintaining the activity of ions within specified limits and the solutions must be presented in the form of a continuous jet (not in the form of drops), it becomes clear that the selection of two capillaries with the same feed rate at 2–3 *atm* (9) and (10) (Fig.1.4) above the surface of the solutions is a rather time-consuming task.

21
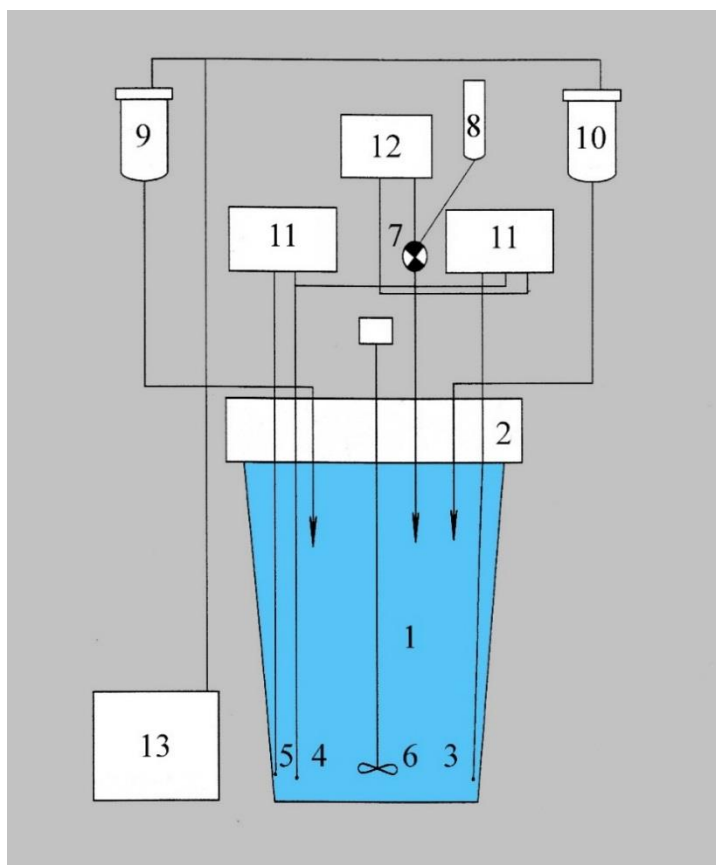
Fig.1.4. Principal scheme of the experimental installation for the synthesis of non-silver nuclei: 1 – thermostated reactor; 2 – cover; 3 – selective electrode; 4 – reference electrode; 5 – pH electrode; 6 – agitator with drive; 7 – solenoid valve automatic titration unit; 8, 9, 10 – vessels for solutions; 11 – ionometer EV-74; 12 – blocks of automatic titration BAT-15; 13 – compressor UK-16 M.

To solve this problem in the experimental setup, it was assumed that when the activities of the controlled ions exceeded the specified limits, the automatic titration unit (BAT-15) and the solenoid valve (7) (Fig.1.4) opened access to the third solution reactor by entering data electrode system in the required interval. If we take into account that the valve was opened for a fixed time and the concentration of the titrating solution is constant, then the correction of the activity of ions at a single inclusion of the valve at different

moments of the synthesis is a variable value (due to changes in the volume of the product). All these reasons are a potential source of non-reproducibility of experimental results. To eliminate the sources of such errors, we acted as follows.

From the made capillaries pairs from approximately were selectedthe same productivity and experimentally determined the ratio of the feed rates of solutions $k = v_1/v_2$. Next, one of the solutions was selected as the main. This can be any of the solutions. Now, if we take into account that during the time of synthesis t the quantities $v_1 t C_1$ and $v_2 t C_2$ of substances (here C_1 and C_2 – molar concentrations of the supplied solutions) are fed into the reactor. Assume, for example, that the synthesis takes place in an excess of ions corresponding to the second substance. Then the deviation from the stoichiometric amount of the second substance, taking into account the volume of solutions supplied, must exactly coincide with the concentration C_0 of the second substance in the initial volume. If to form a suspension, you have to mix solutions that include ions of different valence n_1 and n_2, we obtain:

$$(n_2 v_2 C_2 - n_1 v_1 C_1)t = C_0 n_2 (v_2 + v_1)t.$$

From here we obtain the formula for the concentration of the second solution according to the known first and experimentally found ratio of velocities:

$$C_2 = kC_1 \frac{n_1}{n_2} + C_0(1 + k). \tag{1.3}$$

Using this technique, it was possible to perform such syntheses, when the automatic titration unit, working with dilute solutions, or not connected at all, or turned on very rarely. From our point of view, this technique remains the

23

only one possibleobtaining homogeneous suspensions CaF_2 in cases where there are no ion-selective electrodes needed to control the activity of some ions.

To study the features of crystallization of microcrystals CaF_2 a series of experiments was conducted to establish the dependences of the average size and habit of CaF_2 microcrystals on different parameters of synthesis (temperature, flow rate of solutions, concentration of working solutions and pF).

In this case, the most significant parameter that affects the average size and habit of fluorite microcrystals is pF. Figure 1.5 shows characteristic photomicrographs of CaF_2 aqueous suspensions obtained at different pF.

In general, the dependence of the crystallization of fluorite in aqueous solutions on the value pF can be described as follows. At values pF from 0,7 to 1,6 occurs monotonic growth of average sizes of microcrystals of cuboctahedral cut (Fig. 1.5, a). In the range of values pF from 1,6 to 1,7 microcrystals have a characteristic cruciform shape (Fig. 1.5, b). It should also be noted that in this area pF there is a specific charge state of the microcrystal surface, which leads to the sedimentation of the resulting suspensions occurs abnormally long time (several days), while outside this interval pF the process ends in 2–3 hours.
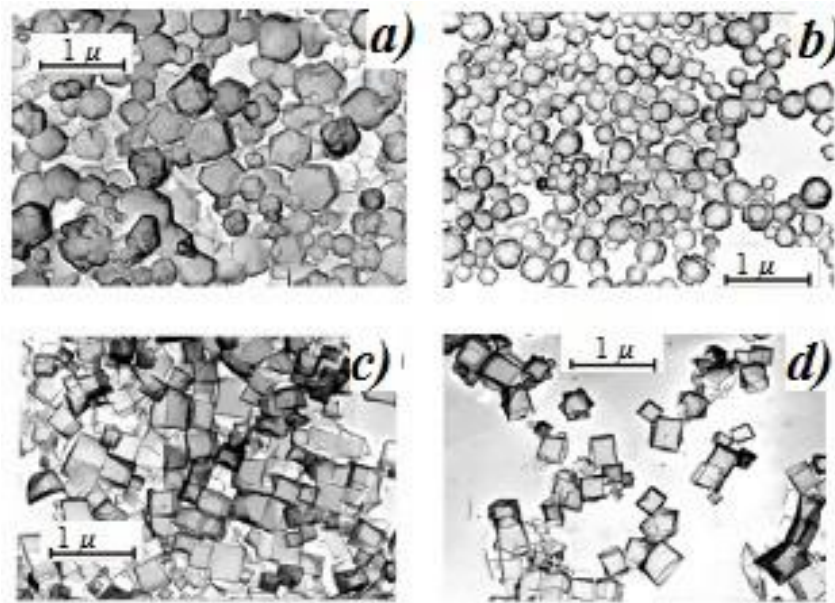
Fig.1.5. Photomicrographs of CaF_2 aqueous suspensions obtained with different pF: a) 1,0; b) 1,65; c) 2,0; d) 3,0.

In the range of pF values from 1,7 to 4,0 in fluorite microcrystals, mainly cubic faces are observed (Fig. 1.5, c, d), although not of ideal shape (etching holes in the centers of faces, or etched vertices and edges are observed).

The dependence of the average size of CaF_2 microcrystals obtained in an aqueous medium from pF is shown in Fig.1.6, a.

The observed maximum of the average sizes of calcium fluoride microcrystals in the range pF 2,2–2,6 can be explained by the fact that these ion activities correspond to the isoelectric point in this system. Hence, during deposition there is a coalescence of nuclei, the surface of which, in this case, is deprived of electric charge, which usually prevents adhesion.
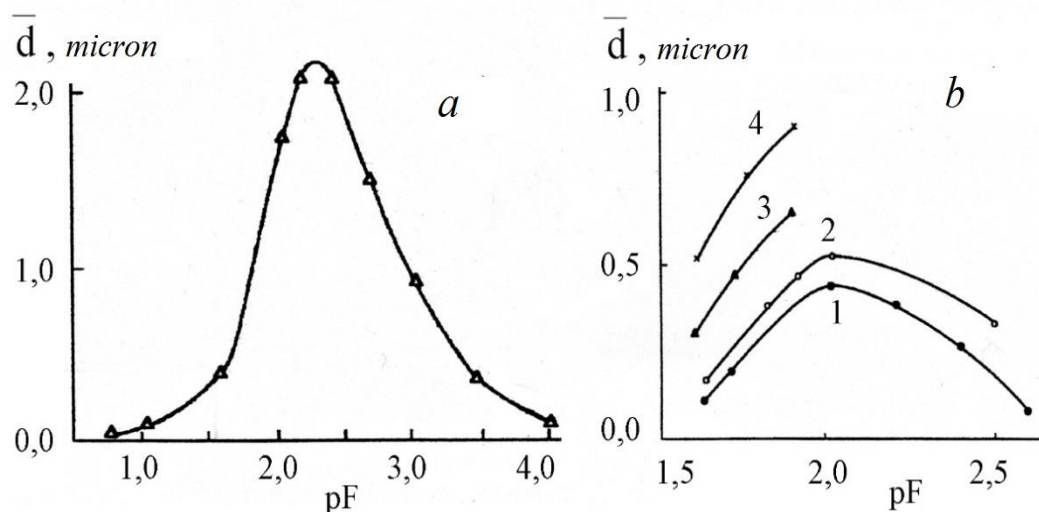
Fig.1.6. Dependence of the average size of CaF_2 microcrystals on pF:

a) synthesis of CaF_2 microcrystals was carried out in aqueous solution from pF values supported by syntheses;

b) synthesis of CaF_2 microcrystals in aqueous-gelatin solutions from pF. Gelatin content (weight %): $1 - 1$; $2 - 0,5$; $3 - 0,2$; $4 - 0,01$.

If the crystallization process is carried out in a water-gelatin medium, it turns out that the introduction of gelatin leads to a decrease in the average size of CaF_2 microcrystals. The facet of the microcrystals has a smoother shape, which is still determined by the pF value. Quantitative effect of gelatin concentration in aqueous solution of the reactor, where the synthesis of fluorite microcrystals takes place, on their average dimensions shown in Fig.1.6, *b*.

Thus, the above data show that the suspension of microcrystals calcium fluoride can be obtained in any size class, which is of interest for use as nuclei in the formation of microsystems "core CaF_2– shell $AgBr$". For this purpose, the microcrystals of calcium fluoride synthesized by us at a temperature of 50°C in water-gelatin medium (20 *ml* of 20% gelatin) in

the pF range of 1,5 to 2,0, which are fed at speeds of 20 *ml* of 0.8 *N NaF* solution and a solution $Ca(NO_3)_2$ prepared according to formula (1.3), are of the greatest interest.

Photomicrographs of such microcrystals are shown in Fig.1.7.
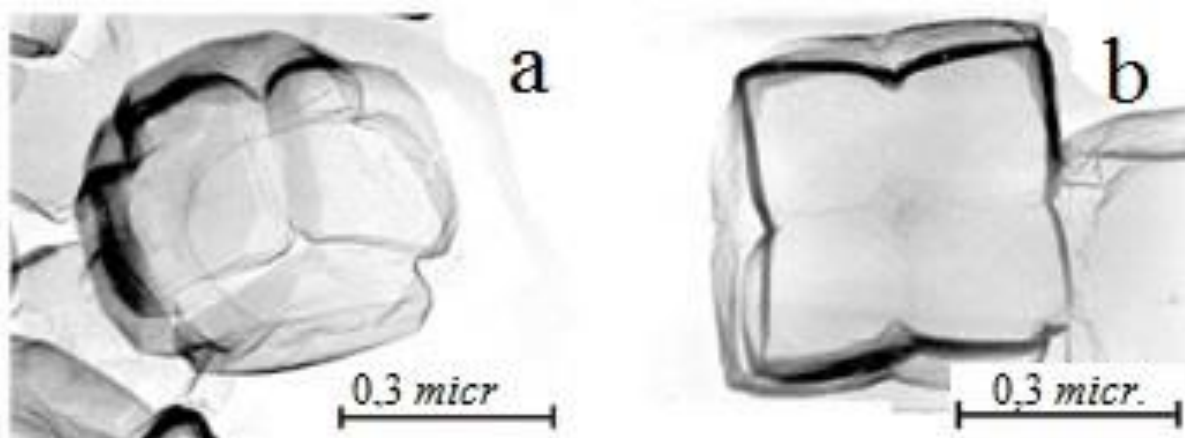
Fig.1.7. Photomicrographs of CaF_2 microcrystals precipitated at pF 1,65 (*a*) and 1,75 (*b*). Replicas with particles of the solid phase of the suspension are treated with a solution Al_2O_3.

On the surface of these microcrystals there is a relatively small number of local areas, apparently characterized by increased reactivity. This fact can be used in the sensitization of these microsystems, and creates good conditions for the next stage – building a shell of silver halide composition. Before building the shell, the aqueous-gelatin suspension containing CaF_2 microcrystals was removed by unreacted substances by centrifugation and washing. Then the aqueous-gelatin solution was replaced, after which it was fed to the reactor to increase the silver halide shell.

1.2.2. The method of building $AgBr$ shell on the CaF_2 nucleus.

As already mentioned, the most important parameters of the synthesis of $AgBr$ microcrystals by the two-jet method are the concentration and rate of supply of solutions, in this case, $AgNO_3$ and KBr, temperature, amount of ammonia and pBr value maintained (from 1,3 to 10,0). These parameters determine the supersaturation and solubility of silver halides, the formation of critical nuclei and the ratio of growth rates of different faces of microcrystals [48] .

Therefore for creation a shell $AgBr$ with the range of values of these parameters should be found on the nucleus CaF_2, at which supersaturation and solubility of silver halides would allow the formation of $AgBr$ nuclei on the surface of non-silver nuclei, but would be insufficient for their spontaneous formation in the solution volume. As a result of the experiments, we came to the following modes of $AgBr$ shell building of CaF_2 nuclei.

Solutions $AgNO_3$ and KBr $1N$ concentrations were fed at a temperature of 50°C in an emulsion beaker at a rate of 20 ml per minute. After the introduction of solutions, the volume of the obtained product is measured and 20% of gelatin is added in the amount required to obtain the concentration of gelatin in the final volume – 3%. Next, the emulsion is cooled and washed in cold distilled water from well-soluble salts (potassium and sodium nitrates).

In this case, the most significant parameter that affects the quality of the scalable silver halide shell is the $AgBr$ solubility condition. Figure 1.8 shows characteristic microphotographs CaF_2 with a shell $AgBr$ built on them, obtained by different variants of crystallization $AgBr$ on the surface of microcrystals CaF_2.
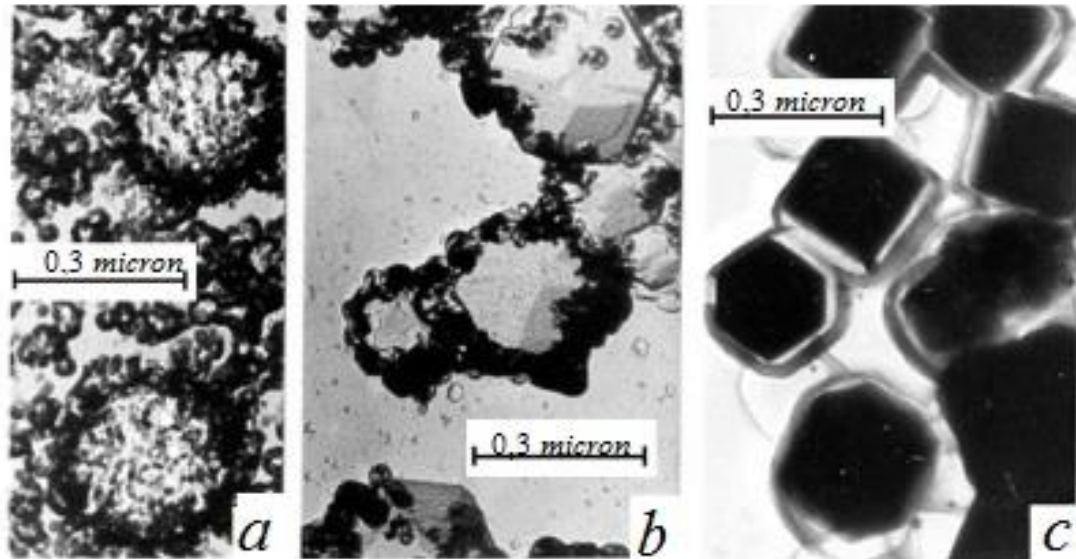
Fig.1.8. Photomicrographs illustrating the results of different crystallization options $AgBr$ on the surface of CaF_2 microcrystals under the conditions: *a*) low pBr (from 1,3 to 2,0), *b*) medium pBr (from 2,0 to 4,0), *c*) high pBr up to 7,0) (solubility $AgBr$ (PS $= [Ag^+] \cdot [Br^-] = 5,3 \cdot 10^{-13}$)).

Replicas with solid phase particles are treated with H_2SO_4 (a, b) and $Na_2S_2O_3$ solutions (c).

From Fig.1.8 it is seen that when building a shell under conditions of low and medium $AgBr$ solubility, the shell has a block structure (Fig.1.8, *a*, *b*). In the case of high solubility, the shell appears smooth, without signs of block structure (Fig. 1.8, *c*). These "core CaF_2- shell $AgBr$" microsystems were used by us for research.

1.3.Spectral sensitization of emulsions containing "core CaF_2- shell $AgBr$" microsystems.

Effective use of dyes (Dye) in solving the problem of expanding the spectral sensitivity of emulsions containing silver halide, requires overcoming a number of problems. At high concentrations of dye, there

is the formation of its *H*- and *J*-aggregates [49]. In this case, the spectral sensitivity of the emulsion may decrease due to the self-desensitization of the dye, which is due to the interaction of different excited and unexcited aggregate forms of the dye, resulting not in the generation of nonequilibrium charge carriers (electrons and holes) from the dye to the *AgHal* microcrystals but luminescence of the dye. The way out of the situation of inefficient use of photoelectrons can be the spatial separation of the thus interacting different aggregate forms of the dye.

A situation similar to self-desensitization arises when two or more types of dyes that absorb light in different regions of the spectrum are used to expand the spectral sensitivity of the silver halide. Their interaction can also lead to self-desensitization of dyes.

The solution of these problems of spectral sensitization is possible with the use of emulsions containing microsystems "non-silver core – silver halide shell". Due to the peculiarities of the structure of heterophase microsystems, sensitizers can be planted not only on the outer surface of the silver halide shell, but also on its inner surface, i.e. on the boundary between the nucleus and the shell.

The technology that allows you to adsorb the dye on the surface of the non-silver core and overgrow it with a silver halide shell, and on the outer surface of the shell, and is the subject of this section.

"Core CaF_2–shell $AgBr$" microsystems were chosen for research, as they are better in their main characteristics compared to heterophase microsystems containing as nuclei PbF_2 or $BaSO_4$ [59–62]. For spectral sensitization of these microsystems, we used different in composition and charge state dyes presented in Table 2.

Table 2. Used dyes

Dye	Name	Charge state	$E_{1/2}^{Red}(V)$	$E_{1/2}^{Ox}(V)$
DyeI	Pyridine salt of 3,3'-di-γ-sulfopropyl-9-ethyl-4,5,4',5'-dibenzothiacarbocyaninebetaine	anionic	−1,12	+0,62
DyeII	3,3'-di-γ-sulfopropyl-1,1'-diethyl-5,5'-dicarboethoxyimide-carbocyaninebetaine sodium salt	anionic	−1,6	+0,63
DyeIII	1,1'-diethyl-quino-2,2'-cyanine iodide	cationic	−1,1	+1,1
DyeIV	3,3'-diethyl-9,11(β,β'-dimtiltrimethylene) thiatetracarbocyanine iodide	cationic	–	–

Spectral sensitization obtained emulsions using these dyes was carried out at a concentration of 10^{-4} *mol* Dye/*mol* CaF_2, which ensured the formation in the emulsion of all forms of aggregation Dye: dimers, *H*- and *J*-aggregates [50].

For experimental studies were made types of emulsions (conditionally *A, B, C, D*), presented in Table 3.

Table 3. Types of studied emulsions

Emulsion	Core	Dye on the core	Shell	Dye on the shell
A	CaF_2	DyeI	–	–
	CaF_2	DyeIII	–	–
B	CaF_2	–	$AgBr$	DyeI
	CaF_2	–	$AgBr$	DyeII
	CaF_2	–	$AgBr$	DyeIII

		DyeI	$AgBr^*$	–
C	CaF_2	DyeII	$AgBr^*$	–
		DyeIII	$AgBr^{**}$	–
D	CaF_2	DyeI	$AgBr^*$	DyeIV
		DyeIII	$AgBr^{**}$	

*for DyeI can be oxidized in solution by silver ions, so the reaction mixture was first fed KBr and $KCNS$, and only then solutions of gelatin and $AgNO_3$.

**for DyeIII aqueous solutions of silver nitrate, gelatin and potassium bromide with ammonia were imcarrierstely added to the suspension.

Finished samples of light-sensitive emulsions were poured on glass plates 9x12 centimeters.

Studies of the reflection and absorption spectra of emulsions were performed at room temperature on SF-10 according to standard methods.

For spectrosensitometric studies, the exposure of plates to light with wavelengths in the range of 400–1100 *nm* was performed in an ISP-3 spectrosensitometer according to standard methods [51].

Surface and deep developers were used to develop the exposed emulsions [40]. The surface developer exhibits only those heterophase microsystems in which the centers of the latent image are on the outer surface $AgBr$ shell. The deep developer exhibits those heterophase microsystems in which the centers of the latent image are not only on the $AgBr$ surface but also in the volume of the shell up to the surface of the

nucleus CaF_2. Measurement of the optical density D of the exposed layers, which is proportional to the concentration of the detected centers of the latent image, was performed on a microphotometer MF-4. Thus, the proposed methods of development allow us to trace not only the position of the centers of the latent image on the entire volume of the silver halide shell of the composite system, but also the concentration of the centers of the latent image depending on the wavelength of illuminating light.

Luminescent studies emulsions were performed at T=77K on the installation and according to the method described in [52]. Registration of luminescence spectra of heterophase microsystems was carried out in two modes:

"Stationary" – luminescence is measured continuously for more than 10^{-3} s with continuous excitation;

"Phosphorescent" – excitation of Π-shaped pulses lasting $\sim 10^{-4}$ s, between which follows "dark" interval lasting $\sim 10^{-3}$ s during which luminescence is registered for $\sim 10^{-4}$ s. After that, the cycle is repeated at a frequency of 800 Hz.

1.3.1.The dependence of the spectral sensitization of the microsystem "core CaF_2 – shell $AgBr$" from the size of the core.

In our experiments, the ratio of ionic activity F^- and Ca^{2+} in nuclear fusion CaF_2(see Section 1.2.1) were selected so that the average size of the nucleus in the microsystem were $\overline{d} = 0,35\ \mu m$ and $\overline{d} \approx 0,05\ \mu m$.

Figure 1.9, and shows the reflection spectra of type *A* emulsions containing DyeI. The average size of the nucleus CaF_2 in the heterophase microsystem was $\overline{d} \approx 0{,}35 \, \mu m$. It is seen that in the reflection spectra there are bands due to the reflection of molecules and *J*-aggregates DyeI (maxima of the bands are shown by arrows in Fig.1.9, *a*).
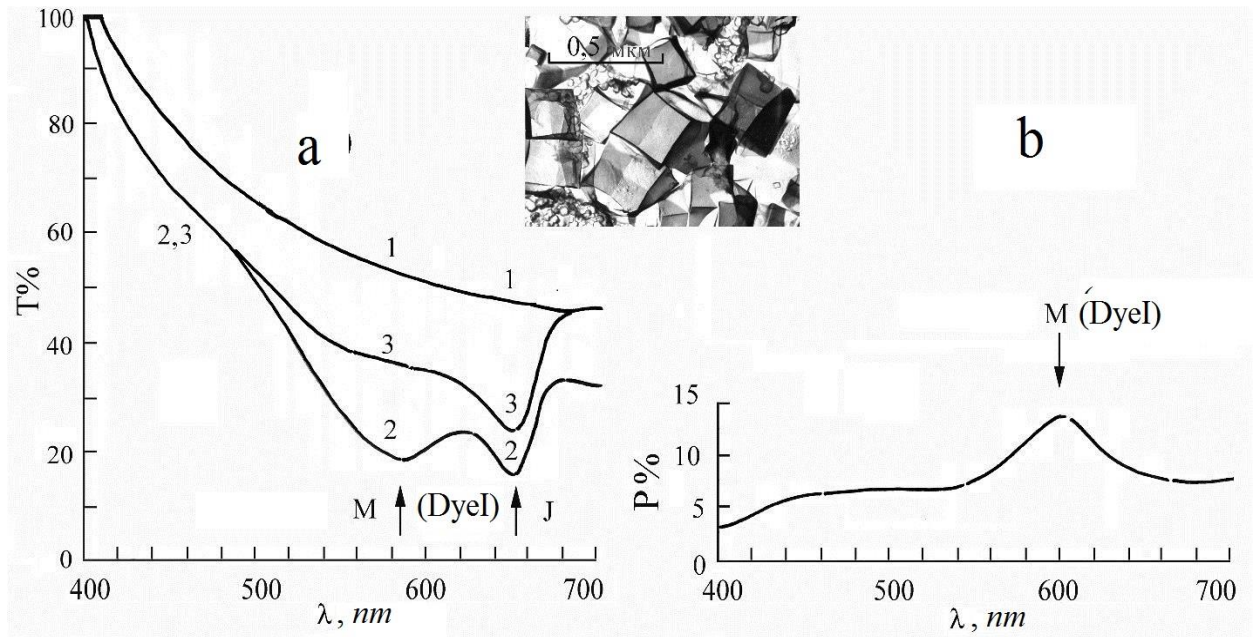
Fig.1.9. *a*) Reflection spectra of type *A* emulsion that do not contain dye (1); emulsion type *A* and contains DyeI (2, 3) before (2) and after (3) washing it with alcohol.

b) The transmission spectrum of alcohol after washing them with an emulsion of type *A* containing DyeI.

Insert Fig.1.9 presents electron microscopic photographs of the nuclei CaF_2 we use ($\overline{d} \approx 0{,}35 \, \mu m$).

After washing with alcohol such an emulsion, the alcohol acquires color and, as shown by studies of transmission spectra, this color is due to DyeI molecules (maximum band width corresponding to DyeI molecules in Fig.1.9, *b* is indicated by an arrow). In the reflection spectrum of the

34

emulsion after treatment with alcohol (Fig. 1.9, *a*, curve 3), the band corresponding to DyeI molecules disappears.

Figure 1.10, *a* shows the reflection spectra of type *A* emulsions containing DyeI. The average size of the nucleus CaF_2 in the heterophase microsystem was $\overline{d} \approx 0{,}05\ \mu m$.
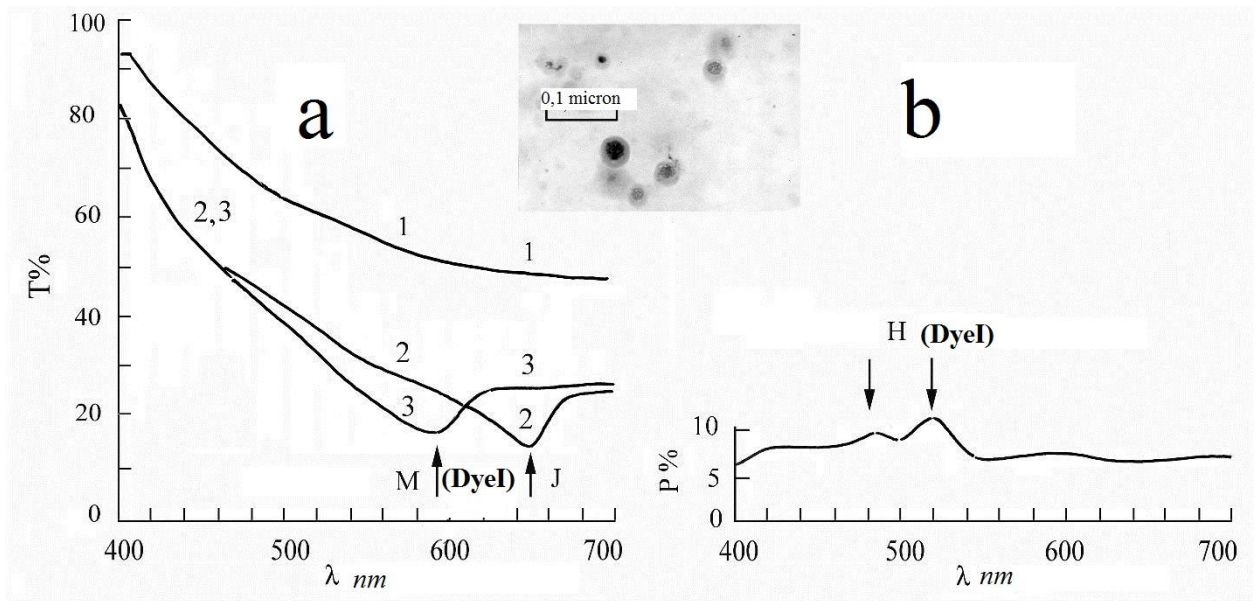
Fig.1.10. *a*) Reflection spectra of type *A* emulsion that does not contain dye (1); emulsion type *A* containing DyeI (2, 3) before (2) and after (3) washing it with alcohol.

b) The transmission spectrum of alcohol after washing them with an emulsion of type *A* containing DyeI.

Insert Fig.1.10 presents electron microscopic photographs of the CaF_2 nuclei used by us ($\overline{d} \approx 0{,}05\ \mu m$.).

As follows from Fig.1.10, *a*, curve 2, in the reflection spectra there are bands corresponding to both molecules and *J*-aggregates DyeI (maxima of bands are shown in Fig.1.10, *a* arrows). However, after washing the emulsion with alcohol, in the reflection spectrum there is only

35

a band corresponding to the molecules DyeI, the same band, characteristic of *J*-aggregates DyeI, is absent (Fig.1.10, *a*, curve 3).

In the transmission spectrum of alcohol after washing the emulsion there are maxima (in Fig.1.10, *b* they are indicated by arrows), corresponding to the absorption of dimers and *H*-aggregates DyeI.

From the analysis of experimental data presented in Fig.1.9 and Fig.1.10, it follows that in the emulsion type *A* containing medium-sized $(\overline{d} \approx 0,05\,\mu m.)$ nuclei CaF_2, the dye is fixed on the surface of the nucleus CaF_2 mainly in the molecular state, and in the emulsion type *A* containing nuclei CaF_2 with medium size $\overline{d} \approx 0,35\,\mu m$ – in *J*-aggregated state.

Figure 1.11 presents the results of spectrosensitometric tests of emulsions of type *B*, *C* and *D*. The average CaF_2 core size in the microsystem was $\overline{d} \approx 0,35\,\mu m$. As follows from the data presented in Fig.1.11, *a*, the optical density *D* of the exposed emulsion type *B* with DyeI after treatment with surface developer (Fig.1.11, *a*, curve 1) increases compared to the optical density D_0 of the unexposed emulsion (Fig.1.11, *a* , curve 3), revealing the maxima (in Fig.1.11, *a*, they are indicated by arrows) in the region of intrinsic absorption of the shell $AgBr$ ($\lambda_{max} \approx 450\ nm$), molecular DyeI ($\lambda_{max} \approx 630\ nm$) and *J*-aggregated DyeI ($\lambda_{max} \approx 690\ nm$).
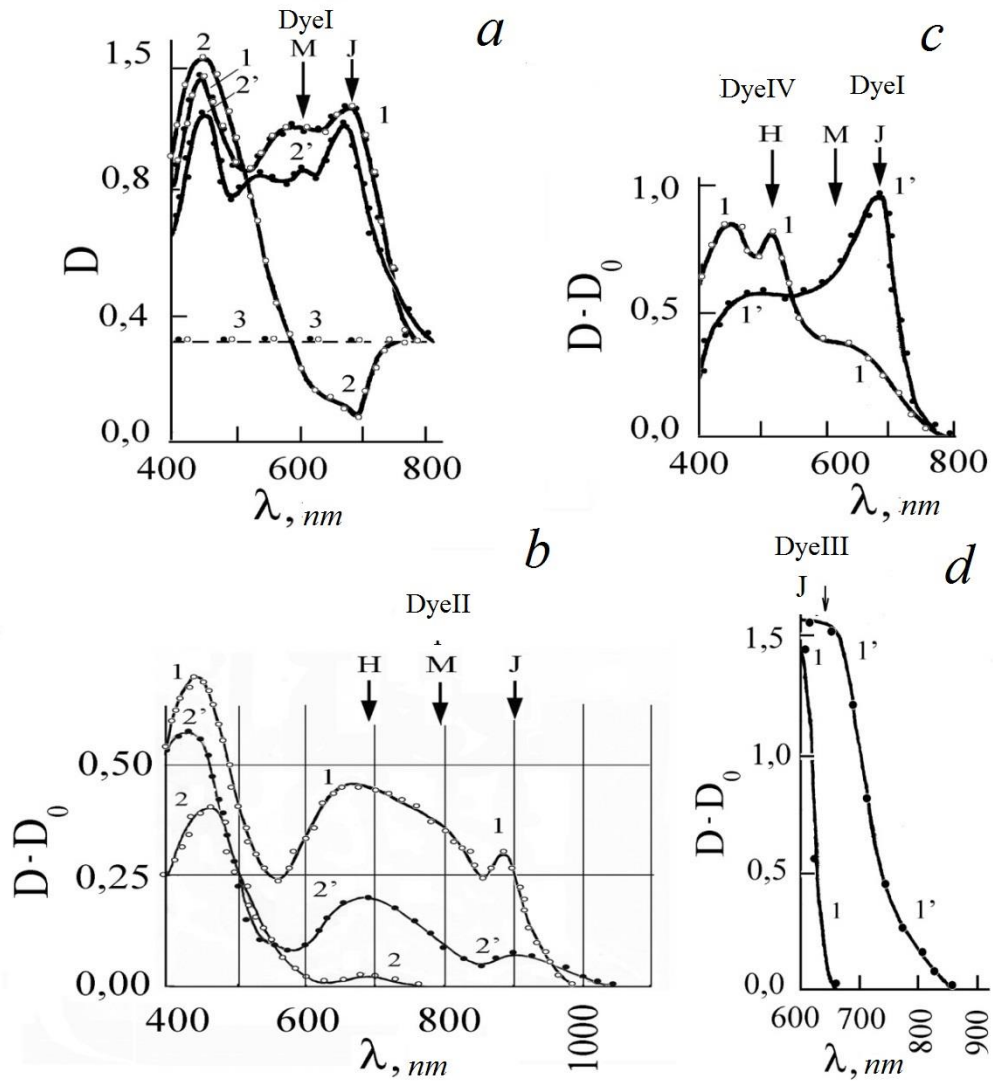
Fig.1.11. *a*) Dependence of the optical density D of the exposed layers of emulsions of type B (1) and C (2,2') containing DyeI on the wavelength of the exposing light after development in the surface (1, 2) and deep (2') developers. The dashed line (3) indicates the optical density of the veil D_0 of unexposed emulsions of type B and type C and manifested in both surface and deep developers.

b) The dependence of the optical density $D - D_0$ of the exposed layers of emulsions of type B (1) and type B (2, 2'), containing DyeI, on the wavelength of the exposure light after development in the surface (1, 2) and deep (2') developers.

37

c) Fragment of the curve of the optical density $D - D_0$ of the exposed layers of emulsions of type *B* (1) and type *C* (1'), which contain DyeIII, from the wavelength of the exposing light manifested in the surface (1) and deep (1') developers.

d) The dependence of the optical density $D - D_0$ of the exposed layers of emulsions of type *G* containing DyeI on the inner, and DyeIV on the outer surface of the $AgBr$ shell, from the wavelength of the exposing light after development in the surface (1) and deep (1') developers.

For the exposed type *B* emulsion with DyeI, a similar increase in optical density D relative to D_0 is observed after treatment with only a deep developer (Fig. 1.11, *a*, curve 2'). After treatment with its surface developer, growth D occurs only in the area of self-absorption of the shell $AgBr$ ($\lambda_{max} \approx 450$ *nm*). In the regions of absorption of molecular DyeI ($\lambda_{max} \approx 630$ *nm*) and *J*-aggregate DyeI ($\lambda_{max} \approx 690$ *nm*), on the contrary, there is a decrease in optical density D relative to D_0 (Fig.1.11, *a*, curve 2).

In the surface developing of the exposed emulsion type *B* with DyeI, the optical density depending on the wavelength of the exposure light has a maximum in the absorption region of the shell $AgBr$ ($\lambda_{max} \approx 450$ *nm*), and a small maximum in the absorption region of DyeI *J*-aggregates ($\lambda_{max} \approx 700$ *nm*) (Fig.1.11, *b*, curve 2).

At deep developing of emulsion of type *B*, as well as for emulsion of type *B*, for optical density from the wavelength of the exposing light, its increase is observed not only in the area of absorption of the shell $AgBr$, but also in the field of molecular absorption *H*- and *J*-aggregates

DyeII ($\lambda_{max}\approx 800$, 700 and 900 *nm*, respectively) up to 1100 *nm* (Fig.1.11, *b*, curve 2').

It should also be noted that for type *B* emulsion, when Dye is fixed on the inner surface of the shell $AgBr$, an increase in optical density *D* relative to D_0 is observed in the longer wavelength region of the spectrum than in the case of type *B* emulsion when the dye is on the outer surface of the shell $AgBr$ (for example, in the case of DyeII up to 1100 *nm*, Fig.1.11, *b* (compare curves 1 and 2'), in the case of DyeI up to 810 *nm*, Fig.1.11, *a* (compare curves 1 and 2'). In other words, the threshold sensitivity of the type *C* emulsion, compared with the type *B* emulsion, is shifted to the long-wavelength region.

This extension is most striking the spectral sensitivity region of the type *C* emulsion relative to the type *B* emulsion in the near-infrared part of the spectrum is manifested for emulsions containing DyeIII (Fig. 1.11, *c* (compare curves 1 and 1')).

As for the emulsion type *D,* according to Fig.1.11, *d,* a positive difference $D - D_0$ occurs after exposure to light from the absorption region of DyeI and DyeIV, while showing maxima at wavelengths characteristic of *H*- and *J*-aggregate forms of dyes.

Earlier in [53] the fundamental possibility of overgrowth of the dye adsorbed on the nucleus CaF_2 by the shell $AgBr$ without specifying the physical state of Dye and its role in the process of spectral sensitization was shown. Comparison of our results unequivocally proves the possibility of shell $AgBr$ overgrowth along with molecules and *J*-aggregates Dye, which are adsorbed on the nucleus CaF_2. However, the possibility of overgrowth of *J*-aggregates Dye adsorbed on the

nucleus CaF_2 , the shell $AgBr$ significantly depends on the ratio of the size of the nucleus CaF_2 and J-aggregates of the dye.

If the size of the nucleus is large enough ($\bar{d} \approx 0,05$ μm) in comparison with the sizes of J-aggregates Dye, then J-aggregates Dye adsorbed on the surface of the nucleus CaF_2 are overgrown with a shell $AgBr$.

Indeed, as follows from Fig.1.11, a, the centers of the latent image when illuminating the emulsion type C with light from the absorption region J-aggregate of the Dye are detected only when the emulsion is developed by a deep developer and are absent when developed by a surface developer. For emulsion type B, when J-aggregates of the Dye are located on the outer surface of the shell $AgBr$, the centers of the latent image when the emulsion is illuminated by light from the region of absorption J-aggregate Dye are detected in the developing of both surface and deep developer. The role of J-aggregates Dye located on the inner surface of the shell $AgBr$, in the process of spectral sensitization differs from the situation when J-aggregates Dye adsorbed on the outer surface of the $AgBr$ shell:

firstly, there is an effect of "enlightenment" – the optical density D of the emulsion type C, exposed to light from the absorption region J-aggregates Dye and developed in the surface developer, is less than the optical density of the veil D_0;

second, the spectral sensitivity of the emulsion is shifted to the long-wavelength region compared to when J-aggregates adsorbed on the outer surface of the shell $AgBr$ (Fig.1.11, a and Fig.1.11, b (compare curves 1 and 2')). This can occur due to the separation of the scalable shell $AgBr$ molecular and J-aggregated Dye. On the inner surface of the shell $AgBr$

remains Dye in the *J*-aggregated state, and molecular Dye is displaced on the outer surface of the shell $AgBr$. Spatial separation of different forms of Dye eliminates their interaction during photoexcitation, which apparently led to recombination luminescence of molecular Dye (i.e., to self-desensitization) rather than to the generation of free charge carriers in silver halides to form a latent image. Thus, it can be considered as the effect of removing self-desensitization.

The role of the shell $AgBr$ in a heterophase microsystem containing nuclei CaF_2 of "large" size consists not only in the spatial separation of molecular and *J*-aggregated Dye, but can also lead to the formation of internal electric fields in the heterophase microsystem, which contribute to efficient charge carrier distribution. Separation of nonequilibrium charge carriers in the case of a heterophase microsystem and provides the effect of "enlightenment" in the emulsion of type C (Fig.1.11, *a*, curve 2). The observed "enlightenment" indicates that the number of neutral clusters Ag_m^0 of silver on the outer surface of the shell $AgBr$ decreases as a result of the reaction

$$Ag_m^0 + p \to Ag_m^+ \to Ag_{m-1}^0 Ag^+ \to Ag_{m-1}^0 + Ag_i^+. \qquad (1.4)$$
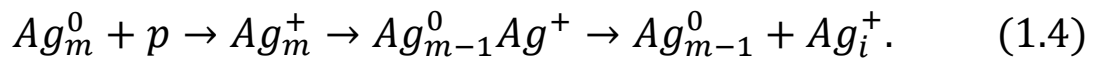
The appearance of holes (p) on the outer surface of the shell $AgBr$ is due to the following reason. The presence of *J*-aggregates of DyeI on the inner surface of the shell $AgBr$ is accompanied by a reaction

$$Ag_n^+ + Dye^0(J-aggregate) \to$$
$$\to Ag_n^0 + Dye^+(J-aggregate). \qquad (1.5)$$
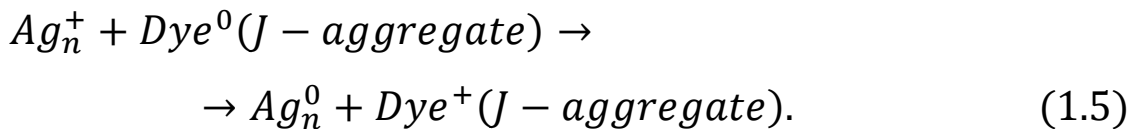
Reaction (1.5) can also be stimulated by the action of light from the region of absorption of DyeI *J*-aggregates. As we found in [53], the main singlet level of the *J*-aggregate DyeI lies below the level of the ceiling of

the valence band (VB) of $AgBr$, resulting in a hole localized on Dye$^+$, passes into VB $AgBr$.

$$Dye^+(J-aggregate) \rightarrow Dye^0(J-aggregate) + p, \qquad (1.6)$$
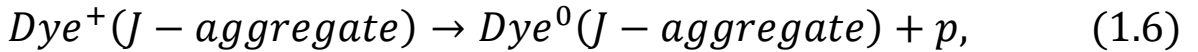
then the hole in the VB migrates to the outer surface of the shell $AgBr$ and provides the reaction (1.4).

Additional evidence of the mechanism of "self-desensitization", which we consider, are low-temperature (T=77K) luminescent studies. If the size of the nucleus is large enough ($\overline{d} \approx 0,05 \ \mu m$) compared to the size of Dye J-aggregates, then, in our opinion, they are adsorbed on the surface of the nuclei CaF_2 while maintaining optical contact with the molecular dye. That is why in the luminescence spectrum there is a band of H-aggregates ($\lambda_{max} \approx 520–540 \ nm$) and the most intense band of luminescence of J-aggregates DyeI ($\lambda_{max} \approx 770–710 \ nm$) (Fig. 1.12, a, curve 1), which is effectively excited when light is absorbed by the Dye (Fig. 1.12, b, curve 1').

In the phosphorescent mode of luminescence registration, both at excitation of molecules ($\lambda \approx 610–630 \ nm$) and DyeI J-aggregates ($\lambda \approx 670–690 \ nm$), the spectrum is characterized by the presence of two luminosity maxima: abnormally delayed fluorescence of Dye J-aggregates ($\lambda_{max} \approx 770–710 \ nm$) and phosphorescence of molecular DyeI ($\lambda_{max} \approx 800–820 \ nm$) (Fig. 1.12, b, curves 2'and 3').

After building on the core CaF_2 with the dye $AgBr$ shell, i.e. the creation of type C emulsion, in the luminescence spectra we observe that in the "stationary" excitation mode the intensity of luminescence of DyeI J-aggregates decreases sharply in comparison with molecular ($\lambda_{max} \approx 610–$

630 *nm*) and *H*-aggregated DyeI ($\lambda_{max} \approx 520–540$ *nm*) luminescence bands (Fig. 1.12, *c*, curve 1).

In the "phosphorescent" mode of luminescence registration, when the shell $AgBr$ is excited by light, an abnormally slow fluorescence of molecular DyeI ($\lambda \approx 620–640$ *nm*) is observed and only slightly of DyeI *J*-aggregates ($\lambda \approx 670– 690$ *nm*) (Fig. 1.12, *c*, curve). 3), and the excitation spectrum of the luminescence of abnormally delayed fluorescence of molecular DyeI contains one maximum, which corresponds to the absorption of the shell $AgBr$ (Fig.1.12, *d*, curve 1').

When excited from the absorption region of molecular BrI, only phosphorescence of molecular DyeI ($\lambda \approx 800–820$ *nm*) is observed in the luminescence spectrum which excitation spectra contains both characteristic band for $AgBr$ shell ($\lambda \approx 620–640$ *nm*), and for molecular DyeI ($\lambda \approx 600$ *nm*) (Fig. 1.12, *d*, curve 2').
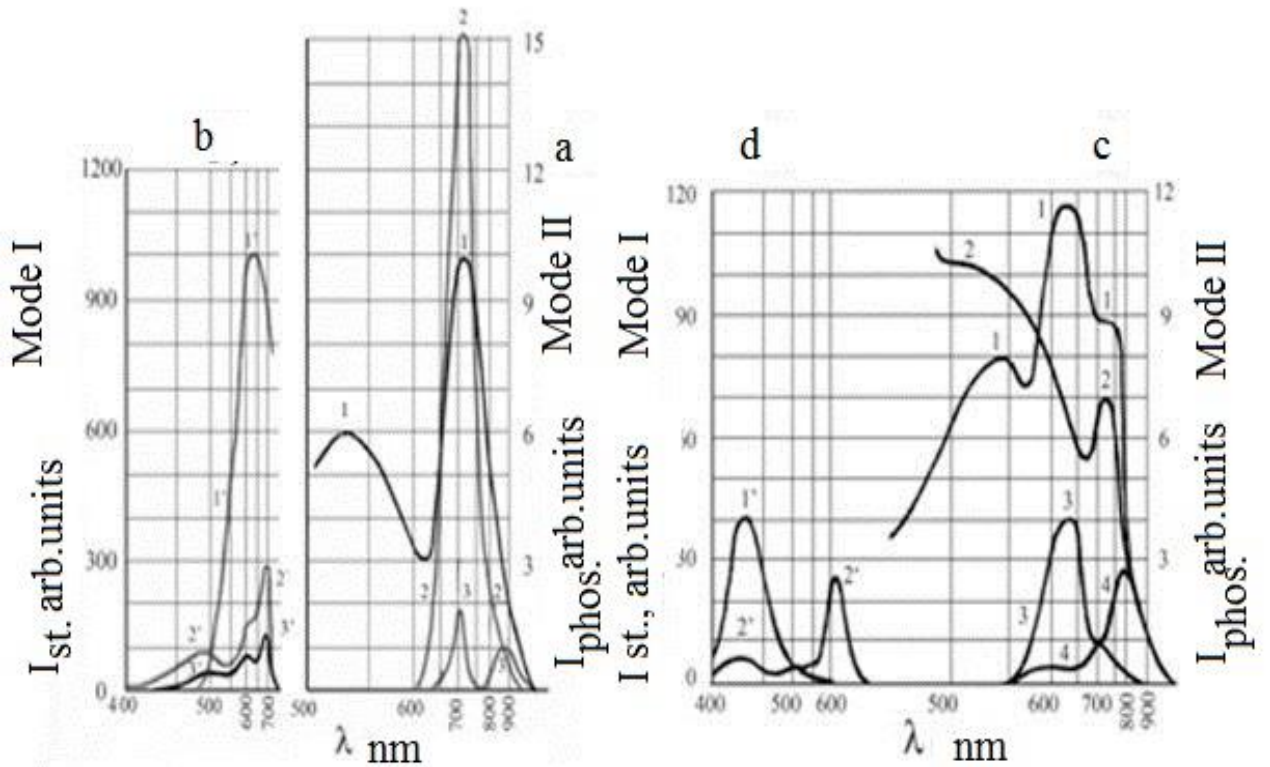
Fig.1.12. *a*) Luminescent spectra (T=77K) of type *A* emulsion, which were measured in the "stationary" (1, 2) and "phosphorescent" (3) modes when excited by light wavelength λ (*nm*): 1 – 337; 2 – 500; 3 – 690,

b) excitation spectra of luminescence (T=77K) of type *A* emulsion, which were measured in stationary (1') and phosphorescent (2', 3') modes for radiation wavelengths λ_{max} (*nm*): 1'– 880; 2'– 720; 3'– 820,

c) luminescence spectra (T=77K) of type *B* emulsion, measured in "stationary" (1, 2) and "phosphorescent" (3, 4) modes when excited by light wavelengths λ (*nm*): 1 – 337; 2 – 450; 3 – 430; 4 – 600,

d) luminescence excitation spectra (T=77 K) of type *B* emulsion, which were measured in the "phosphorescent" (1', 2') mode for luminescence wavelengths λ_{max} (*nm*): 1'– 620; 2'– 800.

Therefore, our spectrosensitometric characteristics, reflection and luminescence spectra indicate that in the heterophase microsystem ($\overline{d} \approx$

44

0,35 μm) the $AgBr$ shell spatially separates the molecular and aggregated dye, which are usually in optical contact, which causes the processes associated with self-desensitization of dyes.

Now let's move on to consider the case where the size of the kernel ($\overline{d} \approx 0,05$ μm) can be compared with the size of the Dye J-aggregate. As mentioned earlier, in this case the greatest "fixation" on the CaF_2 nucleus is felt by the Dye molecules and, therefore, it is natural to expect that the overgrowth of the $AgBr$ shell will lead to displacement on the outer shell of Dye molecules, as was in the case at $\overline{d} \approx 0,35$ μm but J-aggregates of the Dye. Indeed, as follows from luminescent studies (Fig. 1.13, on the example of DyeI), this is the division of aggregate forms of Dye and occurs during the overgrowth of nuclei on the surface of which adsorbed Dye contained in the emulsion type A shell $AgBr$, i.e. the formation of emulsion type B.

In the emulsion of type A ($\overline{d} \approx 0,05$ μm) between molecules and Dye J-aggregates there is an interaction, which is accompanied by phosphorescence of molecular Dye (for DyeI – ($\lambda_{max} \approx 800$ nm, Fig.1.12, a, curve 1) when excited by light from the absorption region of Dye J-aggregate (for DyeI – ($\lambda_{max} \approx 600$ nm, Fig.1.13, b, curve 1').
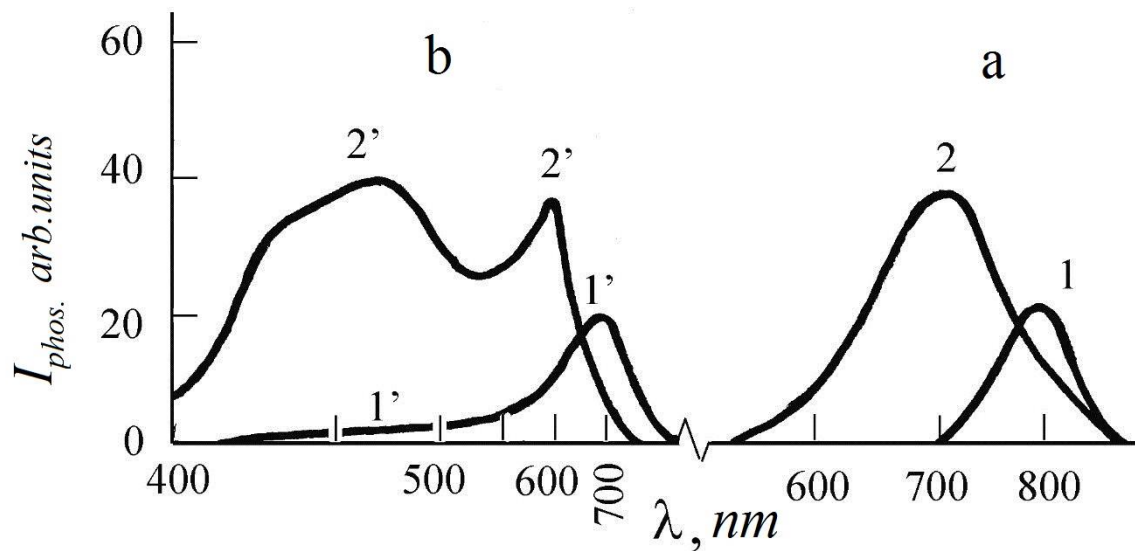
Fig.1.13. The spectra (T=77K) of phosphorescence (*a*) and phosphorescence excitation (*b*) of emulsions ($\bar{d}\approx0,05$ *μm*) contain DyeI: 1, 1'– type *A*; 2, 2'– type *B*:

a) Luminescence spectra (T=77K), obtained by excitation with monochromatic light with λ (*nm*): 1 – 690; 2 – 450,

b) Luminescence excitation spectra (T=77K) with λ_{max} (*nm*): 1'– 800; 2'– 700.

When the shell $AgBr$ is built up, the phosphorescence of molecular Dye disappears when the *J*-aggregate Dye is excited, and luminescence occurs (for DyeI – $\lambda_{max}\approx700$ *nm*, Fig.1.13, *a*, curve 2), which is excited by light from the absorption region $AgBr$ ($\lambda_{max}\approx450$ *nm*), Fig.1.12, b, curve 2 '). As is known [54], such luminescence is due to the abnormally delayed fluorescence of Dye *J*-aggregates adsorbed on the surface of microcrystals $AgBr$.

Therefore, as follows from the above, our experimental data have shown that the silver halide shell in the microsystem "core CaF_2–shell $AgBr$" is able to spatially separate *J*-aggregated and molecular phases of

46

the Dye, which has a positive effect on the expansion of the spectral sensitivity of the finished emulsion and removes the effect of self-desensitization of the dye. The shell too protects dye from the environment, which can have a positive effect on the preservation of light sensitivity of the system as a whole.

In addition, our experimental data also give a positive answer to the question of whether the silver halide shell in a heterophase microsystem is able to perform a spatial separation of different Dyes-sensitizers. The example of DyeI and DyeIV (Fig.1.11, *d*) shows that the silver halide shell in the heterophase microsystem provides a spatial separation of different Dyes-sensitizers, the joint use of which leads to desensitization of the emulsion.

However, questions remain as to the reasons for the separation of aggregates and molecules of the same dye or different dyes. It is also necessary to find out why the dye is fixed on the inner surface of the shell of the heterophase microsystem, and how it depends on the composition of the core of the microsystem.

One of the explanations of the mechanism of spectral sensitization of heterophase microsystems with a nucleus CaF_2, when the dye adsorbed on the inner surface of the silver halide shell, is given in [55], and is associated with the presence of a digestion hole on the surface of the nucleus CaF_2. This explanation has not been experimentally tested, and cannot be extended to the case of spectral sensitization of heterophase microsystems whose nuclei have a different surface structure.

In our opinion, the answers to these questions can be obtained by comparing the spectral sensitization of microsystems with different nuclei.

For the comparative study of spectral sensitization, we selected the "core CaF_2–shell $AgBr$" and "core $AgBr(I)$–shell $AgBr$" microsystems.

1.3.2. Dependence of spectral sensitization microsystems "core – silver halide shell" from the structure of the nucleus.

Synthesis of emulsions containing microsystems "core $AgBr(I)$–shell $AgBr$" was performed by the two-jet ammonia method described in [56].

The supply of uniform ($1N$) $AgNO_3$ solutions, and a mixture of KBr and KI (3 $mol\%$ $iodine$) was carried out at a rate of 6,0 ml/min at a temperature of 60°C and pAg 8,6. As a result of the synthesis, the $AgBr(I)$ nuclei obtained for microsystems were cubic microcrystals size 0,2 μm. Then the dyes were adsorbed on the nuclei, introducing their alcohol solutions into the emulsion and the dyes not adsorbed on the surface of the nucleus were separated by centrifugation. After that, the nuclei $AgBr(I)$ with the adsorbed dye were built up $AgBr$. To prevent the formation $AgBr$ in the emulsion of microcrystals not adsorbed in the form of a shell on the nuclei with dyes, the emulsification temperature was reduced to 50°C, and the feed rate of the solutions $AgNO_3$ and KBr was reduced to 0,4 ml/min; pAg remained unchanged – 8,6. This is due to the fact that the solubility of

$AgBr$ in these conditions is lower than in the synthesis of $AgBr$ nuclei and precipitation occurs only on the $AgBr(I)$ nuclei.

For spectral sensitization microsystems "core CaF_2–shell $AgBr$" and "core $AgBr(I)$– shell $AgBr$" we used DyeI and DyeII (see Table 2).

Spectral sensitization of microsystems by dyes was performed as before in concentration 10^{-4} mol Dye/$mol\ AgBr$. This concentration of dye is chosen so that, in addition to dye molecules, the formation of all forms of dye aggregation was ensured: stable pairs of dye molecules – *H*-aggregates and a stable set of dye molecules *J*-aggregates.

For experimental studies in addition to emulsions of type *A, B, C* and *D*, three more types of emulsions were prepared (conditionally *E*, *F*, *G*), are presented in Table 4.

Table 4. Types of studied emulsions

Emulsion type	Core	Dye on the core	Shell
E	$AgBr(I)$	DyeI	$AgBr$
F	$AgBr(I)$	DyeII	$AgBr$
G	$AgBr(I)$	DyeI	–

Figure 1.14 presents the results of sensitometric and luminescent studies of type *E* emulsion.
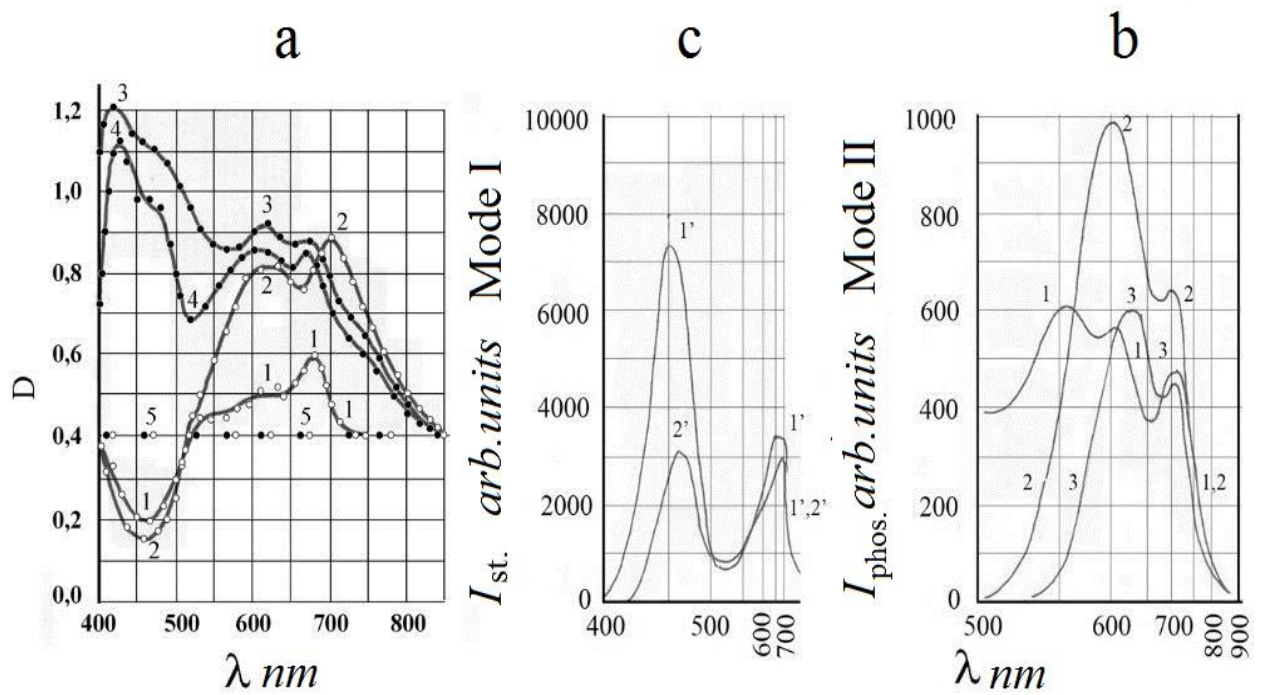
Fig.1.14. *a*) The dependence of the optical densities *D* from the wavelength of light exposure of the emulsion layer type *E* after development in the surface (1) and depth (2, 3, 4) developers with the oxidation time of the surface developed centers *t* (*min*): 2 – 0; 3 – 1, 4 – 2;

b) luminescence spectra (T=77K) of type *E* emulsion, which was measured in "stationary" (1) and "phosphorescent" (2, 3) modes of luminescence registration when excited by light wavelength λ (*nm*): 1 – 430; 2 – 430; 3 – 690,

c) luminescence excitation spectra of type *E* emulsion measured in the "phosphorescent" mode of registration at the wavelength of the maximum radiation intensity λ_{max} (*nm*): 1'– 600; 2'– 750.

As follows from the data presented in Fig.1.14, *a*, curves 3 and 4, in the case of deep developing with oxidation of surface centers, optical density emulsions of type *E* increases in comparison with the optical

density of the unexposed emulsion (Fig. 1.14, *a*, curve 5), and detects maxima in the region of intrinsic absorption of silver halide D_0 ($\lambda_{max} \approx 450$ *nm*), molecular DyeI ($\lambda_{max} \approx 6300$ *nm*) and *J*-aggregate DyeI ($\lambda_{max} \approx 690$ *nm*).

At surface developing (Fig.1.14, *a*, curve 1) or at deep developing without oxidation of surface centers (Fig.1.14, *a*, curve 2), the optical density of type *E* emulsion increases, only in the absorption *M*- and *J*-aggregates DyeI, in areas of intrinsic absorption of silver halide ($\lambda_{max} \approx 450$ *nm*) there is a decrease in the density of blackening relative to the veil. This suggests that when building a shell *AgBr,* unlike type *C* emulsion, the dye is displaced on the outer surface of the shell *AgBr*.

In the luminescence spectra of the emulsion type *E* in the "stationary" mode of registration (Fig.1.14, *b*, curve 1) when excitation of its light from the field of intrinsic *AgBr* absorption ($\lambda=430$ *nm*), as well as for emulsions of type *C* (Fig.1.12, curve 1), fluorescence is observed *H*-aggregates DyeI ($\lambda_{max}=540–550$ *nm*), luminescence of the shell *AgBr* ($\lambda_{max}=600–620$ *nm*), and fluorescence and abnormally slow fluorescence of molecular ($\lambda_{max}=630–650$ *nm*) and *J*-aggregated DyeI ($\lambda_{max}=720–750$ *nm*). The last two bands of luminescence, as in the case emulsions of type B (Fig.1.12, curves 3 and 4), most pronounced in the phosphorescent mode of registration of the luminescence upon excitation light from the area of self-absorption *AgBr* ($\lambda \approx 430nm$), and abnormally delayed fluorescence *H*-aggregates DyeI ($\lambda_{max}=540–550$ *nm)* is absent (Fig.1.14, *b*, curve 2). Also for type *E* emulsion, in contrast to type *C* emulsion, there is no molecular phosphorescence of the DyeI when excited by light from the region of its absorption ($\lambda \approx 600$ *nm*).

It should be noted that in the luminescence of the emulsion type E with λ_{max}=540–550 nm in the "stationary" mode of registration at excitation of its light from the field of own absorption $AgBr(\lambda$=430 $nm)$ may contribute to the luminescence of paired iodine centers $(I_a^- I_a^-)$ and $\{(I_a^- I_a^-)Ag_{i,s}^+\}$ centers of $AgBr(I)$ nucleus with $(\lambda_{max}\approx560$ $nm)$. However, the absence luminescence with $(\lambda_{max}\approx560$ nm) in "phosphorescent" mode at excitation by light from the region of self-absorption $AgBr$ $(\lambda$=430 $nm)$, in our opinion, indicates that the largest contribution to the luminescence of the emulsion type E with $(\lambda_{max}$=540–550 $nm)$ is precisely the fluorescence of H-aggregates of the DyeI.

For type E emulsion in "phosphorescent" mode of registration of luminescence at excitation by light from area of absorption DyeI J-aggregates $(\lambda_{max}$=690–700 $nm)$, in contrast to the type C emulsion, in the luminescence spectrum there is anti-Stokes luminescence of the shell $AgBr$ and abnormally delayed fluorescence of DyeI J-aggregates $(\lambda_{max}$=600–620 nm and 720 nm, respectively) (Fig.1.14, b, curve 3) . Excitation spectra of both anti-Stokes luminescence of the $AgBr$ shell and abnormally delayed fluorescence of DyeI J-aggregates, while "phosphorescent" mode luminescence recordings are described by two maxima corresponding to absorption $AgBr$ $(\lambda_{max}$=430–490 $nm)$ and the absorption of J-aggregated DyeI $(\lambda_{max}$=690–700 $nm)$ (Fig. 1.14, b, curves 1' and 2', respectively).

Note that the anti-Stokes green luminescence in the nucleus $AgBr(I)$ $(\lambda_{max}\approx560$ $nm)$ when excited by light from the absorption region of DyeI J-aggregates in this case is absent. Also noteworthy is the lack of

phosphorescence of the molecular dye DyeI with (λ_{max}=800 *nm*) when excited by light from the absorption region of DyeI *J*-aggregates.

It should be noted that in the case of direct optical contact $AgBr(I)$ and DyeI when excited by light from the absorption region of DyeI *J*-aggregates, there is a green anti-Stokes luminescence of the nucleus $AgBr(I)$ ($\lambda_{max}\approx560$ *nm*) and Stokes molecular phosphorescence of DyeI ($\lambda_{max}\approx800$ *nm*) [57]. Also in direct deposition of the DyeI to the surface $AgBr(I)$ and when excited by light from the region of self-absorption $AgHal$ ($\lambda_{max}\approx430$ *nm*) in "phosphorescent" mode there is a luminescence with ($\lambda_{max}\approx560$ *nm*), and abnormally slow fluorescence of the DyeI *H*-aggregates is completely absent [58].

As already mentioned, spectrosensitometric tests of emulsion type *C*, which contains cationic DyeI (see Table 2), showed that in this case there is an overgrowth of the dye with a light-sensitive shell $AgBr$ (Fig.1.11, *b*). This is convincingly evidenced by the data on the development of the exposed emulsion type *C* in comparison with the emulsion type *B*, which contains DyeII.

Comparative characteristics of the emulsion type *F* (see Table 4) with the emulsion type *C* (see Table 3), containing DyeII, showed that the spectra of optical densities in relation to the veil ($D - D_0$) of the emulsion type *F* with DyeI observed in the same spectral bands as in the case of type *C* emulsion. In contrast to type *F* emulsion for type *E* emulsion there is no expansion of the spectral sensitivity region with DyeI in the long-wavelength part of the spectrum (Fig.1.15, *a*, compare curves 1, 2 and 3), therefore, DyeII when building $AgBr$ to the core $AgBr(I)$ displaced on the outer surface of the shell $AgBr$.
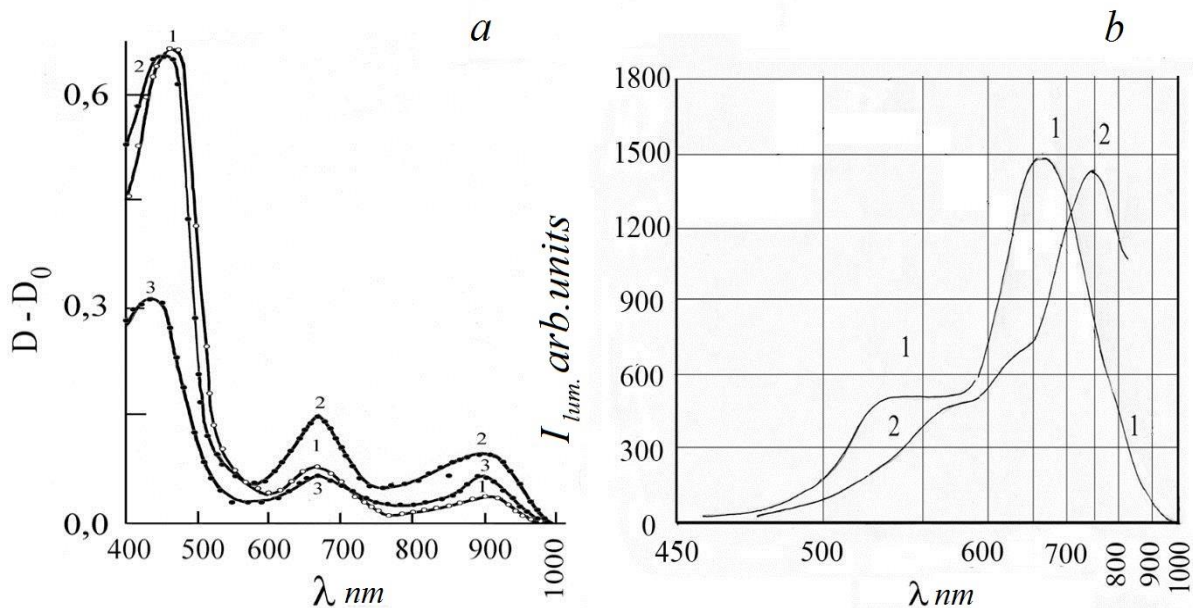
Fig.1.15. *a)* Optical dependence densities $D - D_0$ from the wavelength of light exposing layers of emulsions of type *F* with DyeI after development in the surface (1) and deep (2, 3) developers with oxidation of surface centers t (*min*): 2 – 1; 3 – 20,

b) luminescence spectra (T=77K) type *F* emulsions with DyeII, measured in "stationary"mode at excitation by light wavelength λ(*nm*): 1 – 430; 2 – 900.

In the luminescence spectra of type *F* emulsions with infrachromatic DyeII in the "stationary" mode of registration of luminescence when excited by light from the region of self-absorption $AgBr$ ($\lambda_{\max} \approx 430$ *nm*), there is a green luminescence of paired iodine centers $I_a–I_{a–}$ and centers $\{(I_a^- I_a^-)Ag_{i,s}^+\}$ of nucleus $AgBr(I)$ ($\lambda_{\max} \approx 560$ *nm*), shell $AgBr$ ($\lambda_{\max} \approx 610$ *nm*) and *H*-aggregates *of Dye*II ($\lambda_{\max} \approx 700–750$ *nm*). The last two bands in the luminescence spectrum when overlapping create one wide band with ($\lambda_{\max} \approx 660$ nm) (Fig.1.15, *b*, curve 1).

In the "stationary" mode of registration of luminescence spectra of type F emulsion, when excited by light from the absorption region of DyeII aggregates ($\lambda_{\max} \approx 900$ nm), anti-Stokes luminescence of $AgBr$ shell ($\lambda = 600$–620 nm) and DyeII H-aggregates ($\lambda = 700$–750 nm) were registered. Anti-Stokes luminescence paired iodine centers $I_a^- I_a^-$ and centers $\{(I_a^- I_a^-)Ag_{i,s}^+\}$ of nucleus $AgBr(I)$ ($\lambda_{\max} \approx 560$ nm) is not observed (Fig.1.15, b curve 2).

Thus, based on luminescent data, for the emulsion type F there is no overgrowth of the shell $AgBr$ cationic aggregating infrachromatic DyeII adsorbed on the $AgBr(I)$ nucleus.

To sum up, we can say that for exposed and developed in the surface developer emulsion type C, in the spectral region corresponding to the absorption of molecular and J-aggregated DyeI there is a decrease in the optical density of blackening relative to the veil (Fig.1.11, a, curve 1), and when developed in the deep $-$ increase (Fig.1.11, a, curve 2), this means that the concentration of neutral silver centers of the atomic-molecular degree of dispersion Ag^0 and Ag_2^0 decreases from the inner to the outer surface of the shell $AgBr$, i.e. nonequilibrium electrons and holes generated in molecules and J-aggregates DyeI, fall into the shell $AgBr$ from its inner surface on which DyeI is adsorbed. Indeed, according to our data [57], the anionic DyeI J-aggregates interact with silver halides so that the main level of the DyeI J-aggregate coincides with the VB ceiling of $AgBr$, and the first excited DyeI level corresponds to the level $Ag_{in}^0, n = 2$ in the FB of the silver halide. This state of the levels of the DyeI J-aggregate and Ag^0 allows us to unequivocally explain the appearance of neutral silver centers of atomic-molecular degree of

dispersion $Ag^0_{in}, n = 2$, and the appearance of free holes in the VB of silver halide during photoexcitation of anionic DyeI [58].

In favor of this fact is also evidenced by the fact that in the luminescence spectra of emulsions of type C when excited by light from the absorption region J-aggregates DyeI, no anti-Stokes luminescence of the shell $AgBr$. It is known that if DyeI located on the outer surface of the shell $AgBr$, the anti-Stokes luminescence of the shell $AgBr$ when excited DyeI J-aggregate would take place [57], as we observe for type E emulsion.

Penetration into the shell $AgBr$ nonequilibrium electrons and holes generated in J-aggregates of DyeI in the case of type E emulsion, in contrast to type C emulsion, provides the observed anti-Stokes luminescence of the outer surface of the shell $AgBr$. In our opinion, this clearly indicates that J-aggregates of DyeI when building a shell $AgBr$, in the case of type E emulsion, is displaced on its outer surface. In favor of this we can also cite the fact that in the emulsion type E when it is excited by light from the region of its own absorption $AgBr$ (λ=430nm) there is no green luminescence of paired iodine centers $(I^-_a I^-_a)$ and centers $\{(I^-_a I^-_a)Ag^+_{i,s}\}$ of $AgBr(I)$ nucleus, but there is a fluorescence of DyeI H-aggregates, and when excited by light from the absorption region of DyeI J-aggregates there is no green anti-Stokes luminescence as it happens in direct contact DyeI with core $AgBr(I)$ (emulsion type F), (Fig.1.15, a, curves 1 and 2, respectively).

The above research results suggest that if the shell contains the same monovalent ionic component as the nucleus, as in the case of the nucleusis a silver halide compound, the anionic dye is displaced on the

outer surface of the shell. If the nucleus contains a divalent ionic component, as in the case where the nucleus is not a silver halide compound, the anionic dye remains under the silver halide shell, ie it is overgrown. To a greater extent this applies to the DyeI *J*-aggregates.

Based on this, we can conclude that the ionic component of the nucleus affects the bond strength DyeI *J*-aggregates with the surface of the nucleus, which in the further course of the synthesis determines the possibility of overgrowth DyeI *J*-aggregates by the shell $AgBr$.

This assumption can be confirmed by luminescent studies on emulsions of type *G* (Fig.1.16, *a*, *b*) and type *A* (Fig.1.16, *c*, *d*), in which DyeI, adsorbed on nuclei with different cationic composition, without further shell overgrowth $AgBr$.
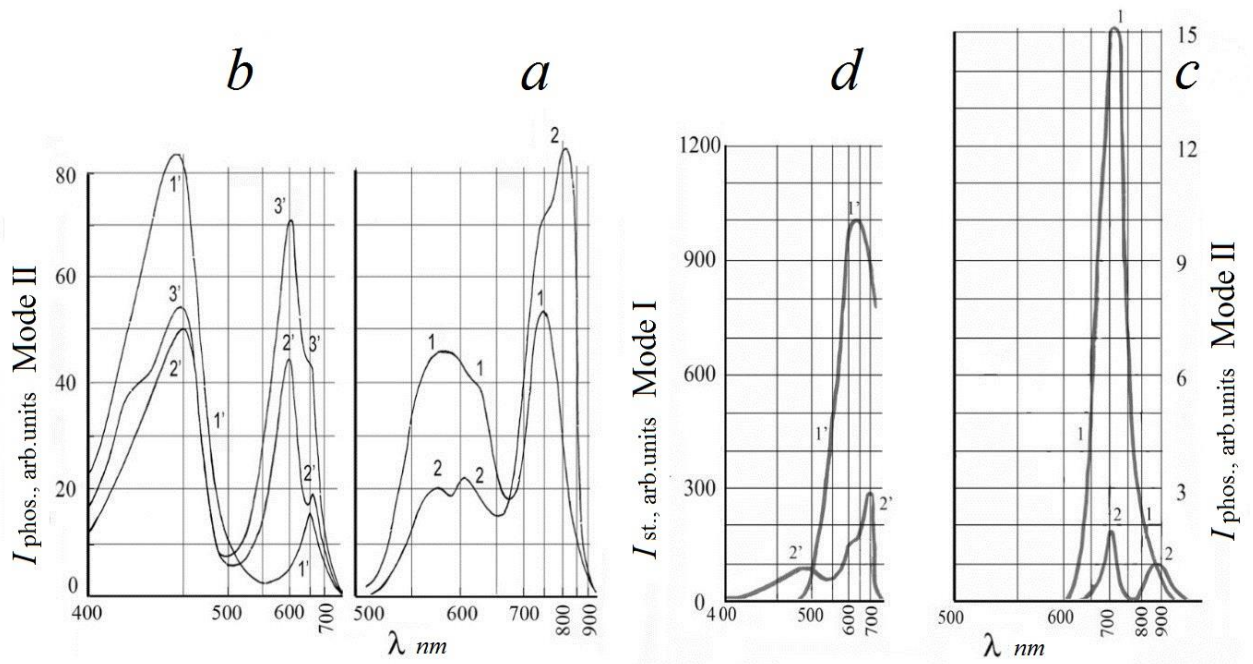
Fig.1.16. *a*) Luminescence spectra at T=77K emulsion type *G*, measured in phosphorescent mode when excited by light wavelength λ (*nm*): 1–430; 2–690.

b) Excitation spectra (T=77K) of luminescence emulsions of type *G* are measured in phosphorescent mode on wavelengths of maximum λ (*nm*): 1'–560; 2'–750; 3'–800.

c) Luminescence spectra (T=77K) of type *A* emulsion measured in the stationary (1) and phosphorescent (2) modes at excited by light wavelength λ (*nm*): 1–600; 2–690.

d) Luminescence excitation spectra (T=77K), measured in stationary (1') and phosphorescent (2') emulsion modes of type *A* for wavelengths λ (*nm*): 1'–880; 2'–720.

For type *G* emulsion in phosphorescent mode the following results of measurements are observed:

- excitation spectrum of the green luminescence band paired iodine centers $(I_a^- I_a^-)$ and centers $\left\{(I_a^- I_a^-)Ag_{i,s}^+\right\}$ in the nucleus $AgBr(I)$ ($\lambda_{max} \approx 560$ *nm*) (Fig. 1.16, *b*, curve 1') is characterized by two maxima at λ=430–470 *nm*, and λ=670–690 *nm*. These maxima correspond to the nucleus' $AgBr(I)$ own absorption and *J*-aggregate of DyeI, respectively;

- in excitation spectra of abnormally delayed fluorescence of DyeI *J*-aggregates on λ=750 *nm* (Fig.1.16, *b*, curve 2 ') and molecular phosphorescence DyeI on λ= 800 *nm* (Fig.1.16, *b*, curve 3 ') there are three maxima corresponding to the absorption of the $AgBr(I)$ nucleus with (λ_{max}=430–470 *nm*), molecular DyeI with (λ_{max}=610–630 *nm*) and *J*-aggregate DyeI with (λ_{max}=650–690 *nm*);

- when the luminescence is excited by monochromatic light both from the absorption region of $AgBr(I)$ (λ=430 *nm*, Fig.1.16, *a*, curve 1) and from the absorption region of *J*-aggregated DyeI (λ=690 *nm*), in the

luminescence spectrum (Fig. 1.16, a, curve 2) there are four bands. These bands are responsible for: centers $(I_a^- I_a^-)$ and centers $\left\{(I_a^- I_a^-)Ag_{i,s}^+\right\}$ in nucleus $AgBr(I)$ with ($\lambda_{max} \approx 560$ *nm*), abnormally delayed fluorescence of molecular DyeI with ($\lambda_{max} = 630$–650 *nm*), fluorescence and abnormally delayed fluorescence of *J*-aggregates of DyeI with ($\lambda_{max} = 720$–750 *nm*), and phosphorescence of molecular Dye with $\lambda_{max} \approx 800$ *nm*.

It should be noted that in the case of excitation of luminescence emulsions of type *G* monochromatic light from the absorption area of *J*-aggregated DyeI ($\lambda = 690$ *nm*) in the luminescence spectrum there are two anti-Stokes bands of luminescence: centers $(I_a^- I_a^-)$ and $\left\{(I_a^- I_a^-)Ag_{i,s}^+\right\}$ centers in $AgBr(I)$ nuclei with $\lambda_{max} \approx 560$ *nm*, and abnormally delayed fluorescence of molecular DyeI with $\lambda_{max} = 630$–650 *nm*). This is confirmed by measurements of the excitation spectra of these luminosity bands, in the spectra of which the excitation maxima at $\lambda = 690$ *nm* are observed (Fig. 1.16, *b*, curves 1'and 2', respectively), for which the absorption of *J*-aggregated DyeI is responsible. If anti-Stokes luminescence centers $(I_a^- I_a^-)$ and $\left\{(I_a^- I_a^-)Ag_{i,s}^+\right\}$ centers in the nucleus $AgBr(I)$ observed before [57], the anti-Stokes abnormally delayed fluorescence of molecular DyeI during photoexcitation of *J*-aggregated DyeI was registered by us for the first time and considered in detail in [58].

Therefore, from the results obtained (Fig.1,16, *a*, *b*) it follows that on the nucleus $AgBr(I)$ both molecules and DyeI *J*-aggregates are adsorbed, which are in close optical contact, in which the photoexcitation is distributed between them as follows. Photoexcitation generated in

nuclei $AgBr(I)$, is transmitted to Dye I molecules and *J*-aggregates, and the photoexcitation generated in DyeI *J*-aggregates is transmitted to the $AgBr(I)$ nucleus and DyeI molecules, providing not only their phosphorescence, but also abnormally delayed fluorescence, as evidenced by the presence of anti-Stokes luminescence. The photoexcitation generated in DyeI molecules is transmitted only to DyeI *J*-aggregates, since in the excitation spectrum of the green luminescence of paired iodine centers $(I_a^- I_a^-)$ and $\{(I_a^- I_a^-)Ag_{i,s}^+\}$ centers. The absorption band of molecular DyeI is absent (Fig.1.16, *b*, curve 1').

The excitation and luminescence spectra of the type *A* emulsion in which DyeI adsorbed on CaF_2, showed that, as in the case of adsorption DyeI on $AgBr(I)$ emulsions of type *G*, in the luminescence excitation spectra DyeI (Fig.1.16, *d*) and luminescence DyeI (Fig.1.16, *c*) there are bands characteristic of the absorption and luminescence of molecular and *J*-aggregated DyeI. However, in the excitation and luminescence spectra changes are also observed. So if for molecular DyeI in the case of an emulsion type *C* abnormally delayed fluorescence observed with λ_{max}=630–650 *nm* and phosphorescence with $\lambda_{max}\approx$800 *nm*, then for emulsion type *A* abnormally delayed fluorescence of molecular DyeI is completely absent, and phosphorescence is observed from $\lambda_{max}\approx$880 *nm* (Fig. 1.16, *c*, curve 2). In addition, in the case of emulsion type *A* photoexcitation of DyeI *J*-aggregates transmitted to the molecular DyeI and leads to it phosphorescence, the intensity of which is minimal, and abnormally delayed fluorescence does not occur, because the anti-Stokes luminescence of DyeI molecules upon excitation of DyeI *J*-aggregates is absent (Fig. 1.16, *c*, curve 2). This suggests that the processes of

transmission of photoexcitation from *J*-aggregated DyeI to molecular in the case of an emulsion type *A* minimized.

All these data, in our opinion, indicate unequal interaction of anionic DyeI with nuclei $AgBr(I)$ and CaF_2, which is caused by the difference in the charges of the cations of the nuclei, which provides a difference in the experimental results for them, and is also responsible for the fact that during overgrowth nuclei $AgBr(I)$ and CaF_2 with the anionic dye adsorbed on them $AgBr$ in the case of the nucleus CaF_2, the dye remains on the nucleus and is overgrown with a shell, and in the case nuclei $AgBr(I)$ displaced on the surface of the shell $AgBr$. In addition, as shown by experimental results [63], the charge of the cations of the nucleus decreases efficiency transmission of photoexcitation from *J*-aggregated DyeI its molecules, which ultimately leads to the expansion of the spectral sensitivity of the heterophase microsystem to the long-wavelength region.

CHAPTER 2. THERMO- AND PHOTOCHEMICAL TRANSFORMATIONS IN MONOLITHIC CGS COMPOSITION *AS-S*.

It is established that there are several narrow temperature ranges within which the efficiency of photoinduced changes in the optical constants of chalcogenide glassy semiconductors is maximal. The processes that take place at low (T<77K) temperatures are the most thoroughly studied, because in this temperature range it is possible to carry out complex studies of optical, luminescent properties and photoinduced EPR signal [64–66]. In the monolithic materials of the system *As-S* we are studying the recording of optical information is most effectively carried out at sufficiently high temperatures close to the softening temperature of the material [67–69]. At these temperatures, photoluminescence and photoinduced EPR signal in CGS are absent, so the authors of most studies have limited the study of the absorption coefficient and refractive index of the material under the action of light [70–75]. Such information is insufficient to establish the nature of photochemical transformations and therefore a special role in this case is played by studies of changes in electrical and photoelectric properties of CGS in the process of photochemical transformations [76–79].

This is due to the fact that most authors [80–84] associate photoinduced changes in optical parameters by changes in the density or population of localized states in the forbidden band. It is also believed that such states determine the photoelectric properties of CGS [84–88]. In this case, photovoltaic methods are the most sensitive and informative in

comparison with optical, which are associated with the measurement of the absorption coefficient and refractive index.

Thus, optical methods do not require special equipment and allow to record the concentration of active centers (not less than $\sim 10^{14}$ cm^{-3}) involved in the transformation, for photoconductivity, this concentration is $\sim 10^{12}$ cm^{-3} [89].

Therefore, quite important information about these processes can be obtained first of all if we study the phenomena of photoconductivity in the conditions of holographic recording [77, 90].

Nevertheless, observations in this direction are not systematic due to the fact that their interpretation is associated with significant difficulties. When measured at direct current, they are due to contact and long-term polarization phenomena, which leads to slight changes in the photoelectric properties of the studied compounds [91, 92]. In addition, CGSs have a very high resistance (more than 10^{12} Ohm/cm), so the relaxation time of the measuring cell is quite long (more than 0,1 s) and does not allow to measure fast-moving processes. Difficulties in interpreting the experimental results when measuring on alternating current are faced mainly by the lack of a technique that allows to distinguish between the relaxation of complexes with dipole moment and the relaxation of the three-dimensional charge, as well as between the processes associated with the transfer of current carriers in localized and non-localized states [93–95]. All this led to the fact that the same experimental data from different authors were explained differently. We have developed and described such a technique in works[96–99].

Thus, when elucidating the mechanism of high-temperature photochemical transformations, questions arise about the relationship between photoinduced changes in the optical and photoelectric properties of CGS, as well as the possibility of describing these changes from the same positions. The next section is devoted to consideration of these questions.

2.1. The mechanism of charge carrier transfer in the CGS composition *As-S*.

The presence in CGS of a higher density of localized states [100–106] (Fig.2.1), located both near the edges of the permitted zones (so-called "tails" of the density of states arising due to lack of long-range order [100, 107, 108] and in the depth of the band gap (arising from short-range disturbances, such as broken or unusual configurations of the chalcogen atom, etc., which are in different charge states D^0, D^+ and D^- [84, 109–111]), leads to the fact that in these materials there are three possible mechanisms of charge carrier transfer: conductivity by delocalized states, conductivity by localized states near the edges of permitted zones and conductivity by deep localized states. The second and third conduction mechanisms are due to the transition of carriers from one localized state to another with the participation of phonons, are called jumping conduction mechanisms. The relative contributions to the total conductivity of the three types of charge carrier transfer will dominate at different temperature ranges.

Consider the temperature and frequency dependences of the above conduction mechanisms in more detail. It should be noted that in *As-S* the mobility of holes is much higher than the mobility of electrons, so we will assume that the current is mainly carried by holes [112], and the Fermi level is shifted closer to the valence band. Then full conductivity *As-S* can be described as follows.
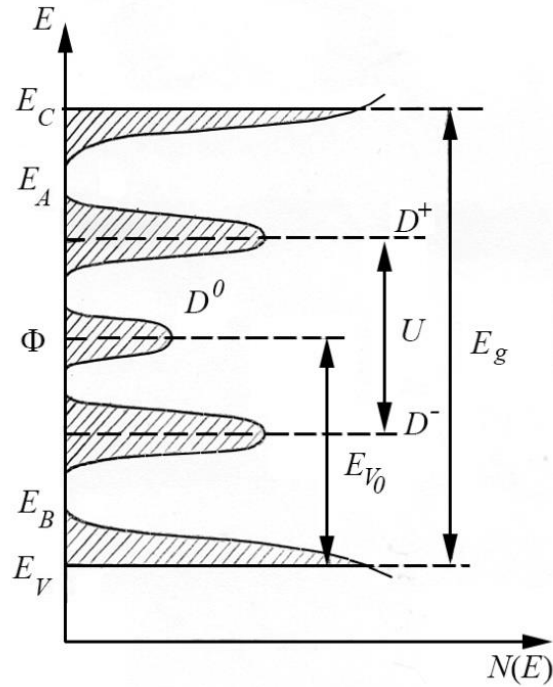
Fig.2.1. Energy spectra of CGS. Localized states are hatched. Φ – Fermi level.

1. Conductivity due to holes in non-localized states with energies E_V (Fig.2.1).

$$\sigma_V = \sigma_{0V} exp\left(-\frac{\Phi - E_V}{kT}\right). \tag{2.1}$$

For most materials $\sigma_{0_V} \approx 10^2 - 10^3 \ Ohm^{-1} cm^{-1}$, the value $\Phi - E_V$ is linearly dependent on temperature [103];

$$\Phi - E_V = E(0) - \gamma T, \qquad \gamma = 4 \cdot 10^{-4} \frac{eV}{K}.$$

The slope of the direct dependence $ln\sigma_V(1/T)$ is equal to $E(0)/k$, and the intersection with the *y*-axis gives the value $(T/k + ln\sigma_{0_V})$.

The frequency dependence of the dynamic conductivity in this case will be described by the Drude-Lorentz formula:

$$\sigma_V(\omega) = \frac{\sigma_{0V}}{1 + (\omega\tau_{e+})^2}. \tag{2.2}$$

Time of relaxation of free holes τ_{e+} is about $10^{-12}-10^{-13}\,c$, therefore up to $c\omega = 10^{10}\,Hz$ frequencies $\omega\tau_{e+} \ll 1$ and, therefore, in this range there is no frequency dependence of conductivity for holes in nonlocalized states.

1.   Conductivity due to holes excited in localized states at the edges of the valence band, conductivity due to holes excited in localized states near the edge of the valence band, and has a jumping character at energies nearby E_B (Fig.2.1).

$$\sigma_B = \sigma_{0_B}exp\left(-\frac{\Phi - E_B + \vartheta}{kT}\right). \tag{2.3}$$

where ϑ the activation energy of the jump.

Relatively σ_{0_B} can be assumed that it is much smaller than σ_{0_V}. This is, in particular, due to the fact that the effective density of states near the energy E_B is lower, which, in particular, is due to the fact that the effective density of states near the energy E_B less than nearby E_V, as well as due to a significant reduction in the mobility of holes at the energy E_V of the separation between localized and nonlocalized states [103].

If in this case we consider the dynamic conductivity, it should be borne in mind that if the conduction is carried out by stimulated phonon jumps on localized states, it increases with frequency ω. Austin and Mott

[113] derived the formula for such conductivity at states $N(\Phi)$ near Fermi energy:

$$\sigma(\omega) = \frac{\pi}{3} e^2 kT [N(\Phi)]^2 \alpha^{-5} \omega^2 \left[ln \left(\frac{\nu_{phon}}{\omega} \right) \right]^4, \qquad (2.4)$$

where ν_{phon} is the phonon frequency (of the order of 1012–1013 s–1), α – describes the decrease of the wave function of the localized state with distance.

In case $\omega \ll \nu_{phon}$, $\sigma(\omega) = const\ \omega^{0,8}$.

In the case we considered, when the charge carriers are transferred to localized states in the tail by the density of states near the edges of the permitted zones, the nature of the transfer mechanism is also related to the thermal activation of the carriers, therefore $\sigma \sim \omega^{0,8}$.

The difference between the jumping conductivity at localized states near the edge of the valence band and the jumping conductivity at states near the Fermi energy can be seen in the study of the temperature dependence of dynamic conductivity $\sigma(\omega)$. Activation energy $\Phi - E_B$ is required to form holes in the tail of the valence band. Therefore, with increasing temperature, the number of holes increases exponentially, therefore, in this case, the dynamic jump conductivity has the same temperature dependence as the statistical (exponential term usually dominates).

When transferred to nearby Φ states, the number of carriers remains constant, and $\sigma(\omega)$ varies linearly with temperature (Formula 2.4).

2. The temperature dependence of the conductivity on deep localized states significantly depends on whether these states are located near the Fermi level or away from it by a significant energy gap. In the

first case, the temperature dependence of the conductivity is subject to Mott's law $\left(\sigma(T) \sim exp\left(-\frac{B}{T^{1/4}}\right)\right)$ [112]. In the second case, the conductivity is activation, and the activation energy of the temperature dependence of this conductivity should be the sum of the energy distance from the Fermi level to the level of defects $U/2$ on which jumps occur (Fig.2.1), and the activation energy jump from one center to another – ϑ. Note that in our experiments, Mott's law is not observed and, therefore, in the materials we study, the density of states near the Fermi level is insignificant.

We studied the temperature and frequency dependences of dark electrical conductivity in CGS systems *As-S* with different sulfur content (from $As_{15}S_{85}$ to As_2S_3). On the curve of temperature dependence of static conductivity for all studied samples there was a break (Fig.2.2), the position of which shifted towards lower temperatures with increasing percentage of sulfur in the samples.
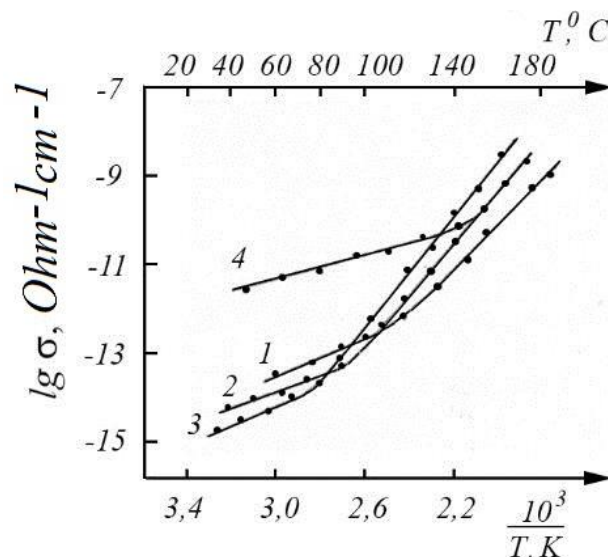
Fig.2.2. Temperature dependence of static (1–3) and dynamic conductivities at ω=500 Hz (4) for samples with different sulfur content: $1 - As_2S_3$; $2 - As_{25}S_{75}$; $3 - As_{20}S_{80}$; $4 - As_{25}S_{75}$.

Above and below the breaking point, this dependence satisfies the ratio:

$$\sigma = C exp\left(-\frac{E}{kT}\right),$$ (2.5)

Where the magnitude C and energy of activation E for low-temperature (C_1, E_1) and high-temperature (C_2, E_2) regions are presented in Table 5.

Table 5.

Material	$C_1, Ohm^{-1}cm^{-1}$	IS_1, eV	$C_1, Ohm^{-1}cm^{-1}$	E_2, eV	$\sigma_0, Ohm^{-1}cm^{-1}$
As_2S_3	$8 \cdot 10^{-7}$	0,45	10^2	1,05	$0,1 - 1,0$
$As_{25}S_{75}$	$4 \cdot 10^{-7}$	0,45	10^3	1,1	10
$As_{20}S_{80}$	$1,0 \cdot 10^{-7}$	0,45	10^5	1,25	$10^2 - 10^3$

As can be seen from the table, in the low-temperature region, the activation energy of conductivity does not depend on the ratio of components, and the value C_1 decreases slightly with increasing sulfur composition. In the high-temperature region with increasing sulfur composition, the activation energy E_2 of conductivity increases, and in the transition from As_2S_3 to $As_{20}S_{80}$ this increase is approximately 0,2 eV. The shift of the intrinsic absorption edge observed with such a change in composition shows that the band gap also increases and the expansion is approximately 0,2 eV. The shift of the intrinsic absorption edge observed with such a change in composition shows that the band gap is also increasing and the expansion is approximately 0,27 eV. Therefore, the equilibrium concentration of carriers due to the conductivity in the temperature range above the breaking point, is provided by the

thermodynamic equilibrium of the valence band and the conduction band and is determined by the Fermi level, which is located near the middle of the band gap.

Simultaneously with the increase in the activation energy of conductivity with increasing sulfur composition, there is an increase in the preexponential multiplier C_2, which contains the temperature coefficient of change of the optical width of the band gap γ and is determined by the formula $C_2 = \sigma_0 exp\left(\frac{\gamma}{K}\right)$. Our optical measurements show that the compounds *As-S* excess sulfur compared to the stoichiometric composition does not lead to a change in the coefficient γ, which is consistent with [114]. For our samples, the value γ is approximately $4 \cdot 10^{-4}$ *eV/K*, regardless of composition. Thus, the increase C_2 is due to a change in conductivity σ_0, the values of which are shown in Table 5.

The dependence of the dynamic conductivity $\sigma(\omega)$ on temperature for these materials is also observed fracture (Fig.2.2, curve 4), the position of which depends not only on the percentage of sulfur in the samples, but also on the frequency of the measuring voltage ω. As the fracture ω position increases, it shifts toward high temperature to the softening temperature of the material.

In the low-temperature region, the dynamic conductivity is much higher and shows an exponential dependence on temperature, with activation energy $E_V(\omega) \approx 0,35$ *eV* (regardless of the composition and frequency ω of the measurement voltage) less than for static (Table 5),

the frequency dependence of the dynamic conductivity in this temperature range has the form $\sigma \sim \omega^{0,8}$ (Fig.2.3).

At temperatures above the fracture, the dynamic conductivity (for samples with excess sulfur content) does not change when changing the frequency of the measuring voltage ω and shows the same dependence on temperature as static (Fig.2.2, curve 4).

The above-described change in the activation energy with temperature (the presence of a break in the dependence $g\sigma(^1/_T)$), in general, can be caused either by a sharp change in the position of the Fermi level, or by a change in the conduction mechanism [91].
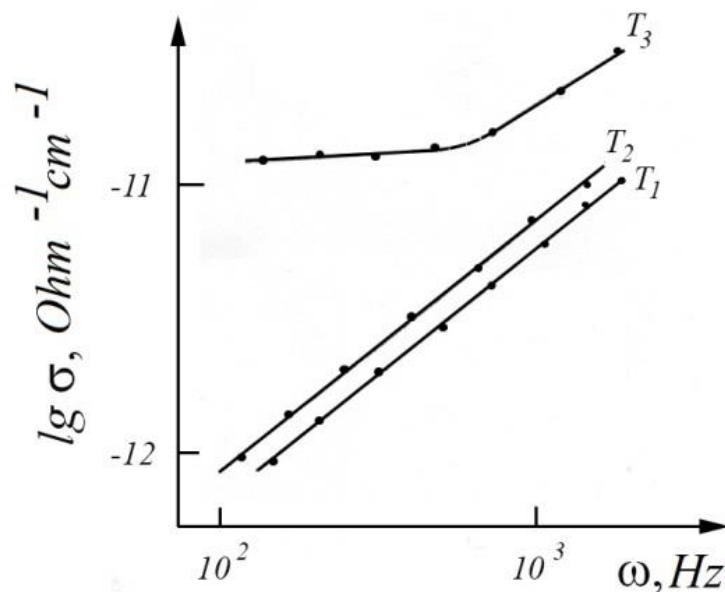
Fig.2.3. Frequency dependence of conductivity As_2S_3: $T_1=55°C$; $T_2=90°C$; $T_3=140°C$.

The latter occurs, for example, if at low temperatures the conductivity is abrupt, and at high – band [93, 115]. In turn, the position of the Fermi level may change, for example, for the following reasons.

71

1. At low temperatures, the conductivity is "defective" (free charge carriers are born due to transitions "defective" level – zone), and at high – own (free carriers are born due to interband transitions).

2. At low temperatures, the conductivity is "defective", and at high temperatures – the so-called "intrinsic – defective" [116], when the increase in the activation energy of conductivity is caused by the formation of compensating intrinsic defects as in halide-alkaline crystals [117].

Note that in these cases, when the change in the activation energy of conductivity is caused by a change in the position of the Fermi level, the mobility of carriers, and hence the preexponential factor in formula (2.5) cannot change significantly. For AHC, these changes did not exceed 10^5 [118].

As can be seen from Table 5, the values of the preexponential factors in the low and high temperatures differ by about ten orders of magnitude. Such a huge difference in our opinion indicates that the mechanism of conductivity in the regions of low and high temperatures is significantly different, and therefore, cannot be explained by the transition from "defective" conductivity to its own.

It should be noted that the change in activation energy can also not be caused by the creation of its own defects, firstly, because in this case σ_0 should not change significantly, and secondly, because the breaking temperature (as example, for As_2S_3 this temperature is approximately 100°C) is not sufficient for such a process (see Section 2.2). In addition, hardening of samples from a temperature above the softening temperature at which the active formation of defects does not change the nature of the

temperature dependence of dark conductivity, while, for example, in AHC, which has "intrinsic – defect conductivity" due to thermal generation of cationic vacancies, the picture is qualitatively different [118, 119].

Thus, a significant change in the activation energy of conductivity and pre-exponential multiplier is due to the fact that at low temperatures there is a jump in conductivity at the levels of deep centers, and at high temperatures conductivity is carried by carrier transfer to states near the mobility threshold E_V (Fig.2.1). (Conduction activation energies due to the transfer of carriers to delocalized states and to localized states located near the edge of the valence band do not differ significantly). This assumption is also confirmed by the fact that the fracture temperature depends on the frequency of the applied voltage ω, namely, with increasing ω fracture temperature increases. In fact, according to modern theoretical ideas [82, 112, 113], jumping conductivity increases in frequency according to the law $\omega^{0,8}$ (Formula 2.4), while band conductivity, depending on frequency according to Drude-Lorentz law, in the field of measured frequencies the frequency does not depend.

It should be noted that the difference in σ_0 (Table 5) depending on the percentage of sulfur, apparently due to the fact that in compositions close to stoichiometric, a significant role is played by the transfer of holes in localized states near the edge of the valence band. While in samples with a significant excess of sulfur, which σ_0 is approximately 10^2–10^3 $Ohm^{-1}cm^{-1}$, the transfer of charge carriers is carried out by delocalized states.

The results show that the activation energy of conductivity in the high-temperature region almost coincides with the distance from the Fermi level to the mobility threshold in the valence band, increasing with increasing sulfur content due to increasing the band gap.

The activation energy of dynamic and static conductivities in the low-temperature region is close to each other (0,35–0,45 eV) and coincide with the distance from the Fermi level to the defect level. (As mentioned above, this activation energy is the sum of two quantities – the energy distance from the Fermi level to the level of defects in which the charge carriers jump, and the activation energy of the jump from one center to another. However, according to the literature [120], energy activation of the electron jump from one defect to another is small and is about 0,1 eV. Therefore, in our conditions, the activation energy of conductivity is determined mainly by the first term.)

These defects, in our opinion, are D centers, a model proposed by Street and Mott [85].

According to this model, the Fermi level is located midway between the levels D^+ and the D centers, which are mostly in equilibrium in the glass. The fact that the position of the Fermi level is determined by different defects is confirmed by the fact that in the temperature range $T > T_g$, which, as will be seen below, there is a significant increase in the concentration of intrinsic defects, the energy of dark conductivity does not change. This result is consistent with the suggestion of Mott and Street [85, 109, 121] that the reaction

$$2D^0 \rightarrow D^+ + D^- \tag{2.6}$$

takes place with the release of energy U, and the equilibrium concentration D^0 of the centers $N_0(T)$ depends on the temperature according to the law

$$N_0(T) = N exp\left(-\frac{U}{2kT}\right),$$
(2.7)

Where U – effective correlation energy.

Low-temperature conductivity, in our opinion, is due to the transitions of electrons from D^0 center to D^+ center or from D^- center to D^0 center. In both cases, the activation of such jumping conductivity must be $\frac{U}{2} + \vartheta$, which according to our data gives the value $U \approx 0.7\ eV$ regardless of the percentage of sulfur in the samples. The release of energy U as a result of reaction (2.6) occurs due to the rearrangement of chemical bonds. Therefore, the independence of this energy from the composition of sulfur in the samples indicates that in different compositions the nature of the defects is the same and these defects (D -centers) are sulfur atoms with unusual bond configurations [122].

The microscopic structure of such defects was proposed in the work of Kastner, Adler and Fritzsche [123] and is shown in Fig.2.4.

Configuration		Energy p level		Energy configuration

C_2^0 ⠐⠶

$$\sigma^*$$
$$E_b + \Delta$$
$$LP \quad 0$$
$$\sigma \quad -E_b$$

$-2E_b$

C_3^0 *

$-2E_b + \Delta$

C_3^+

$-3E_b$

C_3^- **

$-E_b + 2\Delta + U_\sigma$

C_1^0

$-E_b$

C_1^-

$-E_b + U_{Lp}$
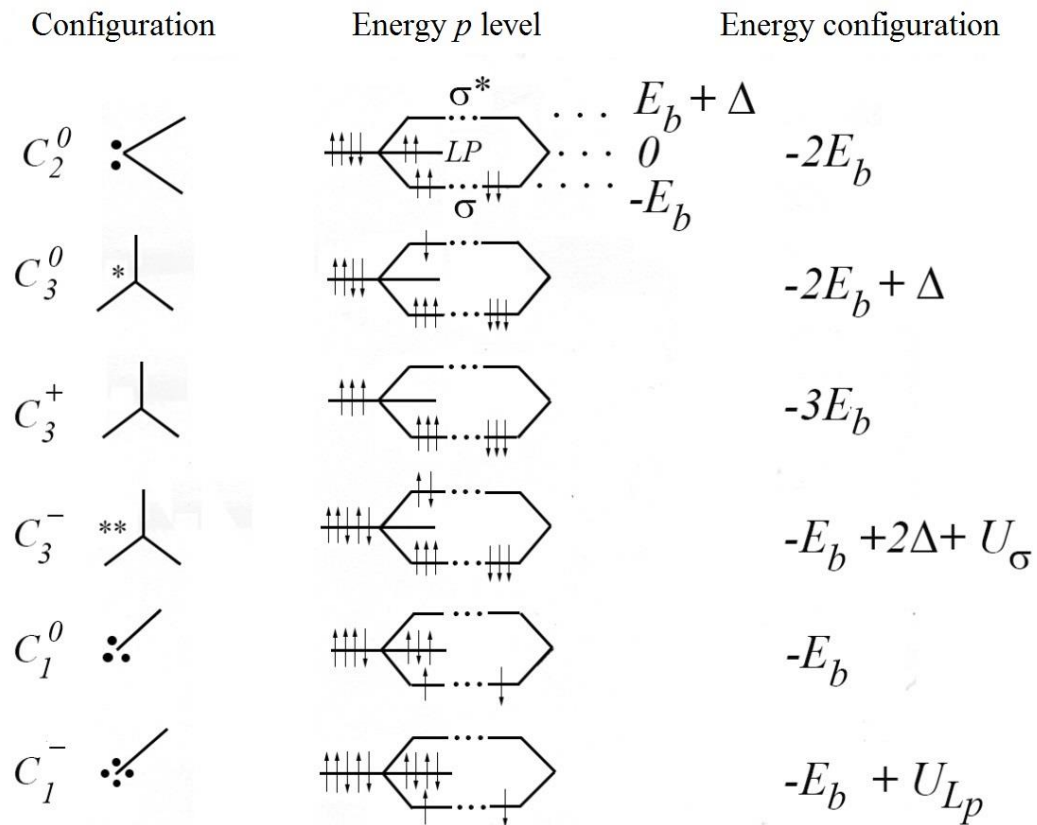
Fig.2.4. Structure and energy of different defect configurations in the material in coordination with two neighbors. The arrows show the spin of the electron.

Here, the defect states are indicated by symbols $C_1^0, C_3^0, C_3^+, C_1^-$, where C is the chalcogen atom, the lower index indicates the coordination of the centers (number of chemical bonds), and the upper – the charge state. Straight lines – connection (σ-state) and anti-binding state (σ^*). Dots are electrons of unshared pairs that do not take part in the formation of bonds.

C_2^0 – the normal configuration of the bound chalcogen atom. In this configuration, antibinders states σ^* are empty, and the energy of the binding electrons with respect to the level of unshared pairs is equal to

$2E_B$, where E_B is the bond energy, which is calculated from the energy level of undivided pairs.

The anti-binding states are shifted upwards from the level of undivided pairs more strongly than the binding states downwards by a magnitude Δ. Therefore, the following configuration (C_3^0 – a neutral atom associated with three others in which one extra electron is placed in the anti-binding orbital placed one superfluous electron) has energy $2E_B + \Delta$, so the energy of creation C_3^0 with C_2^0 consists of Δ, and since the energy of creation C_1^0 with C_2^0 consists E_B ($E_B \gg \Delta$), it is clear that the main is a neutral defect C_3^0, and the state C_1^0 (broken connection according to Mott et. al. [85]) is energetically unfavorable.

Of the negatively charged defects C_3^- and C_1^- the lowest energy has a configuration C_1^- that is a broken bond with four electrons in the state of unshared pairs, its energy is equal to $E_B + U_{LP}$, where U_{LP} – the correlation energy of the interaction of unshared pairs at one node. It is assumed that $2\Delta > U_{LP}$.

Energy $3E_B$ configuration C_3^+ is the only positively charged defect and has minimal energy compared to other defects.

Thus, as follows from the above, the main configurations of defects in the equilibrium state are C_3^0, C_3^+ and C_1^-, and the reaction (2.6) in Kastner's notation has the form

$$2C_3^0 \rightarrow C_3^+ + C_1^-. \qquad (2.8)$$

Based on the model of Kastner et al. [313], we can propose two mechanisms of jumping conductivity, characterized by the following reactions:

$$C_{3A}^{+} + C_{3B}^{0} \rightarrow C_{3A}^{0} + C_{3B}^{+}, \tag{2.9}$$

$$C_{1A}^{-} + C_{3B}^{0} \rightarrow C_{3A}^{0} + C_{3B}^{-}. \tag{2.10}$$
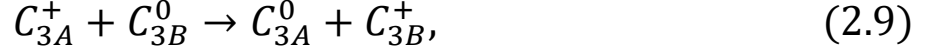
We believe that in our case the jumping conductivity is due to elementary act (2.9), since elementary act (2.10) requires more activation energy, because it must be accompanied by rearrangement of two chemical bonds at node A, while the process (2.9) is not accompanied by a change in coordination (number of chemical bonds) of defects.

Indeed, if the elementary act of electron jump from defect to defect requires low activation energy, then the difference between the activation energies of conductivity in the high and low temperature regions (for As_2S_3 this difference is 0,6 eV) must almost coincide with the energy distance from the acceptor level D^0 to the mobility threshold in the valence band E_{V_0}, which is confirmed by our results of photoelectric measurements (see Section 2.2).

It should be noted that our results show that the so-called bipolar conduction mechanism proposed by Eliot [124] ($C_A^{-} + C_B^{+} \rightarrow C_A^{+} + C_B^{-}$) does not play a significant role in the studied frequency range. Indeed, with such a mechanism, due to the transition of two electrons from D^{-} center to D^{+} center under the action of light of corresponding wavelength, when the concentration of D^0 centers increases and the concentration of D^{+} and D^{-} centers decreases, there would be a decrease in jumping conductivity, i.e. the effect of negative photoconductivity. However, in our conditions such an effect was not observed.

Therefore, low-temperature conductivity is due to jumps of carriers due to reaction (2.9), and in the region of high temperatures (T≥100°C) conductivity is associated with the release of carriers from equilibrium D^0 centers due to the reaction:

$$C_3^0 \rightarrow C_3^- + e^+. \tag{2.11}$$

In the state of thermodynamic equilibrium, the requirements of a detailed balance between the thermodynamic emission of holes from the D^0 centers into the valence band and their capture at the D^- centers must be met, which corresponds to the kinetic equation:

$$W_0 N_0 = p\gamma_p^- N_-. \tag{2.12}$$

Here $W_0 = N_V \gamma_p^- exp\left(-\frac{E_{V_0}}{kT}\right)$ – the frequency of thermal ejection of holes from the D^0 centers in the valence band, N_V – the density of states at the edge of mobility in the valence band, γ_p^- – the coefficient of capture of the hole to the D center.

Given the temperature dependence for $N_0(T)$ (2.7) and the fact that in the absence of thermal defects N_- does not depend on temperature ($N_- \gg N_0$), from equation (2.12) determine the temperature dependence $p(T)$:

$$p(T) \sim exp\left(-\frac{U + 2E_{V_0}}{2kT}\right) \tag{2.13}$$

and, therefore, the distance to the Fermi level is

$$\Phi - E_V = \frac{U + 2E_{V_0}}{2} \tag{2.14}$$

This value is slightly less than half of the band gap, as a result of which we studied the materials and have a p-type conductivity.

These results in studies of the electrical properties of CGS composition *As-S* we will limit ourselves to some conclusions before proceeding to the study of the photoelectric properties of these compounds.

Our studies of the temperature dependence of electrical conductivity allow us to establish in *As-S* systems the presence of several charge carriers. At low temperatures there is a jumping conductivity due to tunnel transitions of carriers from one defect to another, and at high – "band" conductivity in non-localized or localized states near the mobility threshold (Fig.2.2). The activation energy of the jumping conductivity $\sigma_{hop} = C_1 exp\left(-\frac{E_1}{kT}\right)$ is slightly less than the activation energy of the band conductivity $\sigma_V = C_2 exp\left(-\frac{E_2}{kT}\right)$. Therefore, although the hopping mobility μ_{hop} is much smaller than the band ($\frac{C_1}{C_2} \approx 10^{-10}$), due to the difference in activation energy $(E_2 - E_1 \approx 0{,}6 - 0{,}8\ eV)$ at low temperatures, the jump conductivity exceeds the band.

The activation energy of the jumping conductivity, in our opinion, is approximately equal to the distance from the Fermi level to the level of the defects on which the jumps of the carriers occur (up to the jump energy). If we interpret the results obtained within the model D center, then, $E_1 = \frac{U}{2} - \vartheta U$ where U – energy distance between D^+ levels and D^- centers (Fig.2.1), i.e. effective two-electron correlation energy, and ϑ – jump energy. Since the activation energy of the band conduction $E_2 = \Phi - E_V$ (E_V – valence band mobility threshold) is 1,0–1,2 eV, then the

depth of the acceptor level of the D center $E_{V_0} = E_2 - E_1$ and is $0{,}6\ eV$ for As_2S_3 and $0{,}8\ eV$ for $As_{20}S_{80}$ [78].

The correctness of this interpretation of the experimental data is confirmed by the fact that the depth level obtained from studies of the temperature dependence of stationary photoconductivity (see Section 2.2.2) is also $0{,}6$-$0{,}8\ eV$, depending on the composition. Note that the independence of the correlation energy U from the composition shows that in different compositions the nature of the defects is the same.

It is noteworthy that as the sulfur content in the samples of nonstoichiometric composition of the system As-S the pre-exponential multiplier C_2 increases significantly (see Table 5). This means that in such samples with the "zone" transfer mechanism, the mobility efficiency increases with increasing sulfur content. This increase in mobility efficiency, in our opinion, can be explained by a change in the short order. In fact, in CGS, the valence band ceiling is formed by overlapping the p-orbitals of undivided pairs of chalcogen atoms [121, 125]. Therefore, the zone transfer of holes is carried out by tunneling them from one undivided pair to another. When changing the composition of the samples in the direction of increasing sulfur content, the proportion of ties As-S decreases and S-S connections increase. This leads to a decrease in the distance between undivided chalcogen pairs, and the probability of tunneling a hole from one undivided pair to another increases, which leads to an increase in effective mobility.

The increase in the effective mobility of the holes as the sulfur content increases, in our opinion, explains the decrease in the resolution of the materials of the system As-S when recording a hologram in the case

81

of such a deviation from stoichiometry [126]. Indeed, as will be shown in Chapter 3, the recording of holograms in the system *As-S* initiated by free carriers [78] and therefore the resolution of such carriers is inversely proportional to the length of diffusion displacement of holes in the zone $L = \sqrt{Д\tau_{e+}}$, where is the diffusion coefficient, which is related to Einstein's ratio $Д = \frac{kT}{e}\mu$ – with effective mobility μ, τ_{e+} – lifetime of holes in the valence band. (Recording holograms with a lattice period of less L is impossible, as in this case the concentration of carriers in the illuminated and unilluminated areas will be almost the same, which is equivalent to the illumination of a uniform beam).

As can be seen from Table 5, as sulfur content increases, the effective mobility of holes increases by about three orders of magnitude in the transition from As_2S_3 to $As_{20}S_{80}$, and the resolution of such stoichiometry decreases by about an order of magnitude [126], consistent with the proposed explanation.

2.2. Photoelectric studies of thermally stimulated transformations in CGS composition *As-S*.

This section presents the results of the study of temperature and lux-ampere characteristics of stationary photoconductivity, as well as the processes of relaxation of the photocurrent after turning on and off the exciting light. The dependence of the instantaneous relaxation time of the photocurrent $\tau = \frac{\Delta\sigma}{\frac{d\sigma}{dt}}$ on the temperature, the intensity of the exciting light and the total relaxation time was determined t.

Photoconductivity measurements were performed by us on alternating current in the frequency range 100-200000 Hz in order to exclude the influence of electrode phenomena, which largely determine the photoconductivity on direct current and complicate the interpretation of results in most authors [102, 127–129]. Arsenic sulfide samples, which are plane-parallel plates 0,4–0,6 mm thick, were studied. Illumination was performed with a He-Ne laser ($\lambda = 632,8\,nm$) in a direction perpendicular to the direction of the electric field; the dimensions of the sample in this direction were about 10 mm. The intensity of the exciting light did not exceed 0,06 W/cm^2, which, as shown in Section 2.3, is insufficient for the active course of photostructural transformations As-S [86].

2.2.1. The mechanism of generation of nonequilibrium carriers in CGS of As_2S_3 composition.

In order to identify the mechanisms of generation of nonequilibrium carriers when illuminating He-Ne samples with a laser, we investigated the spectral and temperature dependence of the absorption of samples of the system As-S with different sulfur content, as well as the frequency dependence of the dynamic photoconductivity (dependence on the frequency of the added electric field). The curves of the spectral dependence of the absorption are presented in Fig.2.5, Fig.2.6.
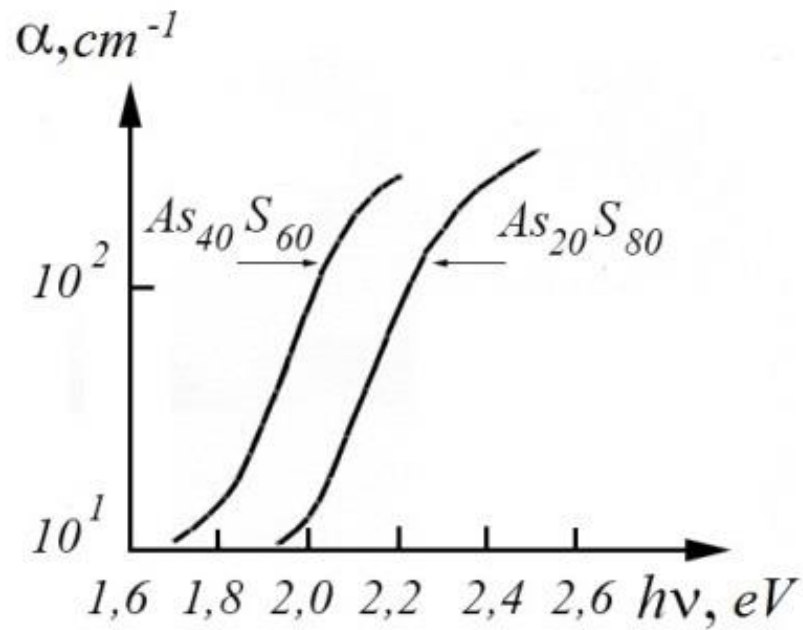
Fig.2.5. Spectral dependence of the absorption coefficient $\alpha(hv)$ for system samples *As-S* with different sulfur content.
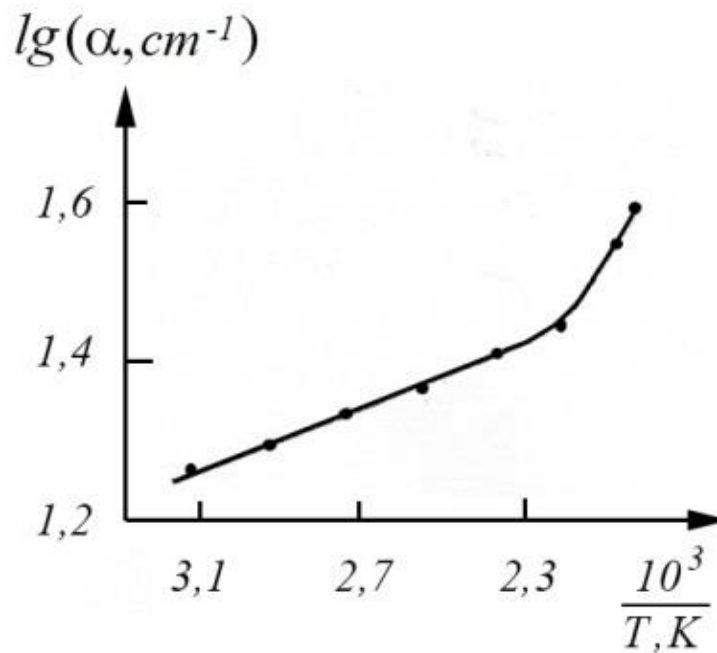
Fig.2.6. Temperature dependence of the absorption coefficient on the wavelength of He-Ne laser radiation ($\lambda = 632,8\ nm$). The energy of the linear section is $\approx 0,03$ eV.

The figures show that the wavelength of the exciting light of the He-Ne laser ($h\nu=1,96$ *eV*) corresponds to the absorption coefficient $\alpha\approx10$ *cm^{-1}* for As_2S_3, which decreases with increasing sulfur content to 1 *cm^{-1}* in $As_{20}S_{80}$. Such small absorption coefficients indicate that under the action of light $h\nu=1,96$ *eV* there are transitions, as a result of which the carrier is pulled out of the deep center (sits on the deep center). Note that according to the literature in the generation of carriers in non-localized states, the optical absorption α is at least 10^3 *cm^{-1}* [110, 130].

In glass semiconductors, optical transitions from deep centers to both localized and delocalized states located near the mobility threshold are possible. If as a result of the elementary act of excitation of the photocarrier passes to the localized state, the jumping mechanism of transfer is possible, which should be manifested in the frequency dependence of the stationary photoconductivity.

Our measurements showed that in the frequency range from 100 to 200000 *Hz*, the stationary photoconductivity for As_2S_3 almost did not depend on the frequency. Thus, under the action of light $h\nu=1,96$ *eV* carriers are born in delocalized states. This result also shows that the generation of nonequilibrium carriers is due to "level-zone" transitions, and not due to transitions between localized states near the mobility threshold. Thus, in the conditions of our experiment, the generation of free carriers occurs as a result of the following reactions, which are schematically shown in Fig.2.7.

$$C_1^- + h\nu \rightarrow C_1^0 + e^-, \tag{2.15}$$

$$C_3^+ + h\nu \rightarrow C_3^0 + e^+. \tag{2.16}$$

Here e^- and e^+ – the electron and the hole in delocalized states hv – the quantum of light.
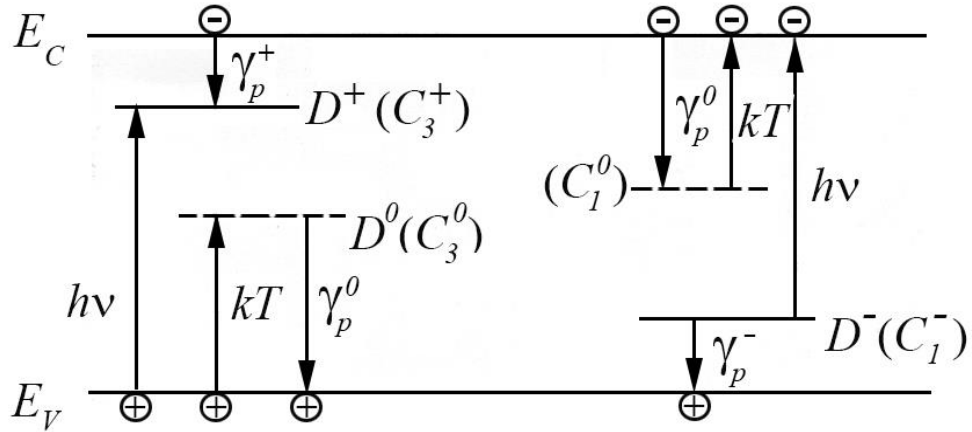
Fig.2.7. Energy levels in the band gap of CGS and the scheme of optical (hv), thermal (kT) and recombination (γ_p) transitions. The direction of the arrows indicates the movement of electrons.

Note that the generation of free carriers in delocalized states can occur as a result of the transition from the neutral D^0-center:

$$C_3^0 + hv \rightarrow C_3^+ + e^-, \tag{2.17}$$

$$C_3^0 + hv \rightarrow C_1^- + e^+. \tag{2.18}$$

However, we found that transitions with a neutral center did not play a significant role.

Indeed, as noted in the previous Section 2.1, the equilibrium concentration $N_0(T)$ of the D^0 centers strongly depends (exponentially with an activation energy of $\approx 0,4\ eV$) on the temperature. Our studies of the temperature dependence of the absorption coefficient (Fig. 2.6) showed that in the temperature range $T < T_g$ with increasing temperature, the absorption coefficient α at the He-Ne laser wavelength increases with an activation energy of only 0,03 eV. Therefore, in the conditions of our experiment, the main role is played by optical transitions (2.15) and (2.16)

of carriers from charged centers, the concentration of which is practically independent of temperature.

2.2.2. Temperature and lux-ampere characteristics of stationary photoconductivity and photocurrent kinetics in As_2S_3.

Figure 2.8 shows the lux-ampere characteristics (LAC) of the stationary photoconductivity of arsenic trisulfide. The figure shows that at low temperatures the LAC is close to 1 (0.9 at 55°C), and with increasing temperature the slope of the LAC decreases to 0,5.
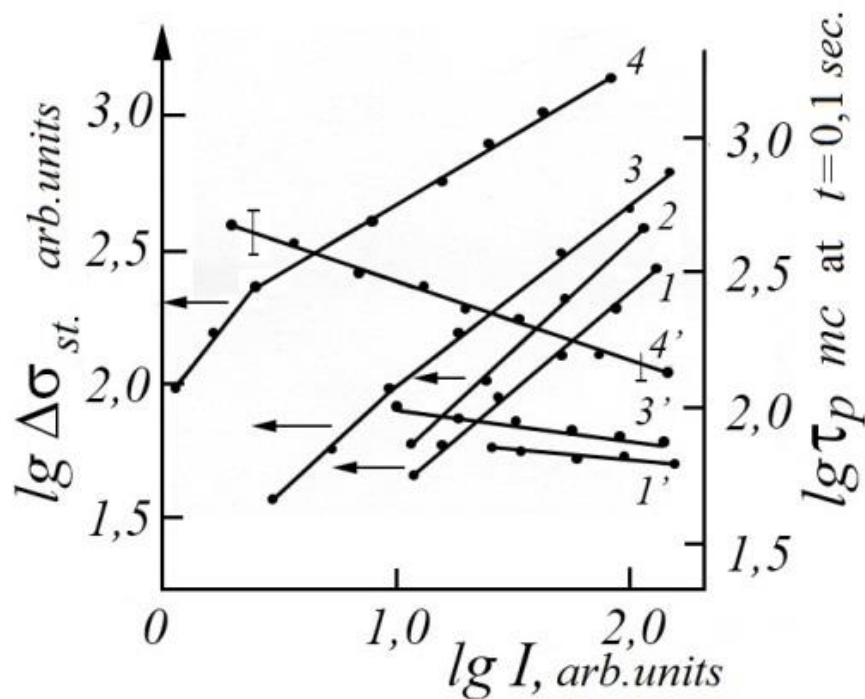
Fig.2.8. Lux-ampere characteristics (1–4) depending on τ_p (1'–4'), determined by formula (2.19), for the moment of time $t=0,1$ *sec* from the light intensity of the He-Ne laser for As_2S_3 at different temperatures ($\omega=290$ *Hz*).

1,1'–55°C; 2– 70°C; 3, 3'–105°C; 4, 4'–165°C.

The strongest reduction in the slope of the LAC occurs at temperatures above 100°C. At low light intensity (not more than 0,02

W/cm²) LAC is more complex. In addition to areas with a slope close to 1 or 0,5, at temperatures above 180°C, there is a section of LAC with a slope exceeding 0,5–0,6. This increase in the slope of the LAC occurs starting from the temperature at which the dark conductivity and photoconductivity become approximately equal. With a further increase in temperature, when the dark conductivity exceeds the photoconductivity (i.e. at temperatures when the photoresponse becomes weak), the slope of the LAC continues to increase approaching unity.

Figure 2.9 shows the temperature dependences of stationary photoconductivity, measured in As_2S_3 on alternating current at different intensities of exciting light. It follows from the figure that at low temperatures (light intensities are high enough I_5, I_6, I_7) photocurrent is almost independent of temperature. Comparison with Fig.2.8 shows that in this area the slope of the LAC is close to one. When the temperature rises, the thermal activation of photoconductivity takes place. At sufficiently high intensities (I_5, I_6, I_7), the activation energy of the photocurrent is approximately 0,3–0,4 *eV*. The variance of activation energy values in the tested samples does not exceed 0,1 *eV*. (Note, however, that with increasing sulfur composition in the samples, the activation energy of photoconductivity increases: for the stoichiometric composition As_2S_3 the most typical is 0,3 *eV*, and for samples with high sulfur content $As_{20}S_{80}$ − 0,4 *eV*). From Fig.2.9 it is seen that for low intensities (I_1, I_2, I_3, I_4) at *T*>100°C activation energy of stationary photoconductivity in As_2S_3 it is about 0,6 *eV*.
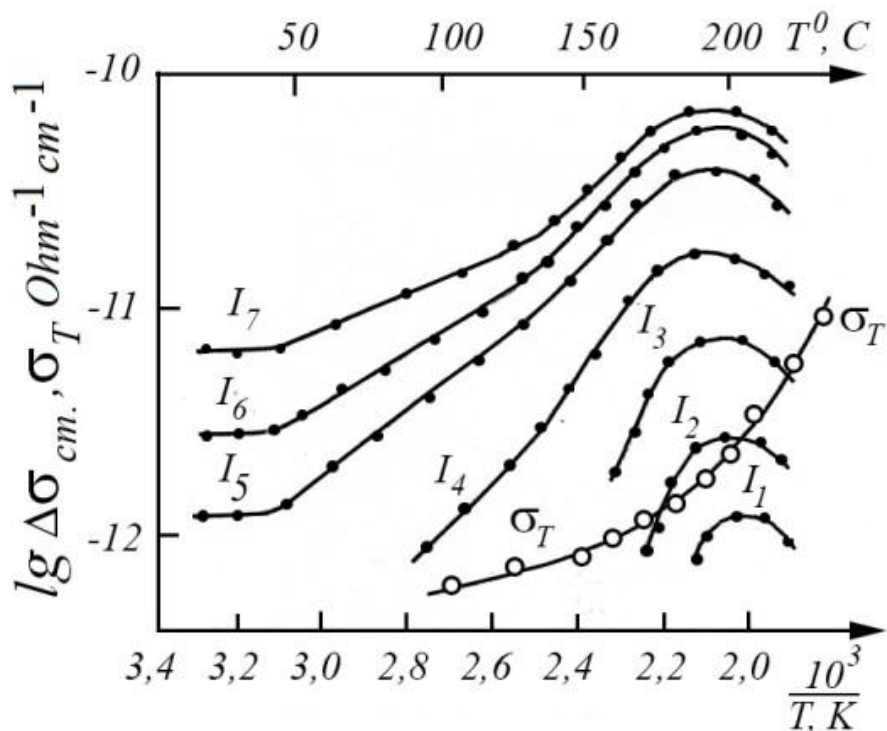
Fig.2.9. Temperature dependence of dark ($\Delta\sigma_T$) and stationary ($\Delta\sigma_{st}$) photoconductivity As_2S_3 ($\omega=290$ Hz), which was measured at different intensities of exciting light ($I_4 < I_5 < I_6 < I_7$).

Thus, with the corresponding decreases in the intensity of excitatory light, the activation energy of stationary conductivity increases approximately twice (note that in the temperature range in which this occurs, coincides with the region in which the slope of the LAC was 0,5).

With a further increase in temperature (above 180°C) for As_2S_3 the maximum temperature dependence of the stationary photoconductivity. For materials of this composition, the maximum temperature depends on the intensity of exciting light: both in the case of strong and weak photo response, the maximum temperature dependence of stationary photoconductivity occurs at the same temperature.

At intensities I_5, I_6, I_7, the slope of the LAC in the field of thermal quenching of photoconductivity did not change, and for low intensities I_3

and I_4 thermal quenching of photoconductivity was accompanied by an increase in the slope of the LAC to unity (Fig.2.8).

Comparisons of temperature dependences of stationary photoconductivity and absorption coefficient at $hv = 1,96\ eV$ (Fig. 2.6 and 2.9) show that in the field of temperature quenching of stationary conductivity there is a sharp increase in the coefficient of light absorption with temperature.

Note that the maximum temperature dependence of the stationary photoconductivity occurs at the softening temperature of the material T_g, so with increasing sulfur composition in the samples the maximum is shifted to the region of lower softening temperatures T_g, for example, in $As_{20}S_{80}$ it lies at 120–130°C.

Measurement of photoconductivity relaxation kinetics was performed under illumination with rectangular light pulses from a He-Ne laser for approximately 15 minutes. The fronts of the light pulse had a duration of approximately 10^{-4} s. If the photoconductivity reaction was monotonic, a rectangular pulse of light for growth and decline can be approximated as

$$\Delta\sigma = \Delta\sigma_{\text{CT}}\left[1 - exp\left(-\frac{t}{\tau_{\text{p}}}\right)\right], \qquad (2.19)$$

$$\Delta\sigma = \Delta\sigma_{\text{CT}}\,exp\left(-\frac{t}{\tau_{\text{c}}}\right). \qquad (2.20)$$

it turns out that τ depends on the amplitude of the illuminance I and the time t elapsed since the jump in light intensity. The results of our measurements (Fig.2.8 and 2.10) showed that for $As_2S_3 - \tau \approx I^{-\varphi}t^{\delta}$.
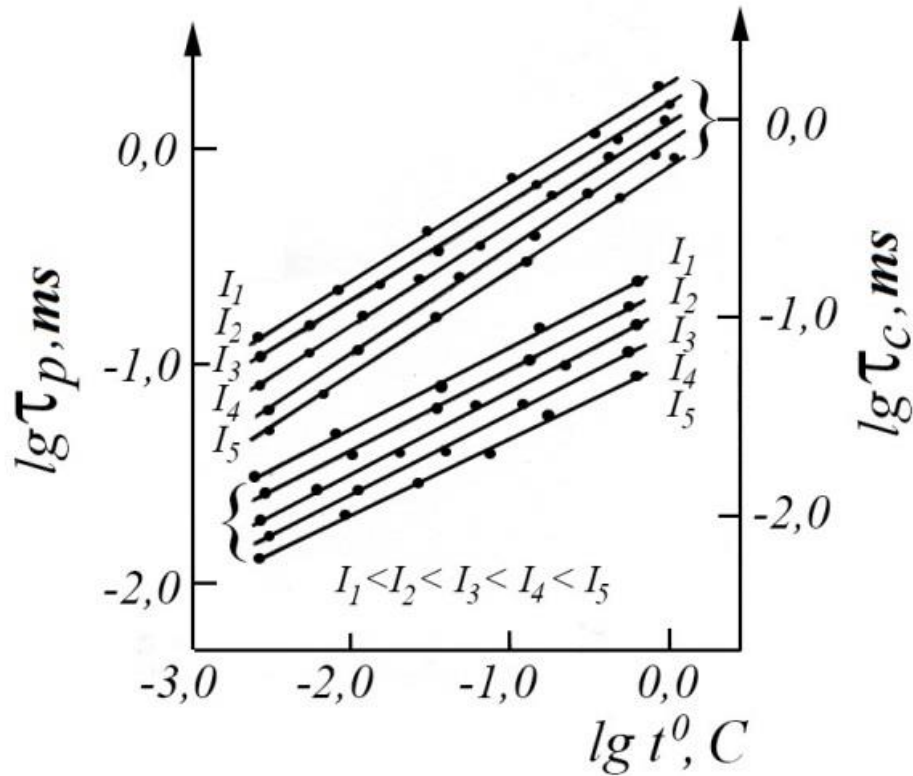
Fig.2.10. The time dependences of the relaxation time for the increase in photoconductivity (τ_p) and the decrease (τ_c) are determined from equations (2.19) and (2.20) at different radiation intensities with $\lambda = 632,8\ nm$ for As_2S_3 at T≈55°C and $\omega = 290\ Hz$.

The explicit division of relaxation curves into fast ($\tau < 10^{-3}\ s$) and long regions, as observed in [128], does not take place in our experiments, i.e. regions with $\tau < 10^{-3}\ s$ can exist only in the initial period $t < 0,005\ s$ when the change in photoconductivity $\Delta\sigma$ is very small ($\Delta\sigma < 0,05\ \Delta\sigma_{st}$).

Values α, φ and γ also depend on temperature. With increasing temperature from 40 to 160°C γ changes: for an increase in photoconductivity – from 0,55 to 0,65, and for a decrease in photoconductivity – from 0,65 to 0,75. The value φ in the same temperature range varies from 0,15 to 0,4.

91

At the used intensities of light, the value τ_p does not depend on temperature, and the process of attenuation of the photocurrent is more complex. At low temperatures (T≤100°C for As_2S_3) τ_c is almost independent of temperature, reaches a maximum at T=180°C, and with further increase in temperature decreases (Fig.2.11).
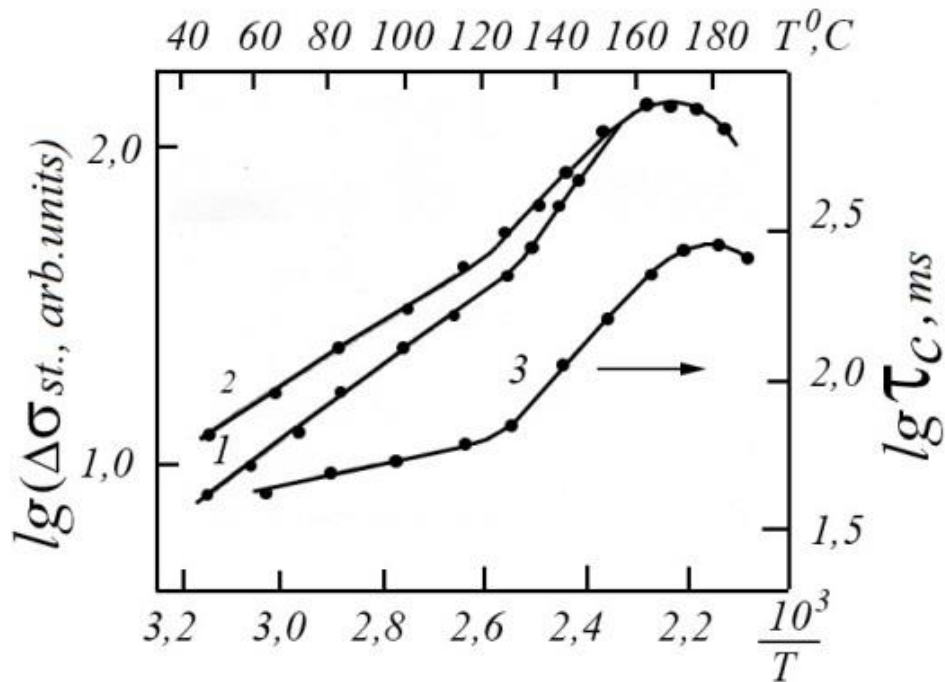
Fig.2.11. Temperature dependence $\Delta\sigma_{st}$ (curves 1, 2) and τ_c, determined by formula (2.20) (curve 3): 1, 3 – sample As_2S_3 which before each measurement is annealed at T≈180°C for 15 minutes; 2 – sample As_2S_3 illuminated by He-Ne laser light at T=140°C for 15 minutes ($\omega = 290\ Hz$).

From Figures 2.9 and 2.11 it is possible to see the correlation between the temperature dependence of the relaxation time τ_c of the decline and the stationary photoconductivity. Indeed, at low temperatures both $\Delta\sigma_{st}$ and τ_c depend on temperature, and at T>100°C both values

increase and reach a maximum at $T = T_g$, and at the further increase of temperature decrease.

There is also some correlation between the dependencies $\Delta\sigma(I)$ and $\tau_c(I)$. Thus, the slope of the LAC ($\Delta\sigma_{st} \sim I^\beta$) and the degree φ ($\tau \sim I^{-\varphi}$) of change vary most strongly at T≈110°C, and at T>110°C φ and the LAC index is close to 0,5 ($\varphi \approx 0,4 \pm 0,1$).

In addition, from the results of our experiments it should be noted that in the whole studied temperature range the sum of the LAC β indicator and the indicator φ is close to one.

2.2.3. The specifics of recombination processes in As_2S_3.

A number of patterns described above – reducing the slope of the LAC at elevated temperatures in the case of a strong photo response (when photoconductivity significantly exceeds the dark conductivity), increasing the slope of the LAC from 0,5 to 1,0 in the transition from strong to weak photo response, complementarity β and φ values as well as activation growth and decrease in photoconductivity with temperature – can be explained by models known in semiconductor physics [131–134]. Similar patterns were observed in other wide-band high-impedance semiconductors [135–141]. However, as described above, there are a number of characteristic features of photovoltaic properties in the materials of the system *As-S*, which distinguish these materials even in a number of other chalcogenide glassy semiconductors. Such specific features primarily include:

1. Dependence of the activation energy of stationary photoconductivity on the intensity of exciting light: with a corresponding

increase in intensity, the activation energy of stationary photoconductivity is reduced by half.

2. Peculiarity of the process of long-term relaxation (decline) of photoconductivity: relaxation time τ_c increases with increasing temperature. This fact indicates a decrease in the recombination rate with increasing temperature, which was not previously observed in other semiconductors, but there are theoretical models of long-term conduction relaxation [142, 143], which predict a decrease τ_c with increasing temperature.

3. In the case of a weak photoresponse ($\Delta\sigma < \Delta\sigma_T$), the photocurrent activation increases with temperature, although all theoretical models known to us predict a decrease in the photocurrent with temperature in the case of a weak photoresponse. It is necessary to emphasize the unusualness of this phenomenon, as even in similar properties of the composition *As-S*e thermal quenching of photoconductivity was observed in the region of weak photoresponsiveness.

4. The temperature of the maximum of the stationary photoconductivity does not depend on the intensity of the exciting light: for both strong and weak photo response, this temperature is equal to the softening temperature of the material T_g. The maximum temperature dependence of stationary photoconductivity, the position of which does not depend on the rate of generation of equilibrium carriers, but may be due to competition of generation and recombination processes, as is usually expected, and in our opinion associated with changes in the nuclear glass subsystem [86].

First, consider the first three features of photovoltaic properties *As-S*, which, as will be shown below, are related only to the processes in the electronic subsystem. The discussion will be conducted with the involvement of theoretical models, which assume that the main defects in CGS are *D* centers. The *D* center model has been used quite successfully to explain, for example, the electrical properties of As_2S_3 (see Section 2.1), as well as the electrical and photoelectric properties of arsenic selenide [85, 87].

In the cited theoretical works, the photoconductivity of CGS was described within the framework of the *D* center model only for the case of "zone-zone" generation of nonequilibrium carriers. Under the conditions of our experiment, as shown above (see Section 2.2.1), the generation of nonequilibrium carriers occurs as a result of "level-zone" transitions. Therefore, to explain the laws of stationary photoconductivity, we will proceed from the assumption that the generation of free carriers (holes) occurs only through recombination

$$D^+ + hv \rightarrow D^0 + e^+. \tag{2.21}$$

A more rigorous review, which will be carried out in the next section, shows that if we take into account the generation of nonequilibrium electrons as a result of the reaction

$$D^- + hv \rightarrow D^0 + e^-,$$
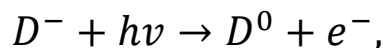
it does not change the pattern of temperature and lux-ampere characteristics of stationary photoconductivity.

Let us now consider the possible recombination channels of nonequilibrium carriers (Fig.2.7). When the system is in equilibrium, the *D* center is mainly in the states D^+ and D^-; therefore, a hole torn by light

from the D^+ center will be captured by the D^- center. Such captures are not recombination processes, because as a result of both generation and capture, the concentration of neutral D^0 centers N_0 increases. The steady-state value of photoconductivity will be established only when, as a result of recombination of nonequilibrium D^0 centers, the increase in concentration N_0 ends. Non-equilibrium D^0 centers can recombine as a result of subsequent reactions

$$2D^0 \rightarrow D^+ + D^-, \tag{2.22}$$

$$D^0 + e^+ \rightarrow D^+. \tag{2.23}$$

Reaction (2.22) is carried out tunneling at the transition of an electron from one D^0 center to another, and the reaction (2.23) is a process inverse to the considered process of generation (2.21) – direct capture of the hole.

We now describe the temperature and lux-ampere dependences in the case when tunnel recombination predominates in stationary conditions. At low temperatures, when the thermal release of holes from D^0 centers in the valence band is insignificant, under the action of light are the following electronic transitions:

$$D^+ + hv \rightarrow D^0 + e^+, \tag{2.24}$$

$$D^- + e^+ \rightarrow D^0, \tag{2.25}$$

$$2D^0 \rightarrow D^+ + D^-. \tag{2.26}$$

These transitions correspond to the following kinetic equations, which describe the balance of free holes and D^0-centers

$$\frac{\partial p}{\partial t} = IqN_+ - p\gamma_p^- N_-, \tag{2.27}$$

$$\frac{\partial N_0}{\partial t} = p\gamma_p^- N_- + IqN_+ - bN_0^2, \qquad (2.28)$$

where q – the cross section of the reaction (2.21), γ_p^- – the coefficient of capture of holes in the D center, b – the coefficient of intercenter tunnel recombination, which is weakly dependent on temperature [86].

To determine the steady-state concentration of photoderms, the condition of electroneutrality must be taken into account

$$n_e + N_- = p + N_+. \qquad (2.29)$$

Since in CGS the concentration of D^+ and D^- centers is high ($N_+ \approx N_- \approx 10^{17}$–$10^{18}$ cm^{-3}) then in photoexcitation, $N_- > n_e N_+ > p$; therefore, the condition of electroneutrality is:

$$N_+ = N_-. \qquad (2.30)$$

Therefore, for stationary conditions from equation (2.27) we obtain:

$$p = \frac{Iq}{\gamma_p^-}. \qquad (2.31)$$

To determine the stationary concentration of photoderms it is necessary to take into account the condition of electroneutrality (2.29):

$$n_e + N_- = p + N_+.$$

Thus, at low temperatures, when the thermal emission of holes is suppressed, the concentration of photocarriers is weakly dependent on temperature, the LAC is close to one, and, as can be seen from equation (2.27), the value τ_c should be weakly dependent on the intensity of exciting light. Note that similar results are obtained at low temperatures (thermal emission of holes in the valence band is small) and in this case, when recombination is carried out as a result of direct capture of holes in the D center.

However, at high temperatures, the activation energy of photoconductivity significantly depends on which recombination channel predominates. In fact, let the temperature be so high that a quasi-equilibrium is established between the capture of holes and their thermal release from the D^0 centers to the valence band:

$$D^- + e^+ \leftrightarrow D^0. \tag{2.32}$$

In this case, the stationary concentration of photoderms is described by the equation

$$P(T) = \frac{W_0 N_0(T)}{\gamma_p^- N_-}, \tag{2.33}$$

where $W_0 = N_V \gamma_p^- exp\left(-\frac{E_{V0}}{kT}\right)$ – frequency of thermal emissions of holes from the D^0 centers in the valence band, N_V – effective density of states in the valence band at the edge of mobility, E_{V_0} – acceptor level of D^0- center. (Equation (2.33) itself is true if the temperature is so high that the inequality holds $W_0 N_0 > IqN_+$).

In the case where tunnel recombination predominates, the concentration of D^0 centers $N_0(T)$ is determined with the equation:

$$bN_0^2 = IqN_+ \tag{2.34}$$

and weakly dependent on temperature. Therefore, the activation energy of photoconductivity almost coincides with the depth of the acceptor level D^0 center, and the LAC indicator, as can be seen from equations (2.33) and (2.34), β=0,5. When direct recombination predominates, the concentration of D^0 centers $N_0(T)$ determined from the equation

$$p\gamma_p^0 N_0 = IqN_+, \tag{2.35}$$

where γ_p^0 – the coefficient of capture of holes on the D^0 centers.

If we multiply equations (2.33) and (2.35), we get:

$$p = \sqrt{\frac{W}{\gamma_p^- \gamma_p^0}} Iq \sim exp\left(-\frac{E_{V_0}}{2kT}\right). \tag{2.36}$$

Equation (2.36) shows that, as in the previous case, the LAC index $\beta=0,5$, but the activation energy of photoconductivity is twice less than in tunnel recombination.

Direct recombination will prevail over tunnel recombination when inequality holds

$$p\gamma_p^0 N_0 > bN_0^2. \tag{2.37}$$

Equation (2.33) is valid regardless of which recombination channel predominates, therefore, using this equation, inequality (2.37) can be written as;

$$W_0 > \frac{\gamma_p^-}{\gamma_p^0} bN_-. \tag{2.38}$$

Concentration of D^- centers N_- decreases with increasing intensity of exciting light. Therefore, it follows from inequality (2.38) that at lower intensities intercenter tunnel recombination will be significant, and at high intensities – direct recombination.

Thus, the change in the recombination channel with increasing intensity of exciting light will be accompanied by a decrease in the activation energy of stationary photoconductivity by half. This is the change in the activation energy of stationary photoconductivity in the temperature range, in which the LAC indicator β is 0,5, observed by us experimentally.

We now show that the change in the recombination channel during long-term relaxation of photoconductivity explains the increase in the

minimum relaxation time τ_c with temperature. In [87] it was shown that the time of establishing a quasi-equilibrium between the capture of holes in the D^- centers and their ejection from the D^0 centers into the valence band is much less than the characteristic time of decline in the concentration $N_0(t)$ of D^0 centers. Therefore, the residual concentration of holes in the area of non-exponential decline in conductivity, which we studied, is given by the expression:

$$p(t) = \frac{W_0 N_0(t)}{\gamma_p^- N_-(t)}.$$

(2.39)

If this is the case $N_-(t) \gg N_0(t)$, then the instantaneous relaxation time τ_c is given by the expression;

$$p(t) = \frac{W_0 N_0(t)}{\gamma_p^- N_-(t)}.$$

(2.39)

If at the same time $N_-(t) \ll N_0(t)$, the instantaneous relaxation time τ_c will be given by the expression:

$$\tau_c(t) = \frac{p}{\left|\frac{\partial p}{\partial t}\right|} \approx \frac{N}{\left|\frac{\partial N_0}{\partial t}\right|} = \frac{1}{f N_0}.$$

(2.40)

Here f is the recombination coefficient.

In the case where long-term conduction relaxation (LTCR) is determined by the tunnel reaction, $f=b$ and is weakly dependent on temperature. In this case, when LTCR is due to the direct capture of holes in the D^0 centers, as shown in [142], $\frac{W_0 \gamma_p^0}{\gamma_0^- N_-} \sim exp\left(-\frac{E_{V0}}{kT}\right)$ and due to the value W_0, which is strongly (exponentially) dependent on temperature. Thus, the temperature dependence of the quantity τ_c is indicated by the temperature dependences of the quantities f and N_0. In stationary

100

conditions, as can be seen from formula (2.34), the value N_0 weakly dependent on temperature, if tunnel recombination prevails. In the case where direct recombination predominates, as can be seen from the formula(2.35),

$$N_0(T) = \frac{IqN_+}{\gamma_p^0 P(T)} \sim exp\left(\frac{E_{V_0}}{2kT}\right), \qquad (2.41)$$

the value $N_0(t)$ decreases sharply with increasing temperature.

From formula (2.41) and the above expressions for f it is seen that if the steady-state concentration of D^0 centers and long-term relaxation conductions is denoted by the same recombination channel, then the instantaneous relaxation time is almost independent of temperature or decreases with increasing. If in stationary conditions the main channel of recombination was direct capture, and LTCR is marked by tunnel recombination, then the instantaneous relaxation time may increase with increasing temperature, as in this case

$$\tau_c(t) = [bN_0(T)]^{-1}, \qquad (2.42)$$

where the value b is weakly dependent on temperature, and $N_0(T)$ decreases sharply with decreasing temperature(see (2.41)).

We now show that in the process of long-term relaxation of conduction, there may indeed be a change in the recombination channel. In fact, as the time elapsed after the excitation light is turned off, the concentration of free carriers will decrease and the concentration of charged D^+ and D^- centers will increase due to the direct capture of holes. As can be seen from inequality (2.38), the increase in the concentration of N_- will lead to the fact that after a long time the main channel of recombination is a tunnel intercentric reaction (2.6): $2D^0 \rightarrow D^+ + D^-$.

In other words, the increase in total relaxation time is fully similar to the intensity of excitatory light in stationary conditions, because the decrease in the concentration of free carriers leads to the fact that the concentration of neutral centers is a tunnel reaction rather than direct capture of carriers.

This interpretation of the $\tau_c(T)$ increase with increasing temperature is confirmed by the fact that growth $\tau_c(T)$ is observed in the same temperature range (Fig.2.11), in which we found the dependence of the activation energy of stationary photoconductivity on the intensity of exciting light (Fig.2.9).

Thus, the first two features of the photoelectric properties of *As-S*, namely, the dependence of the activation energy of stationary photoconductivity on the intensity of excitatory light and increase the relaxation time τ_c with temperature, due to changes in the recombination channel: at low intensities of excitation light or at high relaxation times, when the concentration of free carriers at higher light intensities, when the concentration of free carriers is high, the main channel of recombination is direct capture.

The third characteristic feature of photovoltaic properties in the system *As-S* – activation growth of photocurrent with temperature in case of weak photoresponse - we also associate it with the fact that the intercenter recombination coefficient *As-S* weakly dependent on temperature. Indeed, as shown in [85, 143], in the case of a weak photoresponse due to the high concentration of D centers in CGS, the main recombination channel of nonequilibrium D^0 centers in CGS will be the tunnel crossing $2D^0 \rightarrow D^+ + D^-$ between nonequilibrium and

102

equilibrium D^0 centers. (Of course [131], that with a weak photoresponse in the case of band-band recombination nonequilibrium holes recombine with equilibrium electrons, and because the concentration of equilibrium carriers increases with temperature, there is thermal quenching of photoconductivity with a weak photoresponse). The concentration of nonequilibrium D^0 centers decreases with temperature due to increasing concentration of equilibrium D^0 centers as follows:

$$\Delta N_0(T) = \left[\frac{G}{2bN_0(T)}\right] \sim exp\left(\frac{U + 2U_{эф}}{2kT}\right), \qquad (2.43)$$

where G is the rate of photogeneration, U – the activation energy of tunnel recombination (2.6). It should be noted that due to the strong electron-phonon interaction at the D centers, the tunneling transition of the electron in reaction (2.6) is accompanied by a change in the equilibrium concentration of nuclei. Processes in the nuclear subsystem can occur tunneling at low temperatures and activation at elevated temperatures [293, 320, 323].

The photoconductivity caused by the emission of holes from nonequilibrium D^0 centers depends on the temperature according to the law:

$$\Delta\sigma \sim \Delta p = \frac{W_0 \Delta N_0(T)}{\gamma_p^- N_-} \sim exp\left(\frac{U + 2U_{эф} - 2E_{V_0}}{2kT}\right). \qquad (2.44)$$

In arsenic triselenide $U \approx 2E_{V_0}$ and therefore with a weak photoresponsive photoconductivity decreases with increasing temperature due to thermal activation of the reaction(2.6) [324]. In arsenic triselenide, the ratio between the parameters U and E_{V_0} other. The value U determined by us on the basis of electrical measurements (Section 2.1)

is 0,7–0,8 eV. The value E_{V_0}, which in the case of a strong photo response is equal to the activation energy of photoconductivity in tunnel recombination twice as much as this energy in direct recombination, is 0,6 eV for As_2S_3 and 0,8 eV for $As_{20}S_{80}$. Therefore, photoconductivity can be thermally activated even with a weak photo response, if $2E_{V_0} > U + 2U_{\text{eff.}}$.

This inequality is fulfilled in the samples studied by us, because $2E_{V_0} - U \approx 0,5 - 0,8$ eV, and the value $U_{\text{eff.}}$ is 0,05–0,1 eV. It is difficult to determine $U_{\text{eff.}}$ more precisely, because in the studied temperature range this value is of the order of kT. (Note that the distribution of energy D center levels is also a few hundreds of an electron volt).

The specificity of recombination processes determines the first three features of photoelectric properties in the system As-S. On the other hand, the maximum temperature dependence of stationary photoconductivity, the position of which coincides with the softening temperature for our composition and does not depend on the intensity of exciting light, can only be due to increasing the concentration of intrinsic defects in the material at softening temperature. This is also supported by a significant increase in the activation energy of the optical absorption coefficient in this temperature range.

Investigating the temperature dependence of stationary photoconductivity, we can determine the energy of creation of intrinsic defects W in the system As-S. Indeed, with a weak photo response in the temperature range, when thermal defects can be neglected, the

photoconductivity increases according to the law:

$$\Delta\sigma(T) \sim exp\left(-\frac{\Phi}{kT}\right), \tag{2.45}$$

where Φ is determined by formula (2.44). At high temperatures, when the equilibrium concentration of defects increases with increasing temperature $N \sim exp\left(-\frac{W}{kT}\right)$ as follows from (2.43) and (2.44) (in (2.43) we must take into account that in our case $G = IqN_-$, the photoconductivity decreases by law:

$$\Delta\sigma(T) \sim exp\left(\frac{-\Phi + W}{kT}\right). \tag{2.46}$$

It can be seen that the energy of defect formation is equal to the sum of two experimentally determined values Φ and $E_q = W - \Phi$, where E_q is the energy of thermal quenching of photoconductivity in the region of decline. The value E_q is approximately equal to $0{,}3$–$0.5\ eV$, therefore $W \approx 0{,}6 - 0{,}8\ eV$, which roughly coincides with the energy of the absorption coefficient in the high-temperature region. Accurate determination of the value E_q, and, consequently W, difficult, because at $T > T_g$ the material loses its elastic properties. However, our estimate of W based on the results of photoelectric and optical measurements at temperatures sufficient for effective defect formation seems more accurate than indirect estimates based on photo-EPR and photoluminescence data observed in CGS only at low temperatures (liquid temperature) nitrogen and below).

It should be noted that at temperatures above the softening temperatures, the position of the Fermi level does not change. This fact means that the defects that are formed are D centers, i.e. in equal

quantities, positively and negatively charged centers are created, in the middle between the levels, between which the Fermi level is located. Otherwise, the creation of defects of only one sign would significantly change the activation energy of dark electrical conductivity. Thus, the energy of formation D-centers in the system *As-S* is 0,6–0,9 *eV*.

2.2.4. Jump photoconductivity in composition samples *As-S* with excess sulfur.

As shown by the results of our measurements, with a violation of the stoichiometry of the compound in the direction of excess sulfur, the stationary photoconductivity decreases in the region of temperatures below 80°C, increasing the difference in its values when measured at DC and AC (Fig.2.12). In this region, the photoconductivity increases with increasing temperature with an activation energy of 0,3–0,4 *eV* depending on the percentage of sulfur and passes through the high temperature maximum.
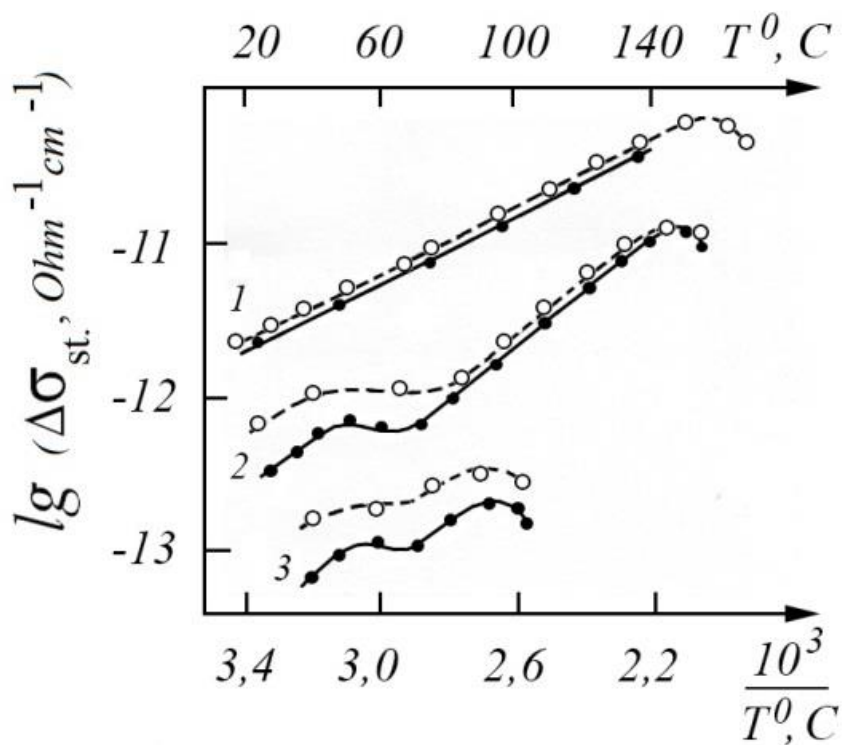
Fig.2.12. Temperature dependence of static (solid curve) and dynamic (dashed curve) photoconductivity (ω=500 Hz): 1 – As_2S_3, 2 – $As_{25}S_{75}$, 3 – $As_{20}S_{80}$.

The position of the high-temperature maximum is determined by the softening temperature of the material (T_g) and shifts toward low temperatures with increasing sulfur. As in the glass of arsenic trisulfide, this maximum is due to thermostimulated creation of its own defects.

The studied photoconductivity was excited by He-Ne laser light ($\lambda = 632,8\ nm$) with an intensity insufficient for the effective course of photochemical reactions [144]. The coefficient of light absorption of this wavelength, which is weakly dependent on the temperature in the region $T > T_g$ and the value of it is small ($\alpha \approx 1\ cm^{-1}$) (Fig.2.5).

Therefore, we believe that under the action of light from a He-Ne laser there is an optical transition involving localized states (see Section 2.1). These states, as in the glass of arsenic trisulfide, in our opinion, are different charged D centers, the concentrations of which are weakly dependent on temperature. However, the mechanism of generation in samples with high compared to the stoichiometric composition of sulfur, apparently slightly different. Because in such samples the width of the band gap is greater than in the glass of arsenic trisulfide (for example, for $As_{20}S_{80}$ $E_g \sim 2,6\ eV$) the energy of laser light is not enough for the transition of carriers from deep centers to delocalized states of permitted

zones. In our opinion, under the action of light, nonequilibrium carriers are transferred to localized states of the tail tails due to reactions (2.15) and (2.16). Here e^-, e^+ – free nonequilibrium carriers in the tails of the permitted zones, which are captured at the level of deep centers or, due to excitation, pass into delocalized states. Such thermo-optical processes are observed in the system As-S in optical fibers [145].

The presence of charge carriers in localized states is evidenced by the frequency dependence of stationary photoconductivity, or, in other words, as our measurements have shown, dynamic photoconductivity exceeds static (Fig.2.12).

As can be seen from Fig.2.12, the difference between dynamic and static photoconductivity is most pronounced in the region of low temperatures, in which the thermal release of carriers is difficult. For example, for warehouse materials $As_{25}S_{75}$ at low temperatures the difference between static and dynamic photoconductivity (ω=500 Hz) is about half an order of magnitude, and at high temperatures it is practically absent.

To explain the reasons for this discrepancy between static and dynamic photoconductivity, we performed temperature quenching of the samples. The glass samples were warmed to softening temperature and rapidly cooled to room temperature. This heat treatment leads to an increase in the concentration of defects in the sample, as evidenced by the increase in conductivity and decrease in stationary photoconductivity throughout the studied temperature range (Fig.2.13), as is the case with increasing sulfur composition in the samples (Fig.2.12). The fact that such a change in composition

leads to an increase in the concentration of defects, according to EPR studies [122].
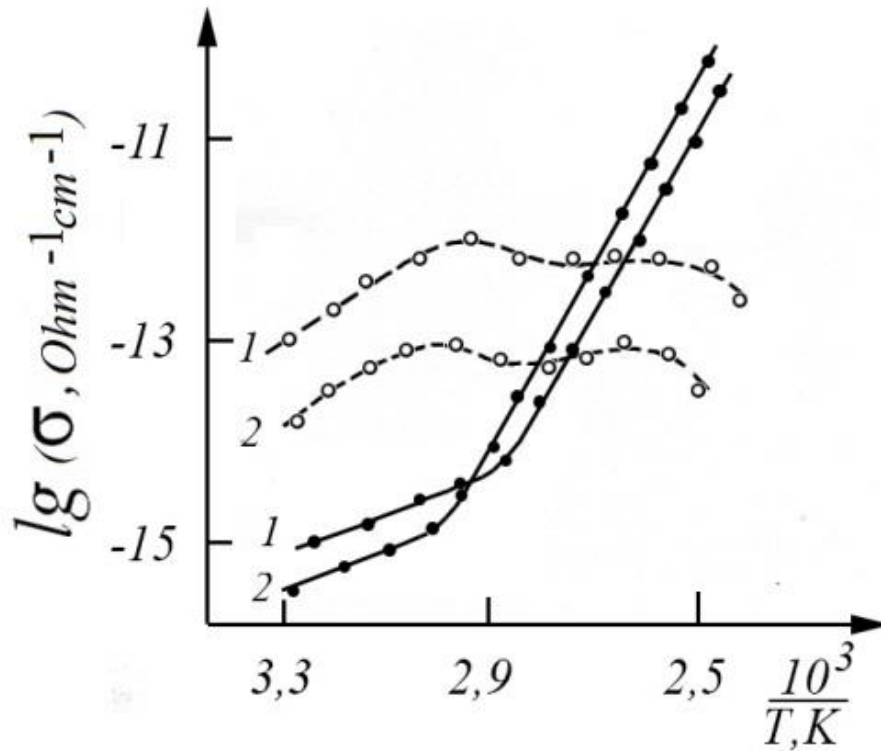
Fig.2.13. Dependence of conductivity (solid curve) and photoconductivity (dashed) on temperature for $As_{20}S_{80}$, measurement on a direct current: 1 – without preliminary temperature processing; 2 – after hardening from T≈120°C.

Increasing the concentration of defects plays a dual role: on the one hand, reducing the lifetime of nonequilibrium carriers in the permitted areas; on the other hand, an increase in the number of places where carriers can be tunneled, and hence the conductivity and photoconductivity. Therefore, we believe that the decrease and increase in the difference between the dynamic and static photoconductivity as the percentage of sulfur (Fig.2.12) and after heat treatment (Fig.2.13) is associated with an increase in the concentration of defects in the sample.

Thus, in the studied temperature range in the materials of the system *As-S* nonstoichiometric composition of photoconductivity are determined by both band transfer of carriers (near the mobility threshold) and jump transfer at the levels of D centers. In this case, the expression for photoconductivity is given by the formula:

$$\Delta\sigma = e\mu_{hop}\Delta N_0 + e\mu_p\Delta p, \qquad (2.47)$$

here μ_{hop} – jumping mobility, which exponentially depends on the concentration of D^0 centers in the sample; ΔN_0 – increasing the concentration of D^0 centers under the action of light; μ_p – mobility of holes; Δp – concentration of photo holes.

We assume that the transfer of nonequilibrium carriers occurs in the same way as equilibrium (Section 2.1), namely, band photoconductivity is determined by delocalized states, and jump - by the following reaction

$$C_{3A}^0 + C_{3B}^+ \rightarrow C_{3A}^+ + C_{3B}^0. \qquad (2.48)$$

The temperature dependence of the band conductivity differs from the temperature dependence of the jumping photoconductivity. At low temperatures, the jumping photoconductivity increases with low activation energy, which is the activation energy of the reaction (2.48). As the temperature increases, the jumping photoconductivity will decrease due to thermally stimulated recombination of nonequilibrium D^0 centers. In our case, such recombination of the D^0 centers occurs, probably, due to direct capture $e^+ + D^0 \rightarrow D^+$, and its thermal activation is associated with an increase in the concentration of free holes. Therefore, in the case of a strong photo response, the concentration of

free holes and, consequently, the band photoconductivity activation increases even when the activation of the D^0 centers decreases with increasing temperature. Therefore, the temperature dependences of the jump and band photoconductivity should be

The figure shows that in the temperature range in which the contribution from the band and jump mechanisms of photocarriage transfer are approximately comparable, the appearance of the maximum temperature dependence of the stationary photoconductivity is possible.
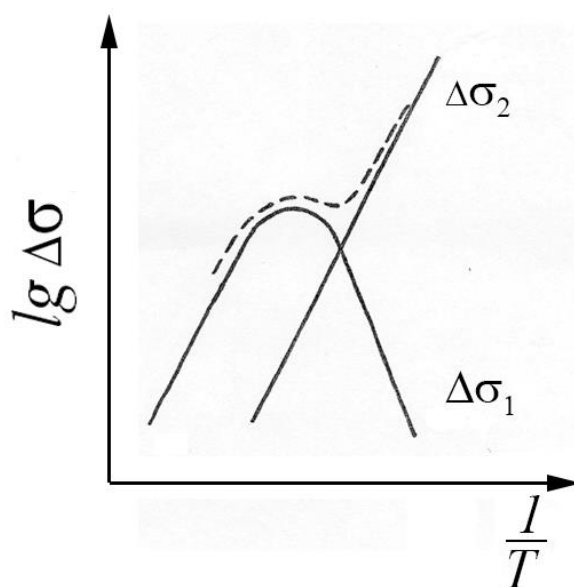
Fig.2.14. Temperature dependence of photoconductivity on localized (hopping $\Delta\sigma_1$) and nonlocalized (band $\Delta\sigma_2$) states. Dotted curve – the resulting dependence of photoconductivity on temperature.

Our research has shown that for system samples *As-S* with an excess of sulfur really appears the maximum temperature dependence of photoconductivity. This maximum is located in the region of about 60°C (Fig.2.12, solid curve). In our opinion, the fact that the appearance of this maximum is really related to the competition of different mechanisms of photocarrier transfer is evidenced by the fact that increasing the frequency

of applied voltage (and, consequently, increasing the jump component of dynamic photoconductivity) leads to temperature dependence of photoconductivity instead of the maximum there is a "plateau" (Fig.2.12, dotted curve).

Now, before we move on to the study of the mechanism of photochemical transformations in systems *As-S*, let's summarize.

We conducted studies of the temperature dependence of stationary photoconductivity in system samples *As-S* at different intensities it was shown that the activation energy of stationary photoconductivity coincides with the depth of the acceptor D^0-center level if the intensity of the excitation light is low and the main recombination channel of nonequilibrium D^0 centers is the tunnel intercenter reaction (2.6) [86].

If the intensity of the exciting light is high and the recombination of nonequilibrium D^0 centers and holes occurs as a result of reaction (2.23), then the activation energy of stationary photoconductivity is twice less than the depth of the acceptor level of the D^0 centers [87]. Such a change in the activation energy of photoconductivity was observed by us experimentally.

In the temperature range, in which the activation energy of stationary photoconductivity depends on the intensity of exciting light, we observed an increase in the instantaneous relaxation time of conductivity τ_c (decline) with increasing temperature (Fig. 2.11). We have shown that such an anomalous increase $\tau_c(T)$ is also explained by the change in the recombination channel in the case when in stationary conditions the main recombination channel was direct capture of nonequilibrium carriers

(holes), and long-term conduction relaxation (LTCR) is associated with tunnel reaction.

Note that there are different views on the nature of long-term conduction relaxations in CGS. The developed theoretical models can be mainly divided into two subgroups. One of them is a model that connects the LTCR with the presence in glassy semiconductors of fluctuating internal fields, which lead to the spatial separation of carriers of different signs[146, 147]. The second group includes models explaining long-term relaxation by carrier capture to deep centers followed by tunnel recombination [132, 142, 147]. In both cases, the decline in photoconductivity will be legal $t^{-\delta}$.

To explain the causes of LTCR, a method based on dependence $\gamma(T)$ studies was proposed, which differs in the above models [142]. It is quite difficult to use such a technique. This is due to the fact that various experimental errors distort the receipt of unambiguous results, as the method actually offers the measurement of the second derivative in time from the final conductivity. In this regard, we propose a method based on the study of temperature dependence τ_c (the first time derivative of the final conductivity) [86].

In fact, in the models of the first group, which associate LTCR with the presence of so-called recombination barriers, with increasing temperature, the instantaneous relaxation time can only decrease, as the probability of thermal transition of carriers through the recombination barrier increases. At the same time, we have shown that if LTCR is due to donor-acceptor recombination, $\tau_c(T)$ can increase when direct recombination predominates in stationary conditions.

Thus, it is experimentally shown that in systems *As-S* long-term conduction relaxation is due to the low rate of intercenter tunnel recombination (2.6), (2.8).

It is also shown that the temperature stimulation of stationary photoconductivity in *As-S* with a small photo response due to the fact that the coefficient of intercenter recombination b is weakly dependent on temperature. The study of the temperature dependence of photoconductivity at low photoresponsiveness for temperatures $T > T_g$ allows us to specify the value $E_{V_0} - \frac{U}{2} \approx 0{,}2 - 0{,}4 \, eV$, which is commensurate with the values of the values E_{V_0} and U mentioned earlier, and the study of this temperature dependence at $T > T_g$ allows to blame the energy of defect formation, which is 0,6–0,8 eV. The small value of the energy of formation of intrinsic defects in the glass we study indicates that these defects are pairs with variable valence C_3^+, C_3^0, C_3^-, and not, for example, broken sulfur bonds.

Indeed, the energy of formation of two neutral defects with unpaired electrons is the bond energy E_b (the next pair of such defects will be unstable, because if broken, the bond can be re-established: broken defects or ends of sulfur chains will be isolated by persistent defects). If such defects have a negative effective two-electron energy, then the transition of an electron from one bond to another releases energy U. Therefore, for the formation of two different charged charged ruptured ligaments requires an energy not less than $E_b - U$, and the energy of formation of one defect of the type "ruptured ligament" is equal to $\frac{E_b - U}{2}$. Communication energy $(S - S)E_b = 4 \, eV)$ [148], and $U =$

$0,7 - 0,8\ eV$. Therefore, the energy of formation of such a defect is 1,5 eV, which is much more than the energy we have determined.

Note that the binding energy As-S more communication energy $S - S$ [148]. Therefore, defects formed due to disconnection As-S also can not be attributed to the main type of defects in the materials studied by us. Quadruple-coordinated arsenic atoms also cannot be the predominant type of defects in the materials we study, as greater hybridization energy [149], which is several electron volts, is required to form an additional bond (basic arsenic valence 3).

The following arsenic defects have been considered in the literature [111]. However, in systems As-S with a composition of sulfur not less than stoichiometric (As_2S_3), such defects differ from pairs with variable valence only by the kinetics of formation, and not by microscopic nature. In fact, in the normal configuration, arsenic is bound to three sulfur atoms. Therefore, in the formation of arsenic vacancies, three free sulfur bonds C_3^0 remain and as a result of the tunnel reaction, charged centers C_3^+ and C_1^- are formed. Weak dependence of the value b on temperature means that the reaction $2C_3^0 \rightarrow C_3^+ + C_1^-$ occurs during the passage of intercarrier states $C_3^+ + C_3^-$. In other words, the electronic bonds pass first, and only then the chemical bonds $C_3^- \rightarrow C_1^-$ are rebuilt, which explains the weak dependence of the activation energy (2.6) on temperature.

2.3. Photochemical transformations in As_2S_3.

Of all the variety of mechanisms of photoinduced processes in CGS, leading to changes in their physicochemical properties [70–73, 81, 150–161], the most attention (especially for monolithic CGS), attract models in which such photoinduced transformation is associated with capture of light-generated nonequilibrium carriers by charged states of defects [84, 159–161]. The change in the charge state of such centers under the action of light is accompanied by a structural change in the atoms around the defects, which leads to photoinduced changes [161].

As shown in the previous Section 2.2, such defects also determine the photoelectric properties of these materials.

Therefore, in this section we consider the first studies on the influence of photostructural transformations in monolithic samples As_2S_3 on their photoelectric properties, and then on the basis of these results possible mechanisms of photostructured transformations in these compounds are discussed. He-Ne laser or xenon lamp was used as a source of radiation that causes photostructured transformations in As_2S_3. Exposure of the samples was performed at different temperatures from room temperature to 220°C.

2.3.1. Influence of optical radiation on stationary photoconductivity and photocurrent kinetics in glass As_2S_3.

The experiment was performed as follows: first, the sample was exposed in a certain optical and temperature regime, then the temperature dependence of stationary photoconductivity,

photoconductivity relaxation kinetics and spectral dependence of optical absorption were measured.

1. The sample was heated to a temperature above 100°C and irradiated with high-power He-Ne laser light (0,07–0,15 W/cm^2) for 15 minutes, after which it was cooled to room temperature.

Measurements showed that as a result of such heat treatment the stationary photoconductivity of the samples increased (Fig.2.11). This increase was observed starting from illumination of the order of 0,08–0,1 W/cm^2 and a temperature of 110–120°C, and at a higher irradiation temperature a greater increase in stationary photoconductivity was observed. The time to establish the initial state of the sample depends on the temperature at which it is stored. This preservation at room temperature for a week does not lead to a noticeable decrease $\Delta\sigma_{st}$, and at the softening temperature T_g of the material, the state with high stationary conductivity disappears in a few minutes. Therefore, to obtain the result at low photoconductivity, the illuminated sample should be annealed at a temperature of 180–200°C for 15–20 minutes.

The increase in stationary photoconductivity after irradiation of the sample was accompanied by a decrease in the relaxation time of the photocurrent (Fig. 2.15). The change in the relaxation kinetics of the photocurrent and the level of stationary photoconductivity for the sample of arsenic trisulfide irradiated in different thermo-optical modes is shown in Fig.2.16. The measurement was performed at temperature 55°C.
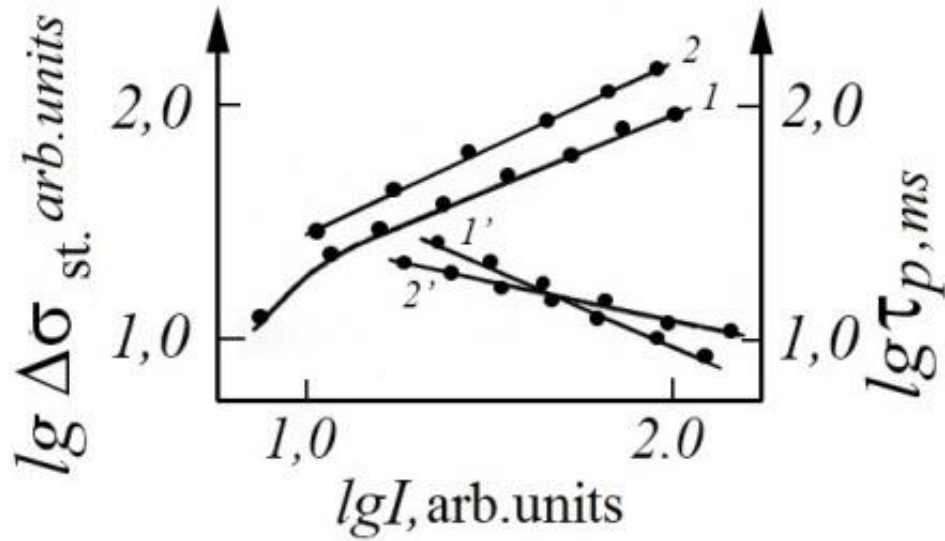
Fig.2.15. Dependence $\Delta\sigma_{st}$ (curves 1, 2) and τ_p (curves 1', 2') on the intensity of exciting light: 1, 1'– the sample is annealed at 180°C for 15 minutes; 2, 2'- exposed to radiation λ=632,8 *nm* at 150°C for 15 minutes; ω=290 *Hz*, T=55°C.

Measurement of optical parameters of the samples showed that irradiation of annealed samples with light with photon energy less than the optical width of the band gap at elevated temperature and subsequent rapid cooling leads to the fact that in the exposed area the edge of fundamental absorption shifts to the short sample), ie there is photographic enlightenment of the material (Fig.2.17). On reducing the refractive index of the material of the system*As-S*as a result of such heat treatment was reported in [77].
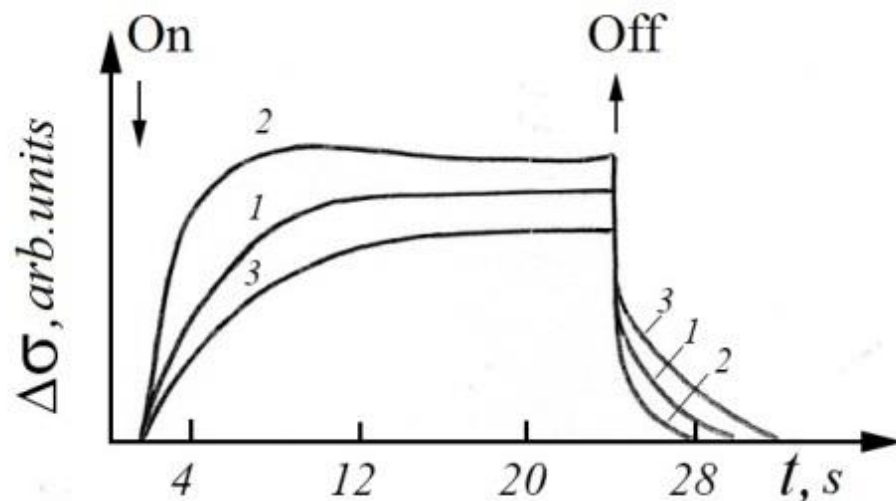
Fig.2.16. Kinetics of photocurrent for As_2S_3 at T=55°C and $\omega = 290$ *Hz*: 1 – sample annealed at 180°C for 15 *min*; 2 – exposed to He-Ne laser radiation at 160°C for 15 *min* (*I*=0,15 *W/cm²*); 3 – exposed to xenon lamp radiation at 20°C for 7 hours (lamp power ~500 *W*).
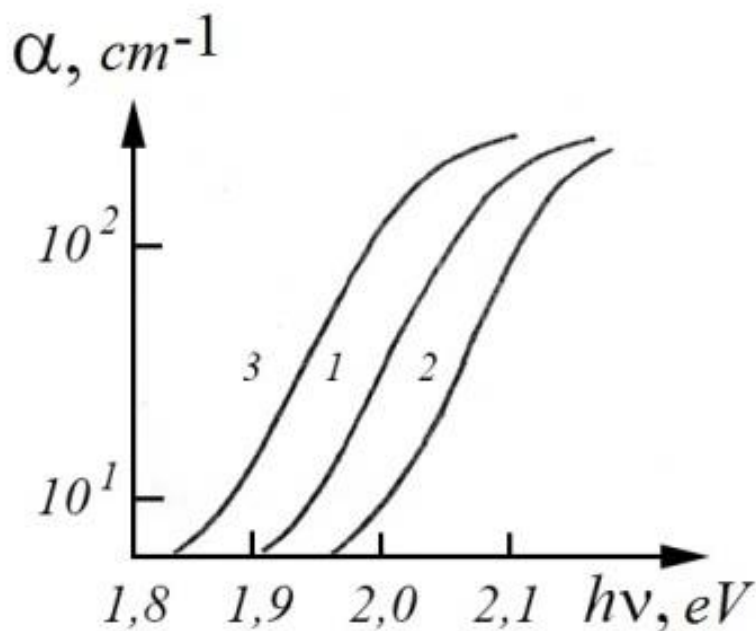
Fig.2.17. The self-absorption edge As_2S_3, measured at 55°C, after annealing at 180°C (curve 1) and exposed at 160°C (He-Ne laser) and 20°C (*Xe* -lamp) (curves 2, 3, respectively).

2. The sample was irradiated at room temperature with a Xenon lamp with a power of 500 W (intensity of undecomposed light) for several hours, after which the stationary photoconductivity was studied. Measurements showed a decrease in the stationary photoconductivity of the sample after such irradiation (Fig.2.16). The initial state of the sample with higher stationary photoconductivity is restored if it is kept for some time in the dark. The temperature dependence of the time of establishment of the initial state indicates that this process requires approximately 0,6–0,8 eV, which roughly coincides with the depth of the acceptor level of the D^0-center defined in Section 2.2. It is also shown that the decrease in stationary photoconductivity is accompanied by an increase in its relaxation time to a stationary value (Fig. 2.16).

Measurement of optical parameters of the samples showed that irradiation of annealed samples at room temperature with intense undecomposed light (or light with photon energy of the band gap) causes a shift of the self-absorption edge to the long-wavelength region of the spectrum i.e. photo-darkening, and a corresponding increase in the refractive index of the material ($\Delta n \sim 0,01$) [77] (Fig.2.17).

Before analyzing the obtained result, we present the data of the study of the spectral dependence of photoconductivity. Figure 2.18 shows the spectral dependences of the stationary photoconductivity for the unexposed sample As_2S_3, as well as exposed in both of the above recording modes.
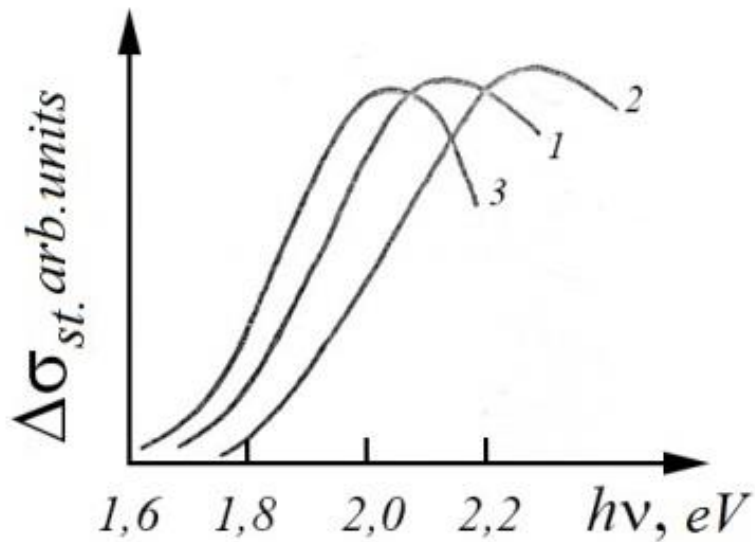
Fig.2.18. Spectral dependences of stationary photoconductivity for unexposed sample (curve 1) and the same sample exposed in the modes described above (curve 2 – irradiated with He-Ne laser at 160°C, curve 3 – irradiated with xenon lamp light at 20°C).

The spectral dependence of the photosensitivity of the unexposed sample (curve 1) had a maximum at $hv \sim 2.1 \ eV$, which corresponds to the absorption coefficient $\alpha \approx 60 \ cm^{-1}$. It should be noted that the flat area at the maximum at higher photon energies indicates that bulk recombination predominates in our samples [131]. After irradiation of the sample with intense undecomposed light, the maximum spectral dependence of the photocurrent shifts toward smaller values, and after irradiation with He-Ne laser light at 170°C, the maximum spectral dependence of the photocurrent shifts toward larger values hv due to the corresponding change $\alpha(hv)$ (Fig.2.18).

The behavior of the short-wavelength region of the spectral dependence of the photoconductivity after irradiation of the sample with its own light attracts attention (Fig.2.18). In this case, the maximum is not

a flat area, as in the case of the sample, unexposed or irradiated with light He-Ne laser, and a sharp drop in photoconductivity. This indicates an increase in the contribution of surface recombination due to the strong absorption near the surface of the undecomposed light of the xenon lamp. This increase in surface recombination can be due to two reasons – the capture of carriers at recombination centers or photochemical reactions on the surface. At low irradiation temperatures, in our opinion, the decisive role is played by the filling of recombination centers, and at higher (near T_g the softening temperature) – photochemical reactions.

Let's move on to the analysis of the reasons that caused photoenlightenment and photodarkening in the materials of the system *As-S*. Currently, two possible mechanisms of photo-darkening are discussed in the literature. One of them explains photo-darkening by the increase in the concentration of D centers due to the autolocalization of excitons [162]. The second connects photo-darkening with the recharging of deep centers under the action of light [163]. The results of our experiments on thermal annealing of the photo-darkened state allow us to prefer the second mechanism. In fact, if photodarkening is associated with recharging deep centers, i.e. the origination of D centers as a result of capture on D^+ and D^- centers of electrons and holes, the restoration of the original state of the sample (erasure of optical recording) when heated will occur mainly due to the process $D \rightarrow D^- + e^+$ the D^0 center is more likely to emit a hole than an electron (Section 2.2). With what energy of activation of such a process, the spacing of the thermal depth of the acceptor level D^0 to the center is to blame, which was taken experimentally by us (the value of 0,6–0,8 eV is approximately the

spacing of the depth of the acceptor level of the D^0 centers in our samples).

Thermal annihilation of defects formed due to autolocalization of excitons should require more energy to activate the electronic process. In addition, our studies were conducted at sufficiently high temperatures, causing thermal decay of excitons, as evidenced by the fact that photoluminescence due to the capture of excitons in the D centers [130], in our conditions was absent, as it was almost completely extinguished at temperature liquid nitrogen. (There is some evidence in favor of the fact that at low temperatures photodarkening is due to the autolocalization of excitons [162], but in our conditions the mechanism of photodarkening is different).

Under the conditions of our experiment, photodarkening caused by filling deep centers with strong electron-phonon interaction is directly evidenced by the fact that centers with a thermal depth of only 0,6–0,8 eV are responsible for optical transitions with an energy approximately equal to 1, 95 eV. The large difference between the thermal and optical depths of the defects confirms Mott and Street's hypothesis of strong lattice distortion (rearrangement of chemical bonds) when recharging the D centers. In other words, in systems As-S it is difficult to draw a line between recharging processes and photochemical reactions, so the number of chemical bonds $e^+ + C_1^- \rightarrow C_3^0$ will change due to the capture of the hole at the D -centers. In the future, for certainty, the processes that do not change the number of defects, we will call recharging, and the processes that change the number of intrinsic defects –photochemical reactions.

In our opinion, photoenlightenment can be associated only with photochemical reactions, and not with the processes of recharging centers with strong electron-phonon interaction. Relatively recently, a model of two adiabatic potentials has been proposed [73], which explains the processes of photo-darkening by optical transitions from the ground metastable state, and the process of photo-enlightenment by the transition from the metastable to the ground state. This model is correct if under the action of light free carriers are not born, and only intercenter transitions occur. However, in the previous section we showed that under the action of He-Ne laser is the generation of carriers. Therefore, under any lighting regime, the concentration of metastable D^0 centers can only increase. Thus, the phenomenological model of the two adiabatic potentials is too simplistic and does not describe the whole variety of processes, happening under the illumination of light in the system *As-S*.

2.3.2. Features of the photo-enlightenment effect in glassy As_2S_3.

In the previous section, it was shown that when the arsenic trisulfide samples were illuminated with He-Ne laser light at elevated temperatures and then rapidly cooled to room temperature, the optical absorption edge shifted to the short-wavelength region of the spectrum (relative to the edge position for unradiated annealed samples). It should be emphasized that the shift of the edge in the short-wavelength region of the spectrum (photoenlightenment) occurs during the exposure of previously irradiated samples and, thus, is not erasure, but the recording of optical information. This kind of photo-enlightenment effect is a characteristic feature of photostimulated transformations in arsenic trisulfide.

124

We found that the effect of photoenlightenment leads to an increase in stationary photocurrent due to the generation of free carriers such as "level-zone". Below we describe this phenomenon in the framework of the D center model.

It should be noted that previously the photoelectric properties of CGS in the D center model were described only for interband (intrinsic) excitation and homogeneous generation of nonequilibrium carriers by sample volume [85, 87], which can occur in very thin samples and in most experiments usually not performed.

First, consider the case of low temperatures (when the thermal emission of holes from the D centers is insignificant) and low intensities of exciting light (when the main role is played by tunnel recombination $2D^0 \rightarrow D^+ + D^-$ of nonequilibrium D^0 centers). However, as shown in Section 2.2, the local concentration of photoholes is given by expression (2.31):

$$p(z) = \frac{I(z)q}{\gamma_p^-},$$

here $I(z) = I_0 exp(-qN_+z)\gamma_p^-$ is the cross section of the capture of holes in the D^- centers, q is the cross section of the reaction $D^+ + h\nu \rightarrow D^0 + e^+$. Then the current density is

$$\Delta i = eE\mu_p \int_0^L p(z)dz = \left[\frac{eE\mu_p I_0}{\gamma_p^- N_+}\right][1 - exp(-qN_+L)]. \quad (2.49)$$

It is easy to see that expression (2.49) as a function of N_+ at fixed $q(h\nu)$ has a maximum at $q(h\nu)N_+L \approx 0,17$. Thus, with weak absorption, a decrease in the concentration of D centers will lead to a decrease in photocurrent with a weakening of generation $q(h\nu)N_+L < 0,1$. In our

case, when $q(hv)N_+L > 1$ the photocurrent will be inversely proportional to the concentration of D-centers, which are also centers of recombination.

Let us now consider the case of sufficiently high temperatures, when the thermal emission of holes from the D^0 centers is large $(W_0 N_0 > Iq)$ and the intensity of the exciting light is large enough so that direct capture of holes at equilibrium D^0 centers prevails over tunnel recombination. In addition, we assume that the probability of ejection of a hole from the D^0 center is greater than the probability of radiative capture of the electron to the D^0 center, i.e. $W_0 > n_e \gamma_n^0$. This ratio at high temperatures was substantiated in [87]. In this case, the optical generation of electrons and thermal recombination of holes occurs as a result of a sequence of reactions:

$$D^- + hv \rightarrow D^0 + e^- \rightarrow D^- + e^+ + e^-.$$
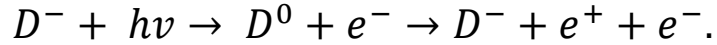
In addition, the following reactions involving free carriers and D centers are possible:

$$D^- + e^+ \rightarrow D^0;$$
$$D^+ + e^- \rightarrow D^0;$$
$$D^0 + e^+ \rightarrow D^+;$$
$$D^0 \rightarrow D^- + e^+.$$
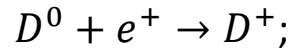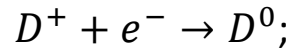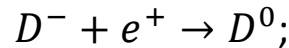
Then, taking into account all the above reactions, we write the equation equations for the concentration of free holes in the valence band and the concentration of free defects in the valence band and the concentration of defects D^-:

$$N_0 W_0 - p\gamma_p^- N_- - p\gamma_p^0 N_0 = 0, \qquad (2.50)$$

$$-qN_-I(z) + NW_0 - p\gamma_p^- N_- = 0, \tag{2.51}$$

here $W_0 = N_V\gamma_p^- \exp\left(-\frac{E_{V_0}}{kT}\right)$, $\beta = 1$, N_V is the effective density of states in the valence band, γ_p^- is the recombination coefficient of free holes at the level of the D center in the charge state, which corresponds to the index γ_p, q –cross section of the reaction $D^- + h\nu \rightarrow D^0 + e^+$.

The system of equations (2.50) and (2.51) is actually a system of two equations with two unknowns p and $\frac{N_0}{N}$. If $\frac{N_0}{N}$ we express in p from equation (2.50) and substitute this value in (2.51), for the concentration of free holes p we obtain:

$$p = \frac{qI}{2\gamma_p^-}\left(1 + \frac{4W_0\gamma_p^-}{qI\gamma_p^0}\right)^{\frac{1}{2}}. \tag{2.52}$$

Given that $W_0N_0 > qIN_-$ and $N_- > N_p$, we get $W_0 \gg qI$. Given this inequality, expression (2.52) simplifies:

$$p(z) = \sqrt{\frac{qI_0W_0}{\gamma_p^-\gamma_p^0}}\, exp\left(-\frac{qN_-L}{2}\right). \tag{2.53}$$

Expression (2.53) takes into account the Bouguer-Lambert law $I(z) = I_0 exp(-qN_-z)$, which is true when $N_0 \ll N_-$.

Neglecting the diffusion spreading of the main photocurrent carriers (holes) and taking into account that the optical density exceeds one, we obtain for the photocurrent density:

$$\Delta i = eE\mu_p \int_0^L p(z)dz = \frac{2}{qN_-}\sqrt{\frac{qI_0W_0}{\gamma_p^-\gamma_p^0}}. \tag{2.54}$$

From formula (2.54) it is seen that in this case the photocurrent is inversely proportional to the concentration of defects, and the activation

energy of the photocurrent is half the distance between the acceptor level of the center and the mobility threshold in the valence band, as

$$N\left(N_- = \frac{N}{2}\right)D^0 W_0 \sim exp\left(-\frac{E_{V_0}}{kT}\right).$$

Therefore, as can be seen from formulas (2.49) and (2.54), regardless of the temperature and intensity of the exciting light, at an optical density above one unit of photocurrent is inversely proportional to the concentration of free defects in the sample.

Neglecting the diffusion spreading of charge carriers is justified if the inhomogeneity of the concentration of photoholes in the scale of diffusion length is insignificant and the recombination time is less than the time of diffusion displacement of the hole (taking into account the adhesion factor) due to uneven generation of photocarriers $(qN)^{-1}$.

The first condition is described by the inequality:

$$\left|\frac{\partial p(z)}{\partial z}\right| l \ll p(z), \tag{2.55}$$

here $l = 10^{-4}-10^{-5}$ cm [86] is the length of the diffusion shear of the hole in the zone (the distance of the diffusion shear of the hole in the zone for the time before the first capture).

Inequality (2.55) is equivalent to the condition and is always satisfied in our case, because the absorption coefficient $qN \approx 10$. One condition (2.55) is sufficient to neglect the diffusion spread of carriers at low temperatures, when the thermal emission of holes from deep D^0 centers is insignificant. At high temperatures, the holes will diffuse, adhering to D^- centers and throw out D^0 centers. Such a diffusion process, limited by traps, will proceed with an effective diffusion coefficient

$Д_{\text{eff.}} = Д\theta$ [304], where $Д$ is the diffusion coefficient of holes in the valence band $\left(Д = \dfrac{kT\mu_p}{l}\right)$ and θ – adhesion factor $\left(\theta = \dfrac{W_0}{\gamma_p^- N_-}\right)$. This diffusion distance is insignificant if the hole recombines before it shifts due to the inhomogeneity of generation $(qN)^{-1}$, which is equivalent to the condition

$$\tau_r < [Д\theta(qN)^2]^{-1}, \qquad (2.56)$$

here τ_r – the recombination time in this case, when tunnel recombination of nonequilibrium D centers predominates, is equal to $\tau_r = (bN_0)^{-1}$ (Section 2.2). Because in this case, then inequality (2.56) can be rewritten as $N_0 = \sqrt{\dfrac{IqN}{b}}$.

$$Д\theta(qN)^2 < (IqNb)^{1/2}. \qquad (2.57)$$

For typical parameters of the system $As\text{-}S$ $Д \approx 0{,}3\ cm^2 s^{-1}$; $\theta \approx 10^{-3} - 10^{-4}$; $b = 10^{-11} - 10^{-12}\ cm^3 s^{-1}$; $qN \approx 10\ cm^{-1}$ inequality (2.57) is consciously satisfied, because in our case $I = 10^{18}\ photon\ cm^{-2} s^{-1}$ ($I = 20\ mW/cm^2$)

As shown in the previous section, in the case where the recombination of holes occurs due to their direct capture at the D^0 centers $(e^+ + D^0 \rightarrow D^+)$, the recombination time is shorter than in tunnel recombination, and inequality (2.56) is even more fulfilled.

Thus, in our conditions it is possible to neglect the diffusion spread of carriers, and the photocurrent, taking into account the total absorption, is inversely proportional to the concentration of the D centers, and its activation energy coincides with the activation energy of jumping photoconductivity.

Thus, the decrease in absorption is directly proportional to the concentration of intrinsic defects in the material, and, consequently, the increase in stationary photocurrent, which at full light absorption is inversely proportional to the concentration of defects, means that as a result of photochemical reaction concentration of D centers decrease.

To elucidate the mechanism of such a photochemical reaction, we studied the kinetics of relaxation of photoconductivity due to the action of intense irradiation, which initiates photochemical reactions.

2.3.3. Study of nonstationary photoconductivity in the process of photochemical reaction on glass As_2S_3.

Measurement of photoconductivity relaxation kinetics was performed under illumination with rectangular light pulses from a He-Ne laser lasting 15 minutes and an amplitude of more than 0,1 W/cm^2. The front of the light pulse has a duration of 10^{-3} s.

Figure 2.19 shows taken on glass As-S relaxation curves of the photo response to rectangular pulses of light of different amplitude from the He-Ne laser. Measurements were performed on alternating current according to the method described in [164, 165] at a temperature of 35°C.
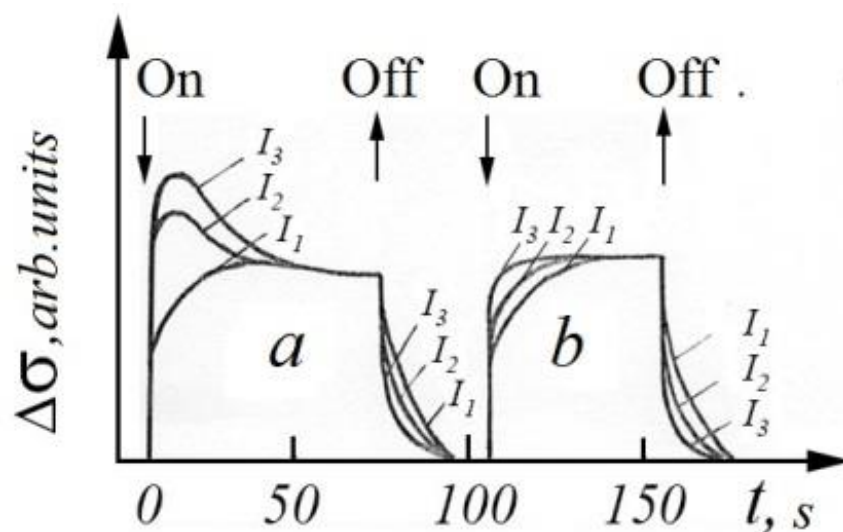
Fig.2.19. Kinetics of photoresponsiveness at primary (*a*) and repeated (*b*) illumination, change at different intensities of exciting light ($I_1 < I_2 < I_3$) in As_2S_3.

As can be seen from Fig.2.19, at the first illumination there is a "flash" nature of the growth of photocurrent (non-monotonic growth), most clearly manifested at high light intensities. When re-illuminated, the photoconductivity monotonically relaxes to its stationary value (Fig. 2.19, *b*). The flash character of relaxation is restored if the sample is kept for some time in the dark, and this time depends on the temperature and varies from a few hours at 35°C to several minutes at 110°C.

Qualitatively similar relaxation curves were observed by us when measuring at direct current. Relaxations of photocurrent are presented in Fig.2.19, may be due to the accumulation and redistribution of bulk space charges, leading to the origination of potential barriers for current carriers, as observed in [129] for the case of sprayed films As_2S_3.

The dependence of dynamic photoconductivity on the frequency and amplitude of the measuring voltage should be observed in the presence of relaxation processes associated with the occurrence of bulk space charges [166–168]. However, in this case, as our experiments have shown, such a dependence is not observed in the frequency range 100–20000 *Hz* (so far sufficient sensitivity of the circuit to photocurrent) and amplitudes up to 60 *V*. Amplitude of photocurrent at constant applied voltage and pulse voltage of this frequency completely coincides for respectively equal time and phases relative to the action of the light pulse. Therefore, the nature of the relaxation of the photocurrent in As_2S_3 alternating current, which

we observed, is due to the physical phenomena occurring in the entire volume of the sample.

We believe that the region of decline on the relaxation curve of the photocurrent (Fig.2.19) is associated with the effect of photo-darkening, because in our experiment the effect of photo-enlightenment is accompanied by an increase in the level of stationary photocurrent. The spectral dependence of photoconductivity also supports this assumption. After irradiation of the sample with intense light, the maximum of the spectral dependence of the photoconductivity is shifted toward lower photon energies $h\upsilon$, as was the case with photodarkening when exposed to the pattern of intense undecomposed light (Fig. 2.18). In our opinion, the effect of photo-darkening is due to the filling of traps with nonequilibrium charge carriers.

In fact, the temperature dependence of the recovery time of the initial state of the sample makes it possible to determine the thermal depth of the levels responsible for the photo-darkened state; this value is 0,6– 0,8 eV, which practically coincides with the depth of the acceptor level of the D^0 centers defined in Section 2.2. Thus, photodarkening is due to the D^0 centers formed as a result of the capture of nonequilibrium electrons and holes on the charged D^+ and D^- centers.

The fact that centers with a thermal depth of only 0,6–0,8 eV are responsible for optical transitions with photon energies equal to 1,98 eV confirms Mott and Street's hypothesis of strong electron-phonon interaction at the D centers. The strong distortion of the lattice when recharging the D center (i.e. with a large difference between thermal and optical depths of the D center) is evidenced by the fact that the action of

infrared radiation in the range of 0,5–1,8 *eV* does not lead to a significant change in relaxation.

At higher temperatures (T>120°C) the nature of photocurrent growth becomes more complex (Fig.2.20, curve 2). On this curve, we associate the growth region with the photoenlightenment of the sample, because it is observed at temperatures and light intensities sufficient to increase the steady-state value of the photocurrent. In this case, the maximum of the spectral dependence of photoconductivity (Fig.2.18) is shifted toward greater *hv*, as was the case with photoenlightenment.

The fact that at a given temperature and light intensity the photo-darkening of the sample is replaced by photo-enlightenment (Fig.2.20), indicates that we believe that the process that leads to photo-darkening and photo-enlightenment is not reversed from a microscopic point of view from a widespread model of two adiabatic potentials. This assumption is supported by the fact that when generating free carriers due to "zone-zone" transitions (when irradiated with intense undecomposed light), when the absorption and, consequently, the filling of traps is large enough, there is a photo-darkening effect conditions, the change in the absorption coefficient is mainly determined by filling the traps.
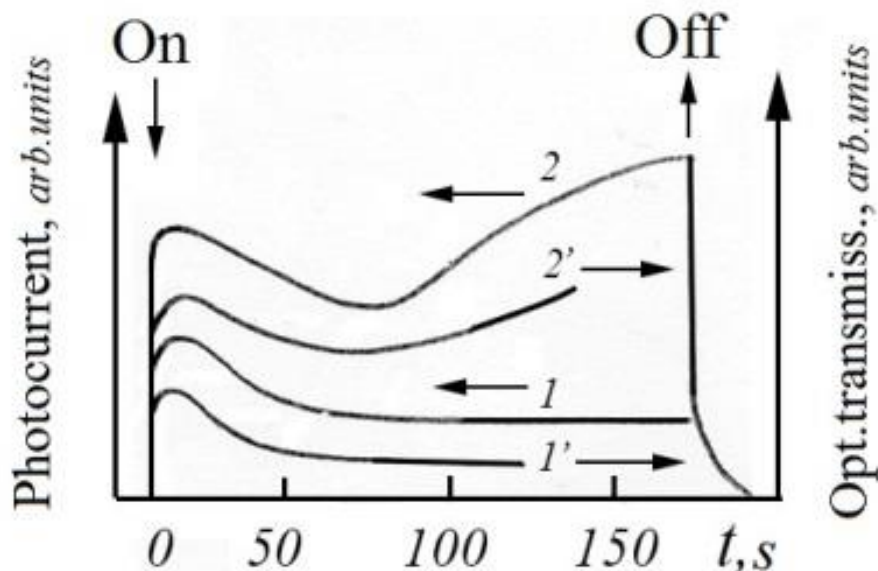
Fig.2.20. Kinetics of photocurrent (curves 1, 2) and optical transmission (curves 1', 2') when the sample As_2S_3 is excited by rectangular pulses of He-Ne laser light with a power of 0,1 W/cm^2: 1,1'– 35°C; 2, 2'– 150°C.

Our assumption is also confirmed by the fact that in order to achieve the photocurrent level of the unexposed sample, the photoenlightened sample should be heated to higher temperatures than the photo-darkened one at a given heating time. These experimental data showed the invalidity of theoretical models linking the effect of photo-darkening and photo-enlightenment with inverse quantum mechanical transitions.

Particular attention is paid to the behavior of the instantaneous relaxation time of the photocurrent τ_p (growth area) in the region of high temperatures (greater than 120°C) when irradiating samples of arsenic sulfide glass with intense light from He-Ne laser [80] (Fig.2.10). It has been shown that τ_p grows according to the law $\tau_p \sim t^\gamma$, where t is the full relaxation time to a stationary photocurrent. Such behavior τ_p, in our opinion, can be associated only with photostructured transformations, and

not with the processes of generation and recombination of nonequilibrium carriers, as in the latter case τ_p should not depend on time. Therefore, the increase in photoinertization at higher intensities of exciting light due to photochemical reactions responsible for changing photoelectric properties. The dependence $\tau_p \sim t^\gamma$ (second order kinetics) indicates that the structural changes are due to the transformation of a pair of defects, and not by changing the power of the deep center in the aftermath of recharging, since the first order of kinetics is responsible for this fall.

The obtained results allow us to propose a microscopic mechanism of photochemical reactions responsible for photoenlightenment.

2.3.4. Discussion of the results and the proposed model of photochemical transformations in glassy arsenic trisulfide.

It is shown that the effect of photo-darkening, which causes an increase in light absorption in the region of photon energies $h\nu = 1{,}95\ eV$, is due to filling traps with nonequilibrium carriers, which are centers with strong electron-phonon interaction, whose thermal depth is $0{,}6$–$0{,}8\ eV$. Comparison with data from photovoltaic and electrical measurements (Section 2.2) allows us to identify these traps with the acceptor levels of the D^0 centers. Therefore, photodarkening is due to reactions $e^+ + D^+ \rightarrow D^0$ and $e^+ + D^- \rightarrow D^0$. Restoration of the initial state of the sample (erasure of photo-darkening, which in the literature is usually called photo-enlightenment [81]) will be carried out by reactions $2D^0 \rightarrow D^+ + D^-$ and $D^0 \rightarrow D^- + e^+$. The reaction $D^0 \rightarrow D^- + e^+$ does not play a significant role, because the probability of ejection from the D^0 center of the electron is less than the probability of ejection of the hole (Section 2.1).

The effect of photoenlightenment (recording of optical information) caused by a decrease in the number of defects as a result of binary reaction is revealed, as evidenced by the increase in photoinertism with increasing light intensity and the dependence of instantaneous relaxation time (growth) of photocurrent $\tau_p \sim t^\gamma$. The abrasion of this effect occurs at temperatures close to the softening temperature of the material, as shown in Section 2.2, when the process of thermal creation of its own defects is effective. Earlier it was shown that the own defects (D-centers) in the studied materials of the system As-S there are pairs with variable valence [123], which are mainly in the states C_3^+ and C_1^-. Therefore, we propose the following microscopic mechanism of photochemical reaction, which is responsible for the effect of photoenlightenment.

Under the action of He-Ne laser radiation, free carriers are created as a result of level-zone transitions (impurity excitation):

$$C_3^+ + h\nu \ \rightarrow C_3^0 + e^+,$$
$$C_1^- + h\nu \ \rightarrow C_1^0 + e^-. \qquad (2.58)$$
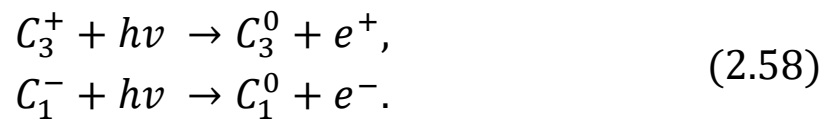
Free carriers is captured by charged D centers, which also increases the concentration of D^0 centers:

$$e^+ + C_1^- \rightarrow C_1^0, \quad e^- + C_3^+ \rightarrow C_3^0. \qquad (2.59)$$
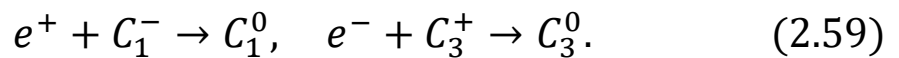
As a result of the processes of generation and capture of carriers, the nearest pairs of neutral centers C_3^0 and C_1^0. Between the following pairs, a tunnel reaction with electron transfer is possible, which converts them to the ground charge state:

$$C_3^0 + C_1^0 \rightarrow C_3^+ + C_1^-. \qquad (2.60)$$

However, another way of evolution of the nearest pairs is possible: the center passes (possibly by activation) to a lower and more favorable

136

energy state C_3^0. At the same time (Fig.2.4) the barrier for creation of atoms with normal coordination of atoms from atoms with an unusual configuration of bonds should be strongly lowered; in other words, the following sequence of reactions is possible:

$$C_3^0 + C_1^0 \rightarrow 2C_3^0 \rightarrow 2C_2^0, \tag{2.61}$$
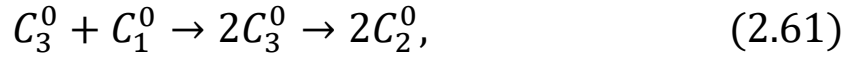
as a result, the number of intrinsic defects decreases (optical "healing" of defects), for example, as shown in Fig.2.21.
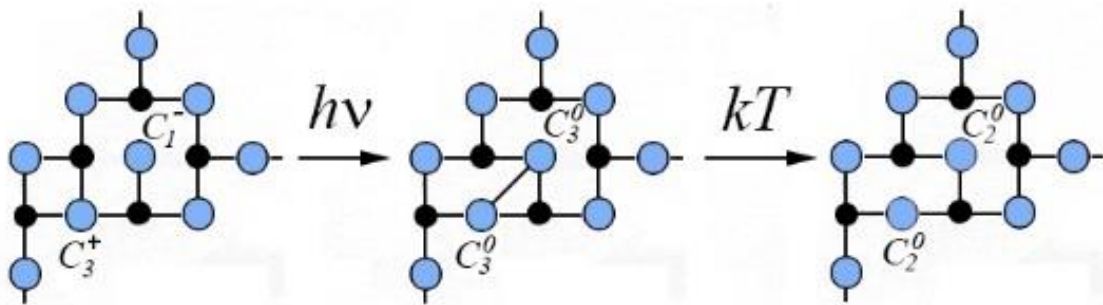
Fig.2.21. "Healing" of its own defects in the material under the action of light, which leads to the creation of normally coordinated atoms (- – sulfur, ● – arsenic).

This photostimulated reduction in the concentration of defects will continue until it is balanced by the thermal creation of defects from atoms with normal coordination of bonds:

$$2C_2^0 \rightarrow C_3^+ + C_1^-. \tag{2.62}$$

It should be emphasized that a similar (2.61) photostimulated two-stage transformation of donor-acceptor complexes was observed in CdS and $CdSe$ [133, 169, 170].

Note that in principle it is possible to create normal atoms from a pair consisting of one charged and one neutral defect, for example, as a result of the reaction:

$$C_3^+ + C_3^0 \rightarrow 2C_2^0 + e^+,$$
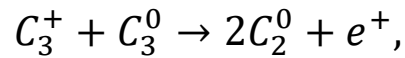
here e^+ means a hole that is near the threshold of mobility, possibly in a localized state. A free hole in this sense arises because atoms with normal coordination of bonds cannot create a deep center, but can create small localized states due to fluctuations in the length of chemical bonds and the angles between them.

Therefore, the activation energy of such a reaction cannot be less than the energy required to transfer the hole from the state C_3^+ to the valence band, which is typically 1,5 eV (Section 2.2). This value is greater than the energy of creation of intrinsic defects (0,6–0,8 eV – Section 2.2), so such reactions cannot significantly change the concentration of defects.

By analogy, the reason for the change in the concentration of defects can not be a decrease due to the reaction between negatively charged and neutral D centers.

It should be noted that as a result of the reaction between the two bonds with normal coordination, and the three-center orbital-deficient bonds[171], which, in our opinion, do not create deep centers in CGS, and may be responsible for the presence of small localized states near the mobility threshold. Due to the fact that the formation of this type is difficult to distinguish from normally coordinated atoms, because in glass there are always fluctuations in the length of chemical bonds and angles between them, creating small localized states, for simplicity we will assume that defects occur as a result of a sequence of reactions (3.61).

Reconstruction of the chemical bond of the approximate vapor, which leads to the "healing" of its own defects in the material, and the corresponding adiabatic potentials are shown in Fig.2.21 and 2.22. Figure 2.22 shows adiabatic potentials that describe the potential energy of the system depending on the location of the nuclei.

The first adiabatic potential (1) corresponds to the ground state – $2C_2^0$, the second (2) – the nearest pairs of neutral centers – $2C_3^0$, and the third (3) – a pair of charged defects – $C_3^+ + C_1^-$. The transition from states 2 and 3 to state 1 corresponds to the "healing" of defects, and the reverse transitions – the formation of defects. The transition from state 2 to state 3 corresponds to the reaction $2C_3^0 \rightarrow C_3^+ + C_1^-$.
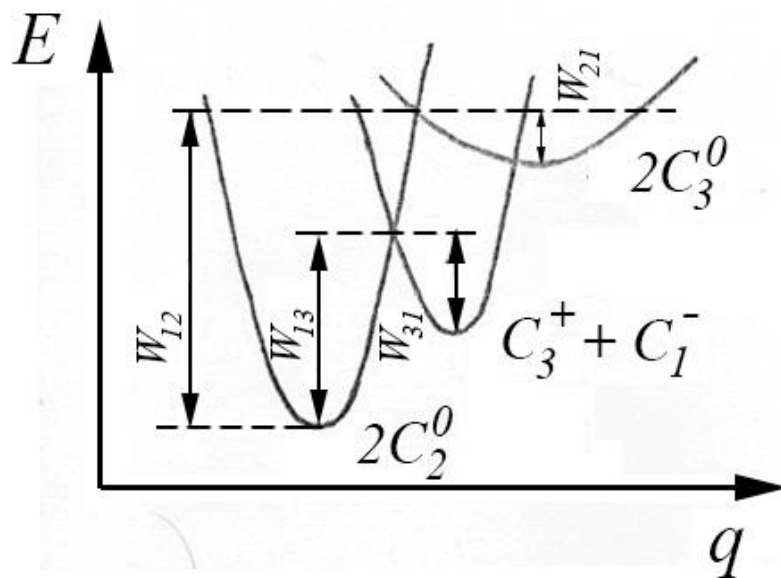
Fig.2.22. Configuration-coordinate diagram of photostructural transformations in system materials $As\text{-}S$.

According to our proposed model of photostructured transformations, the height of the barrier to transition from state 2 to state

1 is less than the height of the barrier to transition from state 3 to state 1. Therefore, under the action of light creating states $2C_3^0$ with C_3^+ and C_1^-, the concentration of defects will reduced until the transition $2 \to 1$ is compensated by the transitions $1 \to 3$ (as seen in Fig.2.22, the barrier to the transition $1 \to 3$ is significantly lower than the barrier $1 \to 2$).

It should be emphasized that in our case the action of light does not cause the transition $3 \to 2$ directly, as such a transition is described by an optical reaction $C_3^+ + C_1^- + h\nu \to C_3^0 + C_1^0$, which does not result in free carriers. However, as shown in Section 2.2, free carriers generates free carriers as a result of optical reactions involving charged centers (2.58). This type of transitions is not shown at all in our figure, because they are transitions involving only one D center, and the adiabatic potentials shown in Fig.2.22 correspond to transitions involving a pair of D centers.

Transitions of type (2.58) could be qualitatively represented if the adiabatic potentials corresponding to states $C_3^0 + C_1^- + e^+$ and $C_3^+ + C_1^- + e^+$ are taken into account in the figure. However, the positions of such adiabatic potentials are not unambiguously determined in principle, because the kinetic energies of the electron and the hole in delocalized states can be arbitrary. Therefore, in Fig.2.22 it makes sense to consider only the thermal transition between different states of the pair of D centers, which occur without the participation of free carriers.

Recently, a number of phenomenological models have become widespread, in which both thermal and optical transitions are considered using configuration and coordinate diagrams of the ground and metastable states of atomic nodes in CGS by comparing them with experimental data that determine energy barriers between different states [70, 73]. This

approach is correct in cases where there are local optical and thermal transitions without the participation of free carriers (intracenter transitions). To describe photostructured transformations in system materials *As-S*, which are initiated by free carriers created by the generation of "level-zone", this approach is ineffective, as it does not reflect the essence of the phenomenon.

We emphasize that even when free carriers have approximately the same energy and the location of the corresponding adiabatic potentials is more or less accurately described to determine the concentration of carriers (upper term population) it is necessary to consider a system of balance equations, as done in Section 2 of this work not the kinetics of local transitions, as in [70, 73]. This is due to the fact that the carriers, which arises as a result of optical transition involving one of the *D* centers, is captured by another center *D*.

In the previous section, the behavior of the time dependence of nonstationary photoconductivity at sufficiently high intensities of exciting light and high temperatures was described. It has been shown that after the excitation light is switched on, the region of the photoconductivity decline changes with the growth region at a given temperature, intensity, and wavelength of the excitation light. We performed simultaneous measurements of the light absorption coefficient under the same conditions. It was found that in the beginning, in the time corresponding to the area of photocurrent decline, photo-darkening is observed, which is then replaced by photo-illumination of the sample during the time corresponding to the photocurrent growth region. In other words, the inverse relationship between photocurrent and absorption when

141

irradiating arsenic trisulfide glass with light of the He-Ne laser is preserved during the transition period of photocurrent growth to its stationary value. This time dependence of the absorption coefficient indicates, in our opinion, that the processes are not inverted from a microscopic point of view. Note that the simultaneous change of optical and photometric properties shows that both photoenlightenment processes and photodarkening processes are initiated by free carriers.

After the excitation light is turned off, the photo-darkening optical recording component disappears in a time approximately equal to the residual conductivity, and the enlightenment component is stored for a longer time and completely erased at a temperature close to the softening temperature T_g of the material in which there is an intense thermal creation of their own defects.

The activation energy of the process responsible for erasing the photo-darkening almost coincides with the depth of the acceptor level D^0 center (0,6–0,8 eV). Therefore, we believe that photo-darkening is due to recharging of the D centers (the origination of D^0 centers under the action of light). In order for the appearance of D^0 centers to lead to photo-darkening, it is necessary that the cross-sectional absorption at $h\nu = 2,0\ eV$ due to the D^0 centers ($D^0 + h\nu \rightarrow D^- + e^+$; $D^0 + h\nu \rightarrow D^+ + e^-$) exceeds the cross-section of the absorption due to the D^+ and D^- centers ($D^+ + h\nu \rightarrow D^0 + e^+$; $D^- + h\nu \rightarrow D^0 + e^-$).

This cross-sectional ratio can be explained based on the results of the work [172]. For centers with a strong electron-phonon interaction of the absorption edge (the lowest photon energy at which light is absorbed) is the sum of the thermal depth of the AO level and the "polaron" shift of

the *OB* (Fig.2.23). At photon energies that exceed the minimum value, absorption will occur and excess energy will be transferred to another electron. The dependence of the absorption cross section on energy will mean the energy dependence of the electronic matrix element (probability) of the electronic transition. As shown in [172], for *p*-electrons the maximum probability of transition will occur at an energy that exceeds approximately twice the smallest value (such a maximum exists because with increasing energy the density of states in the allowable zone increases and the overlap integral between localized and delocalized states decreases).
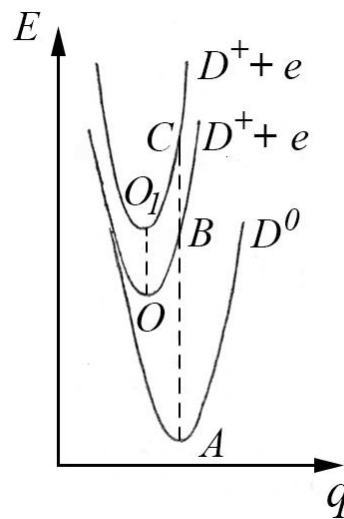
Fig.2.23. Level-zone optical transitions with the participation of a center with strong electron-phonon interaction.

Therefore, in the field of photon energy $h\nu \approx 1{,}96$ *eV* the absorption cross section with the participation of the *D* center (the edge is located on the $E_{V_0} + W \approx 0{,}6 \div 0{,}8 + 0{,}5 \div 0{,}6 \approx 1{,}1 \div 1{,}4 \, eV$) will exceed the absorption cross section with the participation of charged *D* centers (the edge is located on the $AO + W \approx 1{,}4 \div 1{,}5 + 0{,}5 \div 0{,}6 \approx 1{,}9 \div 2{,}1 \, eV$. We

believe that Mott's fair assumption that the edge of self-absorption in the materials of the system *As-S* responsible level-zone transitions.

Under the influence of light in systems *As-S* there are two processes of photo-darkening due to the increase in the cross-section of photon absorption during the creation of D^0 centers from D^+ and D^- centers due to recharging, and photo-enlightenment due to a decrease in the concentration of defects due to the reaction $2C_3^0 \to 2C_2^0$. Therefore, the local change in the absorption coefficient is:

$$\Delta\alpha = \left(q_0 - \frac{q_+ + q_-}{2}\right)N_0 + \frac{q_+ + q_-}{2}\Delta N, \qquad (2.64)$$

here q_0 – cross section of the optical reaction with the participation of D^0 centers, $q^-(q^+)$ – cross section of the reaction with the participation of $D^-(D^+)$ centers, ΔN – decrease in the concentration of D centers due to photochemical reaction $2C_3^0 \to 2C_2^0$.

As can be seen from formula (2.64), depending on the degree of filling of the traps may be dominated by one or another effect. Thus, when generating free carriers by excitation of the "zone-zone" type (irradiation with undisturbed light of a xenon lamp), when the filling of the traps is much less, depending on the temperature and time of irradiation, both effects can be detected.

However, the effect of photo-darkening is erased much easier and at lower temperatures due to the recombination of nonequilibrium D^0 centers. The effect of photo-enlightenment caused by changing the number of defects is erased at higher temperatures and under other conditions lasts much longer than the effect of photo-darkening due to the same reversible recording of optical information in materials *As-S*.

Note that the reaction $2C_3^4 \rightarrow 2C_2^0$ will take place between the nearest pairs of D centers in the material, as well as a result of a diffusion meeting of the D centers. The available results do not make it possible to prefer one of these mechanisms. However, we note that the relative magnitude of the photolight effect is about 10%, which roughly coincides with the fate of the nearest pairs mentioned by Street [173] in the analysis of the mechanisms of radiative recombination in chalcogenide glassy semiconductors.

CHAPTER 3. APPLICATION OF PHOTOCHEMICAL TRANSFORMATIONS IN THE "CORE CaF_2 –SHELL $AgBr$" MICROSYSTEM, CGS AND AHC FOR HOLOGRAPHIC RECORDING OF THREE-DIMENSIONAL TRANSMISSION HOLOGRAMS

3.1. Formation of three-dimensional transmitting diffraction gratings based on "core CaF_2– shell $AgBr$" microsystems

The main idea of using an emulsion with heterophase microsystems "core CaF_2– shell $AgBr$" for two-stage recording of three-dimensional transmitting diffraction gratings (elementary holograms) at room temperature with high diffraction efficiency (DE) is realized at the stage of chemical-photographic processing of holograms, one of the variants of which [59] is schematically presented in Fig.3.1.
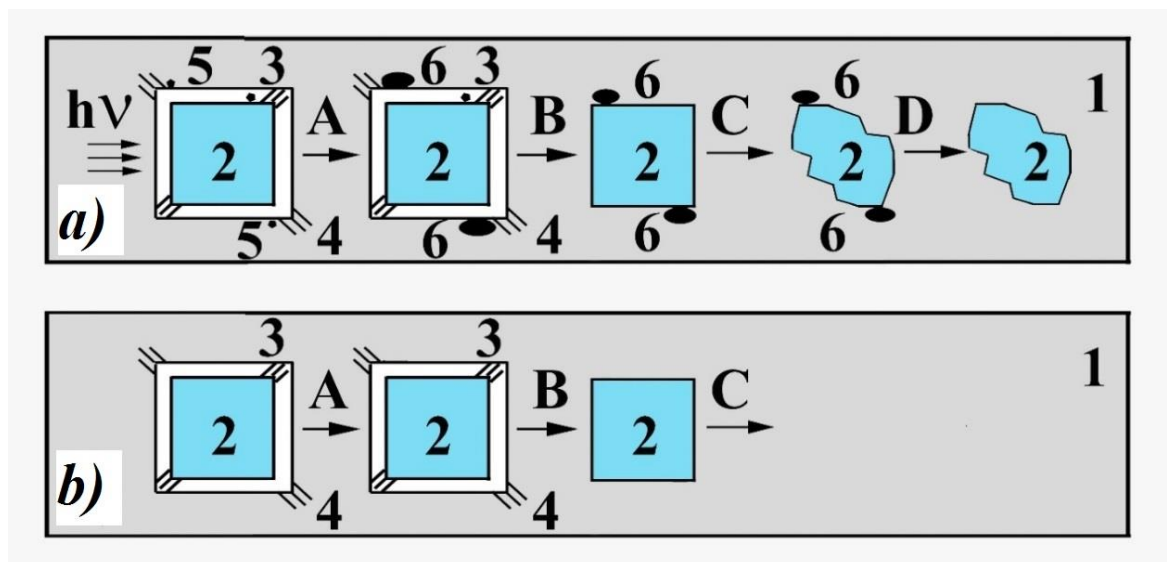
Fig.3.1. Processes occurring in illuminated (antinodes, row *a*) and unilluminated (nodes, row *b*) areas of the elementary hologram.

In Fig.3.1 the following notation is accepted:

1 – binder (gelatin),

2 – nuclei microsystems (in our case it is a CaF_2 microcrystal the size of $\overline{d} \approx 0,04 \, \mu m$);

3 – shell $AgBr$ (shell thickness $\overline{d} \approx 0,005 \, \mu m$);

4 – dye adsorbed on both the outer and inner surface of the shell of the silver halide 3;

5 – centers of the latent image, which occur in the silver halide shell under the action of light;

6 – particles of developed silver.

After lighting the emulsion was subjected to the following treatments:

A – developing. As a result of this operation in microcrystals, which absorbed light, silver particles appear (6) (diluted developer D-19 was used in the experiments, development time up to 30 minutes);

B – fixation, which leads to the dissolution of the silver halide shell;

C – emulsion treatment in 10% solution of $AlCl_3$.

Studies have shown that you can choose the processing conditions at which the dissolution rate of microcrystals CaF_2 with silver particles and without them are not the same. This cancellation of the dissolution kinetics allows you to completely dissolve the microcrystal CaF_2 in those places of the layer where there is no light, and on the surface of which there are no particles of silver (Fig.3.1, row b), and partially preserve the microcrystals CaF_2 in lighted places, on the surface of which there are silver particles (Fig.3.1, row a);

D – bleaching of silver particles by bathing the emulsion layer in a solution of $K_3[Fe(CN)S]$ with the addition of KI.

In addition, another variant of hologram processing is possible [59], in which microcrystals CaF_2 dissolve mainly in illuminated places of the hologram and partially stored in the unilluminated. The stage of processing the emulsion in 10% solution of $AlCl_3$ should be carried out imcarrierstely after the development of the exposed emulsion [62].

Since in unlit areas the shell prevents the penetration of $AlCl_3$ solution into the nucleus, they do not dissolve. In the same lighted places after the developing of the shell the nucleus is broken as a result of the particles of silver formed in it, and the solution $AlCl_3$ penetrates the nucleus and ensures its dissolution. This is followed by processing steps B and D, as in the first embodiment. In the final stage in the second version of the core CaF_2 partially stored in unlit places and holograms are missing in lighted places.

The emulsion with heterophase microcrystals "core CaF_2–shell $AgBr$(I)" is offered for hologram recording has the following properties:

1. The photosensitivity of this emulsion is the same as in the case of silver halide photographic materials.

2. The emulsion can be sensitized to different spectrum areas.

3. In holograms recorded in transmitted light, DE reaches 65%, which indicates a significant magnitude of the phase component in the registered hologram, which is due to differences in refractive indices CaF_2 and binder.

4. Where the recorded holograms significantly depend on the substance binder and, in particular, from the gelatin used in the synthesis, because different types of gelatin differ in the refractive index which significantly depends on the moisture content in gelatin. Because

indicator refraction for CaF_2 – the value is constant, then change n for surrounding binder affects the value of DE. In addition, the DE may vary depending on the presence of binding moisture and organic additives, transparent to visible light.

Thus, in the obtained layers it is possible to preserve the light sensitivity of the silver halide layers and to perform phase recording of the hologram. It is clear that additional research on the selection of the substance of the nucleus of heterophase microcrystals and the binding emulsion layer can increase the DE of recorded holograms, and the use of different sensitizers – to increase the sensitivity of the light-sensitive layer to different regions of the spectrum.

In addition, the proposed emulsion in the process of development does not give a "mustache" (see Section 1) and the developed silver has the form of spherical particles of small size. An example of a particularly fine-grained emulsion with heterophase microcrystals and an emulsion obtained by mechanical mixing of homophase silver halide suspension and a suspension consisting of microcrystals CaF_2, shown in Fig.3.2. [55, 60, 61].
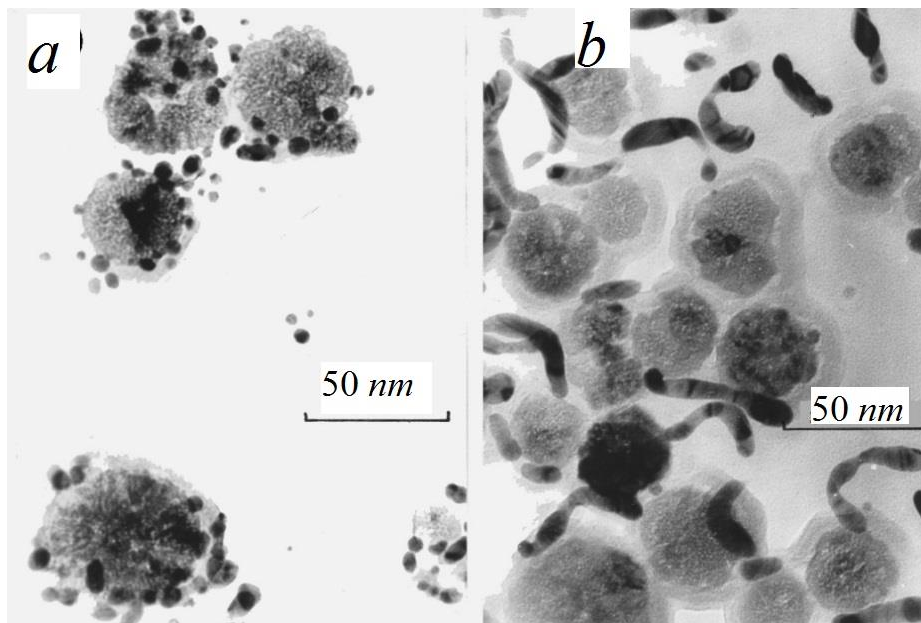
Fig.3.2. Microphotographs of developed microcrystals, especially fine-grained emulsions: *a)* – heterophase composite system; *b)* – obtained by mechanical mixing, especially fine-grained suspensions $AgHal$ and CaF_2.

This difference in the shape of the particles of the developed silver reduces the infectious developing and allows for a more homogeneous developing of the emulsion layer with heterophase microsystems to a considerable thickness. Therefore, the holograms registered in this case are deep.

The conclusions are based on the results obtained during the recording of an elementary transmitting three-dimensional hologram (three-dimensional transmitting diffraction grating) by He-Ne laser radiation with a power of 20 mW according to the usual scheme in beams of equal intensity converging at an angle of 30^0. DE of obtained holograms in transmitting ligt reached 65% and the half-width of the

angular selectivity was less than for the plates PFG-03 and PFG-04 (Fig.3.3), produced in series.

DE, %
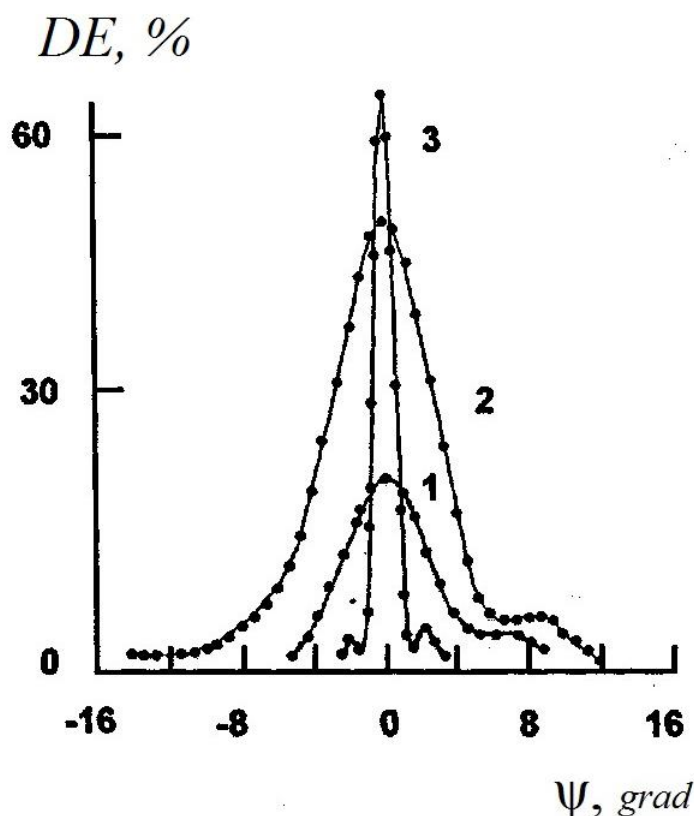
Fig.3.3. Angular selectivity of transmitted elementary holograms recorded on: 1 – PFG-03; 2 – PFG-04; 3 – emulsion with heterophase microsystems "core CaF_2–shell $AgBr$(I)".

This indicates a much greater effective thickness of the hologram, which is registered on the proposed emulsion with heterophase microsystems. As measurements have shown, the effective thickness of the hologram, calculated by the formula $L = \dfrac{\lambda}{\Delta\psi \sin\theta}$, where λ – the wavelength of the reading light, θ – Bragg angle, $\Delta\psi$ – half-width of the angular selectivity (Fig.3.3, curve 3) is almost an order of magnitude greater than in mass-produced materials.

151

Thus, the use of the proposed emulsion allows not only to increase the phase contrast of the recorded interference pattern, but also to increase the thickness of the hologram, which is of fundamental importance for the implementation of its three-dimensional properties.

Another important quality of the studied emulsion was a small change in the thickness of the hologram during processing (less than 10%). Obviously, this is due to the stabilizing effect of calcium fluoride particles remaining in the layers. We know thatin the process of post-exposure treatment, the thickness of the layers of PFG-03 decreases, and the layers of PFG-04 – increases. Therefore, when recording image reflective holograms with red (for PFG-03) or blue (for PFG-04) laser radiation, the color of the image restored by white light will be yellow. The color of the reconstructed image of similar holograms registered by the emulsion with heterophase microcrystals "core CaF_2–shell $AgBr$(I)" corresponds to the color of the laser radiation used during recording. This is another advantage of the proposed emulsion, as it is not necessary to make appropriate corrections (scale factors of the image) to change the thickness of the emulsion.

Emulsions with heterophase microsystems "core CaF_2–shell $AgBr$(I)" can be used not only for technical purposes, for example, when creating holographic optical elements (see Section 4). As our research shows, the achieved thickness of holograms is enough to record the transmitting three-dimensional image holograms in converging beams, according to the scheme shown in Fig.3.4, and restore them in white light as in the case of reflective holograms, obtained by the method of Denisyuk.
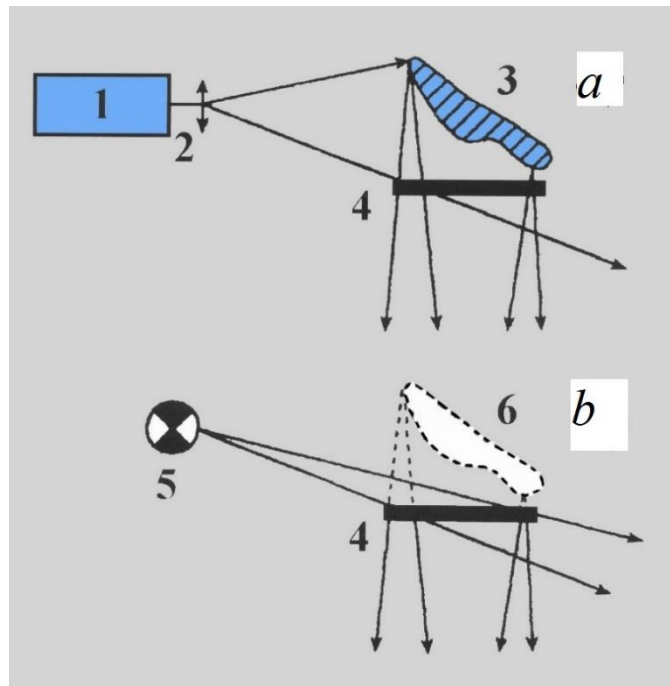
Fig.3.4. The scheme of recording three-dimensional transmitting holograms inconverging beams: (*a*) – recording scheme, (b) – recovery scheme.

It turned out that when the hologram is irradiated with white light, the color of the restored image is uniform throughout the object and there is no overlap of images restored with light from other spectral areas as in the case for thin holograms. In addition, there is no change in the color of the image depending on the angle of view (in the case of iridescent holography). The color of the image changes only when the angle at which the restorative white light falls on the hologram. The described properties of the hologram determine its advantages in comparison with the reflective hologram, as in some cases the internal lighting is much more convenient than the external.

Note also that the three-dimensional transmitting holograms described here are similar in their characteristics to those previously received by Usanov Yu.Ye. with staff on silver halide emulsions [61], which

underwent special treatment. There, as a result of this treatment, microcrystals of silver halide and metallic silver halide were removed from the emulsion, and the resulting microvoids provided the phase contrast of the hologram.

In our case, the increase in phase contrast is determined by the presence of nuclei of heterophase microsystems. Increased phase contrast leads to an increase in the dynamic range of the medium. Experiments on emulsions with heterophase microsystems have shown that this allows four three-dimensional transmitting holograms to be recorded in the same volume, with the DE of each being 20%.

Thus, the use of emulsions with heterophase microsystems "core CaF_2–shell $AgBr$(I)" for recording three-dimensional transmitting holograms allows to realize a light-sensitive medium that preserves, on the one hand, the light sensitivity of silver-silver emulsion, and on the other – provides phase contrast and effective thickness sufficient for recording three-dimensional transmitting holograms with high diffraction efficiency and spectral efficiency in the converging beams. Additional studies of the dissolution rates of the nucleus of heterophase microcrystals under different external conditions can increase the diffraction efficiency of recorded holograms.

3.2. Holographic recording of three-dimensional transmitting diffraction gratings in monolithic CGS and AHC at elevated temperatures.

The main problem of forming a holographic three-dimensional transmitting diffraction grating in the surroundings we are considering is

154

the implementation of the process of recording and fixing in them photoinduced changes that form the grating in one continuous process. We solved this problem by changing the temperature regime for the process of recording and reading a three-dimensional diffraction grating. The lattice was recorded by laser radiation at a temperature above 50°C, and read – at room temperature. In this case, only those photostimulated transformations that are also thermally activated must take part in the formation of the lattice. Activation energy for such processes should be such that at room temperature the photostimulated transformations are "frozen" and provide diffraction to the lattice of any light fluxes (including those that form the lattice), and do not lead to its destruction.

Recording of gratings at elevated temperatures requires additional measures to eliminate various external influences on the stability of the interference pattern that forms the lattice in the process of its exposure. To this end, in addition to the fact that the recording was made in a vacuum, additionally a system of spatial stabilization of the interference pattern was developed [174].

3.2.1. Spatial stabilization system of interference pattern.

Schematic diagram of the installation for holographic recording of a three-dimensional transmitting elementary lattice with a system of spatial stabilization of the interference pattern is shown in Fig.3.5.

Photodiodes (11, 14) are input sensors for the system of spatial stabilization of the interference pattern, which on the principle of negative feedback provides compensation for phase mismatches that occur in interference beams due to vibration and convective fluxes. When recording diffraction gratings without the use of a stabilization system,

interference pattern disruptions lead to the recording of several independent parasitic gratings as a self-diffraction effect, which significantly impairs the properties and reduces the DE of the recorded gratings.
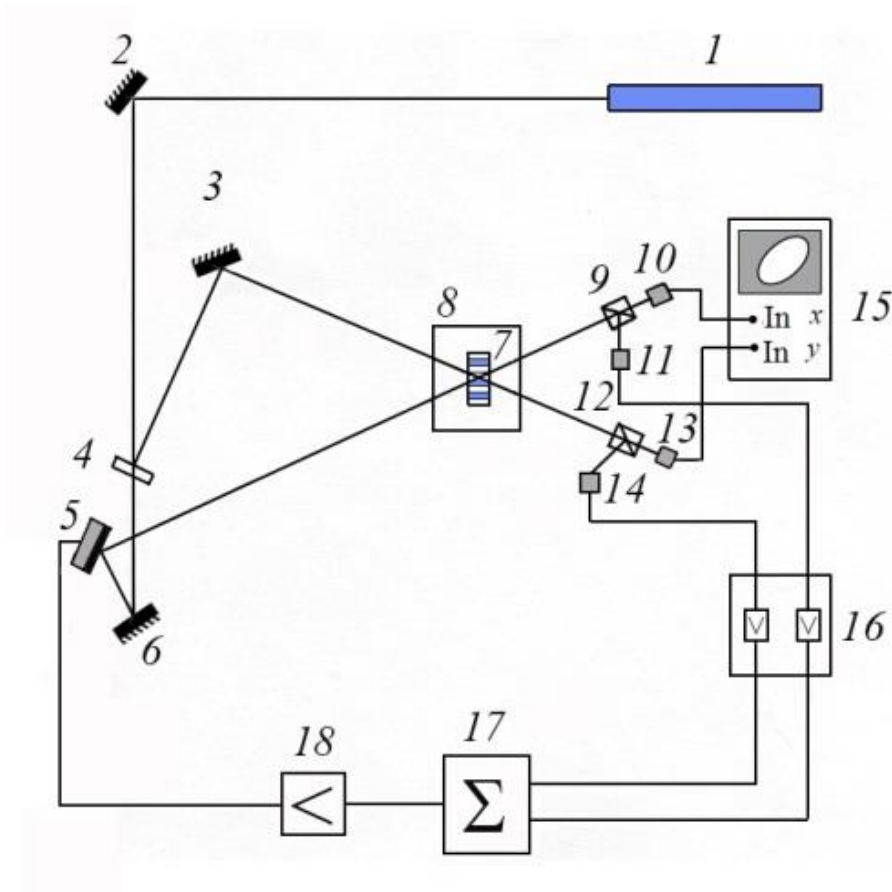
Fig.3.5. Schematic diagram of the installation: 1 – LGN-215 laser; 2, 3, 6 – mirrors; 4 – light divider; 5 – mirror mounted on a piezoelectric crystal; 7 – sample; 8 – oven-thermostat mounted on a rotary table; 9, 12 – light-separating cube; 10, 11, 13, 14 – photodiodes; 15 – oscilloscope; 16 – differential amplifier; 17 – integrator; 18 – high-voltage amplifier.

The signal from the photodiodes (11, 14) is fed to the differential amplifier (16), from which the amplified diversity signal enters the integrator. From the integrator, the test signal, amplified by a high-voltage amplifier (18), is fed to the piezoceramics with a mirror (5), which

changes the optical path of one of the beams, and provides in-phase recording beams. Schematic diagrams of the stabilization unit and differential amplifier are described by us in [175].

Signals from photodiodes (10, 13) fell on the oscilloscope and provided dynamic visual information about the optical characteristics and DE grids, which are recorded directly in the registration process according to our proposed method, which will be described in the next section.

The properties of the materials we used for recording (CGS and AHC) are well studied, and the photostimulated changes in the observed optical absorption and refractive indices are described in many works [96]. However, photoinduced processes that take place in the periodic interference field in holographic recording have not been studied enough. The use for the analysis of holographic data obtained by uniform illumination of the sample is not entirely correct, as it does not take into account the processes of diffusion of carriers and point defects in the interference fringes.

The main reason for these shortcomings is the lack of appropriate principles for measuring holographic characteristics directly in the process of recording holograms. Therefore, our method based on the method of phase-modulated holography is of some interest. In this section, the technique is used to analyze the mechanisms of holographic recording in the materials of CGS and AHC.

3.2.2. Methods for determining the parameters of a three-dimensional transmitting amplitude-phase diffraction grating.

Of the many works devoted to the consideration of light diffraction on three-dimensional lattices[5, 176–182], the theory of connected waves

developed by Herwig Kogelnik [182] became the most widespread. The advantage of their proposed approach is that it allows to explain all the basic properties of three-dimensional gratings, to obtain both theoretical and numerical results, when applied to different types of three-dimensional gratings (absorbing and non-absorbing). In this regard, when developing a method for determining the parameters of the transmitting three-dimensional diffraction grating, we will also adhere to the theory of coupled waves.

To determine the mechanism of holographic recording, measurement methods are needed, which would, at different points in the holographic recording, allow to establish the change in the absorption coefficient $\Delta\alpha$ and the refractive index Δn (amplitude and phase components of the hologram), as well as the phase shift of the spatial distribution $\Delta\alpha$ and Δn relative to the recording interference pattern.

Previously proposed methods that solve the above problems can be implemented only in phase recording [184, 185]. In the case of amplitude-phase gratings, separate measurement of amplitude and phase modulations can be performed only for coherent light with an accuracy of some constant value, provided that during the recording there was no change in average refractive index and absorption coefficient [186–188]. It is also important to emphasize that all the considered methods do not allow to carry out spectral studies of changes $\Delta\alpha$ and Δn in the lattice, as well as to establish the shift of the lattice relative to the interference pattern that created it. Therefore, it is not possible to determine whether there is an increase or decrease in the maxima of the interference pattern α and n (otherwise, if we use the terminology adopted in scientific

158

photography – whether the lattice recording is negative or positive), and hence the role of diffusion processes in the mechanism of holographic recording. The same methods of phase-modulated holography that allow this to be done require the use of expensive and complex equipment [189, 190]. We proposed a simplified version of the method of phase-modulated holography for separate determination of amplitude and phase modulations and their phase shift when recording the amplitude-phase lattice, as well as the method of studying spectral changes $\Delta\alpha$ and Δn in the lattice, which are devoid of the above disadvantages [96, 190].

3.2.2.1. The method of separate determination of the average absorption, amplitude and phase modulations and their phase shift when recording a three-dimensional transmitting diffraction grating.

When implementing this method, the lattice is recorded in the studied material by two convergent coherent light beams of length λ with an intensity equal to I_0 (Fig. 3.6). Then, in the recording environment, as a result of interference, light intensity $I(x)$ changes by law:

$$I(x) = \frac{I_0}{2}\left[1 + \cos\left(\frac{2\pi x}{d}\right)\right], \tag{3.1}$$

here d is the period of the interference pattern.
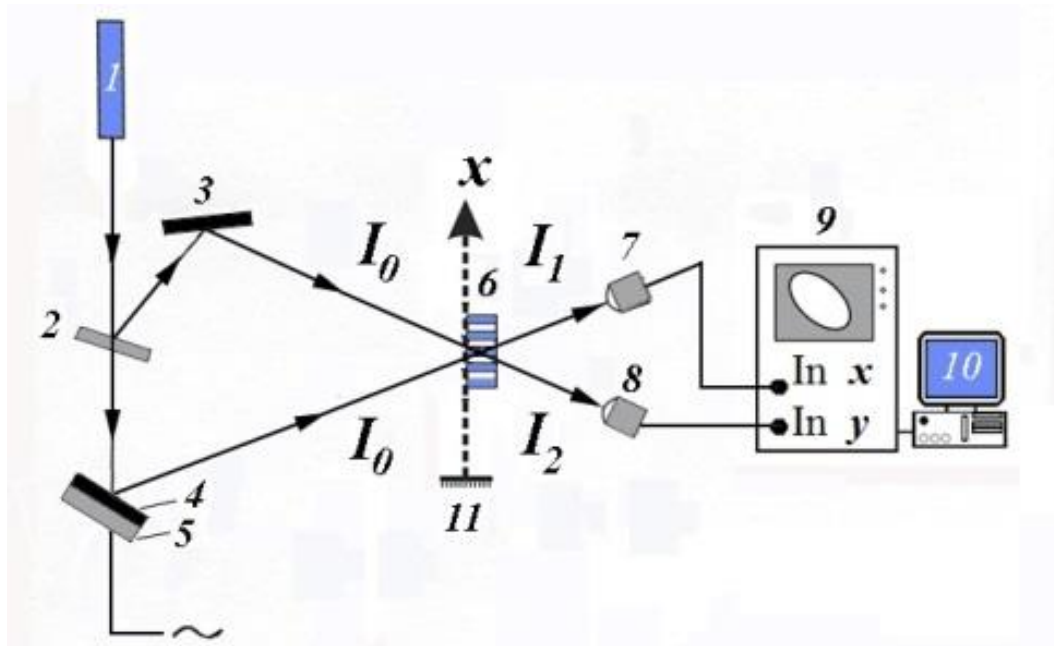
Fig.3.6. Schematic diagram of the installation for determining the amplitude and phase modulations when recording the amplitude-phase lattice.

1 – laser; 2 – light divider; 3,4 – reflective mirror; 5 – piezoceramics; 6 – recording environment; 7, 8 – photodiodes; 9 – oscilloscope; 10 – analyzer (computer); 11 – object on which the three-dimensional lattice is fixed.

The influence of light with a spatial intensity distribution (3.1) leads to a change in the absorption coefficient α and refractive index n of the recording medium, the spatial distribution of which is described by the formula:

$$\alpha(x) = \overline{\alpha} + \Delta\alpha_0 \cos\left(\frac{2\pi x}{d} + \Delta\Psi_\alpha\right), \qquad (3.2)$$

$$n(x) = \overline{n} + \Delta n_0 \cos\left(\frac{2\pi x}{d} + \Delta\Psi_n\right), \qquad (3.3)$$

where $\overline{\alpha}$ and $\overline{n}$ – the average volume of changes in the absorption and refractive indices, $\Delta\alpha_0$ and Δn_0 – the amplitudes of their modulation,

$\Delta\Psi_\alpha$ and $\Delta\Psi_n$ – phase shifts, respectively, the amplitude and phase components of the lattice relative to the recording interference pattern (3.1).

To establish $\overline{\alpha}$, $\Delta\alpha_0$, Δn_0, $\Delta\Psi_\alpha$, and $\Delta\Psi_n$ in the process of recording the lattice, we propose to measure not only the intensities of light beams passing through the light lattice I_1 and I_2, but, in contrast to [186, 192], also analyze the dependence I_1 and I_2 of forced beam phase misalignment $\Delta\varphi$ forming the lattice. As for $\overline{n}$, then for all recording carriers the relation $n = \overline{n} + \Delta n_0 \approx \overline{n}$ is fulfilled and, therefore, $\overline{n} \approx n$.

The mismatch $\Delta\varphi$ achieves short-term (compared to the recording time of the grating) changes in the optical path length of one of the rays due to the displacement of the mirror that reflects radiation and is fixed on the piezoceramics (Fig. 3.6 elements 4 and 5). In this case, the total phase shift of the amplitude and phase components of the lattice relative to the interference pattern is $\Delta\Psi_\alpha + \Delta\varphi$ and $\Delta\Psi_n + \Delta\varphi$.

Each beam of light emanating from the lattice has an amplitude B_1 and B_2, is formed as a result of interference of two rays – the passed, and diffracted. So,

$$B_1 = A_1 exp[-i(\Phi_A - \Delta\varphi)] + S_2 exp(-i\Phi_S), \qquad (3.4)$$

$$B_2 = A_2(-i\Phi_A) + S_1 exp[-i(\Phi_S - \Delta\varphi)], \qquad (3.5)$$

here A_1, A_2, Φ_A and S_1, S_2, Φ_S are the amplitudes and phases (Φ_A and Φ_S) of the beam passing through the lattice and the diffracting beam, respectively.

Taking into account the observed condition of equal intensity of incident light beams and the conclusions of [182] for the amplitude A and

161

S we get:

$$A_1 = A_2 = A = A_0 exp\left(-\frac{\overline{\alpha}L}{\cos\theta}\right)\cos(v - iv_\alpha), \qquad (3.6)$$

$$S_1 = S_2 = S = iI_0 exp\left(-\frac{\overline{\alpha}L}{\cos\theta}\right)\cos(v - iv_\alpha). \qquad (3.7)$$

Here L – the thickness of the lattice θ – Bragg angle, $v = \frac{\pi\Delta n_0 L}{\lambda\cos\theta}$, $v_\alpha = \frac{\Delta\alpha_0 L}{2\cos\theta}$.

Substituting(3.6) and (3.7) in (3.4) and (3.5) and multiplying by a complex related value, we can determine the intensities I_1 and I_2 beams of light emanating from the lattice:

$$I_1 = B_1 B_1^* = AA^* + SS^* + AS^* exp[-i(\Phi_A - \Phi_S - \Delta\varphi)]$$
$$+ SA^* exp[i(\Phi_A - \Phi_S - \Delta\varphi)];$$
$$I_2 = B_2 B_2^* = AA^* + SS^* + AS^* exp[-i(\Phi_A - \Phi_S + \Delta\varphi)]$$
$$+ SA^* exp[i(\Phi_A - \Phi_S + \Delta\varphi)].$$

The diffracted beam is formed as a result of the reflection of incident light from the lattice planes, which have a higher optical density, i.e. in which $n = \overline{n} + \Delta n_0$. It is known [192] that in this case, the reflection is the loss of half-wave and, i.e. $\Phi_A - \Phi_S = \pi$, then for I_1 and I_2 finally get:

$$I_1 = I_0 exp\left(-\frac{2\overline{\alpha}L}{\cos\theta}\right)[ch2v_a - sh2v_a \cos\Delta\varphi - \sin 2v \sin\Delta\varphi], \quad (3.8)$$

$$I_2 = I_0 exp\left(-\frac{2\overline{\alpha}L}{\cos\theta}\right)[ch2v_a - sh2v_a \cos\Delta\varphi + \sin 2v \sin\Delta\varphi], \quad (3.9)$$

Similar expressions for the intensities of the beams passed I_1 and I_2 received in [194, 195] for the case when in the process of recording there is a shift of the lattice, which is registered relative to the spatially stable interference pattern, which is recorded. Thus, the dependences (3.8) and

(3.9) for the intensities of the beams emanating from the lattice are characteristic not only of the phase mismatch with the beams falling on the lattice, but also of the lattice shift relative to the interference pattern being recorded.

Consider now which curve will describe the end of the vector I, if its projections on the orthogonal axes Ox and Oy are given by the values I_1 and I_2 are determined by formulas (3.8) and (3.9), when the phase mismatch between the incident beams $\Delta\varphi$ changes from 0 to 2π (it is assumed that the phase change occurs time when the lattice can be considered stationary). For visual observation of this curve it is enough to submit signals from photodiodes 7 and 8 (Fig.3.6) according to the input x and y the oscilloscope or two-coordinate recorder. As follows from (3.8) and (3.9), when the phase difference $\Delta\varphi = 0, \pi$ and 2π intensity I_1 and I_2 and are equal to each other, regardless of the ratio of amplitude (ν_α) and phase (ν) contribution to diffraction. Therefore, in this case, the end of the vector I is always on the line OO_1 passing through the origin at an angle of 45° (Fig.3.7). At $\Delta\varphi = 0$ or 2π the value I is minimal (to the end of vector I corresponds point 2 on the line OO_1, Fig.3.7).
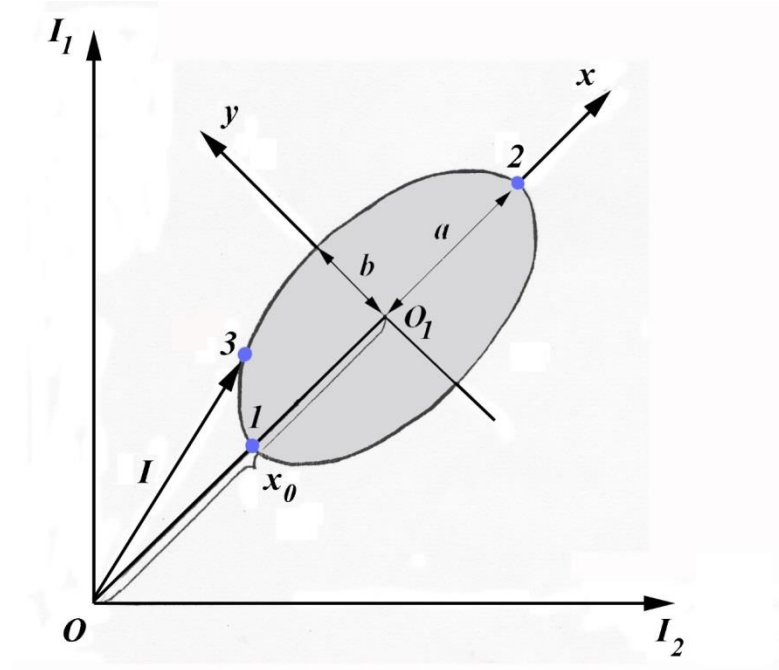
Fig.3.7. The trajectory described by the end of the vector I when the phase mismatch $\Delta\varphi$ between the recording beams changes from 0 to 2π.

If we go to the coordinate system in which the axis Ox coincides with the line OO_1, and its beginning is shifted relative to the point O (Fig.3.7) by a segment $OO_1 = x_0$:

$$x_0 = \sqrt{2}I_0 exp\left(-\frac{2\bar{\alpha}L}{\cos\theta}\right)ch2v_\alpha, \qquad (3.10)$$

then

$$x = -\sqrt{2}I_0 exp\left(-\frac{2\bar{\alpha}L}{\cos\theta}\right)ch2v_\alpha\cos\Delta\varphi,$$
$$y = -\sqrt{2}I_0 exp\left(-\frac{2\bar{\alpha}L}{\cos\theta}\right)\sin2v\sin\Delta\varphi. \qquad (3.11)$$

Hence, excluding the argument $\Delta\varphi$, we obtain a trajectory that describes the end of the vector I and is an ellipse.

$$\frac{x^2}{a^2} + \frac{y^2}{b^2} = 1, \qquad (3.12)$$

164

here

$$a = \sqrt{2}I_0 exp\left(-\frac{2\overline{\alpha}L}{\cos\theta}\right)ch2v_\alpha; \qquad (3.13)$$

$$b = \sqrt{2}I_0 exp\left(-\frac{2\overline{\alpha}L}{\cos\theta}\right)\sin 2v. \qquad (3.14)$$

Having determined for the ellipse the magnitudes a and b of the semi-axes and, as well as the magnitude of the shift of its center from the origin x_0 (Fig.3.7), it is possible to set separately the values of both amplitude and phase modulation and average value lattice absorption $\overline{\alpha}L$. From equations (3.10) and (3.13) we have: $th2v_\alpha = \frac{a}{x_0}$, from here

$$v_\alpha = \frac{1}{2}arcth\frac{a}{x_0}. \qquad (3.15)$$

Accordingly, for the phase contribution and the average absorption from equations (3.10), (3.11) and (3.14) we obtain:

$$\sin 2v = \frac{b}{\sqrt{x_0^2 - a}};$$

$$v = \frac{\pi}{2}m + (-1)^m\frac{1}{2}arc\sin\left(\frac{b}{\sqrt{x_0^2 - a}}\right); \qquad (3.16)$$

here $m = 1, 2, ...$

$$exp\left(-\frac{2\overline{\alpha}L}{\cos\theta}\right) = \sqrt{\frac{x_0^2 - a}{2I_0^2}};$$

$$\overline{\alpha}L = \frac{1}{2}\cos\theta\, ln\sqrt{\frac{2I_0^2}{x_0^2 - a^2}}. \qquad (3.17)$$

Since the magnitude of the half-axis a is proportional to the magnitude of the amplitude, and the half-axis b – phase modulation, in

the case of purely phase recording ($\nu_\alpha = 0$ and, accordingly $\alpha = 0$,) the ellipse becomes straight, parallel to the axis Oy and passes through the point O_1, and in purely amplitude recording ($\nu = 0$ and, accordingly, $b = 0$ at $m = 0$) – in a straight line directed along the axis Ox. In the case of amplitude-phase recording, the shape of the ellipse (elongated along the axis Ox or Oy) depends on the contribution of amplitude or phase modulation. Thus, only by the type of ellipse, without additional calculations, it is possible to qualitatively estimate the ratio of these modulations directly in the process of registration of the lattice [190].

As noted above, the dependences (3.8) and (3.9) are also valid in the case when the phase mismatch $\Delta\varphi$ is formed as a result of the shift of the recorded lattice relative to the interference pattern that creates it. Therefore, if the specified shift occurs during the recording process, the end of the vector I with projections I_1 and I_2 will describe the ellipse given by equations (3.12) – (3.14). Let us now consider some individual cases:

1. The end of vector I is on the line OO_1 and does not change position when writing. This satisfies the condition $\Delta\varphi = 0$ or $\Delta\varphi = \pi$. When the first condition is met and the values I_1 and I_2 are minimal (the end of the vector I corresponds to point 1 on the line OO_1), the lattice is not shifted relative to the recording diffraction pattern and, therefore, the recording is in phase (negative). In the case of $\Delta\varphi = \pi$ intensity I_1 and I_2 maximum (the end of the vector I corresponds to point 2 on the line OO_1), the lattice is shifted relative to the recording image, and the recording is anti-phase (positive). Since in both positive and negative recording, the end of the vector I is on the line OO_1, to determine the nature of the recording it is necessary to conduct additional measurements to determine the

dependence I on the forced phase mismatch between the incident beams. If in such measurements, when the end of the vector I describes an ellipse, there is an increase in the projection I on the axis Ox, hence, the initial value I was minimal and the record was negative. If, on the contrary, at the considered measurement the projection I on an axis x decreases, then, means, the initial value I is the maximum, and record – positive.

2. The end of the vector I corresponds to some point on the plane xOy that does not coincide with points 1 and 2 (for example, point 3 in Fig.3.7). This corresponds to the case $0 < |\Delta\varphi| < 2\pi$. Based on the above considerations and measurement techniques, the position of this point on the ellipse and its displacement in forced phase mismatch, it is possible for any moment of recording to specify the amount of displacement of the amplitude and phase components of the lattice relative to the interference pattern that creates it.

Let us now find out the standard error of the definition of v, v_a and $\overline{\alpha}L$.

Because the magnitude a, b and x_0 of the same order, it is natural to assume that the relative errors of their measurement are the same:

$$\frac{\Delta x_0}{x_0} = \frac{\Delta a}{a} = \frac{\Delta b}{b} = \Omega.$$

In this case, taking into account expressions (3.15), (3.16) and (3.17) for the standard error of the values v_a and $\overline{\alpha}L$ we obtain:

$$\Delta v_\alpha = \frac{\Omega}{2\sqrt{2}} sh4v_\alpha; \tag{3.18}$$

$$\Delta v = \frac{\Omega}{2} \sqrt{1 + \frac{1 + th^4 2v_\alpha}{(1 - th^2 2v_\alpha)^2} tg2v}; \tag{3.18, a}$$

167

$$\Delta(\overline{\alpha}L) = \frac{\Omega \cos\theta}{2}\sqrt{1 + \frac{1 + th^4 2\nu_\alpha}{(1 - th^2 2\nu_\alpha)^2}}. \qquad (3.19)$$

The corresponding dependences for relative errors $\dfrac{1}{\Omega}\dfrac{\Delta\nu_a}{\nu_a}$, $\dfrac{1}{\Omega}\dfrac{\Delta\nu}{\nu}$,

and $\dfrac{1}{\Omega}\dfrac{\Delta(\overline{\alpha}L)}{(\overline{\alpha}L)}$ are shown in Fig.3.8.

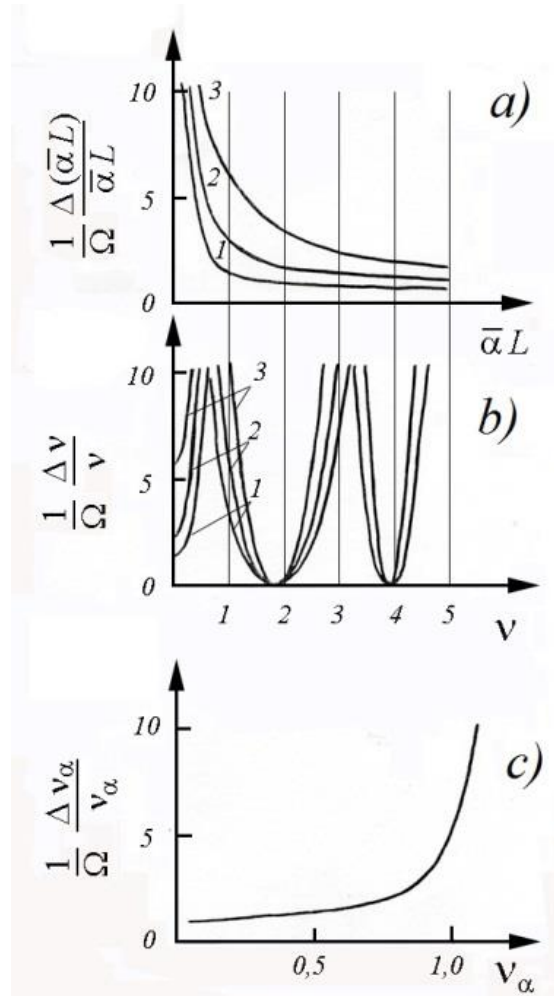Fig.3.8. Determination by formulas (3.15), (3.16) and (3.17) in the bulk transmitting amplitude-phase diffraction grating of the relative error: *a*) average absorption; *b*) the coefficient of phase modulation; *c*) the coefficient of amplitude modulation.

From Fig.3.8 it is seen that in a significant range of values $\nu, \nu_a, \overline{\alpha}L$ and the error of their definition is slightly higher than the error of direct

measurements. For the values $v_a > 1$, $\overline{\alpha}L \approx 0$ and $v = \frac{\pi}{4}m$, where $m = 0, 1, 2, ...$ as derived from (3.18), (3.18, a) and (3.19) the error in determining them is very large and these values should be removed from the measurement.

3.2.2.2. Method for determination of spectral change of average absorption, amplitude and phase modulation of three-dimensional transmitting diffraction grating.

To develop a separate definition of average absorption $\overline{\alpha}L$, amplitude v_α and phase v modulations in the lattice, which allows to obtain these parameters in a wide spectral range without the use of coherent light, should record the intensity I_1 and I_2 (Fig. 3.6), when one light beam of intensity I_0 falls on the already recorded grating (for example, reflected by a mirror 3). In this case I_1, it becomes the intensity $I_Д$ of the light that diffracted on the lattice, and I_2 the light that has passed, and according to [182, 190], they are given by the expressions:

$$\frac{I_Д}{I_0} = I_S = exp\left(-\frac{2\overline{\alpha}L}{\cos\theta}\right)\frac{v^2 + v_a^2}{a}[sin^2\Phi + sh^2 f], \qquad (3.20)$$

$$\frac{I_П}{I_0} = I_R = exp\left(-\frac{2\overline{\alpha}L}{\cos\theta}\right)\left[cos^2\Phi + sh^2 f + \frac{\xi}{a}(\Phi sh2f - f sin2\Phi)\right.$$

$$\left. + \frac{\xi}{a}(sin^2\Phi + sh^2 f)\right], \qquad (3.21)$$

here $v = \frac{\pi\Delta n_0 L}{\lambda\cos\theta}$; $v_a = \frac{\Delta\alpha_0 L}{2\cos\theta}$ $\Phi = \frac{\sqrt{\xi + v^2 - v_a^2 + a}}{\sqrt{2}}$; $f = \frac{\sqrt{\xi - v^2 + v_a^2 + a}}{\sqrt{2}}$

$a = \sqrt{(\xi^2 + v^2 - v_a^2)^2 + 4v^2 v_a^2}$; $\xi = \frac{2\pi L \sin\theta}{\lambda}\delta$, $\delta = \theta' - \theta$,

here $\theta'-$ the magnitude of the angle at which light falls on the grating, $\theta-$ Bragg's angle.

Analyzing expression (3.21), it should be noted that in the simultaneous presence of amplitude and phase modulations, due to the presence in expression (3.21) of the term proportional ξ, the dependence $I_R(\xi)$ becomes asymmetric with respect to the Bragg angle θ (Section 4, Fig.4.13). This effect is a distinctive feature of the amplitude-phase lattice and indicates that the diffraction on such lattices requires a separate independent consideration. Because the special nature of diffraction may be not only scientific but also practical interest, for example, to create optical elements based on asymmetric angular dependence $I_R(\xi)$ [96].

It also follows from equation (3.21) that if the ray incident on the lattice deviates by a sufficient angle δ_0, when there is no diffracting ray (and the condition $\delta_0 \ll \theta$ remains in force), then for intensity $I_R(\lambda, \delta_0)$ light with wavelength λ past, we have:

$$I_R(\lambda, \delta_0) = exp\left(-\frac{2\overline{\alpha}L}{\cos\theta}\right). \tag{3.22}$$

It follows that when measuring intensity $I_R(\lambda, \delta_0)$, at different wavelengths λ, and, if L known, it is possible to establish the spectral dependence of the mean lattice absorption:

$$\overline{\alpha} = \frac{1}{2L}\cos\theta \cdot \ln\left(\frac{1}{I_R(\lambda, \delta_0)}\right). \tag{3.23}$$

In addition, for Bragg irradiation $\xi = 0$,write formulas (3.20) and (3.21):

$$I_S(\theta) = exp\left(-\frac{2\overline{\alpha}L}{\cos\theta}\right)[sin^2 v + sh^2 v_a], \tag{3.24}$$

170

$$I_R(\theta) = exp\left(-\frac{2\bar{\alpha}L}{\cos\theta}\right)[cos^2v + sh^2v_a]. \qquad (3.25)$$

Now, combining equations (3.22), (3.24) and (3.25), it is possible to separate the amplitude and phase components in the diffraction:

$$\frac{I_R(\theta) + I_S(\theta)}{I_R(\delta_0)} = 1 + 2sh^2v_a = ch2v_a.$$

From here

$$v_a = \frac{1}{2}arcch\left[\frac{I_R(\theta) + I_S(\theta)}{I_R(\delta_0)}\right], \qquad (3.26)$$

$$v = \frac{1}{2}arccos\left[\frac{I_R(\theta) - I_S(\theta)}{I_R(\delta_0)}\right]. \qquad (3.27)$$

Thus, by measuring the intensity of the transmitted beam $I_R(\lambda, \theta)$ and $I_S(\lambda, \theta)$ the diffracting beam when illuminating the grating with monochromatic light at a Bragg angle and the intensity of the transmitted no Bragg beam $I_R(\lambda, \delta_0)$ for different wavelengths and, if known, θ and L, thus, taking into account that $v = \frac{\pi\Delta n_0 L}{\lambda\cos\theta}$; $v_a = \frac{\Delta\alpha_0 L}{2\cos\theta}$, we obtain the desired spectral dependence $\Delta\alpha_0$ and Δn_0 [239, 251]:

$$\Delta\alpha_0 = \frac{2\cos\theta}{2L}arcch\left[\frac{I_R(\lambda, \theta) + I_S(\lambda, \theta)}{I_R(\lambda, \delta_0)}\right], \qquad (3.28)$$

$$\Delta n_0 = \frac{\lambda\cos\theta}{2\pi L}arccos\left[\frac{I_R(\lambda, \theta) - I_S(\lambda, \theta)}{I_R(\lambda, \delta_0)}\right]. \qquad (3.29)$$

The next very important characteristics of the three-dimensional lattice are its effective thickness L, angular and spectral selectivity.

3.2.2.3. Methods for determining the effective thickness and spectral selectivity of a three-dimensional transmitting amplitude-phase diffraction grating.

Angular selectivity is characterized by how fast the diffraction efficiency (DE) the lattice decreases to zero when the angle of incidence deviates from the Bragg angle(Fig.3.3). Its numerical value can be set, for example, by the value δ_0 at which the DE of the lattice is minimal, then measuring the parameter δ_0 for the lattice, it is possible to determine the effective thickness of the lattice by this value L.

This parameter is quite important, because the effective thickness of the grid does not always correspond to the thickness of the recording material in which this grid is recorded. To determine L it is necessary to use the dependence of the diffraction efficiency of the lattice $\eta = \frac{I_Д}{I_0} = I_S(100\%)$ on the value of the angle $\delta = \theta' - \theta$ where θ' – the magnitude of the angle at which light falls on the grid, θ – Bragg's angle. Illumination occurs in a plane wave with a length λ that satisfies the Bragg condition:, $\lambda = \frac{d}{2 \sin \theta}$ where d – lattice period. In accordance [182, 190, 251] this dependence is determined by expression (3.20),

$$\eta = exp\left(-\frac{2\overline{\alpha}L}{\cos \theta}\right)\frac{v^2 + v_a^2}{a}[sin^2\Phi + sh^2 f],$$

from which it follows that provided that then $\sin \Phi(\delta_0) = 0$ or $\Phi(\delta_0) = \pi$ DE reaches a minimum value. From here after simple transformations we will receive:

$$\xi = \frac{2\pi\delta_0 \sin\theta}{\lambda} L = \sqrt{\pi^2 + v_\alpha^2 - v^2 v_\alpha^2 - v^2}$$

$$L = \frac{\lambda}{2\pi\delta_0 \sin\theta} \sqrt{\pi^2 + v_\alpha^2 - v^2 v_\alpha^2 - v^2} \qquad (3.30)$$

Or using Bragg's condition, we have $d = \dfrac{\lambda}{2\sin\theta}$

$$L = \frac{d}{\pi\delta_0} \sqrt{\pi^2 + v_\alpha^2 - v^2 v_\alpha^2 - v^2}, \qquad (3.31)$$

here d– lattice period.

All parameters in the right part of expression (3.31) are subject to independent measurement. The following considerations can be used to estimate the spectral selectivity of the lattice. When the lattice is illuminated by a plane wave with a length λ that satisfies Bragg's law ($\delta = 0$), then, as follows from (3.20), the lattice has a maximum DE:

$$\eta = exp\left(-\frac{2\overline{\alpha}L}{\cos\theta}\right)[sin^2 v + sh^2 v_a].$$

Now let the wavelength that falls on the lattice become equal to $\lambda + \Delta\lambda$ where $\frac{\Delta\lambda}{\lambda} \ll 1$. The maximum DE is now observed when illuminated not at the Bragg angle θ, but at a new angle $\theta' = \theta + \delta$. If we continue to illuminate the lattice at the original angle $\theta = \theta' - \delta$, the DE decreases, because now the angle θ is different from the Bragg angle θ' of $-\delta$. The curves of angular selectivity (Fig.3.3) are symmetric with respect to δ, so that, if we know δ, we can determine the decrease in DE, which coincides with $\pm\delta$. The value δ can be expressed in terms $\Delta\lambda$ by introducing new Bragg parameters $\theta + \delta$, $\lambda + \Delta\lambda$ and $2\pi d \sin(\theta + \delta) = \lambda + \Delta\lambda$ into Bragg's law. Assuming that $\sin\delta \approx \delta$ and $\cos\delta \approx 1$, we get

$$\delta \approx \frac{\Delta\lambda}{\lambda} tg\theta. \qquad (3.32)$$

As already mentioned, DE has a minimum at $\delta = \delta_0$, a value that is quite simply determined from the angular selectivity of the lattice (Fig.3.3). If we substitute δ_0 in (3.32), we arrive at the approximate relation for the spectral selectivity of the lattice:

$$\frac{\Delta\lambda}{\lambda} \approx \frac{\delta_0}{tg\theta} = \delta_0 ctg\theta. \qquad (3.33)$$

Here is the deviation on $\Delta\lambda$ corresponds to a decrease in DE to almost zero.

In conclusion, it should be noted that the medium in which the elementary lattice is recorded by two plane waves is not always linear (i.e. amplitude and phase changes in the material are linearly dependent on exposure [196]). This leads to the fact that the profile of the recorded lattice is not strictly sinusoidal [197, 198]. This can be judged, for example, by the presence of diffraction maxima when illuminating such a lattice at an angle multiple of Bragg. For such a lattice, its absorption coefficient and refractive index can be decomposed into a Fourier series by cosines $\sum_{m=0}^{\infty} \Delta\alpha_m \cos 4\pi m x$ and $n(x) = \sum_{m=0}^{\infty} \Delta n_m \cos 4\pi m x$, which is equivalent to the existence of a set of elementary lattices with multiple spatial frequencies. Due to the high angular selectivity of the lattice by the mutual influence of harmonics can be neglected to determine the amplitude of the harmonic $\Delta\alpha_m$ and Δn_m.

Thus, it follows from the above consideration that all the lattice parameters are subject to separate measurement and will allow you to purposefully adjust the recording process in the recording medium, if known photochemical processes responsible for changing these parameters in the lattice.

3.2.3. Holographic record in monolithic CGS composition *As-S.*

As follows from the previous section, photoinduced changes in optical constants in CGS are due to different processes in the region of low (T<20°C) and high temperatures. The low-temperature process is characterized by the phenomenon of photo-darkening as a result of the creation of own defects due to autolocation of excitons [162, 199] and changes in their charge state after capture of nonequilibrium charge carriers [163]. In the region of high temperatures, in addition to photo-darkening, there is also the phenomenon of photo-enlightenment [70, 77, 200], which is caused by the process of "healing" of their own defects (reaction (2.61), Fig.2.21). In addition, at elevated temperatures as a result of inhomogeneous photoexcitation, which occurs during holographic recording, diffusion processes are possible not only non-equilibrium holes and electrons, but also point defects.

As shown by our studies [201, 202], for high-temperature holographic recording and measurement of photoconductivity in the system *As-S* there is a complete analogy of their dependences on the exposure temperature, heat treatment, and so on. Thus, for As_2S_3 holographic recording is noticeable at T>100°C. With increasing temperature, the diffraction sensitivity increases and at T≈170°C (corresponds to the softening temperature of the material T_g) reaches a maximum (Fig.3.9, curve 1) [67]. In the same temperature range, the maximum photoconductivity of this material is observed (Fig.2.9). The activation energy of photoconductivity at temperatures below T_{max} the linear region of dependence $lg(\Delta\sigma)$ (Fig.2.12, curve 1) is 0,4 *eV* and coincides with the activation energy of diffraction sensitivity. With the

violation of the stoichiometry of the compounds in the direction of excess sulfur, the position of the high-temperature maximum is shifted to lower temperatures and is determined by the softening temperature of the material T_g (Fig.2.12). Accordingly, the shift of the maximum for diffraction sensitivity observed (Fig.3.9, curve 2).

The diffraction sensitivity of non-stoichiometric compositions with excess sulfur, as well as photoelectric properties, is significantly affected by pre-heat treatment. After annealing the sample at the softening temperature of the material, the maximum diffractive sensitivity is shifted to the region of low temperatures (Fig. 3.9, curve 3) and observed at a temperature of about 60°C, which corresponds to the temperature at which the maximum jump photoconductivity in these compounds Section 2.2).
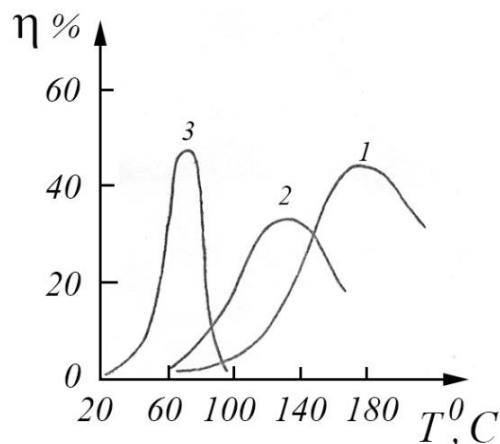
Fig.3.9. Dependence DE elementary gratings recorded at the same absorption energy, from the heating temperature of the plates As_2S_3 (1) and $As_{25}S_{75}$ (2, 3); 2 – before thermal annealing; 3 – after thermal annealing at T≈150°C for 15 minutes.

The amplitude value of the diffraction sensitivity in the maximum region increases with increasing sulfur content in the sample, and the

176

position of the maximum does not depend on the composition of the material in the range from $As_{30}S_{70}$ to $As_{15}S_{85}$ [78].

This correlation between the dependence of photoconductivity and diffraction sensitivity shows that the structural and chemical transformations in *As-S*, which are responsible for high-temperature holographic recording, are initiated by light-generated free nonequilibrium charges, rather than excitons, as is the case at low temperatures [162, 199].

Let us now consider the high-temperature processes that can occur in the system *As-S*, when photostructured transformations can be initiated only by free carriers and under the condition of inhomogeneity of photoexcitation, which for holographic recording varies according to the law (3.1):

$$I(x) = \frac{I_0}{2}\left[1 + \cos\left(\frac{2\pi x}{d}\right)\right],$$

Where d is the period of the interference pattern.

The description of this process will take place within the model of D-centers, taking into account that the system *As-S* is a *p*-type semiconductor and therefore only holes can migrate (see Section 2). Under the action of light He-Ne laser holes from the levels D^+ centers pass into the valence band as a result of the reaction

$$D^+ + h\nu \rightarrow D^0 + e^+. \tag{3.34}$$
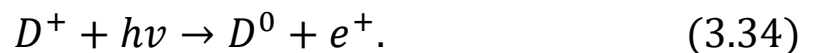
The free hole e^+, captured at the D^- center level, is converted into an electrically neutral polaron (D^0 center) and, if the temperature is high enough (for the system *As-S* T≥100°C), hole can be ejected from the formed D^0 centers to the permitted zone:

$$D^0 \leftrightarrow D^- + e^+. \tag{3.35}$$

In addition, holes can be trapped at the D^0 centers, creating D^+ centers from which thermal release is difficult, as the levels of the D^+ centers are located further from the valence band than the levels of the D^0 centers (Fig.2.4):

$$D^0 + e^+ \leftrightarrow D^+. \tag{3.36}$$

In stationary conditions, the system of equations corresponds to transitions (3.34) - (3.36)

$$[I(x)q_+ + W_+]N_+ = p\gamma_p^0 N_0, \tag{3.37}$$

$$W_0 N_0 = p\gamma_p^- N_-. \tag{3.38}$$

Here $W_0 = N_V\gamma_p^- exp\left(-\frac{E_{V_0}}{kT}\right)$ and $W_+ = N_V\gamma_p^0 exp\left(-\frac{2E_{V_0}+U}{2kT}\right)$ – the rate of thermal emission of holes from D^0 and D^+ centers in the valence band, respectively (Fig. 2.7), N_V – the density of states at the edge of mobility in the valence band, γ_p^0, γ_p^- – the coefficient of capture of holes D^0 and D^- centers, respectively, p – the concentration of holes in the valence band, q_+ – cross section of the reaction (3.34).

Note that, in principle, it is necessary to take into account the tunneling of polarons $2D_2^0 \rightarrow D^+ + D^-$ with the creation of positively (D^+) and negatively (D^-) charged polarons (bipolarons). However, in [87] it was shown that if there is a quasi-equilibrium of capture and release processes (3.35), then, taking into account tunnel pairing, it simply leads to a renormalization of the coefficient γ_p^0 in equation (3.28). First, neglect the diffusion spreading of holes and D^0 centers. Then, given that the

condition of local electroneutrality has the form $N_+ = N_- \approx \frac{N}{2}$, from equations (3.37) and (3.38) we obtain

$$p(x) = \left[\frac{(I(x)q_+ + W_+)W_0}{\gamma_p^0 \gamma_p^-} \right]^{\frac{1}{2}}, \qquad (3.39)$$

$$N_0(x) = N \left[\frac{\gamma_p^-(I(x)q_+ + W_+)}{4\gamma_p^0 W_0} \right]^{\frac{1}{2}}. \qquad (3.40)$$

The spatial inhomogeneity of the distribution of D^0 centers (3.40) causes the formation of a phase-unchanged relative to the intensity distribution (3.1) dynamic polaron lattice, which even at room temperature after shutdown of radiation as a result of the reaction $2D_2^0 \rightarrow D^+ + D^-$ (see Section 2) is erased, and expressions (3.39) and (3.40) at $I(x) = 0$ turn into equations (2.13) and (2.7), determine the uniform distribution of the dark thermal equilibrium concentration of holes and D^0 centers.

Stable after shutdown of radiation (stationary) grating can be obtained if at the recording temperature is the process of "healing" of defects stimulated by radiation as a result of the reaction

$$D^+ + D^- + hv + kT \rightarrow 2D_2^0 + kT \rightarrow D^+ + D^-. \qquad (3.41)$$
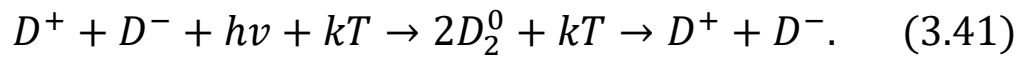
Here D_2^0 corresponds to the state of atoms with a normal bond configuration. To determine the spatial heterogeneity of the distribution of defects $N(x)$, which is caused by these reactions, we use the configuration-coordinate diagram presented in Fig.2.22 and analyzed in Section 2.3.4. In stationary conditions, the system of equations corresponds to the transitions (3.41)

$$W_{13}N_1 = W_{21}N_0 + W_{31}N, \qquad (3.42)$$

179

$$N_1 + N_0 + N = N_2, \tag{3.43}$$

here N_1, N_0 and N the concentration D_2^0, D^0 and $(D^+ + D^-)$ centers, respectively; N_2 – total concentration of atoms involved in transitions (concentration of chalcogen atoms);

$$W_{13} \sim exp\left(-\frac{\omega_{13}}{kT}\right); \;\; W_{21} \sim exp\left(-\frac{\omega_{21}}{kT}\right); \;\; W_{31} \sim exp\left(-\frac{\omega_{31}}{kT}\right)$$

the probability of thermal transitions between states $2D_2^0 \rightarrow D^+ + D^-$, $2D^0 \rightarrow 2D_2^0$ and $D^+ + D^- \rightarrow 2D_2^0$, accordingly.

If we substitute N_0 in (3.42) and (3.43) from (3.40), we obtain

$$N(x) = N_2 \frac{W_{13}}{\left\{ (W_{13} + W_{31}) + (W_{13} + W_{21}) \left[\frac{\gamma_p^-(I(x)q_+ + W_+)}{4\gamma_p^0 W_0} \right]^{\frac{1}{2}} \right\}}. \tag{3.44}$$

It follows from (3.44) that the spatial inhomogeneity in the distribution of defects caused by reaction (3.41) leads to the creation of a "defective" lattice, which is shifted on π relative to the distribution of recording light intensity (3.1) ($N(x)$ more in nodes) and the process of its creation is accompanied by polaron erasure of the lattice.

After shutdown of irradiation the "defective" lattice is rubbed as a result of thermally activated transitions $W_{13}(N_2 - N) \approx W_{13}N_2 \leftrightarrow W_{13}N$, which requires quite high activation energies of $\omega_{13} - \omega_{31} \approx 0{,}6$ eV, and therefore can occur only at high temperatures. At low temperatures (T<120°C), when the reaction (3.41) is not thermally stimulated, this lattice is stable and allows non-destructive reading not only by light from the field of transparency, but also by recording light from the region of self-absorption.

Let us now consider what changes in the distribution of defects will cause the migration of holes and D^0 centers. Spatial heterogeneity of hole distribution (3.39) causes their diffusion, which leads to a violation of local electroneutrality and the origination of an electric field whose intensity $E(x)$. Redistribution of holes stops when the diffusion current is compensated by drift

$$-e^-Д\Delta p = e^-\mu_p p(x)E(x). \tag{3.45}$$

Hole diffusion coefficient Д and their mobility μ_p related by Einstein's relation $Д = \dfrac{\mu_p kT}{e^-}$. Electric field $E(x)$ appears due to the predominance of states D^- in the brighter parts and states D^+ in the less illuminated. Therefore, the Poisson equation has the form

$$div(\varepsilon_0 \varepsilon\, E) = e^-(N_- - N_+). \tag{3.46}$$

The solution of these equations was performed in[361] and for $\Delta N = N_- - N_+$ received

$$\Delta N = \frac{\varepsilon\varepsilon_0 I_0 q_+ \cos\dfrac{2\pi}{d}x \left[I_0 q_+ \left(\cos\dfrac{2\pi}{d}x + \sin\dfrac{2\pi}{d}x + 1\right) + 2W_+\right]}{2e^2[I(x)q_+ + 2W_+]^2}. \tag{3.47}$$

Size ΔN is a bipolar lattice[203] and, as follows from (3.47), it is not shifted relative to the intensity distribution (3.1), the lattice that forms it. After cessation of irradiation, the magnitude of the activation energy of lattice abrasion is determined by the thermal emission of holes from the D^+ centers and is $E_{V_0} + \dfrac{U}{2}$, and according to estimates of CGS of different compositions is from $1\ eV$ to $1,2\ eV$ (see Section 2). Non-destructive reading of the bipolar lattice is possible with light, which does not lead to photocurrent due to nonequilibrium holes. Such conditions are

sufficiently satisfied by light from infrared (IR) spectral regions ($\lambda >$ $650\ nm$). Light from the region of self-absorption ($\lambda < 650\ nm$, Fig.2.18) creates a photocurrent, which leads to a relatively rapid abrasion of the lattice. Thus, being thermally stable, the bipolar lattice in the CGS composition *As-S* unstable to optical reading by light from the region of self-absorption.

A completely different situation is observed if the D^0 centers are involved in diffusion. Diffusion D^+ and D^- centers are not considered by us, as their diffusion requires a fairly large thermal activation energy (approximately 1,5 eV). It occurs intensively at temperatures close to the softening temperature T_g of the material and can only provide mashing of the lattice. The diffusion of the D^0 centers requires much less thermal activation energy and therefore at recording temperatures lower T_g, the lattice formation will be determined mainly by the diffusion of the D^0 centers. Unlike holes, the D^0 centers are neutral and their diffusion caused by the inhomogeneity of distribution (3.40) does not lead to a violation of local electroneutrality and the origination of an electric field that compensates for the diffusion current drift.

In this case, the diffusion of the D^0 centers will occur until their concentration becomes the same throughout the sample $N_0(x) =$ $const = N_{0_{S\text{T}}}$. Establishing a homogeneous distribution $N_{0_{S\text{T}}}$ will lead to a violation of homogeneity in the distribution of defects $N(x) = const$. This is due to the fact that the change in the rate of optical generation of D^0 centers (3.34) due to the inhomogeneities of photoexcitation (3.1) should be compensated by changing the rate of their thermal generation,

and this is possible if there is a change in the concentration of defects N. The spatial distribution of defects $N(x)$ required to maintain the concentration of D^0 centers is the same throughout the sample in the presence of inhomogeneity of optical generation of D^0 centers, can be determined by substituting in formula (3.40) the concentration of D^0 centers $N_{0_{ST}}$, which is established by diffusion.

The distribution (3.48), as well as (3.44), creates a "defective" lattice shifted on π relative to (3.1), and the process of its creation is accompanied by the erasure of the polaron lattice. At temperatures T<120°C, when the reaction (3.36) is not thermally stimulated, this lattice, as well as (3.44), is thermally and optically stable. These lattices differ only in the mechanism of their formation.

Spatial heterogeneity in the distribution of defects (3.40), (3.44), (3.47) and (3.48) leads to modulation of the absorption coefficient α and refractive index $n = \sqrt{\varepsilon}$. For the edge of self-absorption in systems *As-S* responsible level-zone transitions (3.35) (see Section 2.2.1). Therefore, the amplitude component in the region of the self-absorption edge is related to the spatial distribution of the absorption D centers and the modulation of the local change in the absorption coefficient caused by the heterogeneity of their distribution (see Section 2.3.4) has the form:

$$\Delta\alpha(x) = \left(q_0 - \frac{q_+ + q_-}{2}\right)N_0(x) + \frac{q_+ + q_-}{2}(N(x) - N_T)$$
$$+ (q_- - q_+)\Delta N(x). \tag{3.49}$$

Here N_T – thermally equilibrium concentration D centers, which can be determined from (3.44) provided that $I(x) = 0$; q is the cross section

of the capture of the photon by the D center in the charge state, with the corresponding lower index ($q_0 > q_- > q_+$).

The phase component associated with the change in relative dielectric constant ε is due to the polarization (P_+, P_- and P_0) of positively (D^+) and negatively (D^-) charged polarons, as well as electrically neutral polaron (D^0), respectively.

$$\Delta\varepsilon(x) = \left(P_0 - \frac{P_+ + P_-}{2}\right) N_0(x) + \frac{P_+ + P_-}{2}(N(x) - N_T)$$
$$+ (P_- - P_+)(N_- - N_+)(x) \qquad (3.50)$$

Polarization of polaron P includes polarization not only of the D center itself, but also of atoms of its nearest environment, which, due to changes in the charge state of the D center is displaced [84, 160, 161], which leads to changes in length and spatial orientation of bonds between them and, consequently , to change the polarization of this area. Therefore, the phase component of the lattice consists not only of dispersion refraction, corresponding due to the Kramers-Kronig ratio of the absorption bands of the D centers, which mean the amplitude component of the lattice in the region of the self-absorption edge, but also the atoms of the D center. This leads to the fact that with relatively small amplitude modulation in the region of the self-absorption edge, the change in the refractive index in this region can reach quite large values $\Delta n \sim 0{,}2 - 0{,}3$ [154] and the lattice will be predominantly phase.

Let us now determine experimentally the kinetics of change $\Delta\alpha$ and Δn in the process of high-temperature lattice recording As-S and on the basis of the obtained results we will find out which of the above

mechanisms is implemented in the case of the material used *As-S*. To solve this problem, we present $\Delta\alpha(x)$, $\Delta n(x)$ in the form

$$\Delta\alpha(x) = \overline{\Delta\alpha} + \Delta\alpha_0 \cos\left(\frac{2\pi}{d}x + \Delta\psi_\alpha\right),$$

$$\Delta n(x) = \overline{\Delta n} + \Delta n_0 \cos\left(\frac{2\pi}{d}x + \Delta\psi_n\right),$$

here $\overline{\Delta\alpha}$ and $\overline{\Delta n}$ – the average volume of changes in the coefficient of absorption and refraction; $\Delta\alpha_0$ and Δn_0 – the amplitude of their modulation; $\Delta\psi_\alpha$ and $\Delta\psi_n$ – phase shifts, respectively, of the amplitude and phase components of the lattice relative to the recording interference pattern (3.1). As follows from (3.49) and (3.50), the phase shift $(\Delta\psi_\alpha - \Delta\psi_n)$ between $\Delta\alpha(x)$ and $\Delta n(x)$ can be equal to 0 or π. Since our measurements are related to the long-wavelength region of the spectrum from the edge of self-absorption, and in this region the increase $\Delta\alpha(x)$ is accompanied by an increase $\Delta n(x)$, then $\Delta\psi_\alpha = \Delta\psi_n = \Delta\psi$.

In this case, the values $\overline{\Delta\alpha}, \Delta\alpha_0, \Delta n_0$ and $\Delta\psi$ are measurable according to the method proposed by us in [191, 204] which is described in Section 3.2.2. This method is based on the fact that in the process of recording the lattice by two converging beams of light of different intensities I_0 the dependence of intensities of the light beams which have passed through a lattice is analyzed I_1 and I_2 from artificially introduced phase mismatch $\Delta\varphi$ two lattice-forming beams of light due to a short-term (compared to the recording time of the lattice) phase change of one of the incident beams (for example, by means of a mirror mounted on a piezoceramics). Then the total phase shift of the lattice relative to the interference pattern is $\Delta\psi + \Delta\varphi$, and the values I_1 and I_2 are given by the expressions:

$$I_1 = I_0 exp\left(-\frac{\overline{\Delta\alpha}L}{\cos\theta}\right)[ch2v_a - sh2v_a\cos(\Delta\psi + \Delta\varphi) - \sin v\sin(\Delta\psi + \Delta\varphi)],$$

$$I_2 = I_0 exp\left(-\frac{\overline{\Delta\alpha}L}{\cos\theta}\right)[ch2v_a - sh2v_a\cos(\Delta\psi + \Delta\varphi) + \sin v\sin(\Delta\psi + \Delta\varphi)],$$

here $v = \dfrac{2\pi\Delta n_0 L}{\lambda\cos\theta}$; $v_a = \dfrac{\Delta\alpha_0 L}{2\cos\theta}$.

If now $\Delta\varphi$ varies from 0 to 2π, and signals from photodetectors that record intensities I_1 and I_2 are fed, respectively, to the inputs x and y the oscilloscope, then the oscilloscope beam will describe the ellipse (Fig.3.7). Measuring the magnitude of the semiaxes "a" and " b " and shift "x_0" the center of this ellipse relative to the point $I_1 = I_2 = 0$ allows you to determine the amplitude v_α of these measured values and phase modulation v, as well as the change in the average absorption coefficient $\overline{\Delta\alpha}$ in the lattice.

Shift $\Delta\psi$, registered by the lattice relative to the recording spatially stable interference pattern, it is possible to determine at a time when artificial discrepancies between them are absent ($\Delta\varphi = 0$). In this case, the oscilloscope beam is at some point in the ellipse (for example, at point 3, (Fig.3.7)), the coordinates of which x_t and y_t can be calculated by formulas

$$x_t = -\sqrt{2}I_0 exp\left(-\frac{2\overline{\Delta\alpha}L}{\cos\theta}\right)sh2v_a\cos\Delta\psi,$$

$$y_t = -\sqrt{2}I_0 exp\left(-\frac{2\overline{\Delta\alpha}L}{\cos\theta}\right)\sin 2v\sin\Delta\psi.$$

From here

$$\Delta\psi = arctg\left(\frac{y_t}{x_t}\frac{a}{b}\right). \qquad (3.51)$$

186

From (3.51) it follows that at point 1 (Fig.3.7) $\Delta\psi = 0$, at point $2 - \Delta\psi = \pi$.

High-temperature recording in As_2S_3 begins at a temperature of $\sim 100°C$ and is characterized by the following properties:

a) value $\Delta\alpha_0$ and $\overline{\Delta\alpha}$ increases in the process of recording (Fig.3.10, a);

b) during the entire recording time t, the point on the oscilloscope screen reproduces the position of the end of the vector I in position 1 (Fig. 3.7), and, therefore, the resulting grating is not shifted relative to the intensity distribution of its recording light ($\Delta\psi = 0$);

c) the duration of erasing the grating at the recording temperature of 1–2 minutes, at room temperature the grating is thermally stable, although it is easily erased in the case of its illumination with light from the region of intrinsic absorption of material (optical instability);

d) the lower limit of the temperature range at which recording begins (100°C) corresponds to the lowest temperature for establishing the thermodynamic equilibrium of the reaction (3.35) [86, 205];

e) the activation energy of the record is equal to $0,35 \pm 0,05$ eV, which is, in full accordance with formula (3.40), about half the energy from the level of the D^0 center to the valence band of $\frac{E_{V_0}}{2} = 0,3 \div 0,4$ eV;

e) for emerging gratings $\overline{\Delta\alpha} \approx \Delta\alpha_0$ (Fig.3.10, a).

These properties indicate that in this case there is an unbiased with respect to the intensity distribution of the recording light polaron and bipolaron lattice with the characteristics described by formulas (3.40) and

(3.47), as well as the first and third terms in formulas (3.49) and 3.50). Comparison of values $\overline{\Delta\alpha} \approx \Delta\alpha_0$ allows us to establish that almost all nonequilibrium D^0 centers formed under the action of light are involved in the formation of the lattice.
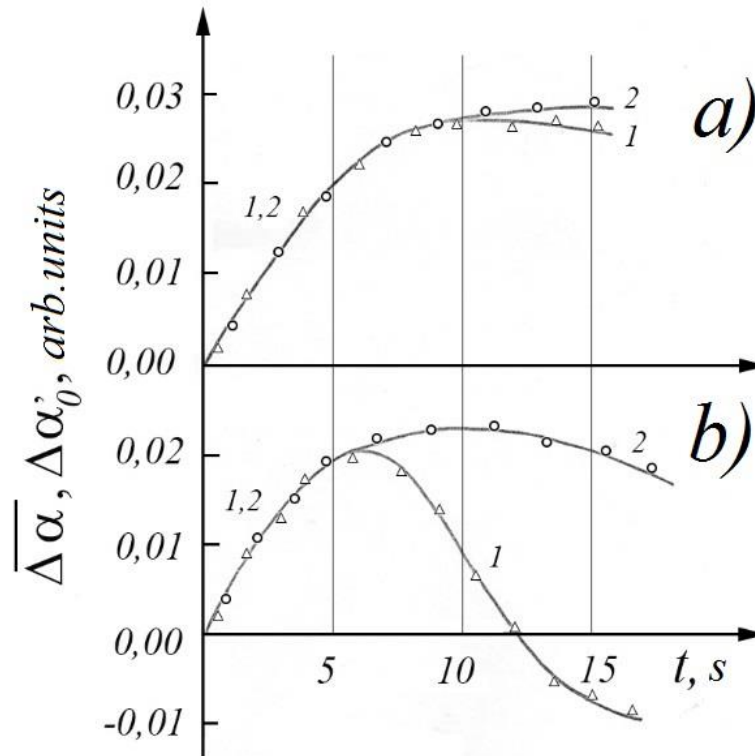
Fig.3.10. Kinetics of change $\Delta\alpha'_0$ (1) and $\overline{\Delta\alpha}$ (2) when recording a three-dimensional lattice in As_2S_3 by He-Ne laser radiation for T (°C): a) – 100; b) – 150. $\Delta\alpha'_0 = \Delta\alpha_0 \cos\Delta\psi$; $\Delta\alpha_0 > 0$, $\cos\Delta\psi = \pm1$.

As the recording temperature increases (T>120°C), the grating begins to acquire the properties described by the second term in formulas (3.49) and (3.50). This, above all, comes from a complex type of dependence $\Delta\alpha_0$ on t and divergence of values $\overline{\Delta\alpha}$ and $\Delta\alpha_0$ in the later stages of recording (Fig.3.10, b). Initially, the D^0 centers responsible for increasing the average absorption and formation of the polaron lattice,

which is not shifted relative to the intensity distribution of the recording light, are formed (the point on the oscilloscope screen displaying the vector I position is at point 1 shown in Fig. 3.7 ellipse). Then the resulting lattice is erased and the resulting lattice, the amplitude and phase components of which are shifted on π by (point on the oscilloscope screen is moved to the recording process from position 1 to position 2 (Fig.3.7)). For offset lattice at temperature below T<120°C (reactions (3.36) and (3.41) are not thermally stimulated) high thermal and optical stability is observed, and diffraction efficiency reaches 90% and is mainly phase in nature.

When forming an offset lattice as a result of erasing polaron (T>120°C) $\overline{\Delta\alpha} > \Delta\alpha_0$ (Fig.3.10, b). This inequality is satisfied only in the case of diffusion of the D^0 center. Hence, the defining mechanism of the formation of the displaced lattice is the diffusion of the D^0 center. To further confirm this conclusion, the following should be noted. If the abrasion of the polaron lattice occurs according to reaction (3.41), the condition $\overline{\Delta\alpha} = \Delta\alpha_0$ would have to be met, and the decrease in the amplitude of modulation of the absorption coefficient $\Delta\alpha_0$ is accompanied by a decrease $\overline{\Delta\alpha}$ not observed in the experiment. As follows from the results of experiments, when erasing the polaron lattice ($\Delta\alpha_0$ decreases), the value $\overline{\Delta\alpha}$ changes slightly (Fig.3.10, b), and even with the complete destruction of the polaron lattice ($\Delta\alpha_0 = 0$) the concentration of nonequilibrium D^0 centers responsible for $\overline{\Delta\alpha}$, reaches a significant value in comparison with the thermal equilibrium concentration of these centers. The process of erasing the polaron lattice is significantly

189

accelerated by reducing the period of the recorded lattice, which also indicates the diffusion mechanism of the formation of the displaced lattice.

Thus, in full accordance with the proposed mechanisms at different stages of high-temperature recording in As_2S_3, we observed all types of lattices, the parameters of which fit into expressions (3.49) and (3.50), and the values of $N_0(x), N(x)$ and $\Delta N(x)$ – formulas (3.40), (3.47) and (3.48).

The results described above are relevant to the case of stoichiometric samples of As_2S_3. For samples $As\text{-}S$ non-stoichiometric composition with excess sulfur can be recorded, the mechanism of which is from the mechanisms described previously. The specified record occurs in annealed samples $As\text{-}S$ at a temperature of $\approx 60°C$ and is characterized by the following properties:

a) in the process of recording the value $(\Delta\alpha_0)$ increases;

b) the amplitude and phase components of the lattice are not shifted relative to the distribution of light intensity that creates the lattice;

c) the lattice formed during recording is characterized by high optical stability when read by light from the region of intrinsic absorption of the material;

d) non-destructive reading can be carried out not only at the recording temperature, but also at higher temperatures;

e) thermal mashing of the lattice begins at T>110°C;

e) there is a clear upper limit of the record $(T_{lim} \approx 115°C)$, exceeding which by a small amount $(\sim 1°C)$ leads to an abrupt termination of the record;

g) the value T_{lim} increases with increasing composition of arsenic in the samples.

These results allow us to conclude that in the considered samples the optical recording is determined by the creation of microscopic inclusions of the sulfur phase and occurs due to the diffusion of D^0 centers that are excess sulfur atoms in the free state C_0^0. At a temperature of ~115°C (melting point of sulfur [206]) clusters of sulfur (Fig.3.11, b, state 4) are destroyed, creating free sulfur atoms (Fig.3.11, and state 1), which have high mobility.
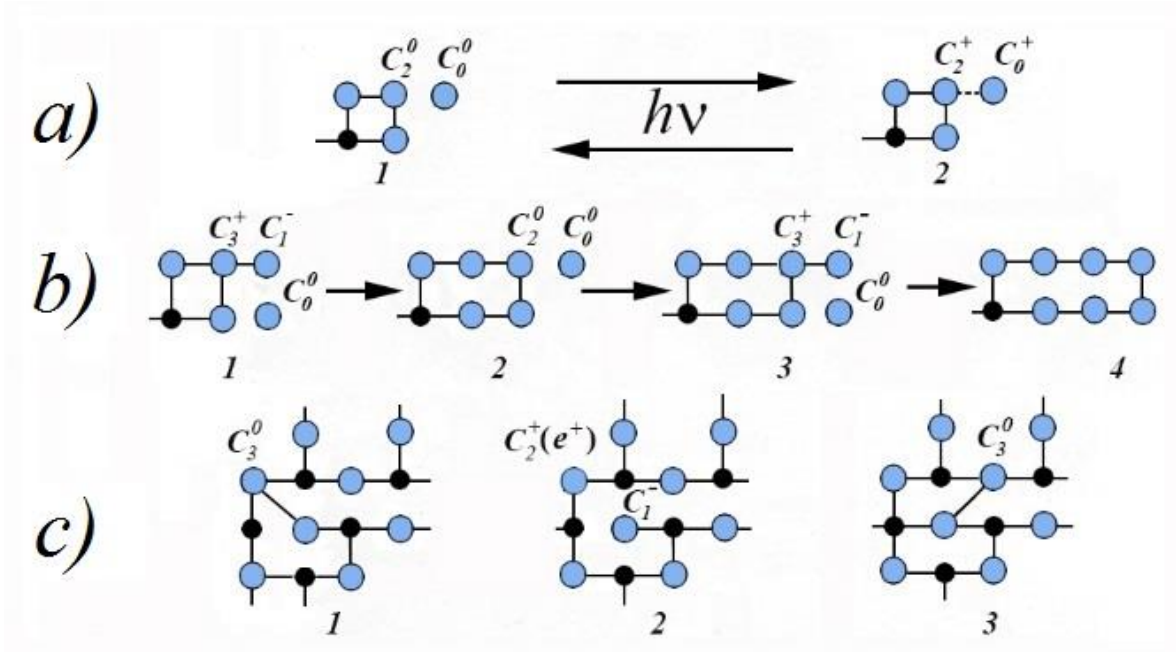
Fig.3.11. Creation of sulfur clusters as a result of diffusion of D^0 centers (a and b) in the compounds of the composition As-S with excess sulfur and the mechanism of diffusion D^0 centers in As_2S_3 compounds (c). The solid lines show the usual covalent bonds between arsenic ($\bullet$) and sulfur () atoms. The dotted line indicates the localized exciton.

The configuration C_0^0 is unstable and with decreasing temperature creates with twice coordinated sulfur atoms of regular structure C_2^0

191

defective pair $(C_2^+ - C_0^-)$ – localized exciton (Fig.3.11, a, state 2). In the absence of light from the region of self-absorption, this state at a temperature near room temperature can persist for a long time. Under the action of irradiation, such an exciton is unstable and after the capture of nonequilibrium electrons and holes is destroyed with the restoration of the original state (Fig.3.11, a, state 1).

Localized exciton can turn into a defective pair consisting of a sulfur atom in unusual bond configurations $(C_2^+ - C_0^-)$ (Fig.3.11, b, state 1), which, in turn, can be the nucleus for the subsequent addition of a free sulfur atom C_0^0 and the gradual creation sulfur cluster (Fig.3.11, b).

Based on these data, it is possible to propose the following mechanism of holographic recording in such compositions. After annealing at the recording temperature (T≈60°C) defects in the sample are in state 2 (Fig.3.11, a). Then under the action of light in places where $I(x) \neq 0$ the process takes place, as shown in Fig.3.11, a the lower arrow.

The sulfur atoms C_0^0 created in this case diffuse in the region of maximum illumination and here on defective pairs $(C_3^+ - C_1^-)$, as on embryos, clusters of sulfur are created, as shown in Fig.3.11, b. This process occurs until all free sulfur atoms in the entire volume of the sample do not form clusters of sulfur, the largest number of which is contained in the minimum illuminance. Sulfur clusters are optically unstable and are destroyed only thermally at T≈115°C [206]. It is known [207] that if in the system *As-S* the sulfur content increases, the self-absorption edge shifts toward short wavelengths, and the refractive index in this region decreases. Therefore, when excess sulfur atoms diffuse from the maximum to the minimum illuminance regions in the recording

process, these regions increase and decrease the absorption coefficient and refractive index, respectively, in these regions for light waves from the region of the self-absorption edge and above. This leads to the creation of a lattice that is not shifted relative to the light intensity distribution (3.1), which forms such a lattice, which is confirmed by our research.

At the end of this section we will summarize.

The mechanism of high-temperature non-destructive holographic recording in the *As-S* system determined by the diffusion of D^0 centers . In the sample with a predominant sulfur content, such defects are excess sulfur atoms in the free state C_0^0, and in *As₂S₃* regular sulfur atoms in an unusual bond configuration C_3^0 and C_1^0. Due to this mechanism, the diffusion of D^0 centers in *As₂S₃* differs significantly from diffusion C_0^0 and is associated with the interconversion of defects C_3^0 and C_1^0. This transformation of defects is more energetically advantageous if it occurs due to the ejection and capture of holes by defects C_3^0 and C_1^0 (Fig.3.11, *c*).

$$C_3^0 \rightarrow C_1^- + e^+ \rightarrow C_1^0 \rightarrow C_3^0.$$
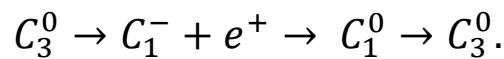
Direct conversion of defects C_3^0 and C_1^0 requires much more energy (see Section 2.1, Fig.2.4), so the diffusion of D^0 centers in *As₂S₃* occurs at temperatures when a dynamic equilibrium is established between the capture and release of the hole in the reaction (3.35) (T>100°C). In the case of inhomogeneous photoexcitation, the result of diffusion of D^0 centers in *As₂S₃* is a violation of the thermodynamic equilibrium of the distribution of defects (*D* centers), and in the case *As-S* with excess sulfur

– the origination of inhomogeneity in the distribution of sulfur phase inclusions.

The diffusion mechanism of high-temperature holographic recording in monolithic samples is proposed [201, 202] is fundamentally different from the mechanisms of local recording, which is implemented in film samples of the composition *As-S* and can be interpreted using coordinate configuration diagrams [70, 152]. This allows a new approach to the question of further ways to improve and prospects for the use of such materials for three-dimensional holographic recording.

3.2.4. Holographic record in additively colored AHCs.

AHC colouring can be performed in two ways – photochemical and additive [117]. In the process of photochemical colouring, the crystal is exposed to ionizing radiation (UV, *X*-ray, α-, β-, γ-beam), which leads to the creation of electronic and hole centers. Holographic recording using such centers [37, 40, 44, 211–214] is characterized by very low optical stability, as they are more efficient recombination processes that overwrite the record. To avoid this, the crystals must be cooled during reading (up to –80°C). A significant disadvantage of such systems is also "fatigue" [211, 215] and the fact that does not provide reversibility of the record. In our work, we used an additive method that gives a stable color. The color centers obtained in this way may be inverse, multiple, virtually losslessly photothermally transformed into other centers. In this case, the crystal is heated in alkali metal vapor at high temperature, due to which its stoichiometric excess is created. As a result, the migration of anionic vacancies and electrons begins in the middle of the crystal, which create *F*-centers, and new layers of the crystal build up on the surface. To

achieve sufficient ionic conductivity, the temperature must be at least 500°C. Hole centers are not formed and the color is stable.

The greatest interest for holographic recording in additively colored AHCs are: photothermal transformation of light-sensitive color centers based on impurities; optical reorientation of anisotropic color centers with dichroism; photothermal transformation of F centers into more complex optically stable color centers.

The best results using light-sensitive color centers based on impurities were achieved in $NaCl$ crystals doped with $MnCl_5 \cdot 4H_2O$ [216–218] and $NaNO_3$ [219–222]. The absorption spectra of such crystals are characterized by strong absorption in the ultraviolet region ($\lambda \approx 300$ nm) and lack of absorption in the visible region (Fig. 3.12, curve 1).
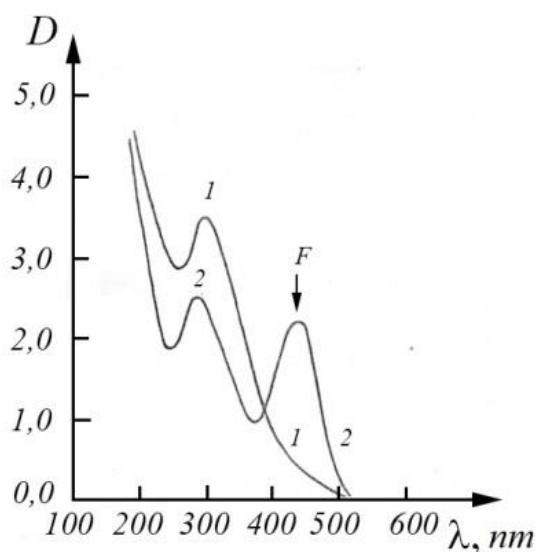

Fig.3.12. Absorption spectra of crystal $NaCl$: $MnCl_2 \cdot 4H_2O$.

1 – after additive coloring.

2 – after irradiation with ultraviolet light ($\lambda=200$–350 nm) at room temperature.

Irradiation of crystals with ultraviolet light in the range of 200–350 *nm* leads to the destruction of impurity centers and the creation of p −centers that absorb in the visible region ($\lambda \approx 465$ *nm*) (Fig. 3.12, curve 2). In the wavelength range $\lambda > 550$ *nm*, such a record is mostly phase, read-resistant, and, as theoretical estimates have shown, DE lattice in this area can reach 60% [54].

A constraining factor in the use of this photoconversion for holographic recording at present is the lack of available coherent radiation in the absorption region of these impurity centers ($\lambda < 350$ *nm*) and therefore the practical implementation of such photoconversion is still ahead.

As for the recording method [224–230], based on the properties of color centers to change orientation under the action of polarized light, the interest in it is mainly due to the fact that the recording and erasing process in this case are purely optical and no fatigue observed. In addition, the reorientation of color centers requires much less energy than their creation and destruction, so it is possible to achieve higher recording speeds. This can be explained by the fact that the surrounding vacancies are involved in the reorientation [231]. A significant disadvantage of this technique when using it for the manufacture of three-dimensional diffraction grating is the need to record and read light of different wavelengths, as the carriers here are the most light-sensitive centers, as well as thermal reorientation of centers over time, that leads to the spontaneous rubbering of the lattice.

Holographic recording using the photoaggregation reaction F–centers [217, 218, 232–237] when it is carried out in the region of elevated temperatures (T>150°C) is thermally and optically stable. The main

disadvantage of this system is that the absorption of photosensitivity centers (*F*-centers) and photolysis products (*M*-, *R*- and *X*-centers) is brought to the visible region and spectrally overlap with each other [238]. Therefore, holographic gratings in the entire visible optical range are mainly amplitude in nature and, consequently, have a small DE (not more than 16%).

The solution to this problem is possible if the products of photolysis use centers that do not absorb in the visible region of the spectrum. We were able to implement the following conditions for an additively colored *KCl:Ca:OH* crystal with different ratios of ingredients [250]. The process of destruction of *F*-centers in such crystals at T>150°C is accompanied by the creation of complexes of *CaOH* or *Ca(OH)*$_2$ which absorb in the IR region ($\lambda \approx 2800$ *nm*) and enlightenment in the visible region as a result of such transformation reaches more than 90% [96].

The next way to eliminate the shortcomings inherent in this method of recording, is to find conditions that get rid of the remnants of light-sensitive *F* −centers in the lattice. This problem was fully solved for the *F* − *X* conversion of both pure and doped impurities in *KCl* and *NaCl* crystals [197, 239, 240–243], and failed in impurity-free *KBr* crystals [244, 245]. To do this, the recording of He-Ne laser radiation must be performed at a temperature of 270–320°C. After recording in the absorption spectrum of such a lattice there are no *F*-centers and there is only *X* -band, due to the centers of the colloidal type (Fig.3.13, [246, 247]), which at room temperature are not destroyed by light even at high power (more than 100 *W/cm*^{2}), thus providing, in comparison with other materials, very high radiation resistance when reading.

As follows from Fig.3.13, in the region of wavelengths less than 650 *nm* and greater than 800 *nm*, the lattice is predominantly phase and its DE reaches about 40% [248]. Abrasion of the grid and preparation for the next recording is carried out by heating the crystal to 450°C and rapid cooling to room temperature.

To determine the physical processes in the crystal during recording and the nature of the recorded lattice, studies of the kinetics of changes in the amplitude of modulation of the absorption coefficient $\Delta\alpha_0$ and refractive index Δn_0, as well as the variance of these parameters in a wide spectral range according to the method described in Section 3.2.2 [204, 249] .
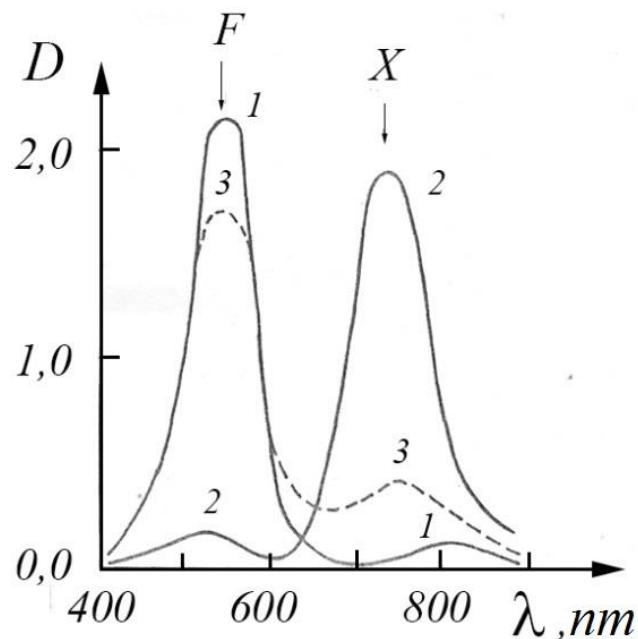
Fig.3.13. The absorption spectra of the *KCl* crystal before and after recording at T=270°C (taken at room temperature).

1 - hardened crystal before recording;

2 - absorption spectrum of the exposed area;

3 - absorption spectrum of the unexposed part of the sample.

Studies have shown that the lattice recorded in *KCl, NaCl* and *KBr* crystals of the exta pure brand is characterized by different dependences $\Delta\alpha_0$ and Δn_0 on the exposure time t, as well as the maximum values of DE (Fig.3.14). From Fig.3.14 it is seen that the recording process for these crystals can be divided into two stages.
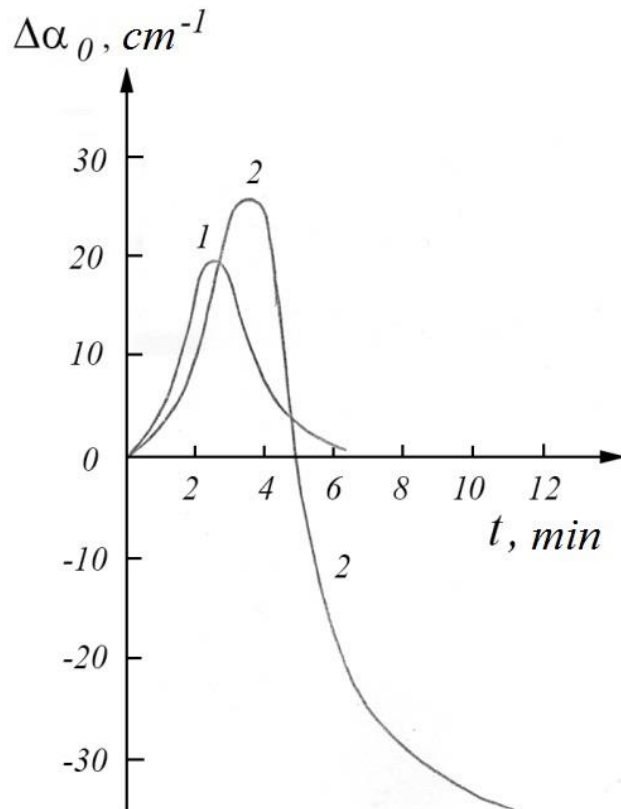
Fig.3.14. Kinetics of change of amplitude of modulation of absorption coefficient ($\Delta\alpha_0'$) in the process of recording lattice in crystals: $1 - KBr$; $2 - KCl$.

First, a positive lattice is formed in the crystal ($\Delta\alpha_0' > 0$), which reaches the optimal parameters, then, by creating *X*-centers in the entire volume of the crystal in the region of maxima and minima of the spatial interference pattern, is completely erased. This is due to the predominant role of the diffusion process of photothermal ionization products *F*-

199

centers (electrons and anionic vacancies) from unlit areas of the lattice in the unlit compared with the diffusion of F-centers from unlit areas in the illuminated [242, 247, 248].

$$\Delta\alpha_0' = \Delta\alpha_0 \cos\Delta\psi; \quad \Delta\alpha_0 > 0, \quad \cos\Delta\psi = \pm 1.$$

In *KBr* crystals, the record ends there. In crystals of *KCl* and *NaCl* then comes the second stage, in which a negative lattice is formed, the spatial distribution of the absorption coefficient in which is shifted on π relative to the distribution of the intensity of the recording light (3.1) ($\Delta\alpha_0' < 0$). The lattice reaches the limiting characteristics in such a recording when only one absorption band is observed in its spectrum due to X-centers[246] (Fig.3.13, 3.15). Comparison of the amplitude modulation ΔD_0 and the average value of the optical lattice density $\overline{D}$ for gratings with the achieved maximum DE revealed a good coincidence of their values $\Delta D_0 \approx \overline{D}$ (Fig. 3.15) throughout our spectral region (400–800 *nm*).
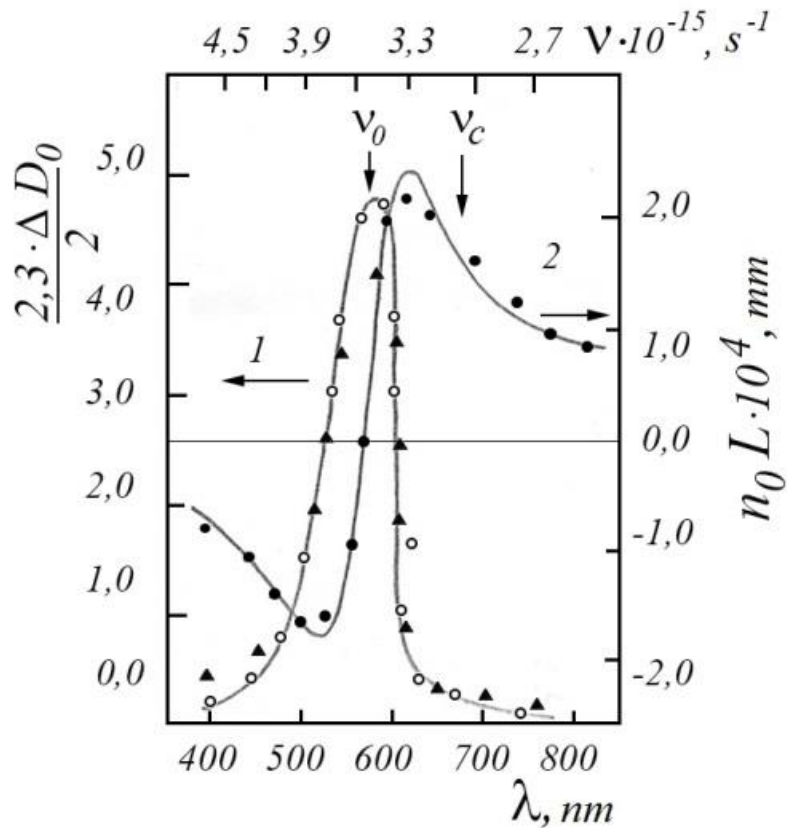
Fig.3.15. Dispersion ΔD_0, Δn and $\overline{D}$ lattice (*NaCl* crystal).

Experimental values: $\circ - \Delta D_0$; $\bullet - \Delta n$; $\blacktriangle - \overline{D}$.

Calculated curves according to the formulas, respectively: 1 – (3.53); 2 – (3.54).

Illumination of such gratings with a recording uniform beam of light with equal energy at the recording temperature did not lead to mashing of the array. These facts indicate that the modulation α of the negative lattice is due to the absorption of X-centers, the concentration of which is maximum in the minima of the recording interference pattern. In the areas of maximum illumination of the interfering waves, there is a destruction of X-centers and in these areas there are no color centers (uncolored crystal).

The reason for the negative lattice in *KCl* and *NaCl* crystals is the presence of acceptor properties in *X*-centers (see Section 2.4.4). In *KBr* crystals, the *X* −centers do not have this property. Non-equilibrium electrons located at *X*-centers in the regions of minimum illumination of the interference pattern charge this region negatively and thus stimulate additional growth of *X*-centers in those regions due to drift diffusion of anionic vacancies under the action of an electric field from areas of maximum illumination.

As a result, in places of maximum illumination, the thermodynamic balance between *F*- and *X*-centers and *X*-centers in these areas are destroyed. Such diffusion in optimal conditions (temperature, exposure) can lead to complete destruction of *X*-centers in places of maximum illumination. Of course, these processes determine the conditions for obtaining optimal holographic characteristics of DE, diffraction sensitivity, non-destructive reading and so on. For example, with "frozen" diffusion (T<220°C) there is a transformation of *F*-centers into *X*-centers under the action of light. However, the DE of the recorded lattices was small (less than 1%) and in the absorption centers for these lattices the absorption characteristic of *F*-centers was found. Obviously, the local equilibrium of the ratio between the concentration *F*- and *X*-centers will depend on the intensity of the recording light. Therefore, the maximum achieved DE will depend on both the exposure during recording and the radiation power, as observed in the experiment. In particular, at low light outputs, recording is virtually non-existent, no matter how large the exposure.

Failure to comply with the law of interdependence leads to deviations from the sinusoidal form of modulation of lattice parameters. It is known that the limit value of DE for a three-dimensional amplitude sinusoidal lattice is 3,7% [16]. However, if we calculate the DE, using the data obtained from measurements $\Delta\alpha_0$ and Δn_0 in the recorded gratings, the contribution of amplitude modulation in the total value of DE is ~6% [198, 251].

This result indicates a deviation of the lattice profile recorded from the sinusoidal shape[197,252]. When illuminating such gratings at angles 2θ and 3θ diffraction maxima were observed with intensities of 0,2 and 0,03, respectively, for intensity θ, which is equivalent to the presence of gratings with frequencies multiples of the fundamental. The effect of such gratings does not affect the diffraction at Bragg angle grating in the case of thick lattices [176, 180, 253] and, therefore, the above consideration in the assumption of a sinusoidal lattice is correct. The restored lattice profiles [197], normalized by the average absorption, are shown in Fig.3.16.

Since Fourier synthesis (ie restoration of the lattice profile) is an incorrect task, the measurement error $\propto_m$ was determined and appropriate regularization was performed [394].
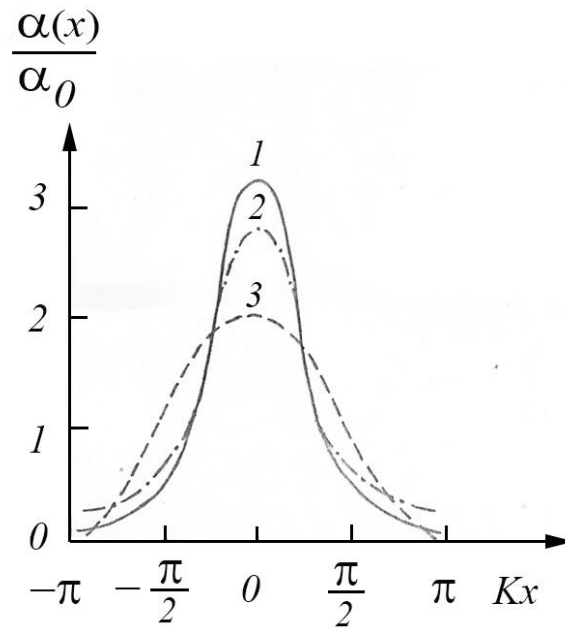
Fig.3.16. Profile of the lattice normalized by the average absorption:

1 – for the *KCl: Na* crystal;

2 – for pure *KCl*;

3 – for an ideal lattice $1 + \cos\left(\frac{2\pi x}{d}\right)$.

When compared with the curve $\left(1 + \cos\left(\frac{2\pi x}{d}\right)\right)$, the very peculiar nature of the lattice is noticeable – narrow sharp maxima and wide gentle minima with absorption close to zero. This feature (together with the absence of F-bands in the absorption spectrum) clearly indicates the important role of diffusion F -centers in the recording process.

Thus, in the spectral region studied by us (400–800 *nm*) the modulation α of the gratings is due to the absorption of only *X*-centers, the spatial distribution of the concentration of which is in antiphase to the distribution of the intensity of the recording light (3.1). As for the measured value Δn (Fig.3.15), as follows from the relationship Kramers-Kronig; it is determined by the values $\Delta\alpha$ in the wavelength range $(0,\infty)$ and, i.e., is associated with a change $\Delta\alpha$ in the spectral regions not covered

by our measurements. However, to what extent the measured values Δn are determined by the absorption X band, it is possible to find out if the absorption band is approximated to the wavelength range $(0, \infty)$ [159, 395].

It follows from the Kramers-Kronig correlation [396]

$$n^2 - \frac{C}{2\omega}\frac{2,3D}{L} - n_0^2 = \frac{2,3C}{\pi L}\int_0^\infty \frac{2nD(\omega')}{\omega'^2 - \omega^2}d\omega',$$

here; $n = \overline{n} + \Delta nD = \overline{D} + \Delta D$.

Considering that $\Delta n \approx \frac{C}{2\omega}\frac{2,3D}{L} \ll \overline{n}$ and $\overline{n}^2 = n_0^2 +$ $\frac{2.3C}{\pi L}\int_0^\infty \frac{2n\overline{D}(\omega')}{\omega'^2 - \omega^2}d\omega'$, we will receive

$$\Delta n(\omega) = \frac{2,3C}{\pi L}\int_0^\infty \frac{\Delta D(\omega')}{\omega'^2 - \omega^2}d\omega'. \qquad (3.52)$$

A stricter consideration [395] leads to a similar expression. The analysis of variance is carried out ΔD the holograms recorded by us showed that $\Delta D(\omega)$ it is satisfactory to approximate the symmetric Lorentz curve:

$$\Delta D(\omega) = \frac{\Delta D_{max}}{1 + \frac{(\omega_0^2 - \omega^2)^2}{g^2\omega^2}}, \qquad (3.53)$$

here ω_0- frequency, $\Delta D_{max}-$ optical density at maximum, $g-$ half-width of the absorption band: $g = g_1 = 0{,}3 \cdot 10^{15}\ s^{-1}$ at $\omega \leq \omega_0$, $g = g_2 = 0{,}48 \cdot 10^{15}\ s^{-1}$ at $\omega > \omega_0$ (Fig.3.15, curve 1).

Substituting (3.53) into (3.52), we have

$$n(\omega) = \frac{2{,}3C}{\pi L} \left\{ \int_0^{\omega_0} \frac{\Delta D_{max} g_1^2 \omega'^2}{[(\omega_0^2 - \omega'^2)^2 + g_1 \omega'^2](\omega'^2 - \omega^2)} d\omega' + \right.$$

$$\left. + \int_{\omega_0}^{\infty} \frac{\Delta D_{max} g_2^2 \omega'^2}{[(\omega_0^2 - \omega'^2)^2 + g_2^2 \omega'^2](\omega'^2 - \omega^2)} d\omega' \right\}.$$

After integrating this expression and if we take into account that $g_1, g_2 \ll \omega_0$, we get

$$\Delta n(\omega) = \frac{2{,}3C}{2\pi L} \left(\frac{\Delta D_1}{g_1} + \frac{\Delta D_2}{g_2} \right) \frac{\omega_0^2 - \omega^2}{\omega^2}$$

$$+ \frac{2{,}3C}{2\pi L} \left(\Delta D_1 ln \frac{16\omega_0^2}{g_1^2} - \Delta D_2 ln \frac{16\omega_0^2}{g_2^2} \right) \frac{\omega_0^2 + \omega^2}{2\omega_0 \omega^2}$$

$$+ \frac{2{,}3C}{2\pi L} (\Delta D_2 - \Delta D_1) ln \left| \frac{\omega + \omega_0}{\omega - \omega_0} \right|. \qquad (3.54)$$

here $\Delta D_i = \dfrac{\Delta D_{max}}{1 + \dfrac{(\omega_0^2 - \omega^2)^2}{g_i^2 \omega^2}}$.

Figure 3.15 (curve 2) shows the dependence $\Delta n(\omega)$, calculated by (3.54) for $g_1 = 0{,}3 \cdot 10^{15} \, s^{-1}$, $g_2 = 0{,}48 \cdot 10^{15} \, s^{-1}$, $\omega_0 = 3{,}364 \cdot 10^{15} \, s^{-1}$, $\Delta D_{max} = 4{,}3$. As follows from Fig.3.15, the experimental values obtained in accordance with (3.29) fit well into the calculated dependence $\Delta n(\omega)$. Good coincidence was observed in other cases, when the shape of the strip was characterized by others g_1, g_2, ΔD_{max}.

The difference between g_1 and g_2 is due to the fact that the process of recording laser radiation acts on both F-centers and X-centers. Therefore, in addition to the destruction of F-centers, there must be a known phenomenon of selective destruction of X-centers [254, 255]. Thus, after the creation of X-centers, further exposure leads to a noticeable weakening of the long-wavelength edge of their absorption bands and to

the asymmetry of this band. In our case, at a recording temperature of approximately 300°C, band asymmetry was observed at an exposure time of $t>2$ min. At smaller t we get a symmetrical band with $g_1 = g_2 = 0{,}48 \cdot 10^{15}$ s^{-1}.

Thus, the measured values Δn are due only to the absorption band X-centers and are satisfactorily described by equation (3.45). Taking into account (3.45) it is possible to determine the conditions necessary to obtain holograms with high DE, and to determine the role of selective destruction of X -centers.

To determine the quantitative dependence of DE on the magnitude of selective destruction, the latter will be characterized g_1 by a constant g_2 in the formula (3.53).

Consider holograms with the maximum depth of modulation D. Then to calculate the DE in expression (3.20) it is possible to put $\overline{\alpha} = \overline{D} = \Delta\alpha_a = \Delta D$. Characteristic spectral dependences of DE for cases of symmetric $(g_1 = g_2 = 0{,}48 \cdot 10^{15}$ $s^{-1})$ and asymmetric $(g_1 = 0{,}3 \cdot 10^{15}$ s^{-1}, $g_2 = 0{,}48 \cdot 10^{15}$ $s^{-1})$ absorption bands are shown in Fig.3.17.
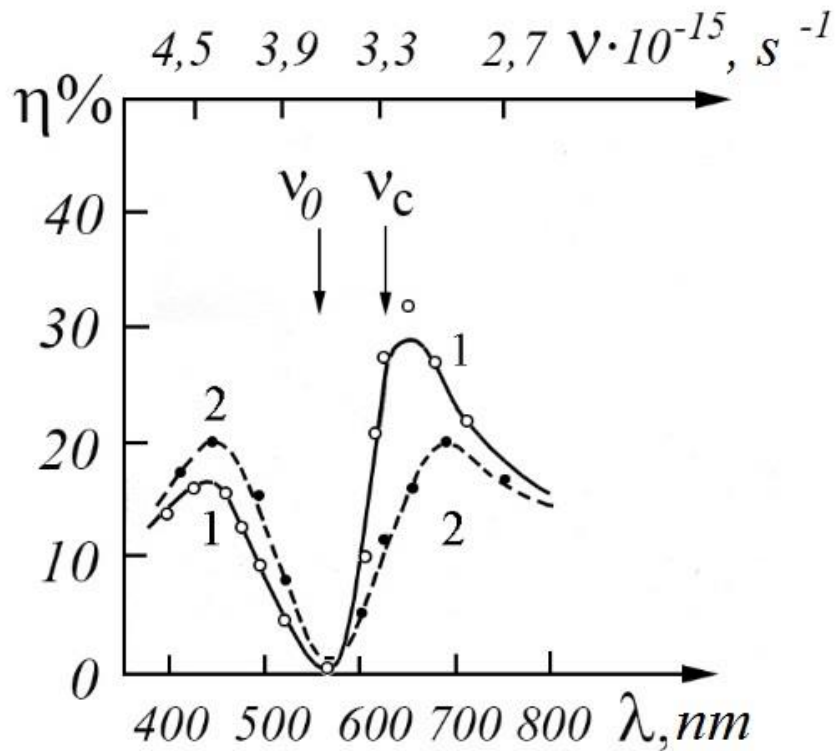
Fig.3.17. Spectral dependences DE lattice. Experimental values η:
● – for a symmetrical band $\Delta D(\omega)$; ○ – for asymmetric band $\Delta D(\omega)$.

Calculated curves for bands $\Delta D(\omega)$,, respectively: 1 – symmetric; 2 – asymmetric.

As follows from Fig.3.17, in the case of an asymmetric band $\Delta D(\omega)$, there is a significant increase in DE in the wavelength range, which corresponds to a smaller value g_1. The reduction g_1 occurs in the frequency range of the recording light ($\omega_c = 2{,}977 \cdot 10^{15}\ s^{-1}$), which is optimal for reading holograms. For the specified reading frequency, at different values ΔD_{max}, the maximum η was determined for a variable g_1 with a typical value $g_2 = 0{,}48 \cdot 10^{15}\ s^{-1}$ (Fig.3.18, curve 2).

From these results it follows that the selective destruction, the effect of which describes the decrease g_1, provides an increase in DE by 10–30% for practically realized values $\Delta D_{max} = 3 - 4$. With increasing

radiation power and exposure, the effect of selective destruction is reduced to a more selective attenuation of the band $\Delta D(\omega)$.
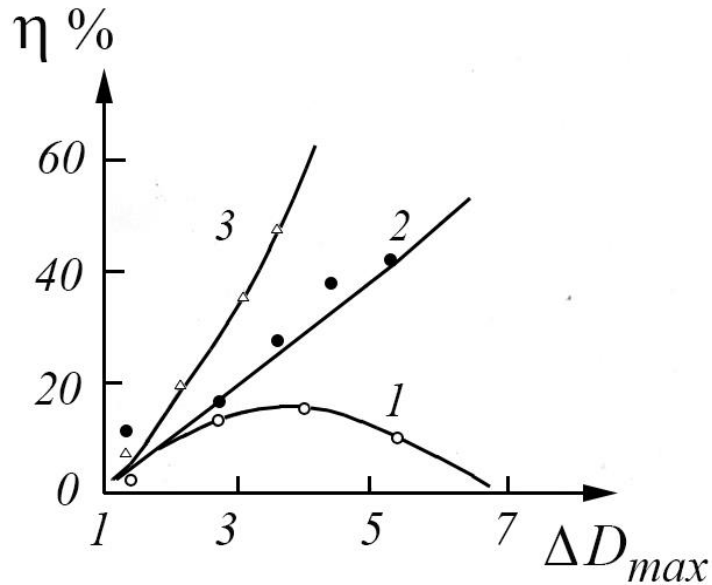
Fig.3.18. Dependence of DE on the amplitude of optical density ΔD_{max} modulation. Experimental values of DE for $\Delta D(\omega)$ in the case of bands: $\circ$ – symmetric; $\bullet$ – asymmetric; Δ – $\Delta D(\omega_c) \approx 0$.

Calculated curves, respectively: 1 – symmetrical; 2 – asymmetric; 3 – $\Delta D(\omega_c) \approx 0$.

Measurement of DE using monochromatic natural light indicates an increase in DE due to strong selective attenuation ΔD, not approximated by an asymmetric Lorentz curve $\Delta D(\omega)$ in the frequency range of the recording light ω_c (Fig.3.17).

The contribution of selective destruction in the increase of DE is easy to estimate for the idealized case (Fig.3.19): $\Delta D(\omega) = 0$ (phase modulation) at $\omega_c - \Delta\omega \leq \omega \leq \omega_c + \Delta\omega$. In another frequency range $\Delta D(\omega)$ is described by formula (3.53).
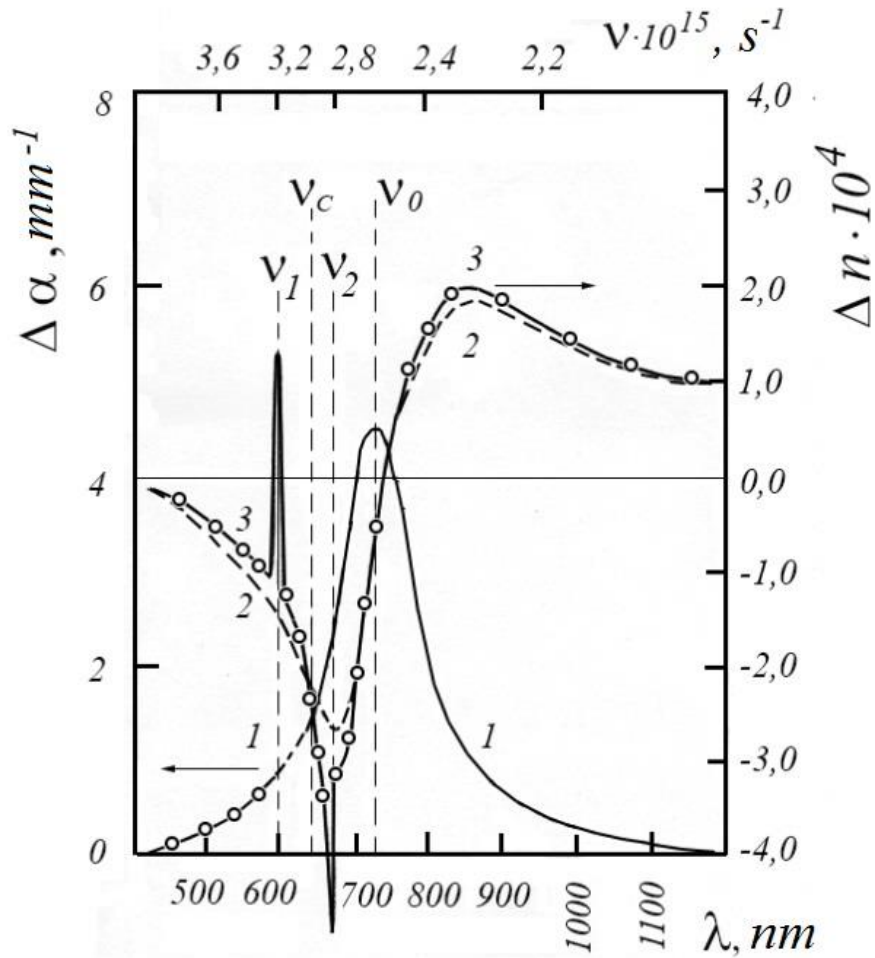
Fig.3.19. Spectral dependences $\Delta n(\lambda)$ in the case of selective destruction of colloidal centers in *KCl*:

1 – spectral dependence $\Delta\alpha(\lambda)$;

2 – spectral dependence $\Delta n(\lambda)$ due to the asymmetric band with $g_1 = 0{,}4 \cdot 10^{15}\ s^{-1}$ and $g_2 = 0{,}3 \cdot 10^{15}\ s^{-1}$ at $\omega_c = 2{,}62 \cdot 10^{15}\ s^{-1}$;

3 – idealized case of complete selective destruction of the band in the frequency range $2{,}817 \cdot 10^{15}\ s^{-1} - 3{,}137 \cdot 10^{15}\ s^{-1}$.

Figure 3.18 (curve 3) shows the calculated values of DE for the case at $g_1 = 0{,}4 \cdot 10^{15}\ s^{-1}$ and $g_2 = 0{,}3 \cdot 10^{15}\ s^{-1}$, $\Delta\omega = 0{,}16 \cdot 10^{15}\ s^{-1}$. The choice of these parameters reflects the quantitative result of strong selective destruction: reduction g_1 and almost complete attenuation

$\Delta D(\omega)$ in the narrow vicinity of the frequencies of laser radiation ω_c. Enhancement of the selective destruction of X-centers is associated primarily with increased illuminance of the crystal during recording. It is possible that the use of more powerful lasers for recording will allow to realize the case of selective complete discoloration ($\Delta D(\omega) = 0$) at the wavelength of the active light (Fig.3.19). Then if the discoloration gap will have steep edges, then at $\Delta D_{max} = 4 - 4,5$ DE it can reach a value of ~60%.

In conclusion, we note that the creation of X-centers under the action of linearly polarized He-Ne laser radiation is accompanied by the appearance of dichroism [400–402] (Fig.3.20) and double beam refraction.

Under the analyzed conditions, ellipsoidal particles formed under the action of recording linearly polarized light may be due to the fact that in the direction of oscillations of the electric vector, particle formation is difficult because, as is known [259], the action of linearly polarized light on a colloidal particle will lead to its destruction in the direction of the electric vector. To clarify the role of anisotropy of X-centers in the formation of phase recording, we recorded the lattices with circularly polarized He-Ne laser light (creation of X-centers in this case does not lead to crystal dichroism). Measurements have shown that the value of the DE of the gratings is practically independent of the polarization of the recording radiation.
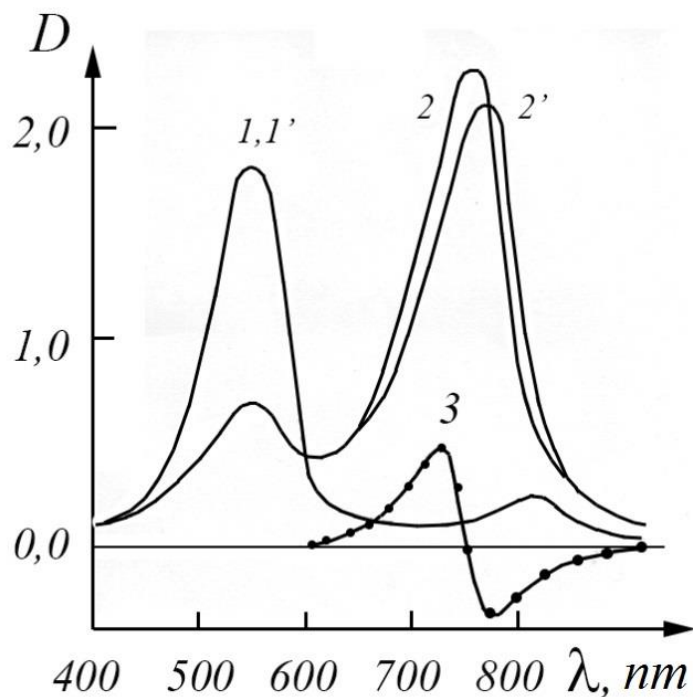
Fig.3.20. The absorption spectra of the *KCl* crystal before (1, 1') and after (2, 2') the recording of the holographic lattice. 1, 2 and 1', 2' are measured, respectively, by linearly polarized light, the electric vector of which is parallel and perpendicular to the electric vector of the recording beam; 3 – dichroism curve (difference of curves 2 and 2').

Thus, the anisotropy observed in *X*-centers formed during the $F - X$ transformation process does not have a significant effect on the phase recording. This is consistent with the above, which assumes that the main contribution to the phase recording is made by the anomalous variance of the refractive index in the area of the absorption band *X*-centers.

We also note the most important results obtained in this section.

Photochromic systems based on $F - X$-transformation of coloring centers in *KCl* and *NaCl* crystals under optimal conditions allows to completely transform *F*-centers into *X*-centers, and the concentration of *X*-centers in the maxima of the interference pattern due to diffusion of *F*-

212

centers in the light gradient will reach almost zero [260, 261]. A necessary condition for this diffusion is the presence of acceptor properties in X-centers. A characteristic difference of such gratings is the modulation of the optical absorption density of only colloidal-type centers, as well as the high contrast due to diffusion pumping of color centers from the regions of interference pattern maxima.

Diffraction efficiency of gratings obtained on the basis of $F - X$ transformation reaches 40% and is characterized by greater angular selectivity $(\delta_0 \approx 3 \cdot 10^{-3} \, rad)$. Non-destructive reading can be performed with light wavelength and power from the visible and near-IR parts of the spectrum at a temperature until the onset of thermal instability X-centers ($\sim$350°C). Thermal reversibility instability provided by heating the crystal to temperatures $\approx$400°C and subsequent hardening. Phase recording based on the $F - X$ transformation is realized due to the anomalous dispersion of the refractive index in the X-band, and the amplitude is determined by the absorption in the X-centers. Theoretically and experimentally it is shown that the contribution of phase recording increases due to the selective destruction of the absorption band of the colloidal type centers and provides an increase in DE by 20~25%. In principle, due to the selective destruction of the color centers it is possible to obtain phase gratings. Non-sinusoidal lattice profile is a consequence of the diffusion nature of the recording process, which also provides an increase in DE by 6–12%.

3.3. Scattering effect in a three-dimensional transmitting diffraction grating.

When recording and reconstructing three-dimensional diffraction gratings, we have to face such insignificant problems for thin gratings as light scattering in a light-sensitive medium and related cross- and intermodulation noises [262–264]. DE as a result of these processes is reduced, so the scattering is usually tried to make as small as possible. On the other hand, the pattern observed in the scattering of light by three-dimensional gratings is extremely characteristic and can greatly facilitate the alignment of the gratings. This is important for both experimental and practical applications, so consider these phenomena.

Most of the available works are devoted to the study of selective light scattering during the registration of three-dimensional dynamic lattices in photorefractive crystals by two pump beams [264–267]. To study the effects of scattering in stationary gratings, which are observed in their reproduction by one of the pump beams, previously used specially made thick-layer emulsions, the thickness of which further increases with swelling [245]. In bulky carriers, such as reoxan, AHC and CGS, these phenomena have not been studied to date, although they are the most significant [269].

As a three-dimensional light-sensitive medium, we used AHSs containing F-centers, in which the scattering effect is much more pronounced than in CGS. For this case, mainly the scattering centers are colloidal potassium particles, which are created by coagulation F-centers in the recording process. Scattered light from such particles has a wide

angular spectrum and, being coherent, interferes with the main light beams, and creates an additional interference pattern. Thus, when holographic recording in a three-dimensional recording medium, next to the main grid should also be recorded and diffractive scattering structure. The diffraction of light on such gratings is characterized by a complex diffraction pattern resulting from the diffraction of the reducing beam on the recorded scattering structure and the scattered light on the scattering structure and the cross lattice. It consists of diffraction maxima, light lines, circles and arcs, the number, size and orientation of which depend on the position of the grating relative to the direction of propagation of diffracting light.

Let the reducing ray lie in the plane of the recording rays. Depending on the angle φ at which it falls on the lattice, we will see different restored diffraction patterns (Fig.3.21).

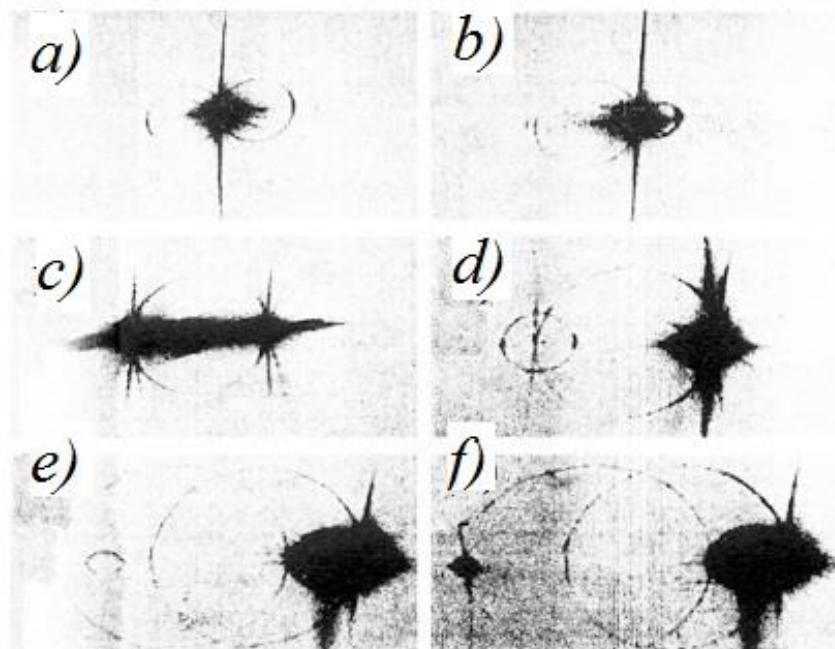Fig.3.21. The reducing ray lies in the plane of the recording rays. The angle φ of incidence varies from 0 to 2θ.

a) $\varphi = 0$; b) $0 < \varphi < \theta$; c), d) $\varphi = \theta$; e) $\theta < \varphi < 2$; f) $\varphi = 2\theta$.

If the reducing beam falls perpendicular to the lattice, symmetrically by the recording beam, then the diffraction pattern will be symmetrical (Fig. 3.21, *a*). It consists of a double scattering circle that touches each other in the zero diffraction order, and a straight line that passes through the zero order and is tangent to both. We will bring the incident ray closer to one of the recorders, then, as the angle φ changes, one circle will increase and the other will decrease (Fig. 3.21, *b*) and disappear completely when the angle φ reaches Bragg (θ). In this case, there is one scattering ring and two tangents to it, passing through the zero and first order of diffraction (Fig. 3.21, *c*).

With a further increase in the angle, the diffraction pattern changes as shown in Fig.3.21, *d*, *e*, *f*. First there is a ring with the center in the vicinity of the first diffraction order (Fig.3.21, *d*), then the ring near the zero diffraction order and, finally, fourth – between the first and second orders of diffraction (Fig.3.21, *e*). Thus, at the position of the lattice, when the second order of diffraction is restored, there are already four scattering rings (Fig. 3.21, *f*). The authors [263], who observed similar phenomena in gratings recorded on thick photographic emulsions, found only three scattering rings. The appearance of the third ring with the center in the first order of diffraction is associated with non-sinusoidal lattice, including harmonics of higher orders with a strong connection. Our research has shown that non-sinusoidal gratings with a strong connection are characterized by the appearance of not one, but at least two additional scattering rings.

To explain the observed phenomena, it is convenient to use the Ewald method known in *X*-ray crystallography, modified by Ragnarsson

[263]. An infinite unstructured recording medium in the Fourier transform space is described by a point, which we will denote as O. Each ray existing in the medium is described by a wave vector, the direction of propagation of which coincides with the direction of propagation of the ray, and the length is proportional $1/_\lambda$. We describe from the point O a sphere of radius $1/_\lambda$, which is called the Ewald sphere. Thus, the projection of the Ewald sphere and wave vectors on the plane of the recording rays is shown in Fig.3.22, a. The dashes indicate the wave vectors of the recording light fields $\vec{K}r_1$ and $\vec{K}r_2$ incident on the recording medium located in the center of the sphere O, and scattered by the medium $\overrightarrow{K^*}r_1$, $\overrightarrow{K^*}r_2$. The modules of all wave vectors describe spheres with centers at points Br_1, Br_2 and B^*r_1, B^*r_2, intersecting the planes of the recording rays with the spheres of these wave vectors Fig.3.22, a are reflected by the arcs Sr_1, Sr_2 and S^*r_1, S^*r_2.
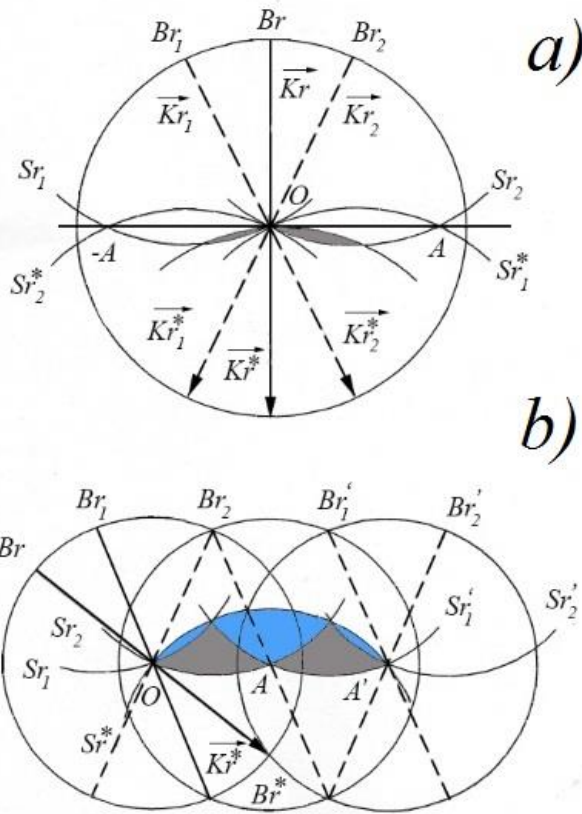
Fig.3.22. Projection of the Ewald sphere and wave vectors on the plane of the recording rays: *a)* – sinusoidal lattice; *b)* – the presence of higher harmonics.

In the recording medium, these four wave vectors coexist, and due to coherence, the sums and differences of the vectors are also present. We are only interested in the differences between the initial and forward-scattering wave vectors, which represent a stationary harmonic distribution of the field intensity and are holographic lattice vectors. Then the spatial spectrum of the main (cross-lattice) will be represented by three points $A, O, -A$ (Fig. 3.22, *a*).

The spatial spectrum of noise gratings is more complex. The beginning of all lattice wave vectors lies at a point O, and the ends will be located on spheres $Sr_1, Sr_2, S^*r_1, S^*r_2$ called spectral. Spectral spheres

$Sr_1 S^* r_1$ also describe lattices that arise as a result of interference of a beam $\vec{K} r_1$ with a scattered beam $\vec{K} r_2$. Accordingly, the spheres Sr_2 and $S^* r_2$ are the result of the interference of the beam $\vec{K} r_2$ with the scattered beam $\vec{K} r_2$ in the vicinity of the point O will also be the spectral region associated with intermodulation noise, which we do not consider.

The hologram reading is illustrated as follows. The part of the recoverable beam $\vec{K} r$ (Fig. 3.22, a), which passes through the hologram, is a wave vector $\overrightarrow{K^* r}$ and reaches the observer at its end point $B^* r$. The sphere of the wave vector $\overrightarrow{K^* r}$ around the point $B^* r$, in this case, intersects the spectral spheres Sr_1 and Sr_2 in two circles. The beginnings of all reconstructed wave vectors will lie at the points of intersection, and the ends – at the point $B^* r$ that corresponds to the fulfillment of Bragg's conditions for diffraction on the recorded scattering structure. Therefore, the observer sees two light rings on different sides of the restoring beam (Fig.3.21, a, b).

The appearance of the third and fourth scattering rings is associated with non-sinusoidal lattice. Given the presence of higher harmonics, the hologram is described not by one sphere of Ewald, but by three. Two additional, shifted relative to the first, on the vector of the cross-lattice, ie constructed from the first and second orders of diffraction A and A'.

If the angle of incidence of the reducing ray is greater than the Braggian, then the sphere of the wave vector $\overrightarrow{K^* r}$ around the point $B^* r$ intersects the circles of four spheres with points Br_1 and Br_2, Br_1' and Br_2' (Fig.3.22, b), and the observer will see four light rings (Fig.3.21, e, f).

In Fig.3.21, *a*, *b* in addition to the two scattering rings there is a vertical line. We believe that this line corresponds to the intersection of the sphere S^*r of the wave vector $\overrightarrow{K^*r}$ with the spheres S^*r_1 and S^*r_2. The lines of intersection of these spheres are circles lying in a plane perpendicular to the plane scattering (Fig.3.22). The central vertical line in Fig.3.21, *a*, is the overlap of the other two circles and its behavior when rotating the reducing beam fully confirms this assumption (Fig.3.23, *a*). When the first order of diffraction is restored, due to symmetry, similar lines pass through it.
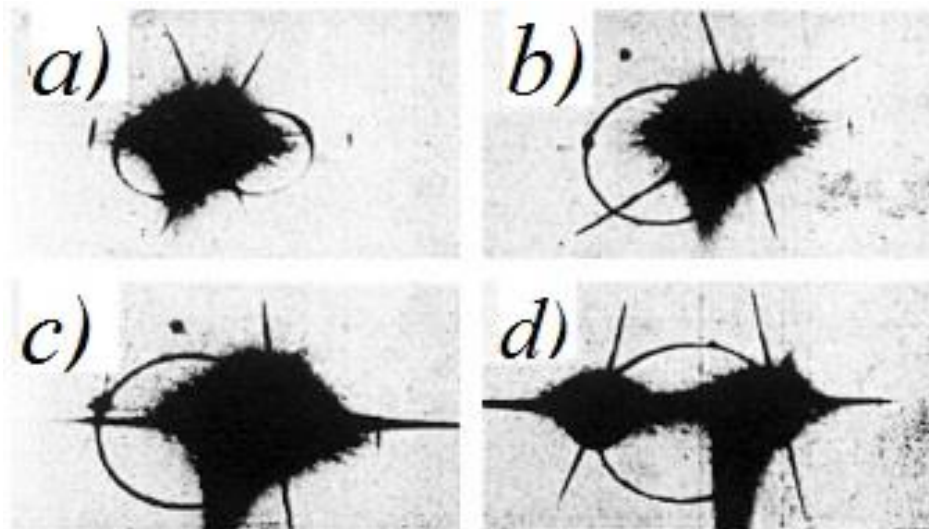
Fig.3.23. The reducing ray is derived from the plane of the recording rays. The angle φ of incidence in the plane of the recording rays varies from 0 to Bragg (θ):

a) $\varphi = 0$; b) $0 < \varphi < \theta$; c) $\varphi \approx \theta$; d) $\varphi > \theta$.

If the reducing ray is deflected up or down by some angle from the plane of incidence of the recording rays, the central vertical line of the diffraction pattern is divided into two intersecting arcs (Fig. 3.23, *a*) and the angle between them is proportional to the deflection angle of the

reducing beam, in turn, retain in the first approximation their geometric dimensions, shifted up or down, respectively.

The course of change of the diffraction pattern in this case when rotating the grating around the axis perpendicular to the plane of incidence of the recording rays is shown in Fig.3.23, *a*, *b*, *c*, *d*. For the initial selected position, in which there is a symmetrical pattern of diffraction (Fig.3.23, *a*). When the lattice rotates, the diameter of one scattering ring increases and the other decreases (Fig. 3.23, *b*). When the angle of incidence of the reducing beam approaches the Bragg, one of the crossed lines (depending on the direction of rotation of the lattice) expands, and turns into a band and begins to approach the plane of the recording beams (Fig. 3.23, *c*, *d*). When the Bragg angle is reached (maximum intensity of the first order), the band becomes horizontal, passes through the zero and first order of diffraction, and the maximum expands.

If in this position you start to tilt the grating to return the reducing beam to the plane of incidence of the recording beams, the band expands even more. Then, when the plane of incidence of the recording rays is reached, the scattered light flux forming this band is evenly distributed throughout the hemisphere beyond the plane of the lattice (the line disappears). This corresponds to the grating recovery of all scattered light.

A similar band occurs when restoring a three-dimensional hologram of real objects with sufficient angular dimensions, as shown in [269]. However, in this case, the length of this line in the form of a strip of the restored image is limited by the size of the object. In our case, since the hologram of scattered light is equivalent to the hologram of a very wide

diffusely scattering object, this line is observed completely, as well as its paired line, passes through the zero order.

In addition to the considered arcs and rings, weak lines are also observed in the diffraction pattern, which are analogous to the Kossel lines known in *X*-ray crystallography. They pass parallel to each other through +1-st and −1-st orders of diffraction and repeatedly scattered isotropic light on the cross-lattice.

The model considered by us is also confirmed by the scattering patterns observed by us in the case when the wavelengths of light used to record and read the hologram are different. Figure 3.24 shows scattering patterns for holograms recorded with a blue laser (λ=488 *nm*) and read with a red laser (λ=633 *nm*).

Then the radius of the sphere S^*r of the wave vector $\overrightarrow{K^*r}$ will be different from the radius of the spheres S^*r_1 and S^*r_2. The lines of intersection of these spheres are circles that can no longer be connected. In this case, the vertical lines (Fig.3.23, *a*) are transformed into arcs (Fig.3.24, *a*), whose behavior when turning (Fig.3.24, *b*, *c*, *d*) is fully consistent with our model.
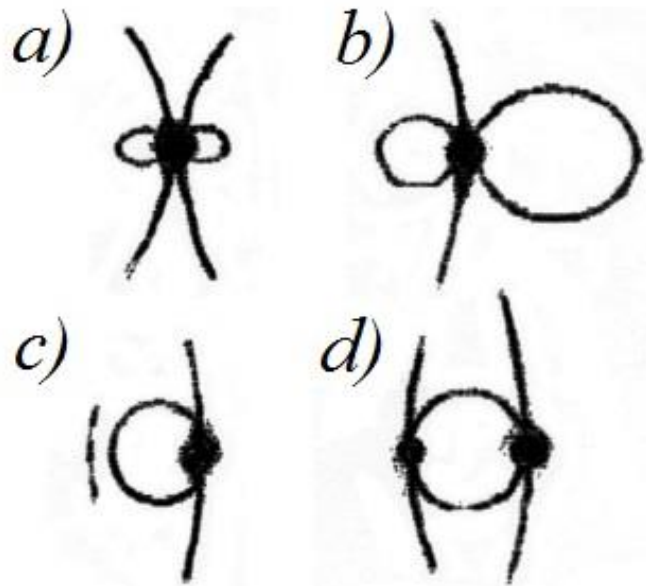
Fig.3.24. Scattering patterns for a hologram written in blue laser ($\lambda=488$ *nm*) and read in red ($\lambda=633$ *nm*).

The reducing ray lies in the plane of the recording rays: *a)* $\varphi = 0$; *b)*, *c)* $0 < \varphi < \theta$; *d)* $\varphi = \theta$.

Thus, as follows from the results, holographic recording in a three-dimensional recording medium forms a scattering structure, the diffraction of which is characterized by a much wider range of properties than those observed in thin or thick-layer holograms [263]. The recorded scattering structure is noisy, it reduces DE and hologram contrast, but may be useful for some applications. For example, by changing the diffraction pattern observed on the screen, it is possible for the scattering structure to perform spatial orientation and pre-alignment of deep holograms, which is important because their angular selectivity can be less than an angular minute.

In [269] the effect of partial recovery of deep holograms was already used to adjust the system. For orientation in the vertical plane we used the rotation of the band of the restored image, and in the horizontal – its width.

In our case, for orientation, you can use not only the rotation and change the width of this line, which has a pronounced character in noise holograms, but also change the size, orientation and number of scattered rings. This expands the capabilities of the method and allows you to automate it.

CHAPTER 4. OPTOELECTRONIC DEVICES BASED ON THREE-DIMENSIONAL TRANSMISSION DIFFRACTION STRUCTURES

Three-dimensional transmission diffraction structures (TTDS) of the optical range, which are a combination of the simplest three-dimensional diffraction gratings, in comparison with the two-dimensional diffraction grating, provided them with light diffraction to acquire the following distinctive properties [177, 178, 182, 190, 270]:

– when diffraction of monochromatic light on a three-dimensional holographic diffraction grating there is only one diffraction maximum and, therefore, as a result of diffraction only two rays are formed – transmitted and diffracted;

– when changing the angle of incidence of the beam on the three-dimensional lattice, energy is exchanged between transmitted and diffracted rays and their intensities change, while the spatial direction of propagation of these rays is preserved. Energy transfer between rays can reach 100%;

– in the diffraction of a white collimated beam of light incident at some angle on the lattice, diffraction is observed only for light of a certain wavelength that satisfies the Bragg condition.

The presence of such excellent properties in TTDS allows to use them as holographic optical elements (HOE) for various optoelectronic devices that have unique properties, unattainable in other ways [271–277]. The purpose of our further presentation is to consider the optoelectronic devices proposed by us [278–285], in which HOE are TPDS.

4.1. Device for amplitude modulation and phase-amplitude conversion of light wave.

Essential elements of many optoelectronic devices are optical modulators, with which you can purposefully change the parameters of optical radiation – amplitude, frequency, phase, plane of polarization.

The principle of operation of optical modulators and, accordingly, methods of light modulation based on the use of various physical effects, such as optoelectric, magneto-optical, etc. [286, 287]. These effects, which describe the interaction of light with matter under the action of various physical factors, allow, in particular, to control the magnitude of refraction and absorption, the length of the optical path of light in matter, which allows them to modulate light.

The proposed method is based on the selective property of a three-dimensional holographic diffraction grating, which consists in the magnitude of the intensity of light fluxes emanating from the lattice: $I_D -$ diffracted and $I_P -$ passed, from the angle $\varphi = \theta + \delta$ of incidence of the original light flux I_0. For the case of a purely phase lattice with DE $\eta = 0{,}5$ (50%), such dependences are presented in Fig.4.1.
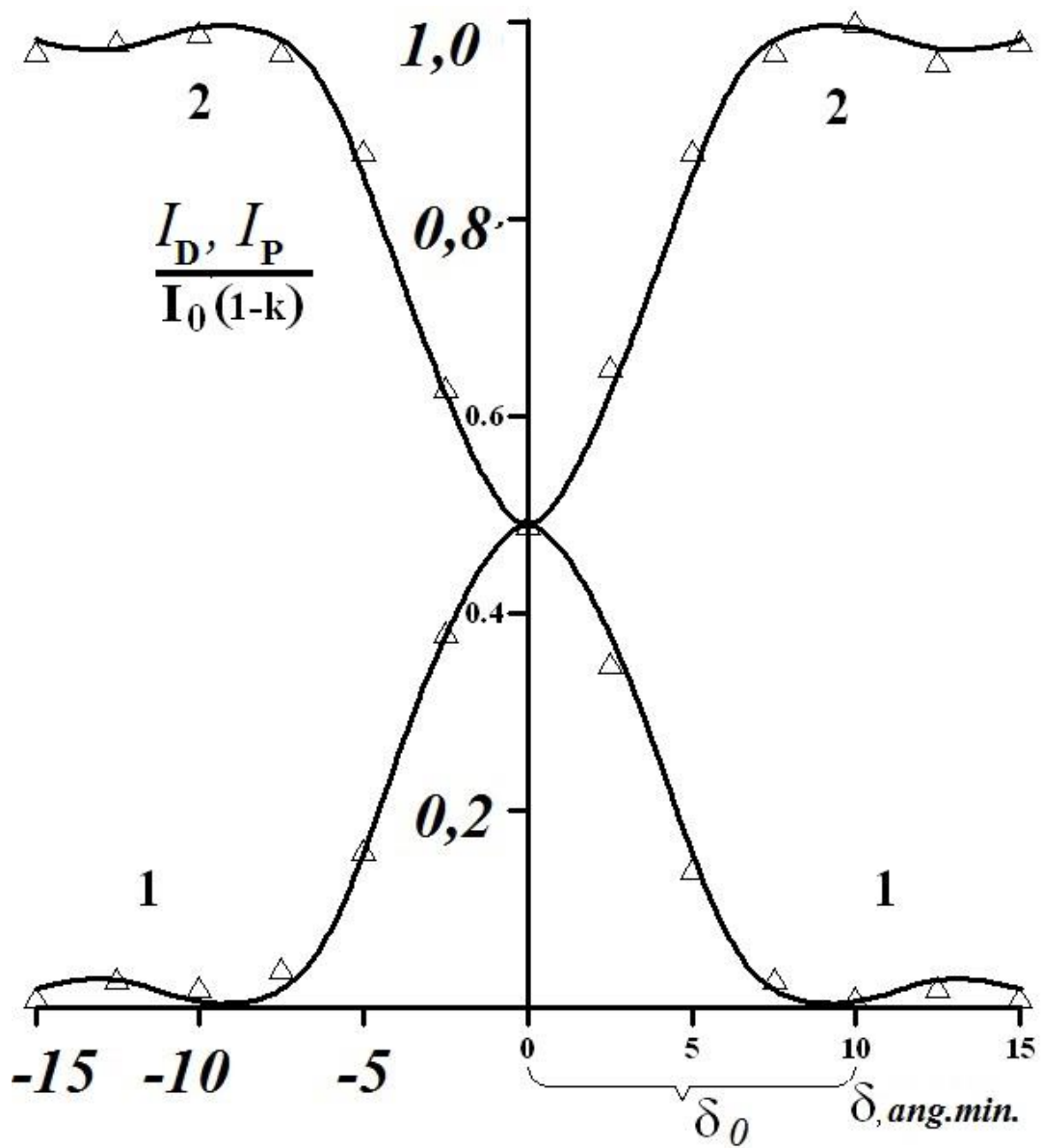
Fig.4.1. Angular dependence of light fluxes: 1 − diffracted I_D, 2 − passing I_P, from the change of the angle of incidence of the lattice of light flux I. Solid line − theoretically calculated by formulas (4.1) and (4.2), symbol Δ − experimental values.

Curves 1 and 2 according to [278] are described by the formulas:

$$I_P = (1 - k)I_0 \left[\cos^2 \left(\xi^2 \delta^2 + v^2 \right)^{\frac{1}{2}} \right.$$

$$\left. + \xi^2 \delta^2 \left(\xi^2 \delta^2 + v^2 \right)^{-1} \sin^2 \left(\xi^2 \delta^2 + v^2 \right)^{\frac{1}{2}} \right], \qquad (4.1)$$

$$I_D = (1-k)I_0 \left[\sin^2(\xi^2\delta^2 + v^2)^{\frac{1}{2}}\right]\left(1 + \frac{\xi^2\delta^2}{v^2}\right)^{-1}, \qquad (4.2)$$

here $\xi = \dfrac{2\pi\bar{n}L\sin\theta}{\lambda}$, $\quad v = \arcsin\left[\dfrac{I_\partial(\theta)}{I_0(1-k)}\right]^{\frac{1}{2}} \approx \arcsin[\eta]^{\frac{1}{2}}$, $\bar{n}$ — the

average refractive index of the grating, L – the thickness of the grating, λ – the wavelength of the modulated radiation, k – the reflection coefficient of the grating.

The modulation of the intensity of diffracted and transmitted optical radiation occurs as a result of time changes in the magnitude of the angle $\delta = \delta_0 f(\omega t)$. Here δ_0 – the value of the angular selectivity of the lattice (Fig. 4.1), $f(\omega t)$ – the periodic function that sets the modulation mode.

The angle δ can be changed in two ways:

1) different time orientation of the lattice relative to the incident beam, or

2) scanning the luminous flux at an angle within the angular selectivity of the lattice (δ_0).

Figure 4.2 (curve 1) shows the results of modulation of the luminous flux of the He-Ne laser $\lambda= 632.8\ nm$) for the first case, when the modulator used a three-dimensional holographic diffraction grating with angular selectivity $\delta_0 = 9\ ang.\,min.$ and $\eta = 0{,}5$ (50%).

The modulating signal is a sinusoidal alternating voltage applied to a rotary device on which the lattice is fixed.
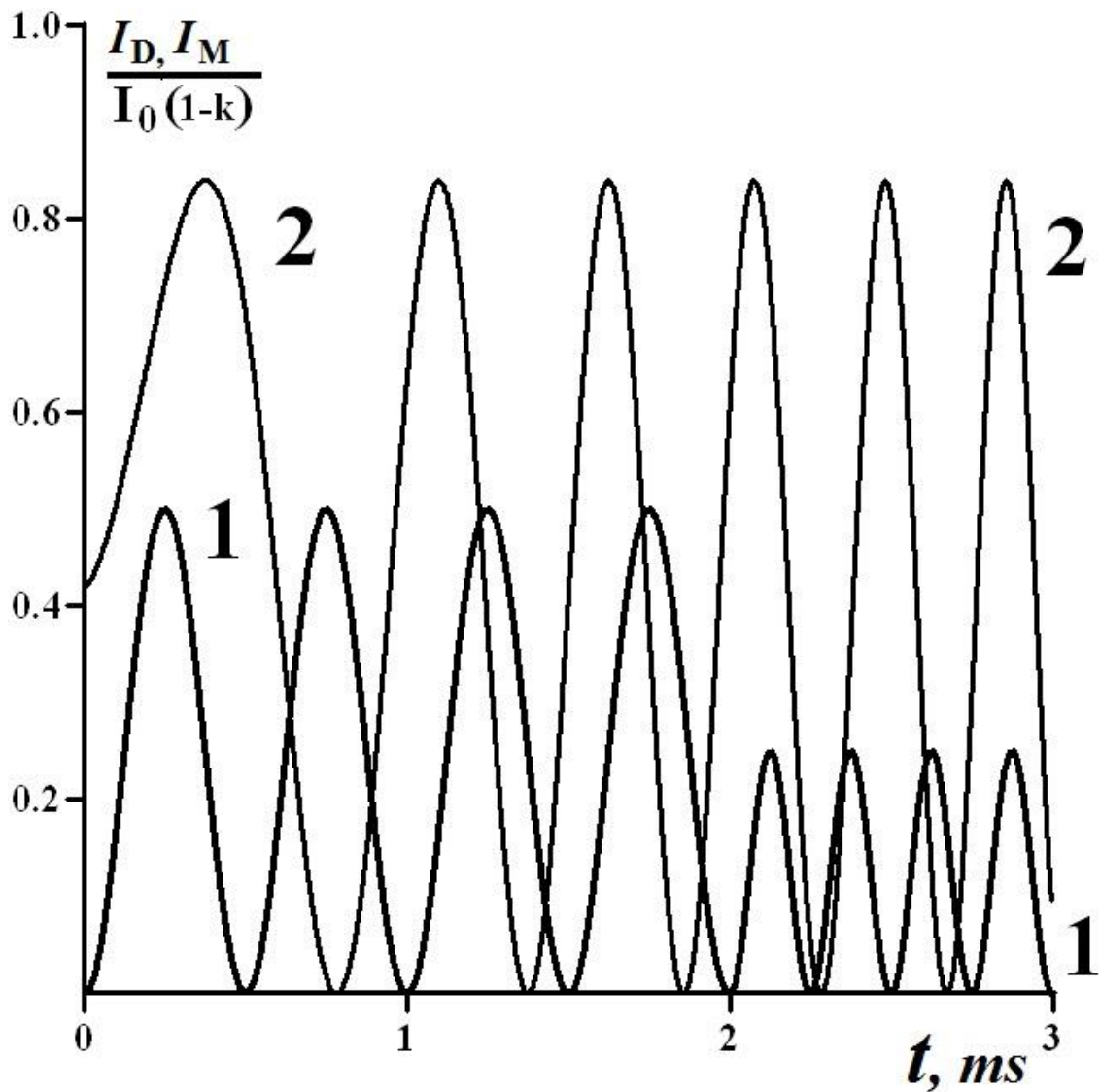
Fig.4.2. Modulating light flux: 1− I_D according to the single-beam scheme, 2− I_M according to the two-beam scheme.

As shown in Fig.4.2 (curve 1), the phase of the modulated light signal does not depend on the amplitude and frequency of modulation. For example, the acousto-optical modulation method, which uses a dynamic three-dimensional diffraction grating for modulation, does not have this property. When modulating light with its help, the phase changes depending on the magnitude of the amplitude and frequency of the modulated signal [269, 287].

The considered method of modulation, as well as acousto-optical, provides modulation of intensity in relation to the incident luminous flux I_0 only within the value of the DE lattice and to achieve 100% modulation of the output luminous flux must use a three-dimensional lattice with $\eta = 100\%$ (provided that $k = 0$).

The manufacture of such gratings is quite complex and not always technically feasible task. However, if optical modulation with some spatial coherence is used for modulation, then 100% modulation at $k = 0$ and for the lattice with $\eta = 50\%$ can be achieved with the help of a stationary bulk diffraction grating. In this case, the modulation is created by changing the phase in one of the beams coming out of the lattice – I_D or I_P, which, in turn, with the help of mirrors are passed through the lattice in the opposite direction, as shown in Fig.4.3.
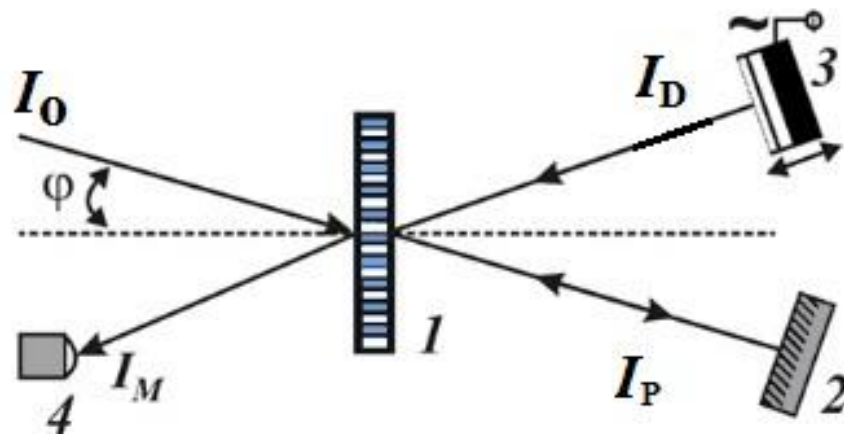
Fig.4.3. Two-beam scheme of optical radiation modulation: 1 – three-dimensional diffraction grating; 2 – a mirror; 3 – mirror on piezoceramics; 4 – photodetector.

As can be seen from this figure, the beam came out of the lattice I_M is the result of the interference of two beams – one passed – $I_P(L)$ and

diffracted – $I_D(L)$. Therefore, in this case for the amplitude A_M of the beam I_M out of the lattice we can write:

$$A_M = A_D(L)e^{-i(\Phi_P - \Delta\varphi)} + A_P(L)e^{-i\Phi_D}, \qquad (4.3)$$

where $A_D(L)$ and Φ_P – the amplitude and phase of the beam $I_P A_P(L)$ passed through the lattice and Φ_D – amplitude and phase of the beam diffracted on the lattice I_P; $\Delta\varphi$ – phase mismatch between the beams I_D and I_P created by piezoceramics (Fig.4.3).

In the case of a purely phase lattice for amplitudes $A_D(L)$ and $A_P(L)$ according to [182] we have:

$$A_D(L) = A_D \cos\nu, \qquad (4.4)$$

$$A_P(L) = iA_P \sin\nu. \qquad (4.5)$$

Substituting (4.4) and (4.5) in (4.3) and multiplying A_M on the complex connected value A_M^*, after simple transformations for intensity of the beam I_M which has left a lattice we receive:

$$
\begin{aligned}
I_M &= A_M A_M^* \\
&= I_D\cos^2\nu + I_P\sin^2\nu \\
&\quad - 2(I_D I_P)^{\frac{1}{2}}\cos\nu\,\sin\nu\,\sin(\Phi_P - \Phi_D - \Delta\varphi) = \\
&= 2I_0(1-k)\eta(1-\eta)[1 - \sin(\Phi_P - \Phi_D - \Delta\varphi)].
\end{aligned}
$$

Diffracted beam $A_P(L)$ is formed by the reflection of the beam I_P from the optically denser planes of the lattice, where $n = \bar{n} + \Delta n$. It is known [192] that in this case, the reflection is the loss of half-wave and therefore $\Phi_P - \Phi_D = \pi$ then for I_M we finally get:

$$I_M = 2I_0(1-k)\eta(1-\eta)[1 - \sin(\Delta\varphi)]. \qquad (4.6)$$

As follows from (4.6), modulation I_M when changing the phase mismatch between the beams $\Delta\varphi$ occurs according to the sinusoidal law

and when $\eta = 0,5,\ k = 0$ the value of the modulated signal is a maximum of: $I_M = I_0$, i.e. 100%.

Figure 4.2, (curve 2) shows the dependence of the intensity of He-Ne laser radiation I_M on the phase change of one of the beams I_D, or I_P, for a three-dimensional diffraction grating, with $\eta = 50\%$. The phase change was performed by an electro-optical device or a mirror mounted on piezoceramics. As can be seen from the figure, the magnitude of the modulated signal, in our case, does not reach 100% relative to the incident luminous flux, and is ≈85%. This is due to the losses that occur when the reflection of light flux from the grille and mirrors, as well as with the inaccurate coordination of the wave fronts of light fluxes I_D and I_P.

It is possible to use such devices as a phase-amplitude converter for the analysis of phase modulations of the signal wave. In the generally accepted schemes of phase-amplitude converters, the combination on the front of the signal and reference waves causes great technical difficulties and losses in intensity [12, 284]. When using this scheme based on a three-dimensional diffraction grating, these conditions are met automatically. Adjustment to bands of infinite width, even for arbitrary fronts of reference and signal waves, is not difficult. This is important when the front of the signal wave is distorted when passing through the test medium, for example, in laser Doppler anemometry. In this case, the magnitude of the phase shift is not determined by the shift of the bands of the diffraction pattern, and by changing the intensity of one of the diffracted streams, which significantly increases the value of the useful signal and facilitates the automation of the observation process. Schematic use of gratings in the transmission paths of optical systems of

laser Doppler anemometers (LDA) is shown in Fig.4.4, *a*, and in the inverse-differential scheme of the receiving path of LDA in Fig.4.4, *b*.
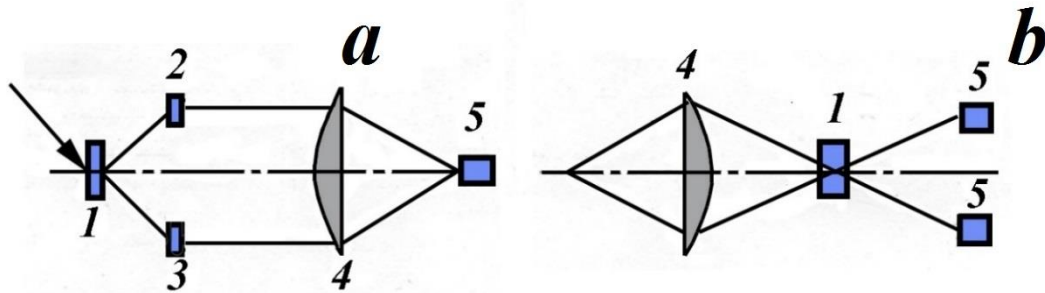
Fig.4.4. Scheme of use of three-dimensional passing diffraction gratings in transmitting (*a*) and receiving (*b*) paths of LDA. 1, 2, 3 – three-dimensional gratings, 4 – lenses, 5 – photodetectors.

As follows from Fig.4.4, *b*, the use of gratings provides two independent channels for the inclusion of radiation receivers and, accordingly, high resolution. Laboratory tests have shown that at a Doppler frequency of 100 *kHz*, the resolution is less than 1 *kHz*. The value of this parameter determines the accuracy of measuring the frequency of the Doppler signal, and, consequently, the accuracy of speed measurement.

Distinctive features of LDA optical circuits using a grating are:

– simplicity and cheapness in manufacturing (especially in comparison with schemes using Wollaston prisms or similar);

– stability in work (resistance to temperature influences of vibration character);

– ability to equalize the intensity of the rays at the point of intersection, which significantly affects the magnitude of the signal;

– possibility of constructing two-component optical circuits (when using lasers that generate radiation with two or more wavelengths or when using dividing elements containing several sublattices in the volume).

The use of combinations of diffraction gratings recorded in the volume of one recording medium [174, 288, 289], allows you to easily implement multi-component laser Doppler anemometers.

4.2. Optoelectronic devices for measuring linear displacements in the nanometer range.

To solve various applications that arise in the development of science and technology, such as tunneling microscopy, in developing the principles of recording information at the nanometer and atomic levels, as well as in creating miniature elements of semiconductor devices and integrated circuits, it is necessary to measure linear displacements. up to several angstroms in automatic mode with feedback [290, 291].

Known optical systems provide measurement accuracy of no more than a few nanometers [292]. We propose methods for measuring linear displacements using the methods described in [279, 280], the accuracy of which is several angstroms.

These methods are based either on measuring the displacement of the three-dimensional transmitting holographic diffraction grating, which is rigidly fixed on the moving object, relative to the interference pattern formed by the convergence of two intersecting laser beams at a Bragg angle for this grid (contact method), or measurement object by non-

contact method, when the lattice is not connected to the moving object. Consider in detail both methods.

4.2.1. Contact method for measuring linear displacements in the nanometer range.

The practical implementation of this method is shown in Fig.4.5.
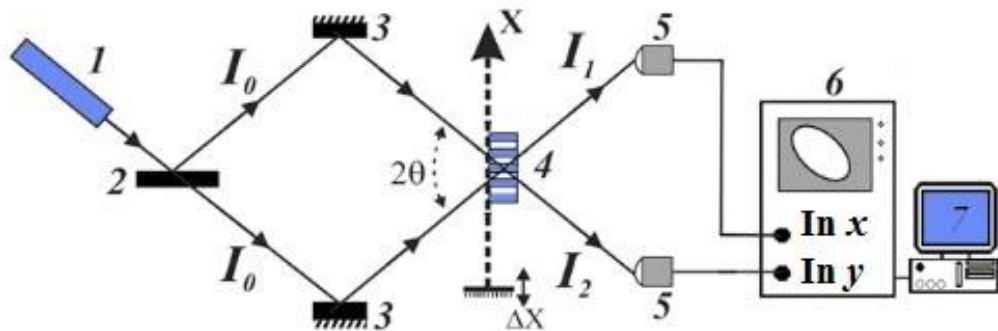
Fig.4.5. Schematic diagram of measuring linear displacements (contact method).

1 – laser, 2 – divider, 3 – mirrors, 4 – three-dimensional transmitting holographic diffraction grating, 5 – photodetectors, 6 – oscilloscope, 7 – computer, 8 – analyzer.

The best results are achieved if the lattice is written by the interference field relative to which the lattice is moved. The lattice used should be amplitude-phase, the amplitude component of the lattice allows to remove ambiguity in determining the direction of displacement, but it should not be significant (so as not to reduce the diffraction efficiency of the lattice).

As follows from the theory of diffraction on a three-dimensional lattice (see 3.2.2), the intensities of the rays emanating from the lattice I_1

and I_2 (Fig.4.5) differently depend on the shift Δx of the lattice relative to the read interference pattern, and are determined by expressions

$$I_1 = I_0 exp\left(-\frac{2\bar{\alpha}L}{\cos\theta}\right)[ch2v_a$$
$$- sh2v_a \cos\Delta\varphi - \sin 2v \sin\Delta\varphi], \tag{4.7}$$

$$I_2 = I_0 exp\left(-\frac{2\bar{\alpha}L}{\cos\theta}\right)[ch2v_a$$
$$- sh2v_a \cos\Delta\varphi + \sin 2v \sin\Delta\varphi], \tag{4.8}$$

here: $v_a = \frac{\Delta\alpha_0 L}{2\cos\theta}$; $v = \frac{\pi\Delta n_0 L}{\lambda\cos\theta}$; I_0 – the intensity of incident rays that form a reading interference pattern; θ – the angle at which the rays I_0 fall on the lattice, which is the Bragg angle for it; $\bar{\alpha}$ – average absorption coefficient in the lattice; L – thickness of the lattice; Δn_0 and $\Delta\alpha_0$ – the amplitude of modulation, respectively, the average values of the refractive indices and absorption; λ – wavelength; $\Delta\varphi = \frac{2\pi\Delta x}{d}$ – phase mismatch between the lattice and the reading interference pattern due to the displacement Δx of the lattice along the axis Ox; $d = \frac{\lambda}{2\sin\theta}$ – lattice period.

Analysis of the dependences I_1 and I_2 on the phase mismatch $\Delta\varphi$ and, accordingly, the analyzer 8 (Fig.4.5) obtain the values of the shift of the lattice (object) Δx is carried out by processing them on a computer in accordance with formulas (4.7) and (4.8).

Let us now consider which curve will describe the end of the vector I if its projections on the x and y axes are given by the values of I_1 and I_2 due to formulas (4.7) and (4.8), when the phase mismatch $\Delta\varphi$ changes from 0 to 2π.

As follows from (4.7) and (4.8), the phase difference $\Delta\varphi = 0$, π and 2π intensity I_1 and I_2 equal, regardless of the ratio of amplitude (v_a) and phase (v) contribution to the diffraction. Therefore, in this case, the end of the vector I, if its projections on the inputs x and y oscilloscope 6 (Fig.4.5) are given by the values I_1 and I_2, specified by formulas (4.7) and (4.8) are always on the line OO_1 passing through the origin at an angle of 45^0. 4.6). When $\Delta\varphi = 0$ or 2π the value I is minimal (the end of the vector I corresponds to point 1 on the line OO_1), and when $\Delta\varphi = \pi$ – the maximum (the end of the vector I corresponds to point 2 on the line OO_1), (Fig.4.6).

If you go to the coordinate system in which the axis Ox coincides with the line OO_1, and its beginning is shifted relative to the point O (Fig.4.6) on the segment $OO_1 = x_0$:

$$x_0 = \sqrt{2}I_0 exp\left(-\frac{2\bar{\alpha}L}{\cos\theta}\right)ch2v_a,$$

then the coordinates x and y any point in this coordinate system is given by expressions

$$x = -\sqrt{2}I_0 exp\left(-\frac{2\bar{\alpha}L}{\cos\theta}\right)sh2v_a\cos\Delta\varphi, \qquad (4.9)$$

$$y = -\sqrt{2}I_0 exp\left(-\frac{2\bar{\alpha}L}{\cos\theta}\right)\sin 2v\sin\Delta\varphi. \qquad (4.10)$$

Hence, excluding $\Delta\varphi$, we obtain that the trajectory described by the end of the vector I $\Delta\varphi$ changes from 0 to 2π represents an ellipse:

$$\frac{x^2}{a^2} + \frac{y^2}{b^2} = 1, \qquad (4.11)$$

where

$$a = \sqrt{2} I_0 exp \left(-\frac{2\bar{\alpha}L}{\cos\theta} \right) sh2\nu_a, \qquad (4.12)$$

$$b = \sqrt{2} I_0 exp \left(-\frac{2\bar{\alpha}L}{\cos\theta} \right) \sin 2\nu. \qquad (4.13)$$
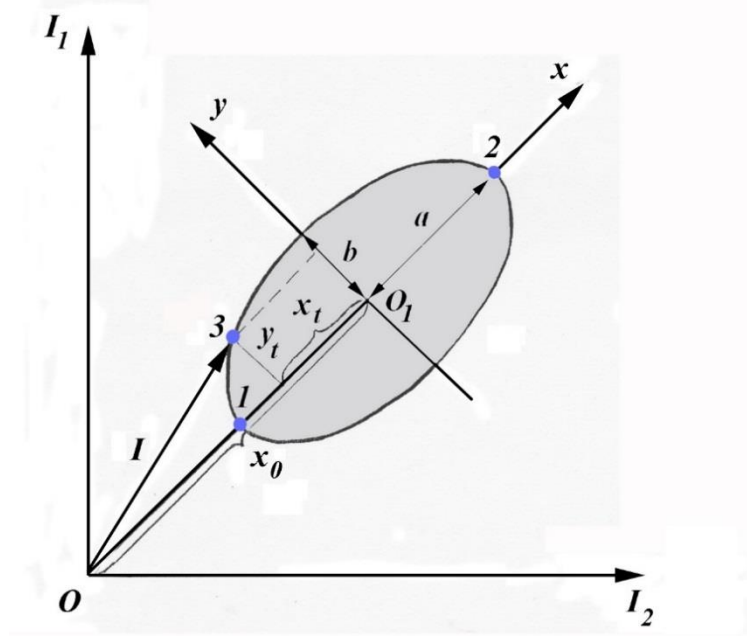
Fig.4.6. The trajectory described by the end of the vector I when the phase mismatch between the beams changes from 0 to 2π.

Determining for this ellipse the magnitudes of the semi-axes a and b, and the coordinates of the end point of the vector I at any time x_t and y_t, (for example, point 3 Fig.4.6), from (4.9) and (4.10) can determine the displacement Δx of the lattice (object) relative to the position, in which $\Delta\varphi = 0$ (point 1 in Fig.4.6)

$$\Delta\varphi = \frac{\Delta x}{d} = arctg \left(\frac{y_t}{x_t} \cdot \frac{a}{b} \right).$$

From here

$$\Delta x = d \cdot arctg \left(\frac{y_t}{x_t} \cdot \frac{a}{b} \right). \qquad (4.14)$$

238

Measurements are greatly simplified if you choose a lattice for which $a = b$ the trajectory is a circle. In this case we have

$$\Delta x = d \cdot arctg\left(\frac{y_t}{x_t}\right). \tag{4.15}$$

The direction of displacement of the lattice along the axis Ox is determined by how the oscilloscope beam is shifted on the ellipse – clockwise or counterclockwise.

Let's find out the standard error of definition Δx. The values y_t and x_t of one order and the relative errors of their definition are the same:

$$\frac{\Delta y_t}{y_t} = \frac{\Delta x_t}{x_t} = \sigma.$$

Then, taking into account expression (4.15), the root mean square error of measurement Δx is calculated by the formula:

$$\Delta(\Delta x) = d \sqrt{\left(\frac{1}{1 + \left(\frac{y_t}{x_t}\right)^2}\right)^2 \frac{\Delta y_t^2}{x_t^2} + \left(\frac{1}{1 + \left(\frac{y_t}{x_t}\right)^2}\right)^2 \frac{y_t^2}{x_t^2} \Delta x_t^2}$$

$$= \frac{d}{1 + \left(\frac{y_t}{x_t}\right)^2} \sqrt{\sigma^2 \frac{y_t^2}{x_t^2} + \sigma^2 \frac{y_t^2}{x_t^2}} = \frac{\sqrt{2} d \sigma \frac{y_t}{x_t}}{1 + \left(\frac{y_t}{x_t}\right)^2}. \tag{4.16}$$

From (4.16) it follows that the maximum error is obtained at $\frac{Y_t}{X_t} = 1$ and is:

$$\Delta(\Delta x)_{max} = \frac{d\sigma}{\sqrt{2}}. \tag{4.17}$$

In the working model of the device we used a grid recorded by He-Ne laser ($\lambda = 632{,}8\ nm$) according to the method described in [69] with

the period $d \approx 450\ nm$. The relative error in determining the coordinates of the point on the ellipse when shifting the lattice using digital input to the computer was $\sigma \le 10^3$. As follows from (4.17), the maximum measurement error in this case

$$\Delta(\Delta x)_{max} \approx 0,32\ nm = 3,2\ \mathring{A}.$$

When using gratings with a shorter period, the measurement accuracy can be significantly improved. As follows from the literature [86], it is not difficult to obtain lattices with the period $d \approx 200\ nm$. For such gratings, the maximum measurement error of linear displacements will be

$$\Delta(\Delta x)_{max} \approx 0,14\ nm = 1,4\ \mathring{A}.$$

These theoretical estimates are made in the assumption of the absence of any noise that reduces the accuracy of measurement (vibration, fluctuations in air density, etc.). In practice, we observe not a point on the ellipse, but a segment of the arc, the length of which is determined by these factors. To increase the accuracy of measurements requires high vibration protection, the absence of convective flows in the air, for particularly accurate measurements requires vacuuming the entire system.

It should be noted that the described method has high accuracy (due to the use of two parallel channels), does not depend on fluctuations in laser power (this is automatically taken into account in the calculations), allows you to unambiguously determine the direction of displacement of the object and allows simple visual observation. from existing other methods.

4.2.2. Non-contact method of measuring linear displacements in the nanometer range.

The peculiarity of the optical method of measuring linear displacements of an object described in the previous section with an accuracy of several angstroms is based on measuring the offset of a three-dimensional transmitting amplitude-phase holographic diffraction grating, which is rigidly connected to the object in the field of independently created interference pattern. However, in many cases it is difficult or impossible to place the diffraction grating directly on the object and ensure the required flow of rays through it, for example, when measuring the linear displacement of any element (part) inside a working unit or structure. In such situations, you need a device that would measure the linear displacement of the object by contactless method, the principle of implementation of which is shown in Fig.4.7.

As in the previous case, the method is based on the properties of a three-dimensional transmitting holographic diffraction grating, which depends on the intensity of the luminous flux I emanating from the grating from the phase mismatch $\Delta\varphi$ between the beams incident on the grating [274].
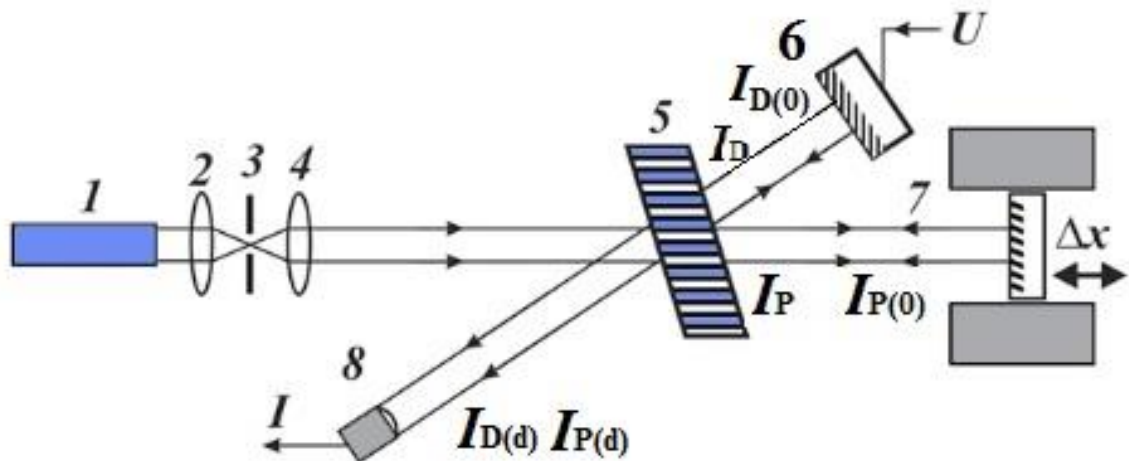
Fig.4.7. Schematic diagram of measuring linear displacements (non-contact method).

1 – laser, 2,4 – lenses, 3 – diaphragm, 5 – three-dimensional transmitting holographic diffraction grating, 6 – mirror mounted on piezoceramics, 7 – object with a mirror-reflecting surface, 8 – photodiode, I – output signal, coming from the photodiode to the computer.

In our case (Fig. 4.7), the beams falling on the lattice 5 are $I_D(0)$ and $I_P(0)$, accordingly, the beam I_D diffracted by the mirror 6 is diffracted by the lattice and reflected by the object 7, which previously passed without deviation through the lattice beam I_P. To meet the condition of strict alignment of light beams propagating in the forward and reverse directions, the object must either have a mirror surface, or it is fixed to a mirror that reflects light. The reflected rays, as well as those coming out of the lattice, must be directed strictly at the Bragg angle to the lattice used in this particular case. Phase mismatch $\Delta\varphi$ between the beams $I_D(0)$ and $I_P(0)$ is created as a result of the shift of the object 7 (Fig.4.7).

Under these conditions, the beam I coming out of the lattice and

falling on the photodiode 8 (Fig. 4.7) is the result of interference of two combined beams: passing $I_P(L)$ and reflected by the object, and then diffracted $I_D(L)$; therefore, in this case for the amplitude A of the beam coming out of the lattice I we can write:

$$A = A_D(L)e^{-i(\Phi_D - \Delta\varphi)} + A_P(L)e^{-i\Phi_P}, \qquad (4.18)$$

where $A_P(L)$ and Φ_P – amplitude and phase of the beam $I_P(0)$ passing on the lattice; $A_D(L)$ and Φ_D – the amplitude and phase of the diffracted beam through the lattice $I_D(0)$; $\Delta\varphi = \frac{2\pi}{\lambda}\Delta x + \Delta\varphi_0$ – phase mismatch between the beams $I_D(0)$ and $I_P(0)$ created by the displacement Δx of the object; λ – the wavelength of the laser radiation, $\Delta\varphi_0$ – the initial phase of inconsistency between the beams.

The greatest modulation of the beam I intensity in the case of phase mismatch $\Delta\varphi$ between beams falling on the lattice can be obtained if we use a purely phase lattice [274], ie a lattice in which only the refractive index changes [275]. Then in the case of a purely phase lattice for amplitudes $A_D(L)$ and $A_P(L)$ in accordance with [182] we have

$$A_D(L) = A_D \cos v, \qquad (4.19)$$

$$A_P(L) = iA_P \sin v, \qquad (4.20)$$

here $v = \arcsin\left(\eta^{\frac{1}{2}}\right), \eta -$ DE lattice.

Substituting (4.19) and (4.20) in (4.18) and multiplying A by a complex-coupled quantity A^*, after simple transformations, the intensity I of the beam coming out of the lattice can be represented as:

$$I = A \cdot A^* = I_D\cos^2 v + I_P\sin^2 v$$

$$- 2(I_D I_P)^{\frac{1}{2}}\cos v \sin v \sin(\Phi_P - \Phi_D - \Delta\varphi) =$$

$$= 2I_0 \eta (1 - \eta)[1 - \sin(\Phi_P - \Phi_D - \Delta\varphi)].$$

It was taken into account that the lattice is purely phase and $I_D = I_0\eta$, therefore, $I_P = I_0(1 - \eta)$.

The diffracted beam $I_P(L)$ is formed as a result of the reflection of the beam $I_P(0)$ from the optically denser planes of the lattice, where $n = \bar{n} + \Delta n$, here $\bar{n}$ – the average refractive index of the lattice. In this case, the reflection is the loss of half-wave and, consequently, then $\Phi_P - \Phi_D = \pi$ for I the final gain

$$I = 2I_0 \eta (1 - \eta)(1 - \sin\Delta\varphi),$$

or given that $\Delta\varphi = \frac{2\pi}{\lambda}\Delta x + \Delta\varphi_0$

$$I = 2I_0 \eta (1 - \eta)\left[1 - \sin\left(\frac{2\pi}{\lambda}\Delta x + \Delta\varphi_0\right)\right]. \qquad (4.21)$$

As follows from (4.21), the change in beam intensity I when the object is displaced occurs according to the sinusoidal law and the intensity reaches its maximum value $I = I_0$ at $\eta = 0,5$ (Fig. 4.8, curve 1).
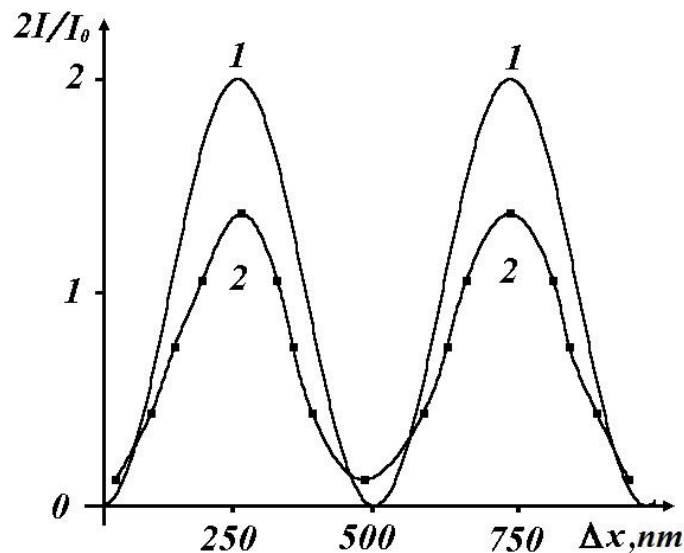
Fig.4.8. Dependence of the magnitude of the output signal I from the photodiode 8 (Fig.4.7) on the shift Δx of the object.

1 – curve calculated by formula (4.21), provided that $\eta = 0{,}5$, $\Delta\varphi_0 = \frac{\pi}{2}$;

2 - experimentally obtained curve.

To implement this method in the circuit of the device, which is shown in Fig.4.7, we used a three-dimensional transmitting holographic diffraction grating, which was recorded according to the method [279]. Diffraction efficiency η the lattice at the wavelength of the He-Ne laser ($\lambda = 632{,}8 \ nm$), which was used in the scheme, was 0,5 (or 50%). The displacement Δx of object 7 (Fig. 4.7) was carried out by piezoceramics and was determined from the calibration graph $\Delta x(U)$ by the amount of voltage U applied to the piezoceramics. The calibration graph was built using the measurement method for Δx shown in Fig.4.5, where the object was a graduated piezoceramics, on the surface of which was attached a diffraction grating. In the experiment, in order to avoid errors associated with hysteresis phenomena, the change in the voltage U that controls the displacement of the piezoceramics was carried out in the same direction as in the calibration – from smaller values to larger ones. The signal from photodiode 8 was applied to the computer. The dependence of the beam intensity I on the amount of displacement of the object 7 is shown in Fig.4.8 (curve 2).

The signal I in this case really changes according to the sinusoidal law. However, its maximum value is 85%, not 100% of the intensity of the incident beam I_0, as follows from (4.21). This is due to losses in the reflection of light from the surface of the lattice and mirrors and insufficiently accurate initial coordination of the wave fronts of light

fluxes I_D and I_P. All these factors in the derivation of formula (4.21) we did not take into account, as they are not fundamental and because the measurement results are not affected, therefore, given these circumstances, to determine the shift Δx, you can use the formula

$$I = \frac{I_{max}}{2}\left[1 - \sin\left(\frac{2\pi}{\lambda}\Delta x + \Delta\varphi_0\right)\right], \qquad (4.22)$$

here I_{max} – the maximum value of the measured signal.

The initial phase of the mismatch $\Delta\varphi_0$ between the beams I_D and I_P and with the help of the mirror 6 (Fig.4.7), fixed on the piezoceramics, take the absolute value equal to $\pi/2$. In this case, when the offset Δx of the object is zero, the output signal I from the photodiode 8 is also zero, and the formula (4.22) takes the form

$$I = \frac{I_{max}}{2}\left[1 - \cos\left(\frac{2\pi}{\lambda}\Delta x\right)\right]. \qquad (4.23)$$

In Fig.4.9, the solid curve reflects the dependence $\frac{2I}{I_{max}}(\Delta x)$ calculated by formula (4.23), and the points correspond to the values of Δx and $\frac{2I}{I_{max}}$, which are obtained experimentally.
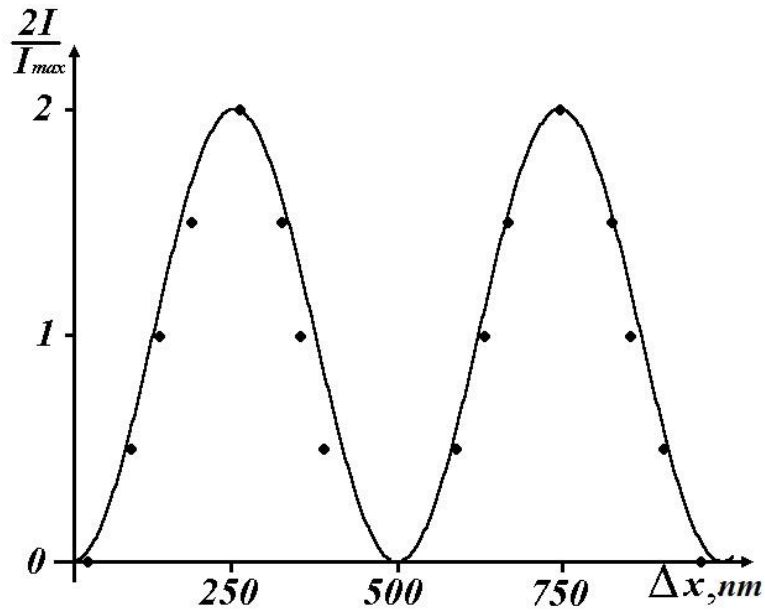
Fig.4.9. Dependence of the magnitude of the output signal I from the photodiode 8 (Fig.4.7) on the offset Δx of the object.

As can be seen from Fig.4.9, theoretically calculated by formula (4.23), and experimentally measured values $\dfrac{2I}{I_{max}}$ for specific quantities Δx are in fairly good agreement (as in Fig.4.8, curve 2, the offset Δx was determined by the magnitude of the control voltage U applied to piezoceramics).

Therefore, when the object is shifted, the change in the magnitude of the measured signal is periodic. If for the period T to accept change of intensity from zero to I_{max}, and then again to zero, for the period T of shift of object will make $\Delta x_{\mathrm{T}} = \lambda$.

Provided that I is in the range from zero to I_{max}, (at $|\Delta\varphi_0| = \dfrac{\pi}{2}$), the displacement Δx of the object is expressed by the formula

$$\Delta x_1 = \frac{\lambda}{2\pi}\left[\arccos\left(1 - \frac{2I}{I_{max}}\right)\right]. \tag{4.24}$$

In the case when I it is in the range from I_{max} to zero and $|\Delta\varphi_0| = \frac{\pi}{2}$) the displacement Δx of the object is expressed by the formula

$$\Delta x_2 = \frac{\lambda}{2} + \frac{\lambda}{2\pi}\left[\arccos\left(1 - \frac{2I}{I_{max}}\right)\right] = \frac{\lambda}{2} + \Delta x_1. \qquad (4.25)$$

It is possible to determine in which interval of change the measured signal I is located by the sign of the derivative functional dependence $I(\Delta x)$ given by the formula (4.22). If $\frac{dI}{d\Delta x} > 0$, then there is the first option, if $\frac{dI}{d\Delta x} < 0$ so, the second.

Thus, the process of measuring the movement Δx of the object is as follows: the displacement of the mirror 6 (Fig. 4.7) achieves at the output of the diode 8 zero signal ($I = 0$). Then we measure the movement Δx of the object. To do this, count the number n of periods of change of the output signal that occurred during the movement, and in the last period of change determine the magnitude of the output signal I and the sign of the derivative $\frac{dI}{d\Delta x}$. If the displacement is determined by the formula. If $\frac{dI}{d\Delta x} > 0$, so then according to the formula $\Delta x = n\lambda + \Delta x_1$. If $\frac{dI}{d\Delta x} < 0$ then according the formula $\Delta x = n\lambda + \Delta x_2 = n\lambda + \frac{\lambda}{2} + \Delta x_1$.

All these calculations are performed by a computer and give the final result.

If the direction of movement of the object changes to the opposite, it can be fixed by changing the sign of the derivative $\frac{dI}{d\Delta x}$ of the output signal. The range of measured shifts Δx is limited by the coherence length

of the laser. The absolute error of measurement of the value Δx_1 is calculated by the formula:

$$\Delta(\Delta x_1) = \frac{\lambda}{2\pi}\left[\arccos\left(1 - \frac{2(I + \Delta I)}{I_{max}}\right) - \arccos\left(1 - \frac{2I}{I_{max}}\right)\right],$$

here ΔI – the absolute error in the definition I of the photodetector 8 (Fig.4.6). The largest Δx measurement error is achieved in the area $I = 0$ and $I = I_{max}$. The value of the maximum absolute error $\Delta(\Delta x_1)_{max}$ at $I = 0$ (or $I = I_{max}$) is

$$\Delta(\Delta x_1)_{max} = \frac{\lambda}{2\pi}\left[\arccos\left(1 - \frac{2(\Delta I)}{I_{max}}\right)\right].$$

For most known serial photodetectors, such as silicon photodiodes, starting with FD-3, at laser power ≈ 5 mW relative measurement error $\frac{|\Delta I|}{I_{max}}$ can be estimated no worse than $\approx 0{,}5 \cdot 10^{-3}$ [275]. Then, provided that $\lambda = 632{,}8$ nm, we have:

$$\Delta(\Delta x_1)_{max} = \frac{\lambda}{2\pi}\left[\arccos(1 - 10^{-3})\right] \approx 4{,}5 \ nm.$$

The minimum absolute error $\Delta(\Delta x_1)_{min}$ is reached in the value of the output signal $I = \frac{I_{max}}{2}$. For this area, the absolute error $\Delta(\Delta x_1)$ is calculated by the formula

$$\Delta(\Delta x_1) = \frac{\lambda}{2\pi}\left|\left[\arccos\left(1 - \frac{2I}{I_{max}}\right)\right]'_I \Delta I\right| = \frac{\lambda}{2\pi} \cdot \frac{\dfrac{2|\Delta I|}{I_{max}}}{\sqrt{1 - \left(1 - \dfrac{2I}{I_{max}}\right)^2}}.$$

Hence, when $I = \frac{I_{max}}{2}$, $\lambda = 632{,}8$ nm and $\frac{|\Delta I|}{I_{max}} \approx 0{,}5 \cdot 10^{-3}$ get

$$\Delta(\Delta x_1)_{min} = \frac{\lambda}{2\pi} \cdot 10^{-3} \approx 0,1 \ nm.$$

We are currently developing an installation in which the computer, using the appropriate controller and software, controls the displacement of the mirror 6 (Fig.4.7) mounted on the piezoceramics, so that in the process of measuring the displacement Δx of the object can be carried out constant adjustment of the initial phase mismatch $\Delta\varphi_0$ between the beams $I_D(0)$ and $I_P(0)$ so that at any shift Δx of the object, the initial phase mismatch $\Delta\varphi_0$ corresponds to the output signal $I = \frac{I_{max}}{2}$.

It is assumed that in this case the absolute measurement error Δx will be the smallest. The results of such studies should be the subject of further research .

4.3. Multichannel spectroradiometer and light divider with controlled ratio of separated beams in the range 0÷1.

Optical elements obtained by holographic optics are very promising for the creation of high-speed multichannel spectroradiometers and light dividers in the visible and infrared regions of the spectrum. In contrast to the known high-speed multichannel photoelectric spectrometers, the radiometer [283] developed by us uses a holographic optical element, which is used both as a modulator (as described in Section 4.1) and as a dispersing system.

In the proposed embodiment, the HOE is a composition of three-dimensional transmitting diffraction gratings, sequentially or

simultaneously recorded by the holographic method with a common reference beam in the volume of the recording medium.

Lattice vectors are oriented in such a way as to provide the required spatial orientation of the separated beams. When a collimated beam of light from an emitting object hits the HOE, each grating, differently oriented to the incident beam, gives at the same time, according to Bragg's condition, only one selective spectral response, which allows to select with the required accuracy components of intensity at certain wavelengths (Fig.4.10).
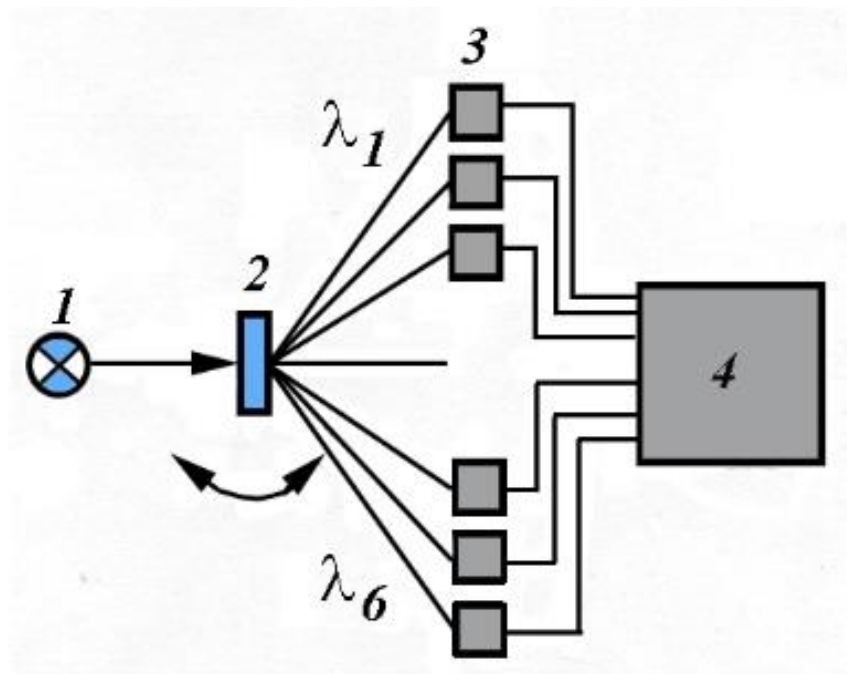
Fig.4.10. Schematic diagram of a multichannel spectroradiometer with HOE: 1 – light source, 2 – HOE, $\lambda_i, i = 1, ..., n$ – wavelengths of the emitted light flux, 3 – photodetectors, 4 – analyzer.

Spectroradiometer with HOE (Fig.4.10), used by us to determine the temperatures of local areas of the flame torch by color pyrometry. Up to 12 separate gratings were created in one HOE, which allowed to select the corresponding number of spectral components of radiation intensity at

different wavelengths without mutual interference. The analyzer 4 can record the intensity of radiation from the photodetectors 3 both DC and AC. In the first case, the HOE used remains stationary, and in the second case, the HOE is oscillated with amplitude, within the angular selectivity of the registered gratings.

Oscillations of HOE with frequency ω provided modulation of intensity with the same frequency. The frequency ω is selected so as to provide the required time resolution of the device (frequency range 10–10^4 Hz). Combination in one HOE of the dispersing system and the modulator working from the low-power generator causes low power consumption and small dimensions of the device.

The same device (Fig.4.10) can be used as a divider of monochromatic light flux by the required number of rays with a controlled ratio of the intensity of the separated beams in the interval $0 \div 1$. Control of the intensities of the separated beams is carried out by changing the orientation of the HOE relative to the incident beam. If the beam needs to be divided into two rays, it is sufficient to use only one three-dimensional diffraction grating. Separated rays in this case are transmitted and diffracted beams [282]. The great advantage of this splitter is that the direction of propagation of the transmitted and diffracted beams does not change when rotating the HOE.

4.4. Optoelectronic devices for measuring angular displacements and sighting.

4.4.1. Optoelectronic devices for measuring angular displacements in one coordinate.

Currently, high-precision remote sensing measurements of angular displacements are performed mainly with the help of optoelectronic angular measuring systems (OEMS), which are based on the autocollimation method of measurement [287].

The essence of this method is that the light flux with a known orientation is sent and then deflected by the object at the desired angle, so that this flux acquires the necessary information. In the autocollimation method, only the property of rectilinear propagation of light flux in a homogeneous medium is used for remote measurement of the angular position of objects from all parameters of light flux and changing its direction of propagation in accordance with the modulating effect of the object under study.

The results of measurements performed using such OEMS largely depend on the parameters of the photoelectric transducer (position-sensitive sensor) – a device that measures linear coordinates in the image plane of the OEMS and its conversion into electric current (voltage).

To implement the measuring functions, OEMS are equipped with various optical elements (lenses, prisms, diaphragms, etc.), mechanical and electromechanical components. Thus, obtaining the necessary data using OEMS is a multi-chain procedure for converting physical information signal, which is a significant disadvantage, especially in the

253

construction of high-precision systems, as the presence of additional conversion units leads to an increase in component errors of this measuring system. Traditional methods of increasing accuracy, based on improving the stability of the characteristics of the elements of measuring circuits and their converting units, have their limits and currently no longer lead to further significant improvements in the quality of OEMS.

Promising in this regard is the use of other measurement methods that would reduce the number of converters. This may be, for example, a method of measuring the angular displacement of objects based on changing the intensity of the information light signal in accordance with the modulating effect of the object under study, rather than changing the spatial position of the light beam, as in autocollimation method.

In this case, there is no need to use position-sensitive sensors to implement the measuring functions of OEMS – it is enough to use only photodetectors for photoelectric signal conversion, as the effect of information conversion for this method depends only on the intensity of incoming light. Currently, there are various receivers that allow you to implement almost all the requirements for modern OEMS in accuracy, speed and other technical design parameters.

This method is possible if you use a three-dimensional holographic diffraction grating as an optical element, as it has the property that when you change the angle of incidence of the object beam on the grating (as a result, for example, rotation of the controlled object) changes the intensity of transient and diffracted rays without changing their spatial location. The curves of the angular dependences of the intensities of the passed I_P (4.1) and diffracted I_D (4.2) rays are completely determined by the lattice

parameters and for gratings with diffraction efficiency $\eta = 100\%$ are shown in Fig.4.11.
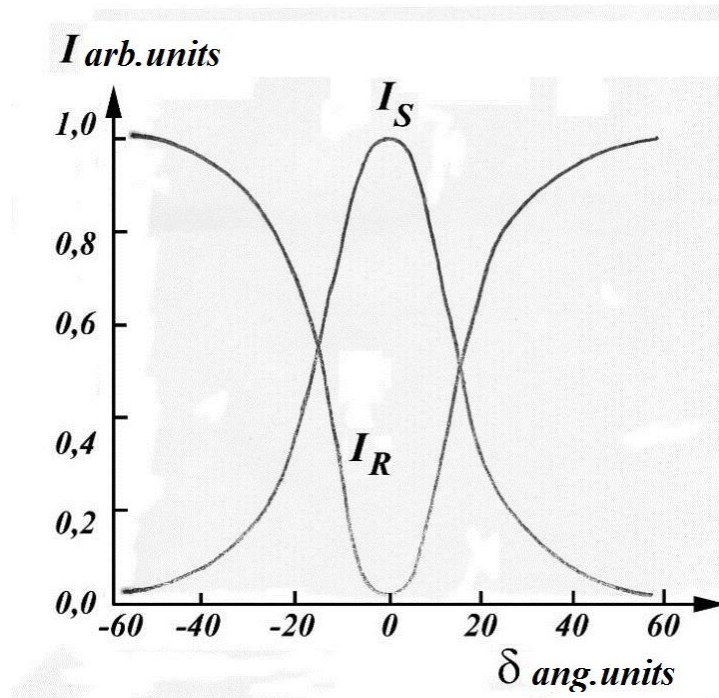
Fig.4.11. Angular dependences I_P and I_D for lattices with DE $\eta = 100\%$.

The direct use of dependences (4.1) or (4.2) to determine the angular displacement of the object δ by changing the intensity of the transmitted I_P or diffracted beam I_D (Fig.4.11) is associated with some shortcomings [88]. If for zero reference to choose, for example, the maximum value of the intensity of the diffracted beam, it corresponds to the extremum of dependence $I_D(\delta)$ and, therefore, in this area, measurements are characterized by large nonlinearity with respect to the direction of displacement of the object to the right or left.

These shortcomings can be eliminated if the difference between the intensities of the transmitted and diffracted rays is used for measurements $\Delta I = I_P - I_D$ [281]. For a purely phase lattice with $\eta = 100\%$ this dependence is presented in Fig.4.12.
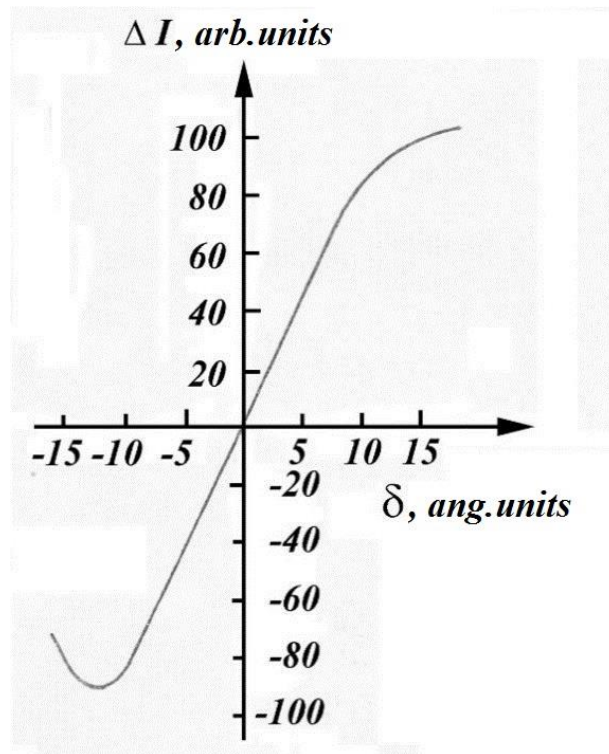
Fig.4.12. Angular dependence $\Delta I = I_\mathrm{P} - I_\mathrm{D}$. (Angular dependences I_P and I_D are shown in Fig.4.11).

In this case, the zero reference is the position when the intensities I_P and I_D are the same and the difference $\Delta I = 0$ (the level of intersection of the curves I_P and I_D in Fig.4.11). As can be seen from Fig.4.12, the dependence $\Delta I(\delta)$ near $\Delta = 0$ is linear, and the direction of angular displacement to the right or left differs in the sign of the output signal ΔI.

The largest linear range and symmetrical measurement limits in this case are achieved at the intersection of the curves of the angular dependences I_P and I_D and at the level of 0,5 of the maximum value. This condition is fulfilled only for lattices with $\eta = 100\%$, with less diffraction efficiency of intersection of curves of dependences I_P and I_D not symmetric concerning the maximum values (Fig.4.13) and the linear range of measurements decreases.
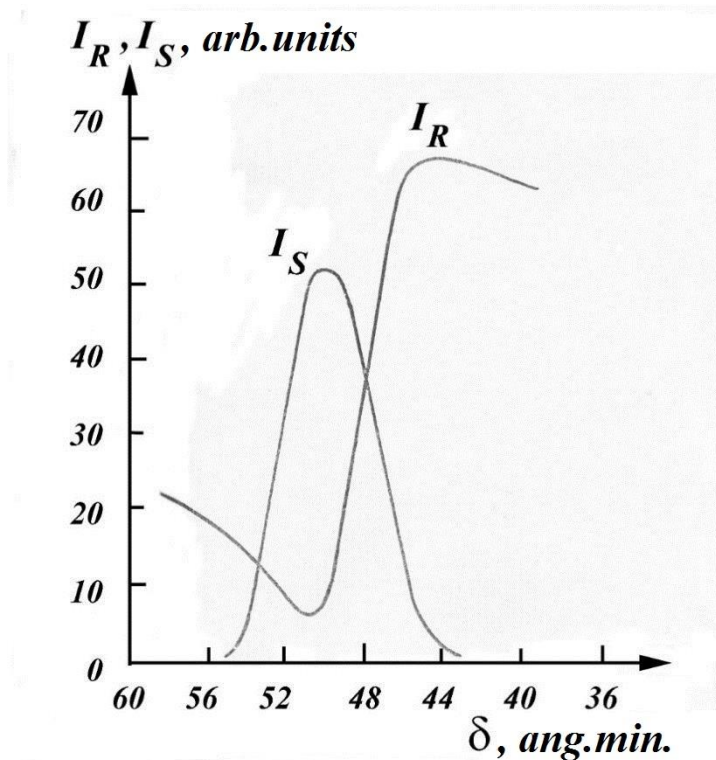
Fig.4.13. Angular dependences I_P and I_D for lattices with DE $\eta = 35\%$.

However, by changing the beam intensity I_P or the sensitivity of the photodetector, it is quite simple to shift the curve I_P parallel downwards and ensure the intersection of the curves I_P and I_D at the level of 0,5 of the maximum value I_D and thus restore the former range of measurements. Preservation of all the properties of the differential measurement method for gratings with $\eta = 100\%$ is also possible if for the angular displacement measurements use HOE, which is a combination of two gratings whose contours intersect at 0,5 of the maximum value of diffracting beams and recorded in the same light-sensitive region. environment [293]. In this case, as an information signal it is possible to use, for example, the difference in intensities of diffracted beams on the

corresponding gratings (Fig.4.14). The optical and electrical circuit of such a device is presented in Fig.4.15.
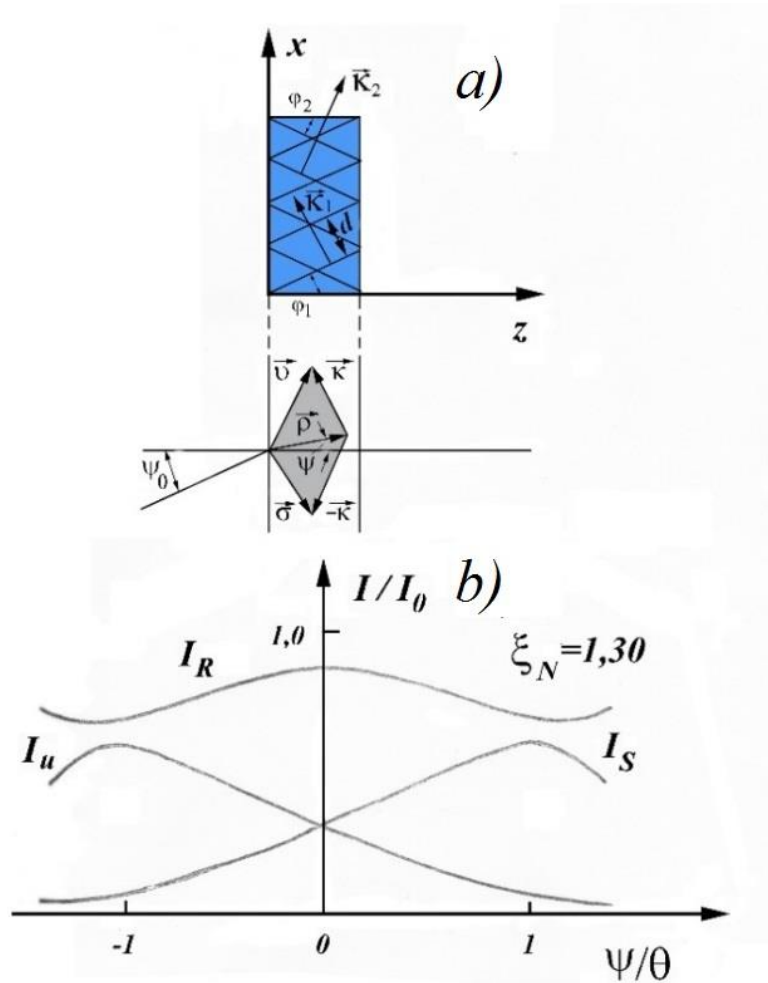
Fig.4.14. *a*) vector diagram explaining the diffraction of light on a three-dimensional combined grating; *b*) the dependence of the intensities of the transmitted beam I_R and diffracted beams I_S and I_u from the angle of incidence of light ψ, which is normalized to the angle of Bragg θ.
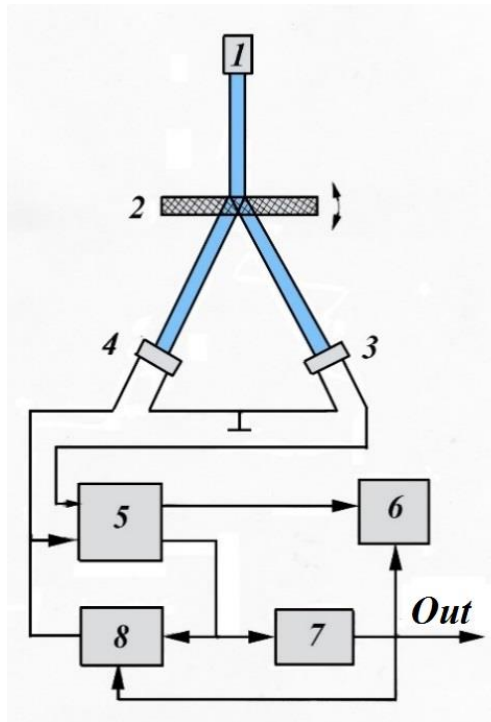
Fig.4.15. Schematic diagram of the angle of the measuring device: 1– emitter; 2 – HOE; 3, 4 – photodetectors; 5 – differential amplifier; 6 – display unit; 7 – three-stable comparator; 8 – gain regulator.

The device works as follows. The luminous flux from the emitter 1 falls on the HOE 2, the angular location of the plane relative to the optical axis of the luminous flux and is the object of measurement. The two diffracted beams coming out of the HOE are registered by photodetectors 3 and 4, which are switched on according to the differential circuit. The signal coming from the differential amplifier 5 enters the display unit 6 and the three-stable comparator 7 for communication with the gain controller 8, which is connected to the feedback circuit of the differential amplifier, and adjusts the sensitivity of the device.

HOE 2 is made in the form of a three-dimensional combined holographic diffraction structure consisting of two sublattices with the same period d and angles of inclination of the dash planes

259

$$\varphi_1 = -\varphi_2 = \varphi = \xi_N \frac{d}{\pi L} + \frac{\lambda}{2d\overline{n}}, \qquad (4.26)$$

here $\xi_N = 0,9 \div 1,3$ is the constant multiplier; L – thickness of the analyzer; λ – wavelength in the air; $\overline{n}$ – the average refractive index of the analyzer.

The analyzer is manufactured on the device, the schematic diagram of which is shown in Fig.4.16.
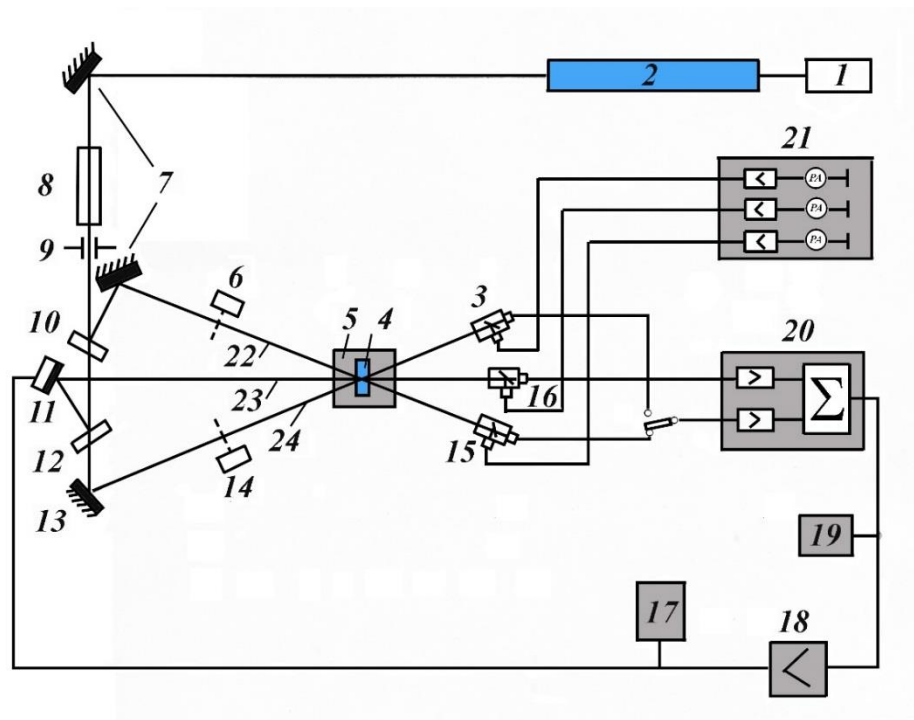
Fig.4.16. Schematic diagram of a device for recording a three-dimensional combined grating: 1 – laser power supply; 2 – laser; 3, 15, 16 – photodiodes; 4 – three-dimensional light-sensitive environment; 5 – oven-thermostat, which is installed on the turntable; 6, 14 – bolts; 7, 13 – mirrors; 8 – beam expander; 9 – diaphragm; 10, 12 – light divider; 11 – mirror mounted on piezoceramics; 17, 19 – oscilloscopes; 18, 20, 21 – electronic blocks of the system of stabilization and determination of holographic characteristics of sublattices; 22, 23, 24 – recording beams.

During the first exposure, the three-dimensional light-sensitive medium 4 is illuminated by two plane waves 22 and 23 incident at angles β_1 and β_2 determined by the ratio

$$\beta_{1,2} = arcsin\left[\bar{n}\sin\left(\varphi \pm arcsin\frac{\lambda_r}{2d\,\bar{n}}\right)\right], \qquad (4.27)$$

here λ_r is the wavelength of the laser radiation that records. The first sublattice is recorded. During the second exposure, the light-sensitive medium 4 is illuminated by two plane waves 23 and 24, which fall at angles $\beta_3 = -\beta_1$ and $\beta_4 = -\beta_2$, and the second sublattice is recorded.

The spatial distribution of the refractive index of the analyzer is described by the expression

$$n(\vec{r}) = \vec{n} + \Delta n_0\left(\cos\overrightarrow{K_1}\,\vec{r} + \cos\overrightarrow{K_2}\,\vec{r}\right), \qquad (4.28)$$

here Δn_0 – the amplitude of the modulation of the refractive index; $\overrightarrow{K_1}(K\cos\varphi, 0, -K\sin\varphi)$ and $\overrightarrow{K_2}(K\cos\varphi, 0, K\sin\varphi)$ – vectors of sublattices, $K = \left|\overrightarrow{K_1}\right| = \left|\overrightarrow{K_2}\right| = \frac{2\pi}{d}$.

The wave equation describing diffraction has the form

$$\nabla^2 E + \left[\alpha^2 + \varkappa\alpha\left(\cos\overrightarrow{K_1}\,\vec{r} + \cos\overrightarrow{K_2}\,\vec{r}\right)\right]E = 0, \qquad (4.29)$$

here $\alpha = \frac{2\pi\bar{n}}{\lambda}$, $\varkappa = \frac{\pi\Delta n_0}{\lambda}$, $\nabla^2 = \frac{\partial^2}{\partial x^2} + \frac{\partial^2}{\partial y^2} + \frac{\partial^2}{\partial z^2}$, E – is the complex amplitude of the wave field.

The solution of the wave equation (4.29) is sought in the form of the superposition of three waves 0 and ± 1 the diffraction orders:

$$E = R(z)exp(-i\vec{\rho}\vec{r}) + S(z)exp(-i\vec{\sigma}\vec{r}) + U(z)exp(-i\vec{u}\vec{r}), \qquad (4.30)$$

where z is the coordinate along the axis perpendicular to the plane of the analyzer; R, S, U – complex amplitudes of waves 0 and ± 1 of diffraction orders, respectively, $\vec{\rho}(\rho\sin\psi, 0, \rho\cos\psi)$ is the wave vector of the wave

incident at an angle ψ (in a light-sensitive medium), $\rho = |\vec{\rho}| = \alpha$, $\vec{\sigma}, \vec{u}$ is the wave vector of diffracted waves determined from the Floquet condition (see Fig.4.14): $\vec{\sigma} = \vec{\rho} - \vec{K}$, $\vec{u} = \vec{\rho} + \vec{K}$.

Substituting expression (4.30) into expression (4.29), after standard transformations we obtain a system of equations

$$C_R R' = i\varkappa(S + U),$$

$$C_S S' + i\Gamma_S S = -i\varkappa R,$$

$$C_U U' + i\Gamma_U U = -i\varkappa R, \qquad (4.31)$$

Where $C_R = \cos\psi$, $C_S = C_U = \cos\psi - \dfrac{K}{\alpha}\sin\varphi$, $\Gamma_S = -\dfrac{K\sin\theta}{\lambda} + K\sin(\psi + \varphi)$, $\Gamma_U = -K\sin\theta - K\sin(\psi - \varphi)$, θ is the Bragg angle in a light-sensitive medium.

The expression for the value included in the system (4.31) is simplified taking into account the small angle ψ ($\sin\psi \approx \psi$, $\cos\psi \approx 1$):

$C_R = 1$, $C_S = C_U = 1 - \dfrac{K}{\alpha}\sin\varphi\cos 2\theta'$, $\Gamma_S = (\theta + \psi)\alpha\sin 2\theta'$, $\Gamma_U = (\theta - \psi)\alpha\sin 2\theta'$, $\theta = \varphi - \theta'$. For the angle of incidence $\psi = \theta$, the Bragg condition for diffraction on the first sublattice and for $\psi = -\theta$ the second sublattice is satisfied.

The solution of the system (4.31) has the form

$$R(z) = \sum_{m=1}^{3} r_m \exp(i\gamma_m z),$$

$$S(z) = \sum_{m=1}^{3} s_m \exp(i\gamma_m z),$$

$$U(z) = \sum_{m=1}^{3} u_m \exp(i\gamma_m z),$$

where the roots of the characteristic equation $\gamma_1 = \frac{2}{L}\left(\frac{2\xi_N}{3} + \sqrt{A}\cos\tau\right)$,

$$\gamma_{2,3} = \left[\frac{2\xi_N}{3} + \sqrt{A}\cos\left(\tau \pm \frac{2\pi}{3}\right)\right].\tau = \frac{1}{3}arccos\frac{B}{A\sqrt{A}}$$

$$A = -\frac{4\xi_N^2 + 12\xi^2 + 6f^2}{9},,,,,.B = \left(\frac{4\xi_N}{3}\right)^3 - \frac{4\xi_N}{3}\left(2\xi_N^2 - 2\xi^2 - f^2\right) -$$

$$2\xi_N f^2 \xi_N = \frac{(\Gamma_S + \Gamma_U)L}{4C_S} \approx \theta\frac{\alpha L}{2}\tan 2\theta' \xi = \frac{(\Gamma_S + \Gamma_U)L}{4C_S} \approx \psi\frac{\alpha L}{2}\tan 2\theta' f =$$

$$\frac{\varkappa L}{\sqrt{C_R C_S}}$$

Now from equation (4.31) taking into account the standard limit requirements $R(0) = 1$, $S(0) = U(0) = 0$, get the expressions for the required coefficients:

$$s_1 = D(\gamma_3 - \gamma_2)\left(\gamma_3 + \gamma_2 + \frac{\Gamma_S}{C_S}\right),$$

$$s_2 = D(\gamma_3 - \gamma_1)\left(\gamma_3 + \gamma_1 + \frac{\Gamma_S}{C_S}\right),$$

$$s_3 = D(\gamma_2 - \gamma_1)\left(\gamma_2 + \gamma_1 + \frac{\Gamma_S}{C_S}\right),$$

here $D = \frac{\varkappa}{C_S(\gamma_2 - \gamma_1)(\gamma_2 - \gamma_3)(\gamma_3 - \gamma_1)}$.

Other coefficients are convenient to write down when using s_m:

$$u_m = s_m \frac{C_S\gamma_m + \Gamma_S}{C_S\gamma_m + \Gamma_u},$$

$$r_m = -s_m \cdot \sqrt{\frac{C_R}{C_S}} \cdot \frac{C_S\gamma_m + \Gamma_S}{\varkappa}.$$

Thus, the expressions for the intensities of transmitted and diffracted beams have the form

$$I_R = I_0 |R(L)|^2 = I_0 \left| \sum_{m=1}^{3} r_m exp(i\gamma_m z) \right|^2,$$

$$I_S = I_0 |S(L)|^2 = I_0 \left| \sum_{m=1}^{3} s_m exp(i\gamma_m z) \right|^2,$$

$$I_u = I_0 |U(L)|^2 = I_0 \left| \sum_{m=1}^{3} u_m exp(i\gamma_m z) \right|^2,$$

here I_0 is the intensity of the incident beam.

Figure 4.14 shows a graphical view of the dependence of the values I_R, I_S and I_u and the value of the angle of incidence ψ normalized to the angle θ.

This graph is very general, as the shape of the curves does not change at different values of the measurement range. The analysis of graphs I_S and I_u shows that when the angle of incidence changes due to energy exchange between the transmitted and diffracted beams, there is a change I_S and I_u with opposite signs that fix the photodetectors mounted on the optical axes of the diffracted beams and connected to the input of the differential amplifier. This minimizes the effect of additive interference caused, for example, by backlighting. The level of intersection of the curves I_S and I_u and is determined by the values of the intensities at the normal incidence of radiation and can be calculated using the parameter ξ_N. The influence of the parameter ξ_N on the normalized angular dependences of the signal $I_\Delta = I_S - I_u$ difference is shown in Fig.4.17.
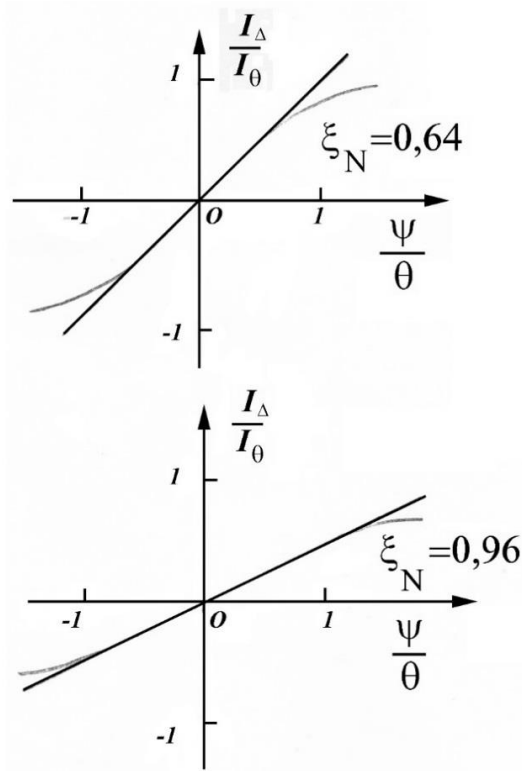
Fig.4.17. Dependence $I_\Delta = I_S - I_u$ on the angle of incidence ψ light normalized to the Bragg angle θ on HOE at various parameters ξ_N.

The change ξ_N leads to a change in the slope and width of the quasilinear section. Since the sensitivity of the device is determined by the product of the width of the linear range on the steepness of the transformation, the optimal values are $\xi_N = 1,0 \div 1,4$. The expression for ξ_N, taking into account the values entered in the system (4.31), can be written as $\xi_N = \dfrac{KL}{2C_S}(\sin\varphi - \sin\theta')$. The formula for calculating the angle φ of inclination of the plane of the strokes of the diffraction gratings HOE will be

$$\varphi \approx \sin\varphi \approx \xi_N \frac{2\cos\theta'}{KL} + \sin\theta' = \xi_N \frac{d}{\pi L} + \frac{\lambda}{2d\overline{n}}\left(1 - \xi_N \frac{\lambda}{\pi L \overline{n}}\right).$$

At real values included in the expression in parentheses, the second component can be neglected, which allows to determine the angles of

265

inclination of the plane of the strokes from the relation (4.26) with an error of not more than one percent.

The dependence of the sensitivity of the proposed device on the main parameters of HOE and photovoltaic circuits is derived taking into account that the sensitivity of the display unit is determined by its division price or discreteness $S_U = \frac{V_{max}}{N}$, where V_{max} – the input voltage corresponding to the maximum angle of incidence, N is a discrete number.

Going to the angular units, we obtain $S_\delta = 2\Delta\psi \frac{S_U \bar{n}}{K_\Phi I_S \Phi}$, where $\Delta\psi$ – half of the linear range, K_Φ – the conversion factor, $\Phi = \frac{\theta}{I_S} \frac{\partial I_\Delta}{\partial \psi}$.

For example, the range of measurements ± 150 at $\xi_N = 1,1, \lambda = 0,78\ \mu m, L = 10\ \mu m, \bar{n} = 1,47, \varphi = 12,4^0, \theta = 9,0^0$. If you use FD-24K photodetectors with a sensitivity of 0,5 A/W at a resistance of 10 $kOhm$, and as an emitter semiconductor laser power of 5 mW, and as an indicator digital voltmeter B7-VGA with a resolution of 1 mV, then in the measurement mode for differential amplifier with a coefficient equal to 2, we obtain the sensitivity $S_\delta = 5\ ang.s.$

In the mode of sight with a range of 3 angular minutes the sensitivity increases 50 times and is 0,1 $ang.s.$

4.4.2. Optoelectronic devices for sighting in two coordinates.

HOE, consisting of two sublattices, allow you to measure the angular displacements of the object in only one coordinate. To measure angular displacements simultaneously in two coordinates, it is necessary to record four sublattices in the volume of the light-sensitive medium, each pair of which provides independent measurement of angular

displacement in its coordinate [277]. The method of recording such HOE [285] was as follows:

1.   The light-sensitive medium 4 (Fig. 4.16) was oriented so that the beam 23 fell normal to the surface of the light-sensitive medium. Then the light-sensitive medium was rotated by $4 \div 6$ *ang.min.* in the direction of ray 24. In this state, rays 22 and 23 recorded the first sublattice.

2.   After recording the first sublattice, the light-sensitive medium returned to $8 \div 12$ *ang.min.* around the axis perpendicular to the plane of incidence of the rays in the direction of the beam 22, and in this direction the rays 23, 24 recorded the second sublattice.

3.   The light-sensitive medium rotated 90^0 around an axis lying in the plane of incidence of the rays and coinciding with the direction of the ray 23. After that, the third sublattice was recorded.

4.   The last, fourth sublattice, was recorded by rays 22 and 23 after the light-sensitive medium, after the recording of the third sublattice, which rotated in the direction of ray 24 by $8 \div 12$ *ang.min.* around an axis perpendicular to the plane of incidence.

When such a diffraction structure is illuminated by a monochromatic beam of light in the direction of the beam 23, four diffracted light beams are formed as a result of diffraction, located in pairs in mutually perpendicular planes (Fig. 4.18).
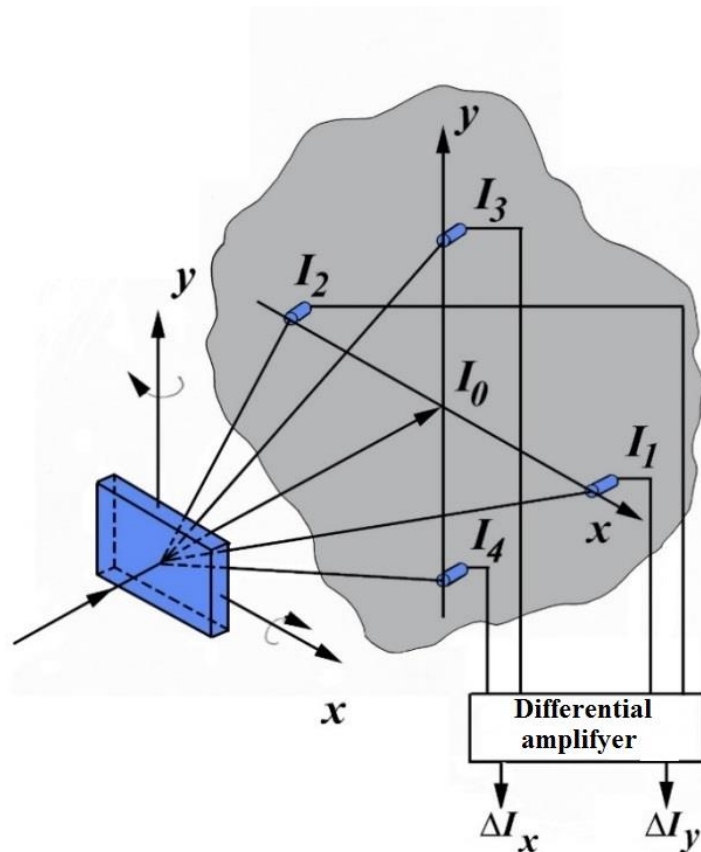
Fig.4.18. Diffraction of light on HOE – medium, in the volume of which four three-dimensional diffraction gratings are recorded: I_0 – beam of passing light; I_1, I_2, I_3 and I_4 – light beams diffracted on 1, 2, 3 and 4 sublattices, respectively.

Intensity of diffracted rays I_1, I_2, I_3 and I_4 depends on the orientation of the HOE relative to the incident light beam. When the HOE rotates around the axis Oy (Fig. 4.18), the intensities of the rays I_3 and I_4 remain unchanged, and change only the intensities of the rays I_1 and I_2. The angular dependences of the intensities I_1, I_2 and I_3, I_4 at the rotation of the HOE around Ox and Oy, accordingly, are shown in Fig.4.19.
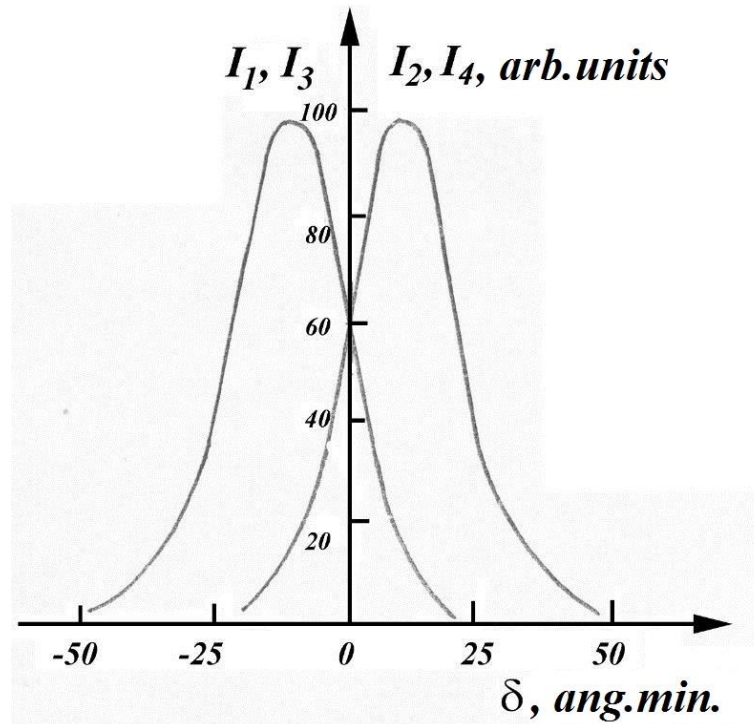
Fig.4.19. Angular dependence of the intensity of diffracted beams on the first I_1, second I_2, third I_3 and fourth I_4 sublattices: I_1, I_2 – when rotating the HOE relative to the axis Oy; I_3, I_4 – relative to the axis Ox.

The level of intersection of the angular selectivity curves I_1, I_2, I_3 and I_4 is determined by the value of the intensities curves I_1, I_2, I_3 and I_4 at the normal incidence of radiation on the HOE. In this case, the intensities of all rays are the same and this position of the HOE corresponds to zero. When changing the angle of incidence, as follows from Fig.4.19, as a result of energy exchange between the diffracted beams is a redistribution of intensities with opposite signs.

Thus, the diffraction of light on HOE has such properties that each pair of sublattices by changing the intensity of the beams diffracted on them can provide independent measurements of the angular displacement of objects at the appropriate coordinate. For this purpose it is necessary to install photodetectors only on the path of each of the diffracted beams

(Fig. 4.18), respectively, connected in pairs according to the differential scheme. Then the magnitude of the output signal of the differential amplifier $\Delta I_y = I_2 - I_1$ and $\Delta I_x = I_4 - I_3$ will be the magnitude and direction of the angular displacement of the light-sensitive medium relative to the incident beam, functionally dependent (4.30), and will be determined by the diffractive structure shown in Fig.4.20.
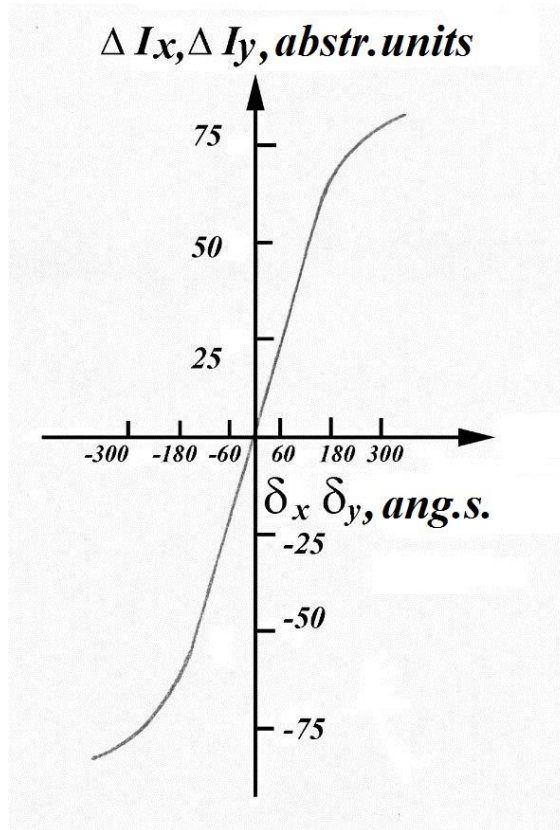
Fig.4.20. Dependence of the output values of the differential amplifier signal ΔI_y and ΔI_x from the angle of rotation of the HOE. δ_x − the angle of rotation of the HOE relative to the axis Oy; δ_y − relative to the axis Ox.

To use HOE in the sighting system, the device must be equipped with an inverse connection that provides compensation, which is caused by any reason for the rotation of the object from the specified direction.

The process of endorsement according to the proposed method is as follows. The device by which the sighting takes place in a given direction is associated with HOE. The laser beam of light falls on the HOE and determines the direction of sight. Light passing through the HOE forms five rays – four diffracted and one transmitted. The radiation passing through the diffraction structure coincides in the direction of propagation with the laser beam incident on the HOE, and does not participate in the operation of the device and continues to provide the direction of sight. The intensities of the diffracted rays are registered by sensors and fed to the input of the differential amplifier. The output signal from the amplifier, which corresponds to the difference $\Delta I_y = I_2 - I_1$, and $\Delta I_x = I_4 - I_3$, is fed to the actuator, which rotates the device depending on the polarity of the signal $(+ - \text{ or } - +)$, in one direction or another around the axis or Ox. In the case when $I_1 = I_2 = I_3 = I_4$ the actuator voltage is not applied, there is no rotation – the device registers the specified direction. If the sighting object (or sighting device) is returned, the redistribution of energy between the beams I_1, I_2, I_3 and I_4 the output of the amplifier signals ΔI_x and ΔI_y, forcing the actuator to rotate the sighting device around the axes Oy or Ox until the beam intensity reaches equality, and signals that return the device, compensate, and the device returns to its original state $(\Delta I_x = \Delta I_y = 0)$.

The process of sighting with the help of HOE can be carried out and scattered from the object of sight laser light. It is relatively easy to do this if the source of scattered light from the object of sight can be considered as a point. In this case, the HOE is placed in the focus of the collecting

lens, and the device registers the specified direction of sight ($\Delta I_x = \Delta I_y = 0$), when the point source of light scattered from the object of sight lies on the main optical axis of the lens. When the point source of scattered light deviates from the main optical axis of the lens, as a result of displacement of the sighting object (or sighting device), signals ΔI_x and ΔI_y appear at the amplifier output and which return the device to the initial state of registration of the specified direction of sight.

Thus, according to the obtained results, the use of angular selective properties of three-dimensional holographic diffraction gratings allows to create on their basis fundamentally new optical electronic devices, characterized by simplicity of design, high accuracy of measurements with wide functionality. It should also be noted that sharper angular selectivity of HOE and, accordingly, higher accuracy of measurements can be achieved when used recording speckle waves [294]. In addition, such HOEs also have a number of new properties and, first of all, translational selectivity [295], associated with the inconsistency of the recorded and read speckle structure. The change in the intensity of the recorded beam by 100% is achieved by shifting the diffraction structure by $\approx 5\ \mu m$. This allows the use of such diffraction structures not only for linear displacements based on two-coordinate HOE (Fig.4.18), as shown in Fig.4.21.
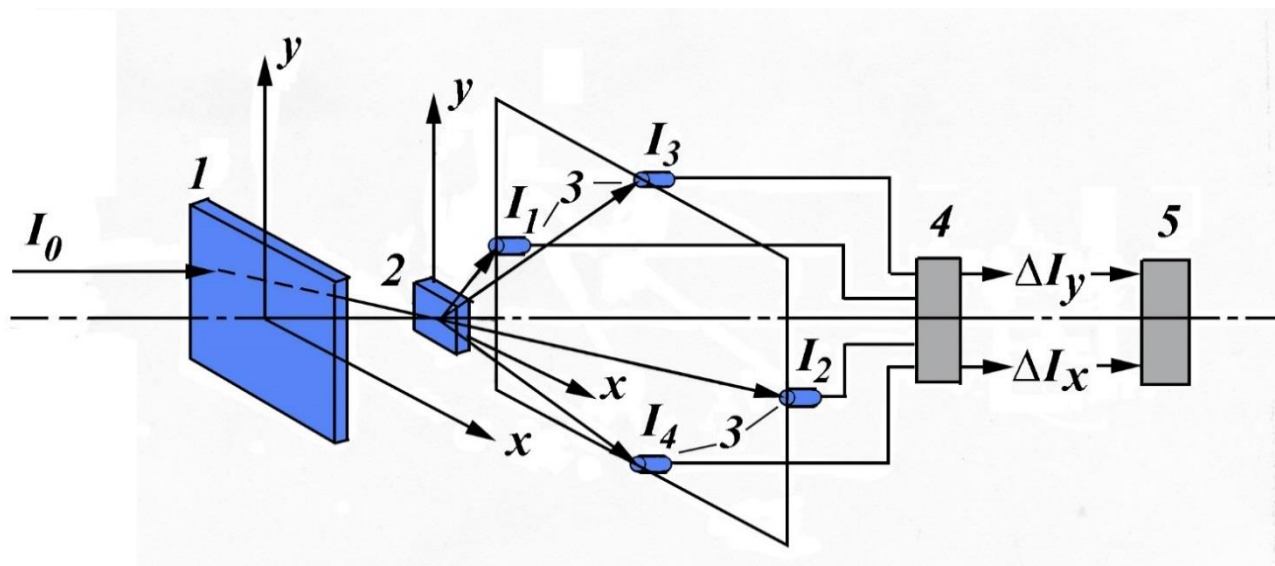
Fig.4.21. Schematic diagram of a two-coordinate sensor of the position of the laser beam based on HOE: 1 – holographic lens; 2 – HOE, consisting of 4 sublattices; 3 – photodetector; 4 – differential amplifier; 5 – indicator device.

When shifting the incident beam I_0 in the direction of the axes Ox or Oy on the surface of the holographic lens 1 changes the angle of incidence on the HOE 2 and, accordingly, the intensity of the diffracted rays I_1, I_2, I_3 and I_4. By changing the intensity of these rays determine the angle of incidence of the beam ψ on HOE 2. So, knowing the spatial location of the angle of incidence of the beam I_0 on the HOE 2, which is the focus F of the holographic lens 1, it is easy to determine the position of the beam I_0 on the holographic lens: $x = F \tan \psi_x$, $y = F \tan \psi_y$. The focal length of the holographic lens determines the range and accuracy of the measurement.

4.5. Registration and reproduction of light beams with topological defects.

Currently, an increasing number of robots are devoted to the study of light beams with dislocations of the wave front, or optical vortices. They can be considered as optical aberrations, fundamentally different from those considered in classical optics. The result of such aberrations on the surface of the wavefront and the simplest of them is spiral dislocation (SD) [296]. In this paper, we limit ourselves to the consideration of beams with SD.

If a beam is present in a beam that is close to a plane wave in its properties, then its wavefront can no longer be represented as a family of divergent surfaces, the distance between which is equal to the wavelength. In the cross section of such a beam there is a special point, around which in the plane perpendicular to the direction of propagation, the phase (argument of the complex field amplitude) varies on $\pm 2\pi$ depending on the direction of the bypass and the dislocation sign (right or left) present in the beam. The wave front in such beams is a spiral surface, the axis of which passes through special points. At these points, the phase of the wave is indeterminate (and, consequently, reaches absolute zero amplitude). Since the direction of propagation of light energy given by the Umov-Pointing vector is perpendicular to the surface of the wavefront, "vortices" of energy flow will occur in the vicinity of SD. These features make light beams with SD and other topological defects, interesting both from a theoretical point of view and, without a doubt, from a practical point of view. There is reason to believe that they should be widely used

in measuring and diagnostic systems [297]. There are already the first works of this kind, for example, related to the analysis of randomly inhomogeneous carriers (including turbulent atmosphere) [298], the vortex optical effect of Magnus can be used to analyze the quality of optical fibers [299] and so on.

However, now the number of such works is still small. Obviously, this is due not only to the novelty of this area, but also to the difficulties of the experimental plan. Obtaining beams from SD is not very difficult. Screw dislocations automatically occur in laser beams with a speckle structure [300], but their location and sign of dislocation cannot be controlled because they are random.

Also, beams with SD can be formed in the resonators of multimode lasers [301], where it is possible to adjust the formation of the so-called Laguerre-Gaussian mode, in which the distribution of radiation in the cross section has the shape of a ring (Fig. 4.22, *b*). In this case, there is a SD in the beam, the axis of which passes through the center of the dark spot. It is possible to obtain more complex modes of radiation with topological defects. This method of obtaining beams with HD is reliable and easy to use, but most modern lasers with a sufficient length of coherence work in single mode, and most do not have the ability to adjust. We used the LG-75 laser in our work.
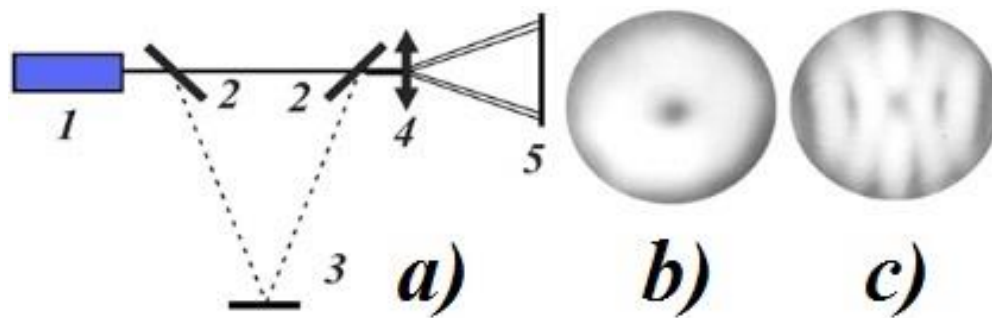
Fig.4.22. *a*) SD scheme in laser radiation that generates Lagerr-Gaussian mode (1 – LG-75 laser, 2 – translucent dividers, 3 – mirror, 4 – lens, 5 – screen);

b) cross section of the output beam;

c) picture of interference of two beams with SD of different signs.

There is another complication associated with the detection of SD. Since SD is a purely phase feature, it is possible to detect its presence only by interference with another beam – the analyzer, for example, as shown in Fig.4.22, *a*. In this case, two beams with dislocations of opposite signs interfere. Inversion of the dislocation sign is achieved if the difference in the number of reflections in the two arms of the interferometer is odd. The presence of SD is determined by the presence of characteristic "forks" (Fig. 4.22, *c*) in the interference pattern in cases of lateral displacement of the beams relative to each other, or loops in the case of radial displacement (change in radius of curvature). The simplest to consider is the case of interference of the beam with the SD and the beam-analyzer with a flat (spherical) wavefront.

Since it is impossible to obtain a stable interference pattern when superimposing the radiation of two lasers, it is necessary to have simple

and reliable ways to convert a beam from SD to a beam with a flat wavefront, or vice versa.

There are several tools that allow you to make such a transformation. One of the simplest ways to create a SD in a Gaussian beam with an initial flat or spherical front is described in [302] and shown in Fig.4.23, *a*.

The essence of the method is to enter the focus area of the laser beam of the object, which provides a sharp phase gradient (thin transparent plate, such as cover glass); which causes the formation of SD. This method is simple and reliable, can be used with any type of laser, but it has its drawbacks.

Fig.4.23. *a*) Scheme of conversion of a beam with a flat front into a beam with SD and its subsequent registration (1 – laser, 2 – translucent dividers, 3 – mirror, 4 – lenses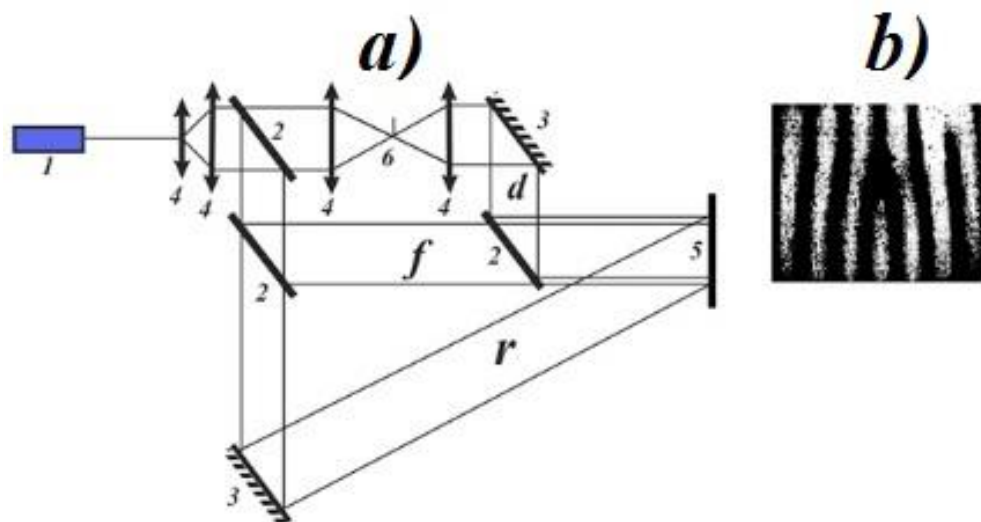, 5 – screen or holographic plate, 6 – cover glass, letters are marked: *d* – beam with dislocation, *f* – beam-analyzer with a flat front, *r* – reference beam for hologram recording);

b) pattern of interference of two beams *d* and *f*.

The main disadvantage of this method is that it is very sensitive to the displacement of all optical elements of the circuit, and therefore have to use standard holographic techniques – rigid mounts, careful protection against vibration, temperature fluctuations and so on.

From an experimental point of view, it is best to use holographic optical elements (HOE) as a source of SD, with which it is known that it is possible to perform almost any transformation of optical fields. Synthesized holograms are ideal, which allow you to get any predefined type of topological defects. This direction was intensively developed by M. S. Soskin and co-workers [303], but the production of synthesized holograms requires appropriate equipment, complex and expensive (at least for artificial production). Therefore, not synthesized holograms were used in this work, but holograms recorded in real conditions.

The method used by us is complex – first a beam with SD is created, respectively, one of the methods described above, and then with its help the hologram is written, which itself can serve as a source of SD in further experiments. For convenience, a beam with a flat or spherical front was used as a reference. The scheme of such a record is shown in Fig.4.23, *a*. Figure 4.23, *b* shows a picture of the interference of the beam with SD and the beam-analyzer with a flat front, which was used for holographic recording.

When restoring the hologram, the beam diffracted on it contains SD. The beam-analyzer for the detection of SD can be obtained in different ways – using standard optical elements (Fig.4.24, *a*), using an additional hologram (Fig.4.24, *b*), or it can be recorded on the same hologram with additional exposure (Fig. 4.24, *c*).
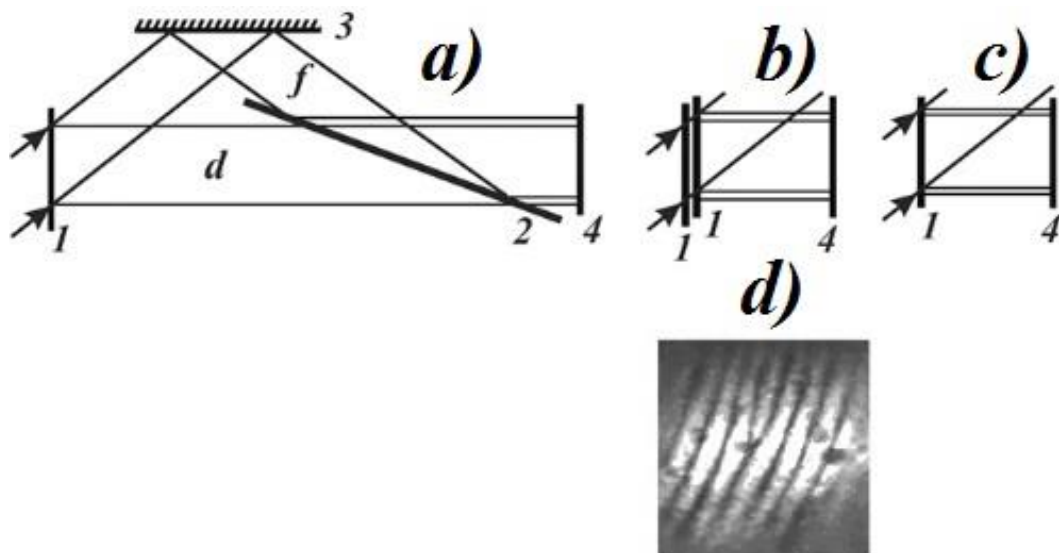
Fig.4.24. Possible options for restore of beams from SD and beams-analyzers: 1 – hologram (HOE), 2 – translucent dividers, 3 – mirror, 4 – screen.

The choice of one of these options depends on the conditions of the experiment. The picture of the interference of the beams obtained according to the scheme of Fig.4.24, *b*, is shown in Fig.4.24, *d*.

In this work, we used a silver halide photographic emulsion with heterophase microsystems of the composition "core CaF_2–shell $AgBr$ (I)" to obtain volumetric transmission holograms, the preparation and use of which is described in Section 1.

This emulsion has the following properties required in this case:

1. The effective thickness of the recorded holograms reached 60 μm, so the obtained HOE had all the qualities of volumetric holograms (when restored there is only one diffraction order, the direction of its propagation does not change when changing the angle of the hologram, and so on).

2. DE recorded holograms in transmitted light reaches 65%.

3. The photosensitivity of this emulsion is the same as in the case of silver halide photographic materials, the emulsion can be sensitized to different parts of the spectrum.

4. An important quality of the studied emulsion is a small change in the thickness of the hologram during processing (less than 10%), and, consequently, small distortions in the holograms.

Thus, we have created materials and developed a technique that allows to obtain highly efficient HOE, which can be used in experimental work as sources of beams with topological defects. Despite the fact that many available methods are now available for obtaining beams from SD [304], the use of such holographic techniques greatly facilitates and simplifies the setting of experiments in singular optics [305, 306], in addition, in most cases it may be the only possible option.

CONCLUSION

The technology of obtaining "core CaF_2–shell $AgBr$" emulsions with heterophase microsystems is proposed, which allows to realize a light-sensitive medium that preserves, on the one hand, the light sensitivity of silver halide emulsion, and on the other – to provide phase contrast and effective thickness sufficient for recording in convergent beams of three-dimensional transmitting hologram with high spectral and angular selectivity.

Specifics of spectral sensitization of heterophase microsystems "core CaF_2–shell $AgBr$", in which the fixation of the dye is possible on both the inner and outer surface of the silver halide shell, compared with conventional silver halide emulsions, allows not only to expand the spectral sensitivity of the emulsion in the long-wavelength part of the spectrum but also use lasers with different wavelengths of radiation for recording volumetric holograms.

To elucidate the mechanism of high-temperature photochemical transformations in CGS and AHC, a research method is proposed that provides the relationship between photoinduced changes in optical and photoelectric properties of CGS and AHC at elevated temperatures, as well as the ability to describe these changes from common positions. Based on the established mechanisms and specific properties of thermally activated photochemical processes in CGS and AHC, a new means of volume holographic recording is proposed, which provides an optically stable volume molecular diffraction structure with controlled parameters.

To eliminate the influence of various external factors on the stability of the interference pattern, which forms molecular diffraction structures

in the process of their exposure at elevated temperatures, we have developed a system of spatial stabilization of the interference pattern in the recording process. In addition, proposed measurement methods that allowed to establish at different points of the holographic recording changes in the absorption coefficient and refractive index (amplitude and phase components of the lattice), phase shift of the spatial distribution of the absorption coefficient and the refractive index of the lattice relative to the recording interference coefficients of absorption and refraction of the lattice.

All this allowed the methods of holographic optics to develop a technology for the manufacture of three-dimensional transmitting holographic optical elements with controlled characteristics for different optical devices that have unique properties that are unattainable in other ways:

- for amplitude modulation and phase-amplitude transformation of a light wave;

- for measuring linear displacements in the nanometer range;

- for the spatial separation of monochromatic light flux, the required number of rays with a controlled ratio of the intensities of the distributed beams in the interval $0 \div 1$;

- for measurement of angular displacements and sighting both on one, and on two coordinates;

- for registration and reproduction of light beams with topological defects.

REFERENCE

1.   Leith E., Upatnieks J. Reconstructed wave fronts and communication theory.//J. Opt. Soc.Am.–1962,–Vol.52, № 10,–P. 1123–1130.

2.   Leith E., Upatnieks J. Wavefront reconstruction with continuous tone objects.//J. Opt. Soc. Am.–1963,–Vol.53, № 12,–P. 1377-1381.

3.   Leith E., Upatnieks J. Wavefront reconstruction with diffused illumination and three-dimensional objects.//J. Opt.Soc. Am.–1964,–Vol. 54, № 11,–P. 1295–1301.

4.   Denisyuk Yu. N. Some problems and prospects of holography in three-dimensional carriers//Optical holography. – Mir: 1982. – V. 2. – P. 691–729.

5.   Gaylord T.K., Moharam M.G. Analysis and application of optical diffraction on gratings//TIIER. – 1985. – V. 73, № 5. – P. 53–103.

6.   Evald P. Crystal optics of visible light and X-rays//UFN. – 1966. – V. 89, Ed. 2. – P. 287–299.

7.   Sukhanov V.I. Three-dimensional deep holograms and materials for their recording//Optical magazine.–1994–№ 1.–Pp. 61–70.

8.   Sakhno S.V., Smirnova T.N., Tikhonov E.A. Characteristics of holographic recording at maximum achievable thicknesses of the recording three-dimensional material//JTP. – 1993. – V. 63, Ed.12. – P. 70-79.

9.   Barachevsky V.A. Photosensitive recording carriers: application in holography. In the book: Yu. N. Denisyuk – the founder of

domestic holography: Collection of works of the All-Russian seminar.//SPb: SPbGUITMO. – 2007. – P. 226–240.

10. Dmitriev A.L. Volume holograms in devices of fiber-optic information transmission systems. // Optical holography with recording in three-dimensional carriers. – L .: Science. – 1989. – P. 112–117.

11. T. Ya. Kalnitskaya, A.M. Korsakova, etc. Holographic light separator on a layer of bichrome gelatin. // Optics and spectroscopy. - 1989. - V. 67, Ed.1. – P. 212–214.

12. Odulov S.G., Soskin M.S., Khizhnyak A.I. Lasers on dynamic lattices. // M .: Nauka. – 1990.

13. B.L. Volodin, S.V. Dolgy, E.D. Melnik, E. Downs, J. Shaw, V.S. Ban.Wavelength stabilization and spectrum narrowing of high-power multimode laser diodes and arrays by use of volume Bragg gratings //Opt. Lett., 29, 1891–1893, (2004).

14. Denisyuk Yu. N. On the mapping of the optical properties of an object in the wave field of the radiation scattered by it. // Dokl. USSR Academy of Sciences. – 1962. – V. 144, Ed. 6.–P.p. 1275–1278; Optics and spectroscopy. Part I. – 1963. –V. 15, №4. – P. 522-532; Optics and spectroscopy. Part II – 1965. – Vol. 18, №2. – P. 286–293.

15. Lashkov G.I., Sukhanov G.I. Rheoxane polymers are a new class of non-silver light-sensitive materials for holography.// Proceedings of the GOI. – 1987. – V. 83, Ed.197. – P. 18–54.

16. Collier R., Berkhart K., Lynn L. Optical holography. Transl. From English–M., Mir, 1973.–686 p.

17. V.A. Barachevsky. Current state of development of light-sensitive carriers for holography (review) //Optics and spectroscopy.–2018–V. 124, issue. 3.–P.p. 371–399.

18. Vanin V.A., Vagin L.N., Korolev V.A. Comparative holographic characteristics of high-resolution photoplates. // Recording carriers for holography. – L .: Science. – 1975. – P. 69–79.

19. New recording carriers for holography. // Ed. V.A. Barachevsky.–L .: Science. – 1983.–199 p.

20. Gomza Yu. P., Kuzilin Yu. E., Melnichenko Yu. B., Shilov V.V. The mechanism of phase contrast formation in recording layers based on bichromed gelatin. // Successes of scientific photography. V. XXVI.–M .: Science,–1990–P.p. 124–136.

21. Kuchinsky S.A., Sukhanov V.I., Khazova M.V. The principle of hologram formation in capillary composites. // Optics and spectroscopy. – 1992. – V. 72, issue 3. – P. 716–730.

22. V.I. Sukhanov, M.V. Khazova, N.S. Shelekhov, etc. Volume phase holograms in light-sensitive systems with capillary structure. // Optical holography with recording in three-dimensional carriers. – L .: Science. – 1989. – P. 86–105.

23. Yavorskaya N.I., Prevarsky S.A., Voznaya S.V. Spectral sensitization of chromed gelatin to red light. // Recording carriers for pictorial holography and cinematography. – L.: Science. – 1979.–P.p. 116–119.

24. Non-silver photographic processes. // Ed. A.L Kartuzhansky. – L .: Chemistry. – 1984.–376 p.

25. Barachevsky V.A., Lashkov G.I., Tsekhomsky V.A. Photochromism and its application. // M .: Chemistry. – 1977.–277 p.

26. Recording carriers for holography. Ed. N.I. Kirillov and V.A. Barachevsky.–L .: Science. – 1975.–165 p.

27. Schwartz K.K. Physics of optical recording in dielectrics and semiconductors.–Riga: Zinatne. – 1986.–232 P.

28. Tyurin A.V., Popov A. Yu., Mandel V.E, Belous VM., Mechanisms of high-temperature holographic recording in composition materials *As-S*. // FTT.–1996–V. 38, № 2.–P.p. 379-390.

29. Belous V.M., Mandel V.E., Popov A. Yu., Tyurin A.V. Holographic recording mechanisms based on photothermal transformation of color centers in additively colored alkali-halide crystals. // Optics and spectroscopy.–1999–V. 87, №2.–P.p. 327–332.

30. Alekseev-Popov A.V., Dyachenko N.G., Mandel V.E, Tyurin A.V. Peculiarities of hologram recording in KCl crystals based on F$\rightarrow$X transformation. // Letters to JETF.–1979–Vol. 5, issue 12.–P.p. 709–713.

31. Ozols A.O. Limit characteristics of amplitude-phase holograms on additively colored KBr crystals. // Izv. AN Latv.SSR. Ser. Phys. and tech. Science.–1978, №5,–P.p. 16 – 25.

32. V.V. Belza, Yu. Yu. Blinets, etc. Optical elements based on chalcogenide glasses. // Journal of Applied Spectroscopy. – 1983. – V. 39, №2. – P. 295–299.

33. A. Tyurin, S. Zhukov, A. Akhmerov. Creation, properties and application of three-dimensional holographic optical elements (based on microsystems "CaF$_2$ core - AgBr shell"). Monograph // LAP LAMBERT

Academic PublishingGmbH & Co.KG.2021. 120 c. ISBN-13: 978-620-4-20857-2. 2021. 120 p.

34. Chibisov K.V. Nature of photographic sensitivity / K.V. Chibisov – M .: Nauka, 1980. – P. 16.

35. Honigman B. Growth and shape of crystals / B. Honigman // - M .: IL: 1961. – P. 15.

36. Processes of real crystal formation edited by N.V. Belov – M.: Nauka, 1977. – P. 15.

37. Belous V.M. Photographic Emulsions with Heterophase Microcrystals of "Non Silver Core – Silver Halide Shell" Type / V.M. Belous, D.G. Nizhner, V.P. Churashov // IS&T's 48th Annual Conference Imaging on the Information Superhighway May 7–11, 1995. – Washington. – P. 337–340.

38. Zhirov N.F. Luminophores (luminous solid compositions) / N.F. Zhirov //– M .: Oborongiz, 1940. – 478 p.

39. Urusov S.V. Theoretical Crystal Chemistry // 1987. M: Ed. MSU, 272 p.

40. Chibisov K.V. Photographic developing / K.V. Chibisov – M.: Science. – 1989. – 208 p.

41. K. Mirofushi, A. Hirata, Y, Tsunoda et. Al. // Proc. Int. Conf. of Phot. Sci., Tokyo 1967, Sec. 1.

42. Protas I.R. High-resolution photographic materials / I.R. Protas//Zh. Nauchn. and Appl. Photo- and Cinematography. – 1969. – Vol. 14, issue. 3. – P. 209–211.

43. Podorozhnaya L.V. Crystallization and properties of homogeneous composite microcrystals of silver halides of photographic

emulsions/L.V. Podorozhnaya: Author's abstract. dis. Cand. techn. Science. – M .: GosNIIChymPhotoProekt, 1992. – 17 p.

44. Moisar E. Der Einflub der Wachstumbedingungen suf die Kristalltracht der Silberhalogenide / E. Moisar, E. Klein,//Ber. Bunsennges. –1963. – B. 67, N 9. – S. 946–956.

45. Claes F.H., Lebeer F., Vanasche W. Cristal habit modification of AgCl by impurities determination // J. Photogr. Sci. – 1973. – V. 21, N1. – P. 21–39.

46. Moisar E. Formation nature and action of sensitivity center and latent image specs // Photogr. Sci. Eng. – 1981. – V. 25, N 1. – P. 45-50.

47. Trivelli A.P. The Silver Bromide Grain of Photographic Emulsions/A.P. Trivelli, S.E. Sheppard//1921, Van Nostrand Cy, N.J., Eastmen Kodak Co., Rochester.

48. Breslav Yu. A., Uksusova V.A. Homogeneous photographic emulsions // ZhNiPFiK – 1974. – Vol.2, issue. 4., P.p. 296–316.

49. Shapiro B.I. Aggregation of cyanine dyes: photographic problems//Advances in chemistry. – 1994. – T. 63, N 3. – S. 243–267; A.V. Tyurin, S.A. Zhukov, O.V. Lamzaki. Interaction of dyes with nanoclusters adsorbed on the surface of AgBr microcrystals.//Optics and spectroscopy. – 2012. – Vol.112, № 5. – P. 771–778.

50. James T.H. Theory of the photographic process//–L.: Chemistry, 1980. 672 p .; A.V. Tyurin, S.A. Zhukov, O.V. Lamzaki. Spectral sensitization of an emulsion containing heterophase microsystems "CaF_2 core – AgBr shell"//Bulletin of the Kharkiv National University, series "Physics", – 2012, № 1020, vol. 17, p.p. 68–73.

51.   Gorokhovsky Yu. N. Spectral research of the photographic process / Yu. N. Gorokhovsky. – M .: Fizmatgiz. – 1960. 183 p.

52.   Zhukov S.O. Photoinduced physicochemical processes and their sensitization in microsystems "core - silver halide shell". Abstract of the dissertation for the degree of Doctor of Physical and Mathematical Sciences. Sciences in the specialty 04/01/17. Odessa, 2018, 43 p.

53.   Belous V.M. Nizhner, N.A. Orlovskaya N.A., and PG Khersonskaya P.G., "Overgrowth of adsorbed dye by a silver halide shell in heterophase microcrystals," Zhurn. Scientific and adv. photogr. and cinematography. – 1990. – Vol. 35, issue. 4. – P. 299–301.

54.   V.M. Belous, V.I. Tolstobrov, V.I., and Shapiro, B.I., "Luminescent investigations of the mechanism of spectral sensitization of 1,1'-diethyl, -2,2' – cyanine by halide-silver photographic emulsions // Optics and spectroscopy. . – 1980. – T. 49, issue. 3. – P. 532-537.

55.   Nizhner D.G. Preparation and Properties of Photographic Emulsions with Heterophase Microcrystals Comprising Nonsilver Cores and Silver Halide Shells / D.G. Nizhner, V.M. Belous, V.P. Churashov // J. Imag. Sci. and Techn. – 1995. – V. 39, №1. – P. 56-66.

56.   Belous V.M., Zhukov S.A., Sviridova O.I. Features of chemical sensitization of photographic emulsions obtained using ammonia. // Chemistry of high energies. – 2005. – V. 39, №1. – P. 36–38.

57.   Tyurin A.V. Churashov V.P., Zhukov S.A., and Pavlova O.V., "Mechanism of anti-Stokes luminescence of silver halide-sensitized emulsion," Optics and Spectroscopy. – 2008. – V. 104, № 2. – P. 249–256.

58. Tyurin A.V. Churashov V.P., Zhukov S.A., Manchenko L.I., and Levitskaya T.F., "Interaction of molecular and polymolecular forms of dye" Optics and Spectroscopy. –2008. – V. 104, № 1. – P. 968–974.

59. W. M. Belous. Photographic emulsion with heterophase microcrystals – a new medium for recording deep three-dimensional transmitting holograms / V.M. Belous, L.I. Manchenko, A. Yu. Popov, etc. // Optics and spectroscopy. – 1999. –V. 86, №2. – P. 344–348.

60. Churashov V.P. Principles and properties of small-silver photographic materials with heterophasic microcrystals for roentgenography and holography the dissertation Author's abstract on degree of cand. physical and mathematical Science. Odessa 2001;

61. A.V. Tyurin, SA Zhukov, VP Churashov. Spectral sensitization by dyes of microsystems "core – silver halide shell". // Optics and spectroscopy. –2015, Vol. 119, № 3, p.p. 107-115.

62. D.G. Nizhner, V.M. Belous, V.P. Churashov, etc. Low-silver photographic materials with heterophase microcrystals // Journal. scientific and adv. Photogr., and cinematogr. – 1992. – V. 37, № 2. – P. 132–139;

63. Tyurin A.V., Zhukov S.A., Berkov Yu. N., Akhmerov A.A., Zelenin P.V. Interaction of photoexcited molecular and polymolecular dye forms adsorbed on the surface of AgHal microcrystals. // Bulletin of Kharkiv National University, series "Physics", – 2010, – P. 210–221.

64. Nizhner D.G., Belous V.M., Chibisov K.V. Peculiarities of the developing of emulsion microcrystals of the type "non-silver nucleus - light-sensitive silver halide shell" // Journal. scientific and approx. photo and cinematography – 1987. V. 32, № 5. – P. 391–393;

65.   A.V. Tyurin, V.P. Churashov, S.A. Zhukov, T.F. Levitskaya, Yu. N. Berkov. Interaction of dyes with Ag_2S nanoclusters adsorbed on AgBr microcrystals. // Optics and spectroscopy. – 2010. – V. 108, № 6. – P. 107–113.

66.   Tyurin A.V., Bekshaev A. Ya., Zhukov S.A. Interaction between the molecular and aggregated states of the photosensitive organic dyes adsorbed on the surface of AgHal microcrystals // Proc. SPIE 11475, Organic and Hybrid Sensors and Bioelectronics XIII, 114751B (21 August 2020).

67.   Bischop S.G., Strom V., Taylor R.S. Optically induced metastable paramagnetic states in amorphous semiconductors. // Phys. Rev. – 1977. – V. 158, N 4. – R. 2278-2294.

68.   Tau1og R.S., Strom V., Bischop S.G. Temperature dependence of the density of optically induced localized paramagnetic states in glassy As_2Se_3. // Phil. Mag. – 1978. – V. 378, N 3. – R. 241–247.

69.   Treacy D.J., Taylor P.C., Klein P.B. Photo darkening and photo structural effects in glassy As_2Se_3. // Solid. State. Commun. –1979. – V. 32, N 6. – R. 423–428.

70.   Karnatovsky V.E., Nalivayko V.I., Zuckerman V.G. Reversible recording of holograms in chalcogenide glassy semiconductors in the region of elevated temperatures. // Quantum electron. – M., 1978. – V. 3, № 1. –P. 219–221.

71.   Zuckerman V.G. Recording holograms in chalcogenide materials of the system *As-S*. // New recording carriers for holography. – L .: Nauka, 1983. – P. 45–64.

72. N.G. Dyachenko. Temperature studies of photoelectric and optical properties of chalcogenide glassy semiconductors of the system *As-S*. / N.G. Dyachenko, V.E. Karnatovsky, V.E. Mandel, A.V. Tyurin, etc. // Autometry. – 1979. – № 3. – P. 78–85.

73. Krasnov V.F., Remesnik B.G. On the mechanism of reversible photostructural transformations in As_2S_3 films. // Autometry. – 1980. – № 6. – P. 101–105.

74. Tanaka K. Photo-induced dynamic changes in amorphous film. // Solid State Commun. – 1980. – V. 34, N 3. – P. 201–204.

75. Ruske E. Reversibility of photo induced edge shift in evaporated amorphous As_2S_3 film. // Phys. Stat. Solidi (a). – 1976. – V. 35, N 2. – K113-K114.

76. B.P. Averyanov. Thermo-optical transitions during photostructural transformations of HSP. / B.P. Averyanov, AV Kolobov, BT Kolomiets, ZM Lyubin. // Letters to ZhZTF. – 1979. –V. 30, issue. 9. – P. 621–624.

77. Zhdanov V.G., Malinovsky V.K. Photoinduced birefringence and dichroism in As_2S_3 films. // Letters to JETF. – 1977. – Vol. 3, issue. 18. – P. 943–946.

78. Vlasov V.I., Semak D.G., Chepur D.V. On the mechanism of photoinduced changes in optical constants in chalcogenide-based glasses*As-S*e. // Izv. High School. Physics –1978.– Vol. 12. –P. 48–52.

79. Lyubin V.M. New in the physics of glassy semiconductors. // Physics of complex semiconductor materials. – L .: FTI, 1979. P. 108–126.

80.   N.G. Dyachenko. Photoinduced changes in the photoelectric and optical properties of vitreous As_2S_3. / N.G. Dyachenko, V.G. Remesnik, A.V. Tyurin and others // UFZh. – 1982. – V. 27, № 8. – P. 1147–1152.

81.   N.G. Dyachenko. Features of temperature dependence of photostructural transformations in system material *As-S*. / N.G. Dyachenko, V.E. Karnatovsky, V.E. Mandel, A.V. Tyurin, etc. // ZhNiPFiK. –1979. – V. 24, issue. 5. – P. 385–387.

82.   V.G. Tsukerman. Characteristic Features of Temperature Dependence of Photoelectric Properties and Photo Structure Transformations in the*As-S*system material. / V.G. Tsukerman, N.G. Djachenko, A.V. Tyurin at. al. // The Proc. Of the International Conference Amorphous Semicond. 1978. – CSSR, Pardubice, 1978. – P. 673–675.

83.   N.G. Dyachenko. Photoinduced changes in optical and photoelectric properties of arsenic vitreous sulfide. / N.G. Dyachenko, L.E. Stys, A.V. Tyurin, etc. // Photochemical processes of hologram registration. – L .: FTI, 1983. – P. 84–88.

84.   V.L. Averianov. Thermal and optical bleaching in darkened film of chalcogenide semiconductors. / V.L. Averianov, A.V. Kolobov, B.T. Kolomiets, V.M. Lyubin // Phys. Solid Status. – 1980. – V. 57, N 1. – P. 61–88.

85.   Street R.A. Recombination in amorphous semiconductors. // Phys. Rev. (b). – 1978. – V. 17, N 10. – P. 3984–3995.

86. Tonaka K. Photo-induced dynamical change in refractive index in amorphous *As-S* film. // Solid State Common. – 1978. – V.18, N 7. – P. 541-546.

87. Semak D.G., Kikineshi A.A., Turyanitsa I.I .On the efficiency of holographic recording on the chalcogenide layer. // ZhNiPFiK. – 1977. –№2. – P. 138–139.

88. Street R. A., Mott N. F. State in the gap in glassy semiconductor. // Phys. Rev. Lettr. – 1975. – V. 35, N 22. – P. 1293-1297.

89. N.G. Dyachenko. Features of photoelectric phenomena in vitreous As_2S_3. / N.G. Dyachenko, A. Yu. Popov, A.V. Tyurin, A.S. Sheveleva. // UFN. – 1983. –V. 28, № 5. – P. 742–748.

90. Stys L.E., Foigel M.G. Deep levels in arsenic chalcogenides. // FTP. – 1979. – V. 13, № 11. – P. 2087–2095.

91. Glassy arsenic sulfide and its alloys. / Ed. Kolomiytsa B.T. - Chisinau: Stiinza, 1981. – 212 p.

92. Nechaeva T.A., Popov A. Yu., Tyurin A.V. Photoconductivity of additively colored KSl crystals containing F centers. // Dep. in VINITI, 12.05.87, № 3412-B87. – 12 p. / Abstract in UFJ. – 1987. – V. 32, № 9. – P.1434.

93. N.G. Dyachenko. On the flash nature of the kinetics of photocurrent growth in vitreous arsenic sulfide. / N.G. Dyachenko, A. Yu. Popov, A.V. Tyurin and others // Phys. and tech. semiconductors. –1982. – V. 16, issue. 10. –P. 1872– 1874.

94. Kolomiets B. T. Lyubin V. N. Photoelectric phenomena in amorphous semiconductors. // Phys. Stat. Sol. A. – 1973. – V.17; N1. P.11-46.

95.   A.N. Aleshin. Isothermal relaxation of dark current in lead sulfide films. // A.N. Aleshin, A.V. Burlak, A.V. Tyurin, etc. // Proceedings of the IV International Conference on Physics and Technology of Thin Films. – Ivano-Frankivsk: Precarpathian University. V.S. Stefanica. 1993, Part II. – P. 260.

96.   Sheveleva A.S. Photoelectric studies of thermo- and photostructural transformations in system materials *As-S*. // Abstract of the candidate's dissertation. – Odessa: OGU, 1983. – 19 p.

97.   A. V. Burlak. Features of electrophysical characteristics of thin PbS layers with low oxidant content. / A.V. Burlak, A.V. Tyurin and others // FTP. – 1992. – V. 26, issue. 3. – P. 546–550.

98.   A. V. Burlak. Mechanism of low-temperature photoconductivity of polycrystalline p-PbS films. / A.V. Burlak, A.V. Tyurin, etc. // Materials IV International Conference on Physics and Technology of Thin Films. – Ivano-Frankivsk: Precarpathian University. V.S. Stefanika, 1993, part II. – P. 383.

99.   Tyurin A.V. Physicochemical processes in alkali halide crystals and chalcogenide glassy semiconductors that determine the registration of three-dimensional holograms. // Abstract of the dissertation for the degree of Doctor of Physical and Mathematical Sciences. – Odessa. - 1995. – 34 p.

100. Dyachenko N.G., Mandel V.E., Tyurin A.V. Relaxation of photoconductivity by alternating current in colored KSl crystals // FTT. - 1970. – V. 12, issue. 5. – P. 1571–1573.

101. Dyachenko N.G., Tyurin A.V., Sheveleva A.S. Generation of cationic vacancies in the process of formation and destruction of colloids in KCl crystals. // FTT.– 1974. –V. 16, issue. 5. – P. 1527–1530.

102. N.G. Dyachenko. Ionic processes in the optical destruction of F-centers in KCl crystals with impurities. // N.G. Dyachenko, V.E. Mandel, A.V. Tyurin, A.S. Sheveleva. // Questions of solid state physics. - Kiev: Higher School, 1976. – P.71–77.

103. Amorphous semiconductors. / Ed. M. Brodsky. Tr. on English – M .: Mir, 1982. – 367 p.

104. Gubanov A.I. Quantum-electronic theory of amorphous semiconductors. – M .: AN SSSR, 1963. – 250 p.

105. Anderson F. Local moments and localized states. // UFN. 1979. – Vol. 127, № 1. – P. 19–40.

106. Mott N., Devis Z. Electronic processes in noncrystalline substances. – M .: Mir, 1982. V. 1. – 368 p. – Vol. 2. – 664 p.

107. Marshall J.M., Owen A.E. Localized states in the gap of amorphous semiconductors. // Phil. Mag. - 1971. – V. 24, N 2. P. 1281 – 1285.

108. Sumrov A.V., Pirogov F.V. Density of localized states at the edge of the valence band of chalcogenide glasses from the concentration series As_xS_{100-x} and As_xSe_{100-x}. // Izv. Academy of Sciences of Latvia SSR. Ser. physical and technical Science. – 1980, – № 2. – P. 35–42.

109. Ovshinsky S.R., Fritsche H. Localized states in the gap in amorphous semiconductors. // IERB Trans. Electron devices. – 1973. –V. 20, N 1. –P. 91-98.

110. Mott H. F. State in the gap in amorphous semiconductors. // Phil. Mag. – 1966. – V. 13, N 6. – P. 989-994.

111. Mott H. F. Electronic processes in amorphous semiconductors. // Advances in physics. – 1967. – V. 16, N 1. – P. 49- 54.

112. Mott H. F., Davis E. A., Street R. A. States in the gap and recombination in amorphous semiconductors. // Phil. Mag. – 1975. – V. 32, N 4. – P. 558-567.

113. Mott N. Electrons in glassy materials. // UFN. – 1979. –V. 127, № 1. P. 41–50.

114. Stys L.E., Foigel M.G. On the nature of D-centers in arsenic chalcogenides. // Letters to JETF. – 1979. –V. 29, issue 4.– P. 209–212.

115. Mott N., Devis E. Electronic processes in noncrystalline substances. - M .: Mir, 1974. – 472 s.

116. Austin I.G., Mott N. F., at all. Conductivity in semiconductors. // Advances in physics. – 1969. – V. 18, N 1. – R. 41–54.

117. Kosek E., Taus J. The absorption edge of amorphous As_2S_3. // Czech. J. Phys. – 1970. – V.B20, N1. – P.94-99.

118. V.S. Vakarov. Hopping conductivity of As_2S_3 films. / V.S. Vakarov, A. Yu. Popov, L.E. Stys, etc. // UFZh, – 1965. – V. 30, № 3. – P. 394-397.

119. Vinetsky V.L., Kholodar G.A. Static interaction of electrons and defects in semiconductors. – Kiev: Naukova dumka, 1969. –186 p.

120. Vorobiev A.A. Ionic and electronic properties of alkali halide crystals. – Tomsk: TSU, 1968. – 306 p.

121. Dyachenko N.G., Tyurin A.V., Sheveleva A.S. Conduction mechanism of additively colored KCl crystals. // Deposited in VINITI, № 7393-73 Dep. – 1973. –11 p.

122. Dyachenko N.G., Tyurin A.V., Sheveleva A.S. Generation of cationic vacancies in the process of formation and destruction of colloids in KCl crystals. // FTT. – 1974. –V. 16, issue. 5. – P. 1527–1530.

123. Mott N. Electrons in disordered structures. – M .: Mir, –1969. –172 p.

124. Kastner M. Defect chemistry of lone-pair semiconductors. // Phil. Mag. – 1976. – V.37 , N 2. – P. 199-215.

125. Mashkovtsev R.I., Zuckerman V.G. On the nature of photoinduced paramagnetic centers in the system *As-S*. // Autometry. – 1980. – № 6. – P. 91–93.

126. Kastner M., Adler D., Fritsche H. Valence-alternation model for localized gap states in lone-pair semiconductors. // Phys. Rev. – 1976. – V. 37, № 2. – P. 1504-1507.

127. Elliot S. R. A.c. conductivity due to intimate pairs charged defect centers. // Solid State Commun. – 1978. – V. 27, N 8. – P. 749-751.

128. Kastner M. Bonding bands, lone-pair bands and impurity states in chalcogenide semiconductors. // Phys. Rev. –1972. – V. 28, N 6. – P. 355-363.

129. Karnatovsky E.E., Zuckerman V.G. On the possibility of temperature control by the properties of holograms in carriers based on chalcogenide glassy semiconductors. // Quantum electron. –M., 1977. – V. 4, № 6. –P. 1296–1298.

130. Kolomiets B.T. Peculiarities of photoconductivity kinetics of arsenic selenide layers in the visible and X-ray regions of the spectrum. / Kolomiets B.T. et al. // FTP. –1972. – V. 6, № 9. –P. 2144–2145.

131. Andriesh A.M. Long-term kinetics of photoconductivity of arsenic vitreous sulfide. / Andries A.M., etc. // Crystal and glassy semiconductors. -Chisinau: Stiinza, 1977. – P. 118–126.

132. Tsiulyanu D.I., Tridukh G.M. On the flash nature of the photo response in thin layers of some glassy semiconductors. // FTP. – 1980. – V. 14, № 4. –P. 634–637.

133. Street R. A. Luminescence anamorphous semiconductors. // Advances in Physics. – 1976. – V. 25, N 4. – P. 397-454.

134. Byub R. Photoconductivity of solid thermals. – M .: IL, 1962. – 559 p.

135. Ryvkin S.M. Photoelectric phenomena in semiconductors. – M .: Izd-vo fiz.-mat. lit., 1963. – 496 p.

136. Loshkarev V.E., Lyubchenko A.V., Sheikman M.K. Non-equilibrium processes in photodetectors. – Kiev: Naukova dumka, 1981. – 263 p.

137. Rose A. Fundamentals of the theory of photoconductivity. M.: Mir, 1966. – 192 p.

138. Kolomiets B.T., Lyubin V.M. Some features of photoconductivity in amorphous layers of three-selenium arsenic. // DAN SSSR. – 1959. –V. 129, № 6. – P. 789–792.

139. Kruglov V.I., Strakhov L.P. Photosensitivity of the vitreous system *As-Se*. // FTP. – 1970. –V. 4, № 8. –P. 1541–545.

140. V.L. Averyanov. Temperature dependence of photoconductivity in As2S3 layers. / V.L.Averyanov, L.N. Karpova, B.T. Kolomiets and others // FTP. – 1972. – V. 6, № 9. –P. 1709–1713.

141. Kolomiets B.T., Mamontova T.K., Stepanov T.N. Fluctuation levels in a glassy semiconductor $Tl_2Se\ As_2Te_3$. // FTP. – 1967. – Vol. 9, issue 1. – P. 27–30.

142. Kruglov V.I., Bobrov A.I. Lux-ampere characteristics of photoconductivity in amorphous semiconductors. // Vestnik LSU. – 1966. –V. 10. –P. 125–130.

143. Main C., Owen A. E. Photoconductivity in amorphous semiconductors. // Electronic and structural Properties of Amorphous Semiconductors. – 1973. – P. 527–541.

144. Kolomiets B.T., Lyubin V.M. On the question of the mechanism of photoconductivity in amorphous chalcogenide layers. // FTT. – 1960, – Vol. 2, issue 1. – P. 52–54.

145. Stys L.E., Foigel M.G. Long-term relaxations of photoconductivity in chalcogenide glassy semiconductors. // FTP. 1981 – V. 15, № 4. P. 761–707.

146. Halpern V. On the photoconductivity of amorphous chalcogenide semiconductors. // Phil. Mag. – 1978. – V. 37, No 4. –P. 423–434.

147. Karnatovsky V.E., Remesnik V.G., Zuckerman V.G. High-efficiency phase recording of holograms on chalcogenide films in the region of elevated temperatures. // Quantum electronics. – 1980. – V. 7, № 5. – P. 1110–1112.

148. Abashkin V.G., Andriesh A.M., Ponomar V.V. Nonlinear light absorption in fibers of arsenic vitreous sulfide in the energy range hν <Eg. // Quantum electronics. – 1962. – V. 9, № 10. – P. 2070–2076.

149. Sheikman M.K., Shik A. Ya. Long-term relaxation of conductivity and residual conductivity in semiconductors. // FTP. – 1976. – Vol. 10, issue 2 – P. 209–233.

150. Kastner M., Hudgens S.J. Evidence for the neutrality of luminescence centers in chalcogenide glasses. // Phil. Mag. – 1978. – V. 37, N 6. –P. 665–681.

151. Street R.A., Lucovssky G. Ionicity effects on defects in glasses. // Solid State Commun. – 1979. – V. 31, N 5. –P. 289–293.

152. Greaves G. M., Elliot S. R., Davis E. A. States in the gap in amorphous compounds. // Advances in Physics. – 1979. – V. 28, N 1. P. 49-58.

153. Strom V., Martin T. F. Photo-induced changes in the infrared vibrational spectrum of evaporate As_2S_3. // Sol. State Commun. – 1979. – V. 29, № 4. – P. 527-530.

154. Gurevich S.B. Reversible recording of holograms on chalcogenide glass films. // ZhTP. – 1973. –V. 43, issue 1– P. 217–219.

155. Lyubin B.M., Fedorov V.A. Reversible effect of photoenlightenment in films of chalcogenide glassy semiconductors of the system As-S. // FTT. – 1981. – V. 23, issue 8. – P. 2315–2330.

156. Malinovsky V.K., Novikov V.N. Non-equilibrium phonons and photo-structural transformations in chalcogenide glasses. // Preprint № 214. – Novosibirsk: Inst. Of Automation and Electrometry, USSR Academy of Sciences, 1983. – 11 p.

157. Turyanitsa I.I., Kikineshi A.A., Semak D.G. The effect of positive photographic recording on the layers of chalcogenide glassy semiconductors // UFZh. – 1979. – V. 24, № 4. – P. 534–538.

158. J. Feinleib. Rapid reversible light-induced crystallization of amorphous semiconductors. / J. Feinleib, J. De Neufville, S. C. Moss, S. R. Ovehinsky. // Appl. Phys. Letters. – 1971. – V. 18, N 6. – P. 254-257.

159. Tanaka K., Kikuchi M. Anomalous photo induced shift optical transmission edge observed in amorphous As_2S_3 film. // Solid State Communication. – 1972. – V. 11. – P. 1311-1314.

160. V.E. Dulenov. Structural and morphological transformations in arsenic sulfide films induced by lighting and heat treatment. / V.E. Dulenov, V.A. Ivanchenko, V.G. Zuckerman, N. Yu. Chernysheva. // Autometry. – 1980. – № 6. – P. 35–91.

161. Lyubin V.M. Structural transformations and chalcogenide glassy semiconductors stimulated by various external influences. // Materials of the report. conf. "Amorphous Semiconductors-84". – Gabrovo (Bulgaria). – 1984. – V. 1. – P. 13–17.

162. D. G. Semak. Features of the dynamic component of optical recording in CGS layers. / D.G. Semak, G.G. Suran, V.I. Mikla, etc. // New recording carriers for holography. Ed. V.A. Barachevsky, – L.: Nauka, 1983. – P. 83–89.

163. D. G. Semak. Features of optical erasure recording on light-sensitive chalcogenide glasses. / D.G. Semak, A.A. Kikineshi, I.I. Turyanitsa and others // Structure, phys.-chem. properties and application of noncrystalline semiconductors. Mater., Conf. "Amorphous

semiconductors-80". – Chisinau, 1980. – P. 231–234.

164. D. G. Semak. Localized states and the mechanism of reversible photostimulated transformations in *As-S*e. / D.G. Semak, M.I. Marian, V.I. Shikla, etc. // Fundamentals of optical memory and environment. – Kiev: Higher School, 1987. – Issue. 18. – P. 52–58.

165. Street R.A. Photoconductivity of amorphous semiconductors. // Solid State. Commun. – 1981. –V. 39, N 2. – P. 263-266.

166. Turyanitsa I.I., Semak D.G. On recording on chalcogenide glasses *As-S*e. // Fundamentals of optical memory and environment, Kiev: Higher School, 1979. – Issue. 10. – P. 69–72.

167. N.G. Dyachenko. Temperature studies of photoconductivity kinetics at alternating current in glassy arsenic trisulfate. / N.G. Dyachenko, A. Yu. Popov, A.V. Tyurin and others // Abstracts. report II Republican Conference on Photoelectric Phenomena in Semiconductors. – Odessa: Higher School, 1982. – P. 109.

168. N.G. Dyachenko. On the flash nature of the kinetics of photocurrent growth in vitreous arsenic sulfide. / N.G. Dyachenko, A. Yu. Popov, A.V. Tyurin and others // Phys. and tech. semiconductors. – 1982. – T. 16, issue 10. – P. 1872–1874.

169. Dyachenko N.G., Tyurin A.V., Sheveleva A.S. Short-term electrical relaxations in alkali-halide crystals. // Izv. High School. Physics. – 1973. – № 6. –P. 101–106.

170. A. Yu. Akhmerov. Dielectric losses and luminescence of silver-doped lithium aluminophosphate glasses. / A. Yu. Akhmerov, V.V. Golubtsov, A.V. Tyurin // Ukr. phys. magazine – 1988. – V. 33, № 10. – P. 1478–1482.

171. Dyachenko N.G., Tyurin A.V., Sheveleva A.S. Relaxation phenomena in additively colored KBr crystals. // FTT. – 1972. –V. 14, issue 10. – P. 3091–3093.

172. N.E. Korsunskaya. Spectroscopic study of the interaction of local centers in CdS crystals. / N.E. Korsunskaya, I.V. Markovich, T.V. Torchinskaya, M.K. Sheinkman. // Radio engineering and electronics. 1979. – Vol. 24, № 4. – P. 829–833.

173. Scheinkman M.K. Increase in photosensitivity and luminescence intensity during photothermal dissociation of donor-acceptor pairs in CdS and CdSe. // Letters to JETF. – 1972– V. 15, issue 11. – P. 673.

174. Popov N.A. A new model of defects in chalcogenide glassy semiconductors. // Letters to JETF. – 1980. –V. 31, issue 8. – P. 437–440.

175. Foigel M.G., Bazhenov V.K., Soboleva T.N. Optical absorption in crystals with deep centers. // Meeting on deep centers in semiconductors. Summary of reports. – Odessa, 1972. – P. 111–112.

176. Street R. A. Non-reductive recombination in chalcogenide glasses. // Solid State Commun. – 1977. – V. 24, N 5. – P. 363-365.

177. Popov A. Yu. Photostimulated processes in alkali-halide crystals and chalcogenide glassy semiconductors when recording bulk holograms. // Abstract of the dissertation for the degree of candidate of physical and mathematical sciences. – Odessa. – 1995. – 24 p.

178. Magnusson R., Gailord T. K. Analysis of multi Diffraction of Thick Gratings. // Journ. Opt. Soc. Amer. – 1977. – V. 67, N 9. P. 1165-1170.

179. Yariv A., Yukh P. Optical waves in crystals. – M.: Mir, 1967. – 616 p.

180. Serdyuk V.M. Transverse diffraction of light beams on bulk gratings. // Zh.TF. – 1992. – V. 62, issue 6. – P. 126–139.

181. Pomerantsev N.M. Diffraction of light in thick layers. // UFN. – 1973. – T. 111, issue 3. – P. 507–524.

182. Magnusson R., Gailord T. K. Diffraction Regimes of Transmission Gratings. // Journ. Opt. Soc. Amer. – 1978. – V. 68, N 6. P. 809-814.

183. Khodkov Yu. A. Solution of the equation of bound waves of the second order for a three-dimensional periodic medium and diffraction efficiency of pseudo-deep holograms. // Optics and spectroscopy – 1993. – Vol. 75, issue 5. – P. 1040–1052.

184. Barachevsky V.A., Dashkov G.P., Tsekhomsky V.A. Photochromism and: its application. – M.; Chemistry, 1977. –280 p.

185. Kogelnik H., Coupted wave theory for thick hologram grating. // Bell. Syst. Techn. – 1969. V. 48, N 9. – P. 2909–2947.

186. Markov V.B., Odulov S.G., Soskin M.S. Recording of phase holograms in lithium niobate crystals. // Recording carriers for holography. L .: Nauka, 1975. – P.127–134.

187. Denisyuk Yu. N., Savostyanenko N.A., Vasil'eva E.I. Peculiarities of hologram recording in reoxane recording medium. // UFN. – 1990. –V. 26. –P. 139–143.

188. Miteeva M.G., Sharlandzhiev P.S. On the experimental separation of the amplitude and phase components of holographic recording. / Materials of the XI All-Union School of Holography. – L .:

LIAF, 1978. –P. 49–57.

189. Tomlinson W. J., Aumiller G. D. Technique for measuring refractive index changes in photochromatic materials. // Appl. Opt. – 1975. – V. 14, N 5. – P. 1100–1104.

190. Bader T. R. Hologram Gratings: Amplitude and phase components. // Appl. Opt. – 1975. – V. 14, N 12. – P. 2818–2819.

191. Zverkov V.A., Savelyev V.V., Vannikov A.V. Holographic methods for the study of photochemical processes in condensed matter and new materials for holographic recording of information. // Successes of scientific photography – 1990. – Vol. 27. – P. 89–102.

192. Bader T. R. Hologram Gratings. Amplitude and Phase components. // Appl. Opt. –1975. – V. 14, N 12. – P. 2818-2819.

193. Belous V.M., Mandel V.E, Popov A. Yu., Tyurin A.V. Determination of amplitude and phase modulations in the process of three-dimensional holographic recording. // Optics and spectroscopy – 1994. – №1. – P. 105–109.

194. Tomlinson W. J., Aumfller G. D. Technique for refractive index changes in photochromatic materials. // Appl, Opt. – 1975. – V. 14, N 5. – P. 1100–1104.

195. Landsberg G.S. Optics. – M .: Nauka, 1976. – 926 p.

196. Vinetsky V.L., Kukhtarev N.V. Dynamic holography. – Kiev: Naukova Dumka, 1983. – 86 p.

197. Alekseev-Popov A.V., Gevelyuk S.A. Influence of the shift between amplitude and phase components on the properties of three-dimensional amplitude-phase holograms. // Optical holography with recording in three-dimensional carriers.– L .: Nauka, 1989. – P. 25–32.

198. Miller M. Holography. – L .: Mashinostroenie, 1979. – 207 p.

199. A.V. Alekseev-Popov. Features of hologram recording in KCl crystals based on F-X transformation. / A.V. Alekseev-Popov, N.G. Dyachenko, V.E. Mandel, A.V. Tyurin. // Letters in ZhTF – 1979. – Vol. 5, issue. 12. – P. 709–712.

200. Alekseev-Popov A.V. On the limiting diffraction efficiency of bulk amplitude holograms. // ZhTF. – 1981. – V. 51, № 6. – P. 1275–1278.

201. D.A. Vladimirov, V.E. Mandel, A. Yu. Popov, A.V. Tyurin. Optimization of hologram recording on additively colored KCl crystals. // Optics and spectroscopy. – 2005. – V. 99, № 1. – P. 155–158.

202. Biegelsen D.K., Street R.A. Photo induced Defects in Chalcogenide Glasses. // Phys. Rev. Lett. – 1980. V. 44, N 12. P. 803–806.

203. Kolomiets B.T., Lyubin V.M., Fedorov V.A. Features of the enlightenment effect in vitreous films *As-S* // Letters to ZhTF.– 1979. –Vol. 5, issue. 1. – P. 3–8.

204. V.M. Belous, V.E. Mandel, A. Yu. Popov, A.V. Tyurin, Yu. B. Shugailo. Diffusion mechanism of holographic recording in amorphous arsenic sulfide // Holographic research methods in science and technology: Proceedings of the School – Symposium. Yaroslavl: YAGPU them. K.D. Ушинского. – 1997 –P. 100–106.

205. Belous V.M., Mandel V.E., Popov A. Yu., Tyurin A.V. Mechanisms of high-temperature holographic recording in materials of *As-S* composition. // Solid state physics. – 1996. –V. 38, № 2. – P. 379–390.

206. Stys L.E. Bipolaron mechanism of photostructural transformations of chalcogenide glassy semiconductors. // Uspekhi nauchn. фотогр. – 1990. – V. XXVI. – P. 41–45.

207. V. M. Belous. Express method for determining amplitude and phase modulations in the process of recording a three-dimensional transmitting diffraction grating. / V.M. Belous, V.E. Mandel, A. Yu. Popov, A.V. Tyurin // Abstracts of the 16th scientific and technical conference "High-speed photography, photonics and metrology of fast-moving processes". – M .: VNIIOFI, 1993. – P. 30.

208. Stys L.E., Voigel M.G., Peculiarities of donor-acceptor recombination in weakly doped compensated semiconductors. UFTP. – 1985. – Vol. 19, issue. 2. – P. 217–223.

209. Pauling L. General Chemistry. – M.: Mir, 1973. – 360 p.

210. Teteris J. Photo induced optical absorption in *As-S*e. // Phys. Status Solidi (a), – 1984. – V. 83, N 1. – P. K47-K50.

211. Kravets A.M., Zhaksalikova A.A., Kravets F.S. Volume holograms on NaCl and NaCl: Ca crystals. // Journal of Science. and applied photography and cinematography. – 1976. – V. 21, issue 5. – P. 359–362.

212. Vorozheykina L.F., Mumladze V.V., Shatalin I.D. Holograms in irradiated crystals of potassium chloride. // Magazine app. spectroscopy. – 1978. –V. 29, issue 3. – P. 552–554.

213. Verezin P.D., Kompenets I.N., Kravets A.N. Amplitude-phase holograms on radiation-colored NaCl crystals. // Optics and spectroscopy – 1977. –Vol. 42, no. 1 – P. 180–183.

214. Tubbs M., Scrivener G. Cathodochromic and photochromic alkali halide crystals for optical information storage. // Phys. Stat. Solidi. – 1971. – A7, № 1. – P. 155-156.

215. Bessent R. C., Runciman W. A. Information storage in potassium iodide. // Brit. Journ. Appl. Phys. – 1966. – V. 17, N 8. – P. 991-993.

216. Kravets A.N., Berezik P.D. Diffraction efficiency of holograms on NaCl: Ca crystals. // Optics and spectroscopy – 1976. – Vol. 41, no. 4. –P. 634–636.

217. Mackin A.S. Holographic recording on electron beam colored sodium chloride crystals. // Appl. Opt. – 1970. – V. 9, N 7. – P. 1658–1664.

218. Melik-Gaikazyan I. Ya., Kravets A.I., Zhaksylykova A.A. Optical stability of F-centers in "split whiskers" and filamentous KCl crystals. // Izv. HighSchool. Physics. –1976. – № 1. – P. 132–135.

219. Pavlov A.N., Sedov V.V. The mechanism of low-energy photothermal recording of optical information on sodium chloride crystals. // Journal of Science. and appl. photo and cinematography. – 1988. – Vol.33, № 2. – P.114–119.

220. Pavlov A.K. Multicolor recording of optical information on NaCl: Mn crystals. // Journal of scientific and appl. photo and cinematography. – 1982. – V. 27, № 3. –P. 191–194.

221. Korenchuk A.F., Pavlov A.N., Sedov V.B. The mechanism of multicolor recording of optical information on halogenalkaline crystals. // ZhNiPFiK. – 1989. – V. 34, № 3. – P. 224–227.

222. V.V. Golubtsov. Peculiarities of radiation coloring and

recording of bulk holograms on NaCl crystals with dipole oxygen centers. / V.V. Golubtsov, A.V. Goldenberg, S.E. Lukashuk, V.E. Mandel. // Optics and spectroscopy, – 1979. – Vol. 47, no. 1. – P. 146–150.

223. Golubtsov V.V., Goldenberg A.B. Thermo-optical transformations of centers in NaCl crystals with oxygen-containing impurities. // Optics and spectroscopy, – 1977. – Vol. 42, no. 1. – P. 117–121.

224. Goldenberg A.B., Golubtsov V.V., Lukashuk S.B. Photochromic properties of additively colored oxygen-sensitized NaCl crystals. // Optics and spectroscopy, – 1978. – Vol. 44, no. 5. – P. 942–946.

225. Goldenberg A.B., Golubtsov V.V., Lukashuk S.B. Recording of the image in the far ultraviolet region of the spectrum on additively colored oxygen-sensitized NaCl crystals. // Letters to ZhTF. – 1978. – V. 4, № 7. – S. 375–378.

226. Ozols A.O. Limit characteristics of amplitude-phase holograms on additively colored KCl crystals. // Izv. Academy of Sciences of Latvia SSR, ser. phys. and tech. Science. – 1978, № 5. – P. 16–25.

227. Roder V. Storage properties of F_A-center holograms // Opt. Communs. – 1972, – V. 6, N 3. – P. 270-274.

228. Schneider I. Dispersion and diffraction by anisotropic centers in alkali halides. // Phys. Rev. Lett. – 1974. – V. 32, N 8. – P. 412-415.

229. Shono Y. Inuzuka T., Hochino T. Image Recording on F_A-centers crystals by He-Ne lazer. // Appl. Phys. Lett. – 1973. – V. 22, N 6, – P. 299-300.

230. Yazaki T., Imai T., Kishi I. The element of reversible optical memory in M-centers in NaF crystals. // Izv. USSR Academy of Sciences, ser. phys. – 1977 – Vol. 41, № 4– P. 727–732.

231. Schneider I., Gringerich M.E. Diffraction by M-centers in KCl. // Appl. Optics. – 1976. – V. 5, N 10. – P. 2428-2431.

232. Blume H. Highly efficient dichroic phase holograms in KCl:Na // Opt. Acta. – 1974. – V.21, N5. – P.357-363.

233. Nikolova L., Todorov T., Stefanova P. Polarization sensibility of the photo dichroic holographic recording. // Opt. Communs. –1978. – V. 24, N 1. – P. 44-46.

234. Baldaccini G., Gallerano G.P., Grassano U.M., Meucci M., Scacco A., Somma F., Tiourine A.V., Tonelli N. Optical Pumping and Reorietation F_A-centres in KCl:Li$^+$. // Phys. Stat. Solidi (b). – 1984. – V. 122. – K.83-K.86.

235. N.G. Dyachenko, V.E. Mandel, A.V. Tyurin, A.S. Sheveleva. Ability to use F-Z_1 transformation in KCl crystals to record optical information. // Optics and spectroscopy – 1975. – Vol.38, – P. 1023–1025.

236. Bodryagin V.I., Kudryavtsev A.A., Shatalov A.A. Recording of optical information on X-centers in crystals. // Instruments and techniques of the experiment. – 1973. – № 4.– P. 216–217.

237. Gros M. KCl:K prepared for highly efficient holographic storage. // Journ. Opt. Soc. Amer. – 1977. – V. 67, N 12. – P. 1691-1692.

238. L.F. Vorozheykina, V.V. Mumladze, T.G. Khulordova, I.D. Shatalin. Recording of holograms in irradiated NaCl crystals by helium-neon laser radiation. // Letters to ZhTF. – 1976. – Vol. 4, issue. 2. – P. 99-102.

239. K. K. Schwartz. Use of colored AHCs to record holograms. / K.K. Schwartz, D.P. Bandere, J. J. Kristapson, etc. // Problems of holography. – M .: MIREA, 1973. – Issue. 3. – P. 181–183.

240. Stadnik B., Homatt M., Hoff F. Research of new materials for holographic recording. // Autometry. – 1974, № 1. – P. 18–22.

241. Vorobiev A.A. Color centers in alkali halide crystals. Tomsk: TSU, 1968. – 390 p.

242. A.V. Alekseev-Popov, N.G. Dyachenko, V.E. Mandel, A.V. Tyurin. Dispersion of optical parameters in thick amplitude-phase holograms. // Optics and spectroscopy – 1979. –Vol. 47, no. 3. – P. 583–587.

243. N.G. Dyachenko, V.E. Mandel, T.A. Nechaeva, A.V. Tyurin. Recording of amplitude-phase holograms at colloidal type centers in NaCl crystals. // УФЖ. – 1980. – V. 25, № 4. – P. 622–627.

244. Mandel V.E. Recording of bulk phase holograms on additively colored KCl: Cu crystals. // Letters to ZhTF. – 1977. – Vol. 3, issue. 19. – P. 999–1002.

245. A.c. № 686523 (USSR). Crystal for recording phase holograms. / N.G. Dyachenko, V.E. Mandel, A.V. Tyurin, A.S. Sheveleva. – 1979.

246. A.c. № 586524 (USSR). Crystal for recording phase holograms. / N.G. Dyachenko, V.E. Mandel, A.V. Tyurin, A.S. Sheveleva. –1979.

247. N.G. Dyachenko, V.E. Mandel, T.A. Nechaeva, A.V. Tyurin. Recording of holograms based on F-X transformation of color centers in additively colored KBr crystals. // UPhZH. – 1987. – V. 32, № 3. – P.

361–362.

248. A.c. № 1327705 (USSR). Crystal for recording holograms. / N.G.Dyachenko, V.E. Mandel, T.A. Nechaeva, A.V. Tyurin. – 1987.

249. A.c. 1459490 (USSR). A method of manufacturing a bulk diffraction grating in additively colored KCl crystals. / N.G. Dyachenko, V.E. Mandel, T.A. Nechaeva, A.V. Tyurin. –1988.

250. N.G. Dyachenko. Volumetric diffraction grating based on alkali halide crystal. / N.G. Dyachenko, V.E. Mandel, A.V. Tyurin et al. // Abstracts of the 4th All-Union Scientific and Technical Conference "Photometry and its metrological support". – M.: VNIIOFI, 1982. – P.412.

251. A.V. Alekseev-Popov. Recording and storage of optical information at colloidal type centers in alkali-halide crystals. / A.V. Alekseev-Popov, N.G. Dyachenko, A.V. Tyurin, etc. // Abstracts of the seventh All-Union seminar on optical and electro-optical methods and means of transmission, transformation, processing and storage of information. – Moscow: Institute of Management Problems, 1981.– P. 13-14.

252. Alekseev-Popov A. Yu., Gevelyuk S.A., Tyurin A.V. Influence of the structure of manifested silver on the spectral characteristics of volumetric holograms. // Proceedings of the IV All-Union Conference on Holography. – Riga; IFAN, 1985. – Vol. 1. – P. 67–68.

253. A.c. № 533079 (USSR). Photochromic material. / N.G. Dyachenko, V.E. Mandel, A.V. Tyurin, A.S. Sheveleva. – 1976.

254. Alekseev-Popov A.V., Gevelyuk S.A. Determination of the

contributions of amplitude and phase modulation to the diffraction efficiency of bulk holograms. // Optical holography. - L .: Nauka, 1983. – P. 14–24.

255. Bendall C. R., Guenther B. D., Hartman R. L. Thick amplitude holograms: effect of nonlinear recording. // Appl. Opt. – 1972. – V. 11, N 12. – P. 2992-2993.

256. Kermisch D. Efficiency of Photochromic Gratings. // J. Opt. Soc. Am. – 1971. – V. 61, N 9. – P. 1202-1206.

257. Bodryagin V.I., Andyshula N.A. Thermal transformation of X-centers in NaCl crystals. // FTT.– 1974. – V. 16, № 4. – P. 1010–1014.

258. N.G. Dyachenko, V.E. Mandel, A.V. Tyurin, A.S. Sheveleva. Using selective destruction of colloid-type centers to record high-performance holograms on alkali-halide crystals. // Letters to ZhTF. – 1979. – Vol.5, issue. 13. – P. 791–795.

259. Bezruchko V.M. Periodic dichroism of colored alkali-halide crystals induced by plastic deformation. // FTT. 1972. – T. 14, issue 10. – P. 2935–2939.

260. Golubtsov V.V., Glauberman A.E., Goldenberg A.E. Anisotropy of alkali-halide crystals with quasi-metallic and colloidal centers. // FTT. – 1975. – V. 17, № 10. – P. 3053–3056.

261. Mandel V.E., Nechaeva T.A., Tyurin A.V. Influence of *X*-center anisotropy on the diffraction efficiency of holograms recorded in KCl based on F-X transformation. // Letters to ZhTF. – 1981–V. 7, issue 8. – P. 492–493.

262. Bezruchko V.M., Bodryagin V.I., Shatalov A.A. Anisotropy of colloids and the Weigert effect in sodium chloride crystals. // FTT. –

1970. – T. 12, vp. 4. – P. 1091–1094.

263. Belous V.M., Mandel V.E., Popov A. Yu., Tyurin A.V. Holographic recording mechanisms based on photothermal transformation of color centers in additively colored alkali-halide crystals. // Optics and spectroscopy. – 1999. –V.87, № 2. – P. 305–310.

264. Popov A. Yu., Tyurin A.V., Vladimirov D.A. Computer modeling of photoinduced diffusion-drift instability in space-periodic light fields. // Bulletin of Cherkasy University series "Physical and Mathematical Sciences". – 2003. – Issue. 53. – P. 122–131.

265. Zeldovich B. Ya., Shkunov V.V., Yakovleva T.V. Calculation of noise and quantitative substantiation of the mode theory of volume holograms. // UFN. –1986. – Vol. 149, no. 3–P. 511–525.

266. Ragnarsson S. Scattering effects in thick holograms. // Appl. Opt. – 1978. – V. 17, N 1. – P. 116-127.

267. Magnusson R., Gaylord T. Lager scattering induced holograms in LiNbO$_3$. // Appl. Opt. – 1974. – V. 13, N 7. – P. 1545-1548.

268. Sturman B. Goulkov M., Odoulov S. Polarization degenerate parametric light scattering in photorefractive crystals. // Appl. Phys. B. – 1993. – N 56. – P. 193-199; 223–228.

269. Gulkov M. Yu. Light-induced selective light scattering in photorefractive crystals in schemes with two pump beams. / Abstract of Cand. dissertation. – Kiev: Institute of Physics of the Academy of Sciences of Ukraine. – 16 p.

270. Yakimovich A.P. Dynamic self-amplification of scattering noise when recording bulk holograms. // Optics and spectroscopy. – 1980. –V. 49, issue. 2. – P. 354–358.

271. V.E. Mandel, V.A. Neklyudov, A. Yu. Popov, A.V. Tyurin. Scattering effects in volumetric holograms. // Optics and spectroscopy. – 1991. – V. 70, issue. 6. – P. 1286–1290.

272. Denisyuk Yu. N., Savostyanenko N.A., Zubritskas V.I. The effect of partial reduction in volumetric holograms. // Optics and spectroscopy. – 1987. –V. 63, issue. 5. – P. 1100–1104.

273. Aristov B.V. Shekhtman V.S. Properties of three-dimensional holograms. // UFN. – 1971. – T. 104, issue 1. – P. 51–76.

274. Vinetsky V.L., Feingold M.I. Regimes of Bragg diffraction and light channeling in bulk gratings. // UPHZH. – 1984. –V. 29, № 11. –P. 1628–1631.

275. Butters J. Holography and its application. – M .: Energiya, 1977. –224 p.

276. V.V. Belza. Optical elements based on chalcogenide glasses. / V.V. Belza, Yu. Yu. Blinets et al. // Journal. appl. spectroscopy. –1983. – V. 39, № 2. – P. 295–299.

277. R. R. Gorin. Hologram optics at the Vavilov State Pedagogical Institute. / R.R. Gorin, S.N. Koreshev, G.B. Semenov, V.V. Smirnov. // Optical magazine. – 1994. – № 1. – P. 26–39.

278. Barachevsky V.A., Kozenkov V.M. Non-silver and unusual light-sensitive materials for holography and optical information processing. // Сб. "Recording carriers for holography". – L.: Science. – 1975. – P. 26–41.

279. Dmitriev A.L. Volumetric holograms in devices of fiber-optic information transmission systems. // Optical holography with recording in three-dimensional carriers. – L.: Nauka, 1989. – P. 112–117.

280. Turukhano B.G., Turukhano N., Methods for creating two-coordinate holographic diffraction gratings. // Application of holographic methods and tools. –L.: FTI. – 1989. – P. 175–184.

281. Mandel V.E., Nechaeva T.A., Popov A. Yu., Ryzhkov A.V., Tyurin A.V., Shugailo Yu. B. Application of a three-dimensional stationary lattice for amplitude modulation of light. // Optical magazine. –1994, № 10. – P. 19–21.

282. Belous V.M., Mandel V.E., Popov A. Yu., Tyurin A.V., Shugailo Yu. B. Method for measuring small linear displacements in the nanometer range. // Reports of the Academy of Sciences of Ukraine.– 1994, № 9.–P.p. 91–94.

283. Mandel V.E., Popov A. Yu., Tyurin A.V., Shugailo Yu. B. Non-contact method for measuring linear displacements. // Optical magazine.–2003. –V. 70, № 6.–P.p. 57–61.

284. Zelenin V.S., Mandel V.E., Tyurin A.V. Angle measuring device based on three-dimensional diffraction gratings. // Scientific instrumentation. – 1991, issue 4. – P. 95–98.

285. Dyachenko N.G., Mandel V.E., Nechaeva T.A., Tyurin A.V. Light separator on a volumetric holographic diffraction grating. // Instruments and techniques of experiment - 1984, № 4. – P. 241–242.

286. Mandel V.E., Popov A. Yu., Tyurin A.V. High-speed spectroradiometer with hologram optical element. // Abstracts of the XVI All-Union Scientific and Technical Conference "High-speed photography, photonics and metrology of fast-moving processes". – Moscow. – 1993. –P. 23–25.

287. V.M. Belous, V.E. Mandel, A. Yu. Popov, A.V. Tyurin. The

use of volumetric diffraction gratings in some optical measuring devices. // Abstracts of the XV All-Union Scientific and Technical Conference "High-speed photography, photonics, and metrology of fast-moving processes". - M .: VNIIOFI. – 1991. –P. 56.

288. A.c. № 1696855 (USSR). Two-coordinate optoelectronic protractor. / K.A. Garibashvili, N.G. Dyachenko, A.V. Tyurin and others – 1991.

289. Mustel E.R., Parygin V.N. Methods of light modulation and scanning.–M .: Science. 1970–295 p.

290. Kapichin I.I. Optoelectronic angle measuring systems. – M .: Tekhnika, 1966. – 321 p.

291. V.P. Klochkov, L.F. Kozlov, I.V. Potykevich, M.S. Soskin. Laser anemometry, remote spectroscopy and interferometry. // Handbook. – Kiev: Naukova dumka, 1985. – P. 180.

292. Belous V.M., Mandel V.E., Popov A. Yu., Tyurin A.V., Zaremba V.G., Gotsulsky V. Ya., Sidorov V.I. Laser Doppler anemometer with hologram optical element. // Proceedings of the 2nd regional scientific and technical exhibition "Perspective XXI", Odessa. – 2000. – P. 31.

293. Gurin V.S. Scanning tunneling microscopy and registration of information at the nanometer level. // Journal. scientific and approx. photos. – 1993. – V. 38. № 3. – P. 67–68.

294. Davydov V.N. Optical scheme of an interferometer for measuring the displacements of a two-coordinate table of a lithographic installation. // Optical magazine. – 1993, № 1. – P. 77–78.

295. Korotkevich V.P., Khanov V.A. Modern laser interferometers.

– Novosibirsk: Nauka, 1985. – 184 p.

296. A.c. №1426186 (USSR). Optoelectronic device for measuring angular displacements and sighting. / A.V. Alekseev-Popov, G. Ya. Kivensor, N.M. Ramishvili, A.V. Tyurin. – 1988.

297. Markov B.G., Khizhnyak A.I., Shishkov V.F. Angular selectivity of volumetric phase holograms recorded by a speckle structure. // UGZh. – 1985. –V. 30, № 4. – P. 508–510.

298. Darsky A.M., Markov V.V. Volume holograms with reference monodisperse speckle wave. // Quantum electrodynamics. – 1989. – V. 16, № 3. – P. 1060–1067.

299. Soskin M.S., Vasnetsov M.V., Basistiy I.V. Optical wavefront dislocations. // SPIE Proceedings.–1995–Vol. 2647–P. 57–62.

300. Bekshaev A. Ya. Mechanical properties of the light wave with phase singularity. // SPIE Proceedings, 1999. – Vol. 3904. – P. 131-139.

301. Arsenyan T.I., Korolenko P.V., Kulagina E.A., Fedotov Ya. Ya. Estimation of the structural characteristic of the refractive index fluctuation in the distribution of wavefront dislocations in the interference pattern. // Radio engineering and electronics.–1994–V. 39.–№ 9.–P.p. 1247–1251.

302. Butkovskaya V.V., Volyar A.V., Fadeeva T.A. Vortex optical effect of Magnus in multimode fibers. // Letters to ZhTF.–1997–V. 23,–№ 16.–Pp. 76-81.

303. Angelsky O.V., Besaha R.N., Mokhun I.I., Sopin M.O. About thin structure of speckle field. // SPIE Proceedings.–1996–Vol. 2778–P. 357–358.

304. Green L.E., Korolenko P.V., Fedotov I.N. On the generation of laser beams with a helical structure of the wavefront. // Optics and spectroscopy.–1992–V. 73.–№ 5.–Pp. 1007–1010.

305. Alexeyev A. N., Borodavka O. S., Shvedov V. G., Zhilaitis V. Z. Birth and evolution of the optical dipoles on the dielectrical transparent wedge. // SPIE Proceedings, IV International Conference "OPTDIM99" – 1999. – Vol. 2487. – P. 56.

306. Soskin M. S. International Conference on Singular Optics. // SPIE Proceedings. – 1997. – Vol. 3487. – P. 156.

307. Angelsky O. V., Besaha R. N., Mokhun I.I. Appearance of wavefront dislocations under interference among beams with simple wavcfronts. // SPIE Proceedings. – 1997. – Vol. 3317. – P. 97–100.

308. Popov A.Yu., Manchenko L.I., Tyurin A.V., Shugailo Yu.B. Registration and reproduction of light beams with topological defects. // Photoelectronics. – 2000. – Issue. 9. – P.126–129.

309. Bekshaev A., Sviridova S., Popov A., Rimachevski A., Tyurin A. Optical vortex generation by volume holographic elements with embedded phase singularity: Effects of misalignments // Ukr. J. Phys. Opt. – 2013– Volume 14 – Issue 4 – P. 171–186.